Spectroscopy of neutron-deficient Tellurium isotopes using a large γ-ray spectrometer plus ancillary detectors

Thesis submitted in accordance with the requirements of
the University of Liverpool for the degree of Doctor in Philosophy

by

Andrew John Boston

Oliver Lodge Laboratory

February 1999

I'm sure glad that's over with. But you know, I've learned something today.

Season 1 episode 12

South Park, 1998

This thesis is dedicated to my Mum and Dad.

Abstract

High spin states in the neutron deficient isotopes ^{109,110}Te have been populated, using the ^{58}Ni(^{58}Ni,2pα)^{110}Te and ^{58}Ni(^{58}Ni,2pαn)^{109}Te exit channels, respectively. The experiment was performed at the Lawrence Berkeley National Laboratory using a 250 MeV ^{58}Ni beam, supplied by the 88 inch cyclotron, incident on a thin ^{58}Ni target. The GAMMASPHERE γ-ray spectrometer has been used in conjunction with the MICROBALL charged particle detector and an array of neutron detectors in order to provide clean exit channel selection.

A detailed spectroscopic study of the even-even ^{110}Te nucleus has established a number of new low-spin band structures. Cranked shell model calculations have been used to assign possible configurations for the newly observed structures. These structures have revealed evidence for octupole correlation effects at moderate spin. Evidence is also cited for the existence of specific non-collective oblate states which are able to compete with rotational structures in this regime.

Four high-spin $\Delta I = 2$ band structures showing the characteristics of smooth band termination have been identified for the first time. Possible configurations are proposed for these structures using calculations based on a configuration-dependent shell-correction approach using a cranked Nilsson potential without pairing correlations.

Two $\Delta I = 1$ coupled band structures showing characteristic cross-over γ-ray transitions have been identified. These bands are observed to extend up to high spin and provide the first evidence in the A$\sim$110 region of the nuclear chart for coupled smooth terminating band structures. These coupled bands have provided vital information regarding how angular momentum is generated at high-spin in nuclei within close proximity of a shell closure.

The level scheme for the even-odd ^{109}Te nucleus, has been significantly extended with the addition of two new band structures. This nucleus has provided evidence for octupole correlation effects and the existance of specific non-collective oblate states.

Acknowledgements

It seems like I've been writing this thesis for ever, so I'd like to take this opportunity to thank everybody that's helped me over the last three and a half years, apologies if I miss you out.

I'd like to thank Profs P.J. Twin and E. Gabathuler for allowing me the opportunity to pursue this research at the University of Liverpool. A special thanks goes to my supervisor, Dr. Paul Nolan, for his help and encouragement throughout the course of this work.

I'd like to thank Dr. Eddie Paul, the one man who's kept me on the straight and narrow over the last three years. The many informative discussions 'down the Oxford' about the merits of cranked Nilsson-Strutinski calculations is much appreciated. Eddie gets a special thanks for reading this entire work and not being too scathing about it, well less scathing than he was about my chillies. Dr Dave Cullen must get a special mention for being so happy the whole time, he's the only man who can make statistics sound interesting. Thanks Dave for advice on $|g_K - g_R|$ values and other high K stuff! Thanks to Dr Adrian Semple for teaching me that a trip down town was more educationally beneficial than an afternoon of work. Cheers Ade for being my 'third year'.

The computer staff must have a big mention. Over the last three years we've seen more new computers than hot dinners, so thanks go to Dr John Cresswell, Dr. Ian Hibbert, Jomar Hønsi, Janet Sampson, and Linda Pratt. Ian must get a special mention for reading this entire work and for surviving several trips to Strasbourg with us.

I'd like to thank the Engineering and Physical Sciences Research Council (EPSRC) for the receipt of a PhD Studentship and a Cooperative Award in Science and Engineering (CASE) provided by BNFL Instruments is also gratefully acknowledged.

I'd like to thank Dr John Smith for proposing the experiment that got me this far and the staff at the Lawrence Berkeley National Laboratory, who made every experiment at GAMMASPHERE run so smoothly, should receive a medal.

Well the 2nd floor nuclear structure group, rarely have a such bunch of such upstanding individuals been in a place at any one time. I'll start with Cliff Lownes and Terry Burns who single handedly have kept the second floor lab running over the years, thanks. I'd like to thank all members past and present but particularly my fellow finalists Paul Greenlees and Alan Reed. And the A$\sim$130 group that means, Dr Dave Joss, Sarah Shepherd, Helen Scraggs, Chris Fox and Andy Walker. A special thanks must go to Helen for keeping me sane and for proof reading this entire work. Thanks also to Dr Roger Allatt, Dr Duncan Applebe, Dr Kevin Cann, Dr James Cocks, Dr Sefa Ertürk, Dr Martin Smith, Dr Anna Wilson the past nuclear structure group and Alex Keenan, Steven King, Debbie Hawcroft, Ade Chewter, Mike Taylor, Neil Hammond, Colin Moore, Cath Scholey and Hannah Chantler. Thanks everyone!

Contents

Introduction

Information can be obtained about the structure of a complex nuclear system (such as the tellurium isotopes studied in this work) by observing how the nucleus behaves when exposed to extremes. Whether it be extremes of isospin, or the extreme of high angular momentum. It allows us to test nuclear models in an attempt to understand the complex many-body quantum mechanical problem that is a nucleus.

Recent developments in high resolution γ-ray spectroscopy have allowed the construction of large multi-detector arrays. In this work the GAMMASPHERE spectrometer, situated at the Lawrence Berkeley National Laboratory, has been used to obtain a large high statistics data set containing information about nuclei situated in the A$\sim$110 region of the nuclear chart.

The extremely neutron deficient region of the nuclear chart with A$\sim$110, contains a wealth of nuclear structure information. The physics of the region is dominated by the close proximity of the Z=50 spherical closed shell, which has the consequence that nearby nuclei have a close to spherical ground state configuration. This manifests itself with the observation of strongly single particle level structures typified in nuclei such as ^{108}Sn [wad96] and ^{109}Sb [sch96] at low spin.

These exotic proton rich nuclei provide an ideal case in which to observe the competition between the collective and single particle degrees of freedom. With a limited number of valence nucleons available outside the ^{100}Sn closed core, collective modes of excitation are theoretically possible. In this valence space level structures may be observed up to termination. If the nucleus is excited into a high spin state the opportunity to investigate how angular momentum is generated in nuclei close to a shell closure is afforded.

This thesis concerns the study of the extremely neutron deficient tellurium isotopes ^{109}Te and ^{110}Te. Chapter one introduces the important concept of nuclear models which are used to describe the complex nuclear system. The high-spin high-statistics experiment performed at the GAMMASPHERE γ-ray spectrometer is described in chapter 2, along with the techniques used to isolate ^{109,110}Te from the total data set. The experimental results obtained are presented in chapter 3. Chapter 4 contains a discussion of the results. Aspects of the band structures obtained are compared with theoretical calculations in an attempt to characterise the observed nuclear structure phenomena. Finally chapter 5 offers a brief conclusion to this work, along with suggestions for future study. Significant proportions of the results have been submitted to international scientific journals.

Chapter 1

Nuclear Models

Introduction

The nucleus is a complex quantum mechanical object. In order to gain a full understanding of the experimental nuclear structure information obtained in a high-spin nuclear structure experiment, a knowledge of nuclear theory is required. Nuclear models have been developed in an attempt to describe experimentally observed nuclear phenomena in heavy nuclei, where the complexity of solving analytically the mathematics of the many-body problem would be too complex. This chapter discusses the modified harmonic oscillator potential which is used to describe a deformed nucleus as part of the Nilsson model. Collective and single-particle rotational degrees of freedom are introduced and discussed in the context of this work. Finally octupole deformation is introduced in an attempt to detail the more exotic nuclear shapes that are observed in nuclei with N$\sim$Z$\sim$56.

1.1 The Shell Model

1.1.1 Introduction

One of the first models which attempted to explain the properties of the nucleus was the liquid drop model (LDM). It relied on analogies between the nucleus and a liquid drop such as its very low compressibility and a well defined surface. However experimental evidence for magic numbers (N or Z = 2, 8, 20, 28, 50, 82 and 126) indicated that nuclei with these combinations of protons or neutrons were more tightly bound than the LDM predicted.

The shell model provided remarkable clarification of the complicated details of atomic structure, therefore it was extended into the nuclear regime. In the atomic shell model, shells were filled with electrons in order of increasing energy, consistent with the requirements of the Pauli principle. The transformation of this model to the nuclear case required a radical rethink of two major assumptions.

Firstly, in the atomic case the potential was supplied by the Coulomb field of the nucleus. In the nuclear case the fundamental assumption of the shell model is that the motion of a single nucleon is governed by an average potential generated by all the other nucleons. Secondly, in the atomic case the electrons move freely in orbits, relatively free from collisions with other electrons. In the nuclear case it is assumed that collisions cannot occur. This assumption is based on the the fact that if two well bound nucleons collide the energy required to excite one of them to the valence band required more energy than the nucleons are likely to transfer. Therefore the model assumes nucleons move in almost unperturbed single-particle orbits within the nucleus.

The shell model Hamiltonian is composed of the average potential plus the sum of the individual kinetic energies of all the independent nucleons,

$$H = \sum_{i=1}^{A} \left[T_i + V_i(r) \right]. \tag{1.1}$$

T_i presents the individual kinetic energies of the nucleons, $V_i(r)$ represents the form of the potential. The choice of nuclear potential is important; it should be able to account for the considerable differences between the motion of nucleons at the nuclear surface and those within the interior. However, without the inclusion of a non-central component, the choice of potential will not be able to predict the correct magic numbers. Examples of common nuclear potentials, which have been used to model the nuclear potential include the square well, the harmonic oscillator and the Woods-Saxon. A representation of these potentials is shown in Fig. 1.1. The square well potential is a somewhat over simplified description, therefore it is not discussed in the following sections.

1.1.2 The Harmonic Oscillator Potential

The harmonic oscillator potential can be written,

$$V(r) = -V_0 + \frac{1}{2} M \omega^2 r^2, \tag{1.2}$$

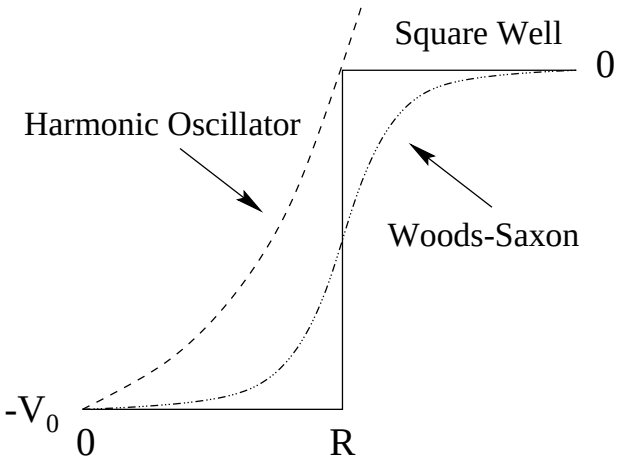

Figure 1.1: An illustration of three nuclear wells which have been used to model the nuclear potential.

where V_0 is the well depth, M is the mass of a nucleon and ω is the frequency of the simple harmonic motion of the particle. The potential tends to infinity for large r. The eigenvalues of the Hamiltonian are,

$$E_N = \left(N + \frac{3}{2}\right)\hbar\omega \tag{1.3}$$

where N is the total number of oscillator quanta. For each value of N there is a degenerate group of levels with different orbital angular momentum quantum number l, defined as $N = (2n + l)$, where n is the radial quantum number. The parity of the levels is given by,

$$\pi = (-1)^N. \tag{1.4}$$

The levels belonging to a specific N are termed an oscillator shell and each can be occupied by $(N + 1)(N + 2)$ identical nucleons; the total occupations and labels are shown in table 1.1. The harmonic oscillator potential predicts the first three magic numbers correctly, however for heavier nuclei the results are poor. In order to improve the model the effect of a spin-orbit interaction was considered.

Nucleons have an intrinsic spin, therefore a non-central spin-dependent force can be added to the harmonic oscillator potential in the form of a spin-orbit coupling,

$$V(r) \rightarrow V(r) + V_{so} \quad ; \quad V_{so} = f(r)\mathbf{l}.\mathbf{s} \quad ; \quad f(r) = \lambda\frac{1}{r}\frac{d}{dr}V(r). \tag{1.5}$$

$\mathbf{l}$ is the orbital angular momentum quantum number, $\mathbf{s}$ is the intrinsic spin angular momentum quantum number and $f(r)$ is the strength of the spin-orbit coupling. The angular

N	Levels	$E_N\,(\hbar\omega)$	Occupation	Total
0	1s	3/2	2	2
1	1p	5/2	6	8
2	1d,2s	7/2	12	20
3	1f,2p	9/2	20	40
4	1g,2d,3s	11/2	30	70

Table 1.1: Harmonic oscillator potential results

momenta couple to give the total angular momentum $\mathbf{j}$,

$$\mathbf{j} = \mathbf{l} + \mathbf{s}. \tag{1.6}$$

The potential splits the degenerate levels with $j = l \pm \frac{1}{2}$. The $j = l + \frac{1}{2}$ states are lowered in energy relative to the $j = l - \frac{1}{2}$ states resulting in each j state holding $2j + 1$ identical particles. The splitting is proportional to l which has the effect of lowering levels with the highest j quantum numbers allowing them to penetrate into the major oscillator shell below $(N - 1)$. These states are termed intruder states and are of opposite parity to the natural states. The inclusion of the spin-orbit force allows the model to correctly predict all the experimentally established magic numbers. The states are now labelled by nlj, eg $2d_{5/2}$.

1.1.3 The Woods-Saxon Potential

The Woods-Saxon potential represents the most realistic nuclear potential, chosen as a intermediate example of the square well and harmonic oscillator potentials. The potential has the form,

$$V(r) = \frac{-V_0}{1 + \exp[(r - R_0)/a]}, \tag{1.7}$$

where R_0 is the mean nuclear radius and $a \sim 0.5$fm is the surface diffuseness.

1.2 Deformation Parameters

In order to fully describe a realistic nuclear shape, the concept of nuclear deformation has to be introduced. The most important type of nuclear deformation is quadrupole, which corresponds to an ellipsoidal shape for the nuclear surface. This type of deformation is

denoted X_2 where X is the deformation parameter. Octupole, hexadecapole and higher degrees of freedom are denoted by X_3, X_4, ...

Two primary shape parameterisations have been developed in order to describe a deformed nucleus. The deformation parameter β is commonly used with regard to the Woods-Saxon potential, where the nuclear potential can be defined in terms of the distance of a point **r** from the nuclear surface. The deformation parameter ε, used extensively in this work, is used with the Modified Harmonic Oscillator or Nilsson potential, discussed in sec. 1.3. This formalism defines the deformed nucleus in terms of stretched coordinates, resulting in an alternative shape parameterisation.

1.2.1 β_2 deformation

The surface of a non-spherical nucleus can be expressed [ben89] as the sum of spherical harmonics $Y_\lambda(\theta)$,

$$R(\theta,\beta) = C(\beta)R_0\left[1+\sum_\lambda \beta_\lambda Y_\lambda(\theta)\right] \tag{1.8}$$

where R_0 is the radius of the sphere of the same volume and $C(\beta)$ is a conservation of volume term. Quadrupole deformation can be represented by the deformation parameters β_2, which measures the RMS deviation of the nuclear surface from a sphere of radius R_0 and γ which describes the triaxiality of the nucleus.

1.2.2 ε_2 deformation

The Modified Harmonic Oscillator or Nilsson potential requires the introduction of a different deformation parameter. This formalism defines the deformed nucleus in terms of non-Cartesian, stretched coordinates which introduces an alternative shape parametisation [ben89],

$$R^2(\theta,\varepsilon) = \frac{\hbar}{m\omega_0(\varepsilon_2)}\left[\frac{1-2\varepsilon_2/3+\varepsilon_2\cos^2\theta_t}{(1-2\varepsilon_2/3)(1+\varepsilon_2/3)}\right]\rho^2 \tag{1.9}$$

where ε is a whole set of deformation parameters and ε_2 represents quadrupole deformation. For a full explanation of this parameterisation see section 1.3.

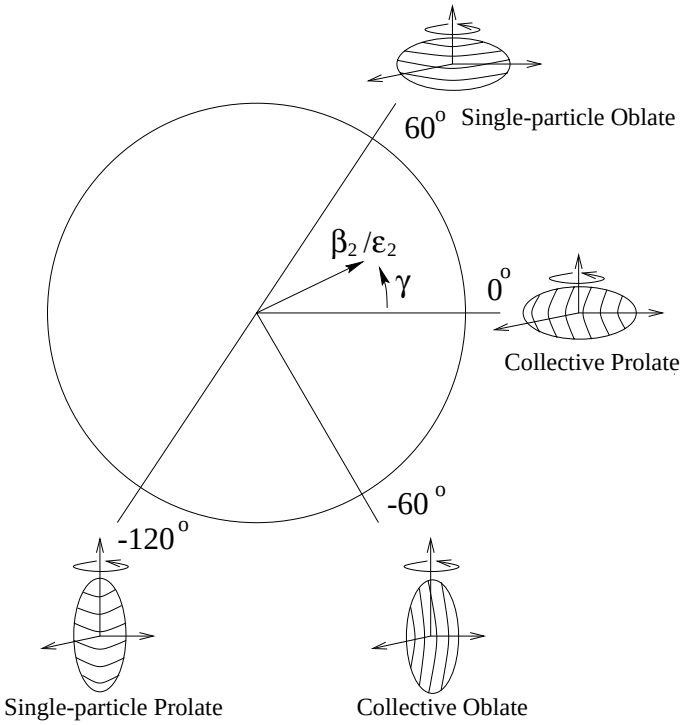

Figure 1.2: A schematic illustration of the (ε_2, γ) plane showing the Lund Convention.

1.2.3 Transformation between the β and ε shape parameterisations

Transformation between the two shape parameterisations is made possible by calculating a series of multipole moments generated by the surface descriptions of eqn. 1.8 and eqn. 1.9 [lob70, ben89]. The shape in the β-parametrisation is considered equivalent to a shape in the ε-parametrisation if,

$$\frac{Q_\lambda(\varepsilon)}{Q_0(\varepsilon)} = \frac{Q_\lambda(\beta)}{Q_0(\beta)} \quad \lambda = 2, 3, ...\lambda_{max}. \tag{1.10}$$

For small deformations the assumption that $\varepsilon_2 \approx 0.95\beta_2$ may be used.

1.2.4 The Lund Convention

A convenient way to describe the nuclear shape uses the Lund convention [and76] to define γ, illustrated in Fig. 1.2. Values of γ =0° and $-120°$ correspond to collective and single-particle prolate shapes respectively, while values of γ=$-60°$ and 60° correspond similarly to collective and single-particle oblate shapes. Triaxial shapes in this regime are found about intermediate angles.

1.3 The Deformed Shell Model

The shell model potentials discussed so far describe a spherically symmetric nuclear field. Such a spherical configuration would be expected for 'magic' closed shell nuclei, or those near a closed shell such as ^{110}Te studied in this work. However for nuclei away from closed shells or excited state configurations of near closed shell nuclei the existing model is inadequate. The concept of nuclear deformation, for which experimental evidence such as rotational bands and large quadrupole moments exists, needs to be added to the models.

1.3.1 The Anisotropic Harmonic Oscillator Potential

Deformation is usually introduced along the z-axis such that $x = y \neq z$. For an axially symmetric shape with z defined as the symmetry axis, the Anisotropic Harmonic Oscillator (AHO) potential can be written,

$$V_{AHO} = \frac{1}{2}M[\omega_{\perp}^2(x^2 + y^2) + \omega_z^2 z^2], \tag{1.11}$$

where $\omega_{\perp}$ and ω_z are the frequencies of the simple harmonic motion perpendicular and parallel to the nuclear symmetry axis, respectively. Deformation is introduced using the parameter ε,

$$\omega_z = \omega_0 \left[1 - \frac{2}{3}\varepsilon\right] \quad ; \quad \omega_{\perp} = \omega_0 \left[1 + \frac{1}{3}\varepsilon\right], \tag{1.12}$$

and $\omega_0^3 = \omega_{\perp}^2 \omega_z$ ensures conservation of volume. The energy difference between N major shells, $\hbar\omega_0$ defines the oscillator frequency, ω_0

$$\hbar\omega_0 = 41A^{-1/3}\left[1 \pm \frac{N-Z}{3A}\right] \text{(MeV)} \tag{1.13}$$

which due to ω_0 having an isospin dependence must be corrected using a minus sign for protons and a plus sign for neutrons. In order to simplify calculations the AHO model introduces 'stretched' coordinates defined as,

$$\xi = x\sqrt{\frac{m\omega_{\perp}(\varepsilon)}{\hbar}}; \quad \eta = y\sqrt{\frac{m\omega_{\perp}(\varepsilon)}{\hbar}}; \quad \zeta = z\sqrt{\frac{m\omega_z(\varepsilon)}{\hbar}}, \tag{1.14}$$

such that $\rho^2 = \xi^2 + \eta^2 + \zeta^2$ and the angle in stretched coordinates may be defined as $\cos\theta_t = \zeta/\rho$. The potential may now be written as,

$$V_{AHO} = \frac{1}{2}\hbar\omega_0(\varepsilon_2, \varepsilon_4)\rho^2\left[1 - \frac{2}{3}\varepsilon_2 P_2(\cos\theta_t) + 2\varepsilon_4 P_4(\cos\theta_t)\right]. \tag{1.15}$$

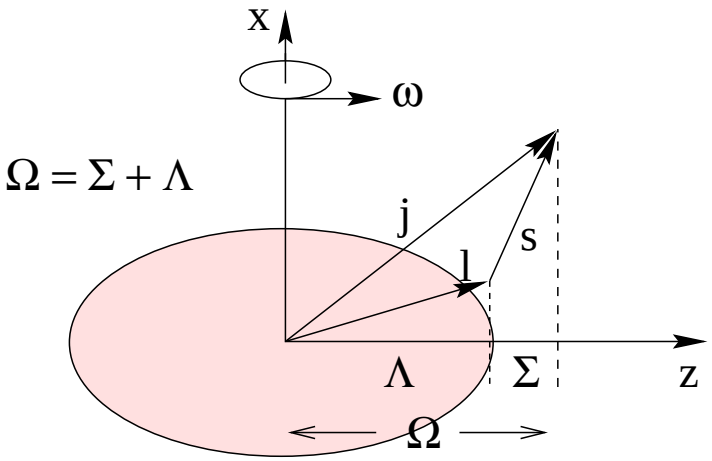

Figure 1.3: An illustration showing how the orbital angular momentum quantum number **l**, the intrinsic spin angular momentum quantum number **s** and the single-particle angular momentum **j** are related. The figure illustrates how they are projected onto the symmetry axis in a deformed axially symmetric nucleus.

Equation 1.15 includes quadrupole and hexadecapole deformation parameters ε_2 and ε_4 respectively. The $P_2(\cos\theta_t)$ term is a second order Legendre Polynomial, an extension to this for the higher multipole hexadecapole deformation case is shown.

The AHO Hamiltonian eigenvalues can be written:

$$E_{Nn_zn_\perp} \approx \left[N + \frac{3}{2}\right]\hbar\omega_0 - \frac{1}{3}\varepsilon[2n_z - n_\perp]\hbar\omega_0, \tag{1.16}$$

where $N = n_z + n_\perp$. The expression is simply the spherical harmonic oscillator minus a correction term, proportional to deformation. The eigenstates are labelled by the asymptotic quantum numbers, $[Nn_z\Lambda]\Omega^\pi$, and they are valid for large deformation, axial symmetry and no rotation. N is the principal quantum number, n_z the number of oscillator quanta parallel to the symmetry axis, Λ the component of the orbital angular momentum **l** along the symmetry axis, Ω the component of the single-particle angular momentum along the symmetry axis ($\Omega = \Lambda \pm \frac{1}{2}$) and π is the parity of the state. **j** and **l** are no longer good quantum numbers, but their projections Ω and Λ are.

Fig. 1.3 shows how the quantum numbers discussed so far are related. Each level $[Nn_z\Lambda]\Omega^\pi$ is two-fold degenerate because states with $\pm\Omega$ have the same energy. This is a lower degeneracy than for the spherical case because the spherical degree of symmetry has

been broken.

1.3.2 The Modified Harmonic Oscillator Potential

Nilsson [Nil69] formulated changes to the anisotropic harmonic oscillator potential in order to produce the correct shell structure. The Nilsson or Modified Harmonic Oscillator (MHO) potential is written;

$$V_{MHO} = V_{AHO} - \kappa\hbar\omega \left[2\mathbf{l_t}.\mathbf{s} + \mu(\mathbf{l_t}^2 - \langle \mathbf{l_t}^2 \rangle_N)\right] \tag{1.17}$$

where κ and μ are adjustable coupling parameters obtained by fitting to experimental energy levels. They are different for each major oscillator shell. The spin-orbit interaction cancels out in the centre of the nucleus and is at its strongest at the nuclear surface where the asymmetric distribution of nucleons is largest. The addition of an l^2 term flattened the radial shape of the potential, while the inclusion of the **l.s** term ensured the correct magic numbers were obtained. For this reason the MHO model is also known as the Nilsson model.

A plot showing energy levels versus quadrupole deformation is usually termed a Nilsson diagram. Such a plot for protons is shown in Fig. 1.4. There are a few important points which should be emphasised;

- The magic numbers are seen as regions of low level density at zero deformation.
- The onset of deformation causes the spherical levels which where obtained previously (sec.1.1.2) to split into $(N+1)$ levels each of degeneracy $2(n_\perp + 1)$.
- Levels with low Ω quantum numbers are lowered in energy for positive ε deformations, which represent a prolate shape. Conversely for negative ε deformations, oblate shapes, the levels are raised in energy. Intruder negative parity orbitals from the $h_{11/2}$ subshell can be clearly identified.

Levels with the same quantum numbers (Ω, π) cannot cross, instead they exchange their trajectories and characteristics at the crossing.

1.3.3 Deformed Woods-Saxon Potential

The deformed Wood-Saxon potential can be written as;

$$V_{WS}(\mathbf{r}, \beta) = \frac{-V_0}{1 + \exp[dist_\Sigma(\mathbf{r}, \beta)/a]}, \tag{1.18}$$

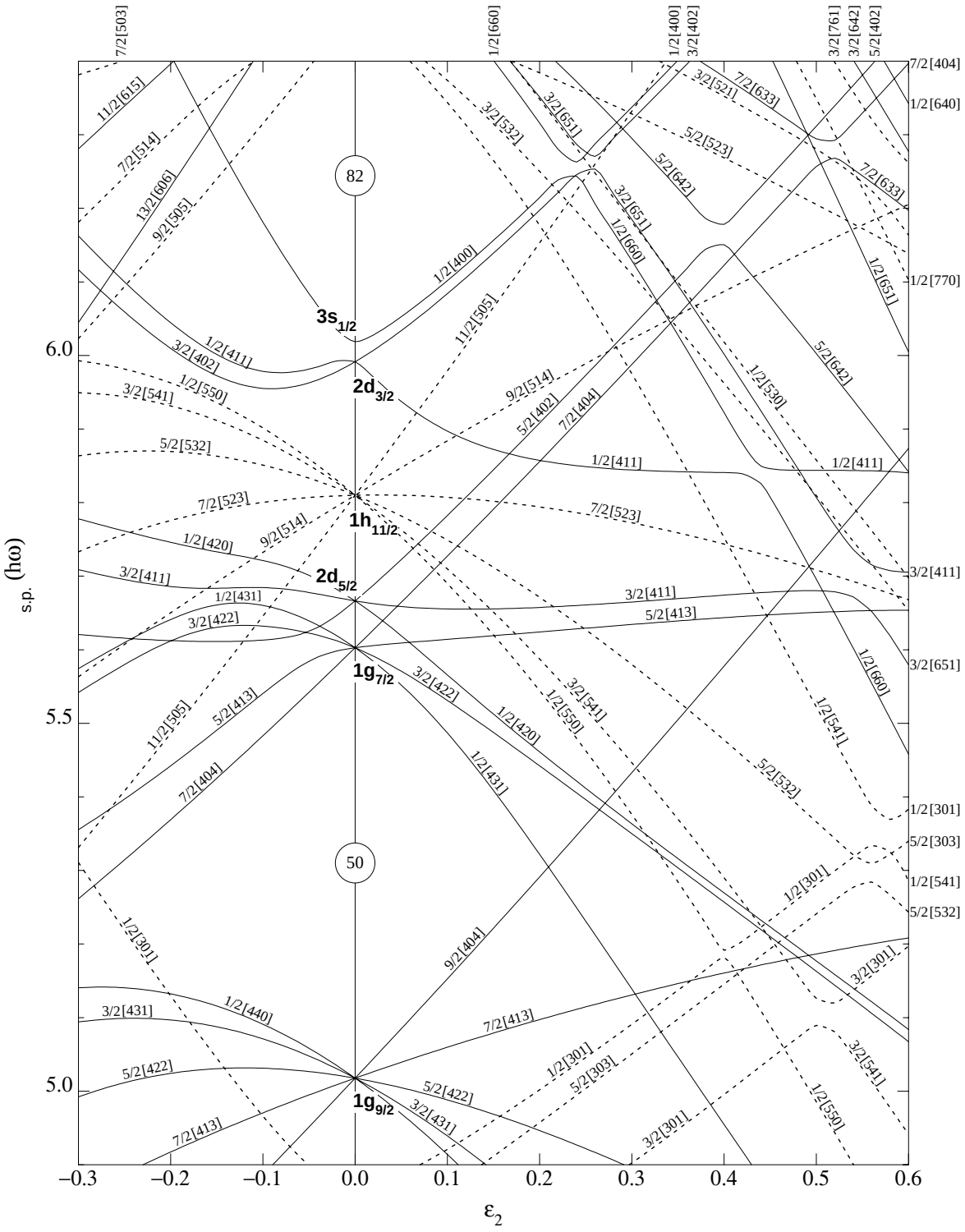

Figure 1.4: A proton Nilsson diagram, showing single-particle energies as a function of deformation. Positive (negative) parity levels are shown as solid (dashed) lines. Notice how negative parity $h_{11/2}$ intruder orbitals penetrate into the lower N=4 orbitals.

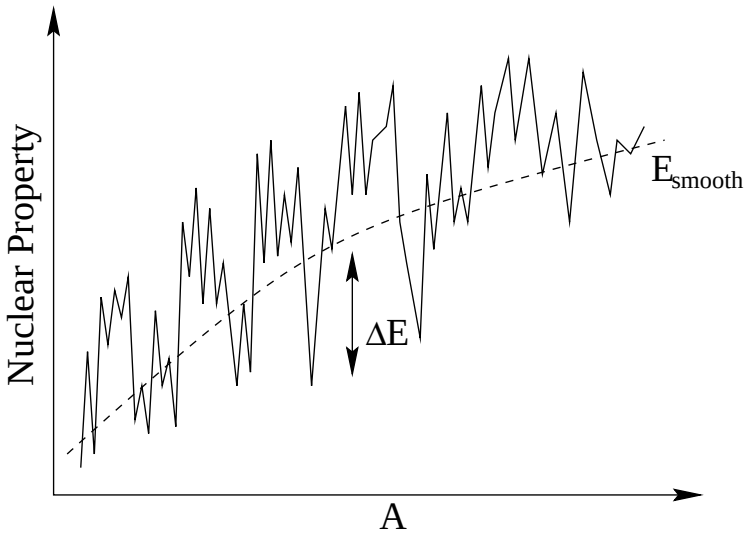

Figure 1.5: A schematic illustration showing the irregular behaviour of a nuclear property such as the nuclear binding energy. The Strutinksi shell correction terms are indicated.

where $dist_{\Sigma}(\mathbf{r}, \beta)$ is the distance between the point $\mathbf{r}$ and the nuclear surface Σ, β denotes the shape parameters that uniquely specify Σ which will usually be limited to quadrupole (β_2) or hexadecapole (β_4) degrees of freedom. The Woods-Saxon potential has not been used for this work and so this brief description is included just for completeness.

1.4 The Strutinski Shell Correction

A nuclear property such as the nuclear binding energy shows an irregular behaviour with mass, a schematic diagram of such behaviour is shown in Fig. 1.5. The values of the property consist of an oscillatory part ΔE on top of a smooth part $E_{\rm smooth}$. Strutinksi [str67, str68] proposed to use the shell model to obtain ΔE and the liquid drop model to calculate $E_{\rm smooth}$ since it represents a bulk property. The Strutinski shell correction approach combines the advantages from both models in order to provide an accurate reproduction of the experimental nuclear ground state energies.

The total shell model energy can be divided into smooth ($\widetilde{E}_{sh}$) and oscillatory (ΔE_{sh}) components,

$$E_{sh} = \sum_{i=1}^{A} \epsilon_i = \widetilde{E}_{sh} + \Delta E_{sh} \tag{1.19}$$

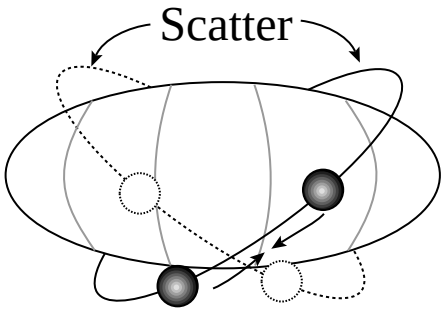

Figure 1.6: A schematic illustration of paired nucleons orbiting an axially symmetric deformed nucleus in time-reversed orbits.

ϵ_i represents the nucleon single-particle eigenvalues. The total energy of the nucleus is now treated as the sum of two components,

$$E_{tot} = E_{ldm} + \Delta E_{sh} \tag{1.20}$$

where E_{ldm} is the macroscopic contribution from the liquid drop model and ΔE_{sh} is the correction term derived from fluctuating part of the shell model energy. The addition of the ΔE_{sh} term enabled ground state energies as a function of deformation to be determined. Predictions from the Strutinski procedure are generally presented in the form of potential energy surfaces.

1.5 Pairing and Quasiparticles

The Nilsson model is unable to explain a number of experimental observations such as;

- The ground states of all even-even nuclei have $I^\pi = 0^+$.
- Level gaps exist in even-even nuclei which are absent in neighbouring odd nuclei.

The inclusion of pairing correlations provides an explanation to many of the outstanding problems. The Pauli exclusion principle forbids paired nucleons from having the same set of quantum numbers. The paired nucleons therefore orbit in time-reversed orbits interacting twice per orbit, where they may scatter into different pairs of time-reversed orbits, illustrated in Fig. 1.6. The scattering of the pairs of nucleons from one time-reversed orbit to another results in a smearing out of the Fermi surface. This means that states near the Fermi surface

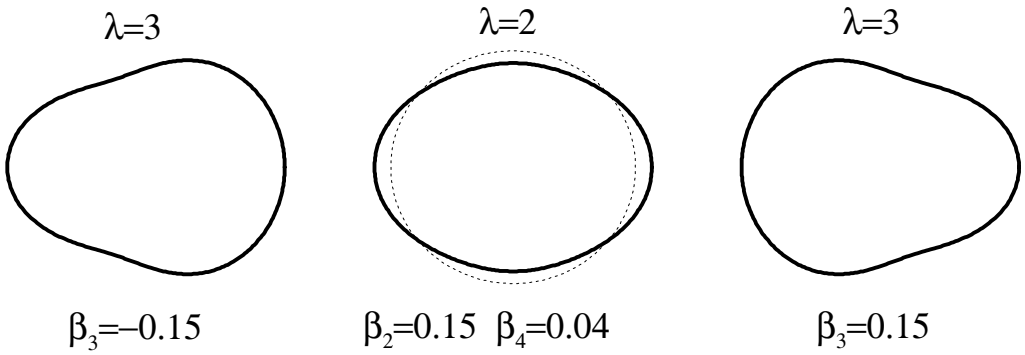

Figure 1.7: Nuclear shape changes corresponding to quadrupole ($\lambda = 2$) and octupole ($\lambda = 3$) deformations.

have a finite probability of being occupied or not occupied. It is useful to introduce the concept of quasiparticles which describe a state in terms of its probability of being occupied by a particle (V_ν) or a hole (U_ν). Well below the Fermi surface $V_\nu = 1$ and $U_\nu = 0$, the converse is true well above the Fermi surface and the probabilities are mixed near the Fermi surface.

1.6 Nuclear Vibration

Near closed shells, where the nuclei are spherical in their ground states, the action of a quadrupole residual interaction causes the nucleus to oscillate in shape. The nucleus effectively has a dynamic deformation caused by quadrupole surface vibrations, see Fig. 1.7. The potential for such a phenomenon can be written,

$$V_{vib} = \sigma_\mu \left[\frac{1}{2} C |\alpha_{2\mu}|^2 + \frac{1}{2} B |\dot{\alpha}_{2\mu}|^2 \right] \tag{1.21}$$

where C is a parameter which represents the restoring potential and B is associated with the mass carried in the vibration. The eigenvalues are:

$$E_n = E_0 + n\hbar\omega; \qquad \omega = \sqrt{\frac{C}{B}}. \tag{1.22}$$

E_0 represents the intrinsic and zero point motion of the oscillations. The energy levels for different n are equally spaced (Fig. 1.8). Each phonon is of positive parity and carries two units of angular momentum. For example, in the case of a two quadrupole phonon excitation, the maximum possible spin is 4^+. For quadrupole vibrations, transitions are

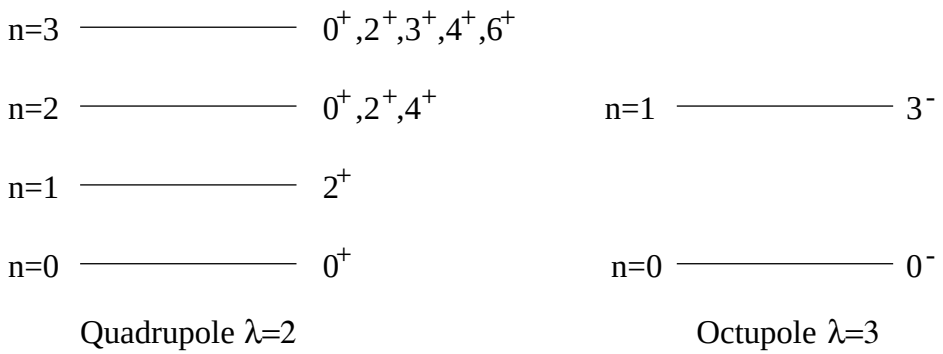

Figure 1.8: A typical level structure for a spherical vibrator.

only allowed between states with $\Delta n = \pm 1$. Octupole vibrations are also possible, and in this case each phonon is of negative parity and carries three units of angular momentum. For this case the first excited state will be 3^-.

For an axially-deformed nucleus collective vibrational motion is still possible. Quadrupole vibrational motion can now be classified in terms of β-vibration, where the vibration is aligned along the symmetry axis preserving axial symmetry and γ-vibration, a dynamic time dependent excursion from axial symmetry. The ratio of the 4^+ energy levels to the 2^+ energy levels can be used to classify the nucleus as a vibrator or a rotor. For vibrational nuclei, the energy ratio is equal to 2.0 ($E \propto n$), while for rotational nuclei 3.33 is the limit ($E \propto I(I+1)$).

1.7 Nuclear Rotation

1.7.1 Introduction

Collective rotation of a spherical nucleus is not allowed, because rotation about a symmetry axis is forbidden by quantum mechanics. For an axially deformed shape, collective rotation may occur about an axis perpendicular to the symmetry axis. This has the consequence that rotation becomes a possible mode of excitation for deformed nuclei.

The total angular momentum I of an axially symmetric deformed nucleus, rotating about an axis perpendicular to the symmetry axis can be attributed to,

- The collective angular momentum of the core (**R**).
- The intrinsic angular momentum of unpaired valence nucleons (**J**).

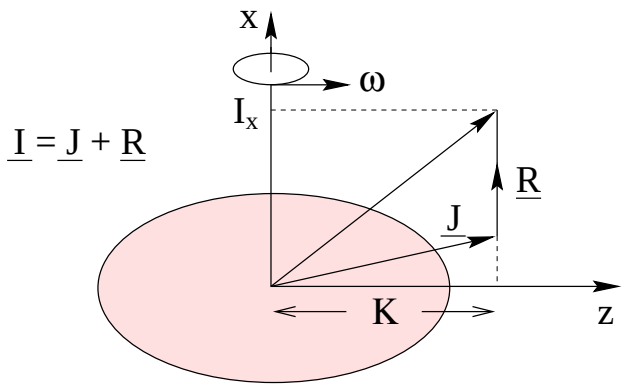

Figure 1.9: An illustration showing how **I**, **R**, **J**, Ω and K are related.

This can be written,

$$\mathbf{I} = \mathbf{R} + \mathbf{J}. \tag{1.23}$$

The projection of **I** onto the symmetry axis is the same as the projection of **J** and is denoted by K, where K is the sum of the individual Ω values.. An schematic diagram illustrating these quantities is shown in Fig. 1.9.

1.7.2 Rotational Frequency and Moments of Inertia

The rotational frequency of a deformed nucleus can be expressed as,

$$\hbar\omega = \frac{dE}{dI_x}, \tag{1.24}$$

where I_x is the projection of I onto the rotation axis, $I_x = \sqrt{I(I+1)^2 - K^2}$. The collective rotation of the nucleus is experimentally observed as a rotational band of states with energy,

$$E(I) = \frac{\hbar^2}{2\mathcal{J}^{(0)}} I(I+1), \tag{1.25}$$

where $\mathcal{J}^{(0)}$ defines the static moment of inertia. A rotational band consisting of stretched quadrupole ($\Delta I = 2$) transitions gives the simple relation $\hbar\omega \approx E_\gamma/2$.

Nuclear moments of inertia are typically less than 50% of the rigid-body moment of inertia $\mathcal{J}_{rig}$ and significantly larger than the hydrodynamic value at low spin. The effect of pairing is to make nuclear matter behave more like a fluid. It is helpful to think of the nucleus as a rigid core plus a fluid of valence nucleons.

Two further moments of inertia can be introduced to describe the collective nuclear rotation. Assuming maximum alignment on the x-axis ($I_x \sim I$), the kinematic moment of inertia, $\mathcal{J}^{(1)}$, is defined as,

$$\mathcal{J}^{(1)} = \hbar^2 I_x \left[\frac{dE}{dI_x}\right]^{-1} = \hbar \frac{I_x}{\omega} \tag{1.26}$$

and the dynamic moment of inertia, $\mathcal{J}^{(2)}$, is defined as,

$$\mathcal{J}^{(2)} = \hbar^2 \left[\frac{d^2E}{dI_x^2}\right]^{-1} = \hbar \frac{dI_x}{d\omega} \tag{1.27}$$

The kinematic and dynamic moments of inertia can be rewritten for experimental measurements of stretched electric quadrupole (E2) γ-rays,

$$\mathcal{J}^{(1)} = \hbar^2 \left[\frac{4I - 2}{2E_\gamma}\right], \tag{1.28}$$

$$\mathcal{J}^{(2)} = \frac{4\hbar^2}{\Delta E_\gamma}, \tag{1.29}$$

where ΔE_γ represents the difference in energy between two adjacent γ-rays in a cascade. The $\mathcal{J}^{(2)}$ is not dependent on the spin (I), and is therefore an extremely useful quantity experimentally where spins have not firmly been assigned. The $\mathcal{J}^{(2)}$ is very sensitive to changes in the internal structure, such as particle alignment effects.

1.7.3 Particle Rotor Coupling

The coupling of extra valence nucleons to a closed core occurs between two extreme regimes, the strong coupling limit or deformation alignment (DAL) and the weak coupling limit or rotation alignment (RAL). Fig. 1.10 shows an illustration of the two coupling extremes. In the deformation aligned limit the vectors precess around the the symmetry axis. This occurs for large deformations and low rotational frequencies. The angular momentum quantum number **j** is coupled to the deformation and K is a good quantum number. Single particle energy levels in the rotating frame (Routhians) are near degenerate with small level splitting. A rotational band has spins given by $I = K, K+1, K+2...$ with states of energy,

$$E_{def}(I) = \frac{\hbar^2}{2\mathcal{J}^{(0)}} \left[I(I+1) - K^2\right] \tag{1.30}$$

For nuclei with smaller deformation or rapid rotation such that the Coriolis force is so strong that coupling to the deformed core is negligible, the particle rotor system approaches

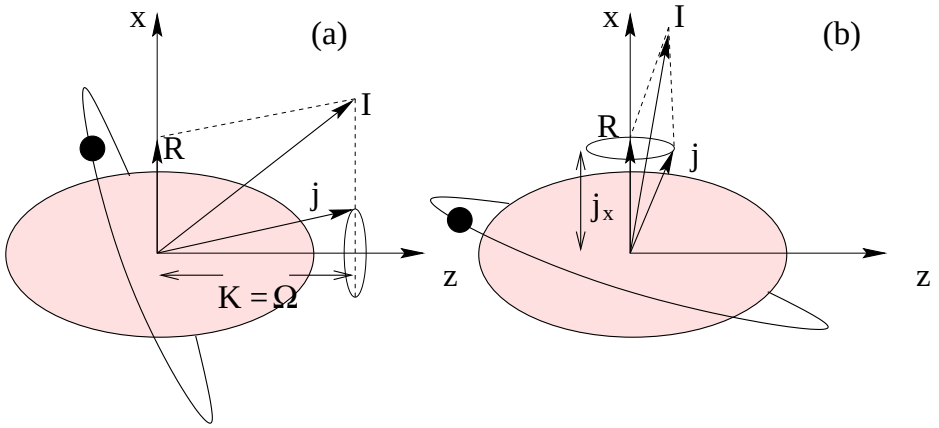

Figure 1.10: An illustration showing the (a)strong and (b)weak coupling limits.

the rotation aligned limit. The Coriolis force aligns the angular momentum vector with the rotation axis, such that **j** precesses about the rotation axis. The spin members of a rotational band are given by $I = j, j+2, j+4$ with states of energy,

$$E_{rot}(I) = \frac{\hbar^2}{2\mathcal{J}^{(0)}}(I - j_x)(I - j_x + 1). \tag{1.31}$$

1.8 The Cranked Shell Model

The Cranked Shell Model, first introduced in 1954 by Inglis, provides a microscopic description of nuclear rotation. It is able to describe collective as well as single-particle rotation and combinations of these two extremes. This is important since it provides a means of investigating the effects of the Coriolis and centrifugal forces on single particle orbits.

A rotation is externally imposed on a nuclear potential, on an axis x which is perpendicular to the symmetry axis. The potential is time dependent and can be described by the time-dependent single-particle Schrödinger equation,

$$i\hbar\frac{d\Psi_L}{dt} = H_L\Psi_L. \tag{1.32}$$

H_L and Ψ_L are the single-particle Hamiltonian and wavefunction of the system, respectively. By transforming into the rotating (intrinsic) frame of reference using a rotation operator,

$$\mathcal{R}_x = \exp\left[\frac{-iI_x\omega t}{\hbar}\right], \tag{1.33}$$

the Schrödinger equation becomes,

$$i\hbar\frac{d\Psi_{int}}{dt} = (H_L - \omega I_x)\Psi_{int} \equiv H^{\omega}\Psi_{int}. \tag{1.34}$$

The total cranked Hamiltonian (or Routhian) can now be written,

$$H^{\omega} = H_L - \omega I_x \tag{1.35}$$

H^{ω} represents the sum of routhians, or single-particle energies (h^{ω}) of the orbitals in the rotating frame, over all independent nucleons. The $(-\omega I_x)$ term arises due to the Coriolis and centrifugal forces in the rotating frame of reference which act to align the single-particle orbits, increasing the angular momentum on the rotation axis. As pairs of particles are broken, the nucleus will become less fluid, resulting in a change in the moment of inertia. This will be observed as a discontinuity in a plot of moment of inertia against rotational frequency.

1.9 Signature and Parity

The Nilsson model releaved the level degeneracy with states only degenerate with respect to $\pm\Omega$. The time-reversal symmetry is broken by the cranking Hamiltonian which is symmetric for rotation about the x-axis. The only symmetries that remain are space reflections (parity) and a transformation of 180° defined by the rotation operator. For a rotation of 2π the rotation operator (eq.1.33) leaves the wavefunction unchanged for even-A nuclei, but changes the sign for odd-A nuclei,

$$\mathcal{R}_x^2 = (-1)^A. \tag{1.36}$$

$\mathcal{R}_x^2$ represents a 2π rotation. The eigenvalues are $r = \pm 1$ for even A and $r = \pm i$ for odd A. The signature is hence defined by,

$$r = \exp[-i\pi\alpha], \tag{1.37}$$

where α is the signature exponent quantum number, which gives

$$\begin{aligned} I = &\quad 0, 2, 4, .. \;\; \alpha = 0, r = +1, \\ I = &\quad 1, 3, 5, .. \;\; \alpha = 1, r = -1, \\ I = &\quad \tfrac{1}{2}, \tfrac{5}{2}, \tfrac{9}{2}, .. \;\; \alpha = +\tfrac{1}{2}, r = -i, \\ I = &\quad \tfrac{3}{2}, \tfrac{7}{2}, \tfrac{11}{2}, .. \;\; \alpha = -\tfrac{1}{2}, r = +i. \end{aligned} \tag{1.38}$$

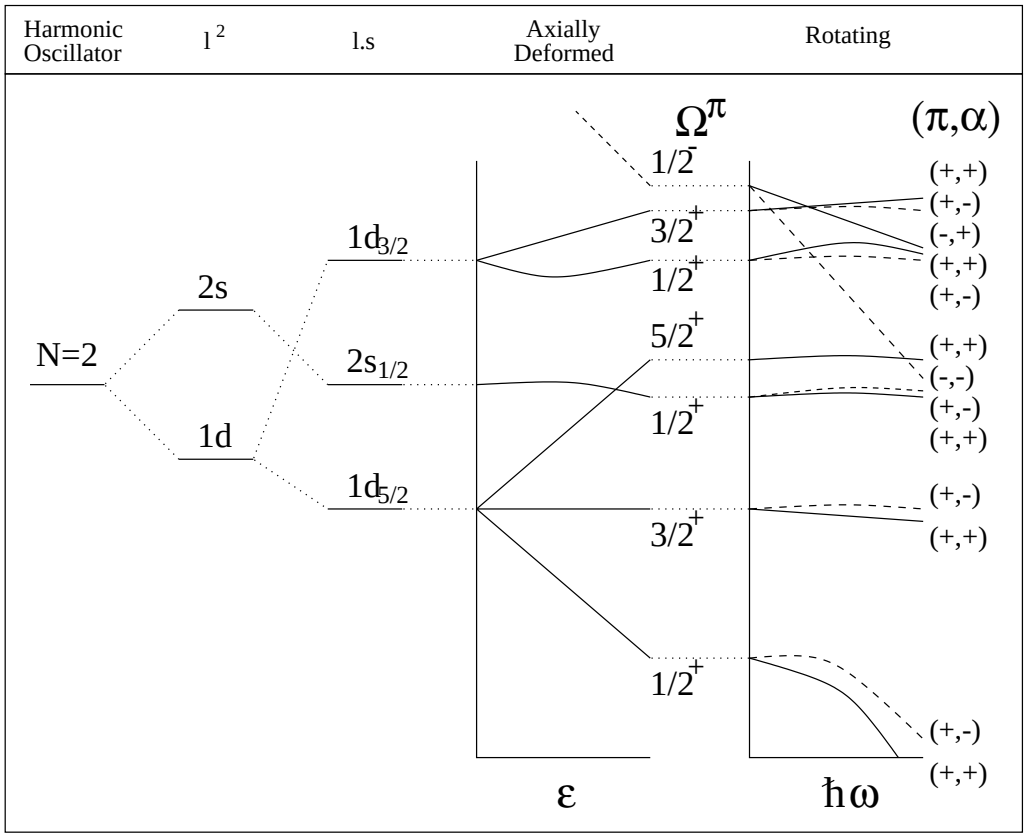

Figure 1.11: A schematic energy spectrum for shell model states generated by various nuclear potentials. Here $\alpha = +(-)$ means $\alpha = +1/2(-1/2)$.

This can be conveniently expressed by,

$$I = \alpha \mathrm{mod} 2. \tag{1.39}$$

Cranking Routhians are generally labelled by parity and signature (π, α). The Coriolis term in the cranking model splits each orbital into two levels of opposite signature exponent ($\alpha = \pm\frac{1}{2}$). This experimentally manifests itself by the formation of two distinct signature partner bands. The magnitude of this signature splitting depends on the magnitude of the angular momentum projection onto the rotation axis, j_x. An orbit with high j_x (low Ω) will have a large signature splitting. A single-particle routhian diagram can be constructed to show how single-particle energy levels vary as a function of rotational frequency. An illustration of the effect each of the models discussed has on the single-particle energy levels is shown in Fig. 1.11. The right hand side of the figure shows the effect of rotation.

1.10 The HFB formalism

The Hartree-Fock-Bogoliubov (HFB) formalism is introduced in order to include pairing effects in cranked shell model calculations. The HFB treatment leads to quasiparticle excitations in the rotating frame, where the Hamiltonian is defined as,

$$H_{\nu}^{\omega} = H_{sp} - \Delta(P^{\dagger} + P) - \lambda\hat{N} - \omega I_x. \tag{1.40}$$

H_{sp} is the single-particle Hamiltonian, Δ represents the pairing gap which originates from the smearing of the Fermi surface, $(P^{\dagger} + P)$ are pair creation and annihilation operators, $\hat{N}$ is the particle number operator and ωI_x is term arising from the Coriolis and centrifugal forces. The nucleus contains a finite number of particles therefore the chemical potential (Fermi level), λ and the rotational frequency, ω, are used as Lagrange multipliers to conserve the number of particles $\hat{N}$ and angular momentum I_x, respectively. The eigenvalues of the HFB Hamiltonian are quasiparticle routhians.

A quasiparticle routhian diagram can be constructed in the same way as a single-particle routhian diagram. The quasiparticle diagram is constructed relative to a reference or vacuum configuration which corresponds to the Fermi surface. The excitation energy of the vacuum is the sum of the energies of the occupied states.

1.11 Transition Probabilities and Multipole Moments

The energy of an electromagnetic radiation field can be described in terms of a multipole moment expansion. For example, the nuclear magnetic dipole moment (M1) is sensitive to nuclear magnetic moments and hence single particle aspects. The nuclear electric quadrupole moment (E2) is sensitive to the nuclear charge distribution and hence collective effects such as deformation.

The matrix element for a transition from a state $|I_2, M_2\rangle$ to a state $|I_1, M_1\rangle$ can be written,

$$\langle I_2 M_2|\hat{O}_{\lambda\mu}|I_1 M_1\rangle. \tag{1.41}$$

The Wigner-Eckhart theorem allows this matrix element to be expressed as,

$$\langle I_2 M_2|\hat{O}_{\lambda\mu}|I_1 M_1\rangle = (2I_2 + 1)^{1/2}\langle I_1 M_1 \lambda\mu|I_2 M_2\rangle\langle I_2||\hat{O}_{\lambda}||I_1\rangle, \tag{1.42}$$

L	Electric Transitions (s^{-1})	Magnetic Transitions (s^{-1})
1	$\lambda(E1)=1.590\times10^{15}E_\gamma^3B(E1)$	$\lambda(M1)=1.758\times10^{13}E_\gamma^3B(M1)$
2	$\lambda(E2)=1.225\times10^{9}E_\gamma^5B(E2)$	$\lambda(M2)=1.355\times10^{7}E_\gamma^5B(M2)$
3	$\lambda(E3)=5.708\times10^{2}E_\gamma^7B(E3)$	$\lambda(M3)=6.313\times10^{0}E_\gamma^7B(M3)$

Table 1.2: Transition probabilities for the lowest multipoles. E_γ is in MeV, $B(E\lambda)$ in $e^2fm^{2\lambda}$, $B(M\lambda)$ in $\mu_N^2 fm^{2\lambda-2}$.

where $\langle I_2||\hat{O}_\lambda||I_1\rangle$ is a reduced matrix element and $\langle I_1 M_1 \lambda\mu|I_2 M_2\rangle$ is a Clebsch-Gordon coefficient. The interaction and geometry are therefore separated and all the nuclear structure information is contained in the reduced matrix element. Bohr and Mottelson [Boh75] have calculated reduced electric and magnetic transition probabilities in terms of rotating multipoles, results for the three lowest multipoles are shown in table 1.2.

1.11.1 Magnetic Dipole Moments

The magnetic moment of a single nucleon can be represented by the sum of the magnetic moment due to the orbiting protons $\mu_{orb} = g_l l \mu_N$, which can be thought of as a nuclear current and the moment due to the intrinsic spin of the constituent nucleons $\mu_{spin} = g_s \mu_N$,

$$\mu_N = \mu_{orb} + \mu_{spin} \tag{1.43}$$

g_l and g_s are the orbital and spin angular momentum g-factors, respectively. μ_N is the nuclear magneton. The magnetic dipole operator for the nucleus can be obtained by summing over all the nucleons,

$$\mu = \mu_N \sum_{i=1}^{A} \left(g_{l_i} l_i + g_{s_i} s_i\right). \tag{1.44}$$

In order to simplify the process of obtaining the dipole moment of the nucleus, the magnetic dipole moment is often separated into two components; that due to the rotating core and that due to the intrinsic spin of any valence nucleon. The core contribution can be estimated assuming the protons are evenly distributed throughout the nucleus, which is rotating with angular momentum **R**.

$$\mu = g_R \mathbf{R} \mu_N, \tag{1.45}$$

where g_R is the rotational g-factor describing the collective rotation, which is approximately equal to Z/A. This expression applies to even-even nuclei with no intrinsic excitation (K=0). For K$\neq$0, the contribution to the magnetic moment from the valence nucleon is important, another g-factor g_K is defined,

$$g_K = g_l + \frac{1}{\Omega}(g_s - g_l)\langle\Omega|s_z|\Omega\rangle. \tag{1.46}$$

This g-factor is strongly dependent on the state which the valence nucleon occupies, it is therefore very useful in the classification of states. The total angular momentum may be written **I**=**R**+**j**, hence the total magnetic dipole moment is,

$$\mu = \left[g_R I + [g_K - g_R]\,\frac{K^2}{I+1}\right]\mu_N. \tag{1.47}$$

1.11.2 Electric Dipole and Quadrupole Moments

The electric dipole moment arises due to a difference between the centre of mass and centre of charge in the nucleus, it can therefore only occur in a reflection asymmetric nucleus, discussed in section 1.12.1 or for the case of Giant Dipole Resonance.

The electric quadrupole moment is defined in terms of the charge density ρ of the nucleus,

$$eQ(\mathbf{r}) = \int \rho(\mathbf{r}) r\,(3\cos^2\theta - 1)dV \tag{1.48}$$

where **r** is the radius vector which subtends the angle θ with respect to the symmetry axis. If the nucleus is spherical the integral over the volume is zero and there is no intrinsic quadrupole moment. For a deformed nucleus however, a static quadrupole moment will be observed. Positive quadrupole moments are characteristic of a prolate deformed shape and can be related to the quadrupole deformation parameter ε_2 by,

$$Q_2 = \frac{4}{5}Zr_0^2A^{2/3}\left[\varepsilon_2\left(1+\frac{1}{2}\varepsilon_2\right) + \frac{25}{33}\varepsilon_4^2 - \varepsilon_2\varepsilon_4\right]. \tag{1.49}$$

The experimentally measured value of the quadrupole moment Q_t can be related to Q_2 by,

$$Q_t = Q_2\frac{\cos(\gamma+30^\circ)}{\cos(30^\circ)}. \tag{1.50}$$

The calculation of reduced matrix elements for the electric and magnetic, dipole and quadrupole cases yields the following expressions for the reduced transition rate,

$$B(M1) = \frac{3}{4\pi}\left[g_K - g_R\right]^2 K^2|\langle I_I, K, 1, 0|I_f, K\rangle|^2\mu_N^2, \tag{1.51}$$

$$B(E1) = \frac{3}{4\pi} D_0^2 |\langle I_I, K, 1, 0 | I_f, K \rangle|^2, \tag{1.52}$$

$$B(E2) = \frac{5}{16\pi} Q_0^2 |\langle I_I, K, 2, 0 | I_f, K \rangle|^2, \tag{1.53}$$

μ_N is the intrinsic magnetic dipole moment, D_0 and Q_0 are the intrinsic electric dipole and quadrupole moments, respectively. $\langle I_I, K, 2, 0 | I_f, K \rangle$ is a Clebsch-Gordon coefficient for vector addition.

1.12 Octupole Correlation Effects

1.12.1 Introduction

The neutron deficient ($N \sim 58$) tellurium ($Z = 52$) nuclei lie in a region of the nuclear chart where states with $\Delta l = \Delta j = 3$ ($h_{11/2} \leftrightarrow d_{5/2}$) are close to the Fermi surface, which is expected to lead to octupole correlation effects [But96]. The interaction of such orbitals occurs above each of the major shell gaps, where intruder orbitals penetrate into the shell below. This occurs for nuclei which have N or Z close to 34, 56, 88 or 134 (octupole magic numbers) and the interaction is particularly strong for nuclei which have both N and Z near to one of these values. The octupole-driving interacting levels get closer together as the particle number increases, and therefore heavier nuclei will exhibit the strongest octupole correlations. The best studied and most well developed region is centered around the light actinide nucleus ${}^{224}_{90}\mathrm{Th}_{134}$, which is predicted to have the largest octupole deformation. Other regions of interest are centered around the lanthanide nucleus ${}^{146}_{56}\mathrm{Ba}_{90}$ and weaker effects are expected in nuclei such as ${}^{112}_{54}\mathrm{Xe}_{58}$ with N$\sim$Z.

Quadrupole deformation is described by the parameter β_2 or ε_2. A nucleus with a non-zero β_3 or ε_3 is termed octupole deformed. An axially deformed reflection-symmetric nucleus is invariant under space inversion and a rotation of 180° about an axis perpendicular to the symmetry axis, however a reflection-asymmetric shape will break these two symmetries. This difference is required in order to explain the observation of low lying negative-parity states in even-even nuclei such as ${}^{224}\mathrm{Ra}$. An octupole deformed shape is reflection asymmetric or pear shaped, illustrated in Fig. 1.7.

In a similar way to quadrupole deformation, octupole deformation may be static or dynamic, corresponding to a true octupole deformed nucleus or shape fluctuations (vibration)

about a reflection-symmetric shape, respectively. In order to measure the extent of octupole deformation a measurement of the electric octupole moment B(E3) would need to be made. The E3 γ-ray decay intensity is however 10^4 times weaker than the E1 and E2 strengths. The degree of octupole deformation must therefore be inferred indirectly from the obtained nuclear level scheme.

1.12.2 Experimental Evidence

The experimental signatures for octupole deformation effects include low lying negative parity states in even-even nuclei, alternating parity rotation bands and enhanced E1 transitions between positive and negative parity states. Typical values for $B(E1)$ in an octupole deformed nucleus are $\sim 10^{-3}$ Weisskopf units (W.u.). This is only a fraction of the single-particle estimate, however the values are a few orders of magnitude larger than those measured in other regions of the nuclear chart, $\sim 10^{-5}$W.u.

An intrinsic electric dipole moment, induced by the displacement of the centre of charge from the centre of mass has been postulated to explain the enhancement of E1 strength [Lea82]. The effect is induced by the tendency of the protons to gather at the narrow end of the octupole shape, at the point where the radius of curvature of the equipotential surface is smallest.

Octupole deformation is discussed in detail in Ref. [But96]. ^{110}Te is discussed within the scenario of octupole collectivity in sec. 4.4.

Chapter 2

Experimental Techniques

Introduction

This chapter describes the experimental techniques used to study nuclei produced at high angular momentum. A discussion of how the nucleus may be excited is accompanied by a description of the principles of γ-ray detection. Recent developments in high resolution γ-ray spectroscopy have allowed the construction of multi-detector arrays and a description of the GAMMASPHERE facility, from which the work presented in this thesis was taken, is included. Finally, the techniques used to improve the sensitivity of a high-spin spectrometer are discussed.

2.1 Compound Nucleus Formation

In order to study a nucleus at high spin, a reaction mechanism must be used which populates states at high angular momentum with sufficient energy and cross-section. A heavy-ion fusion-evaporation reaction is the best way of experimentally producing high spin states with large cross-sections; this involves accelerating a beam of heavy ions ($A \geq 4$) in order to bombard a target. The heavy ions in the beam will fuse with the target nuclei to form a compound nucleus if the impact parameter (b) is small compared to the nuclear radius and the incident energy is high enough to overcome the Coulomb barrier. The Coulomb barrier for a particular beam target combination can be simply calculated using,

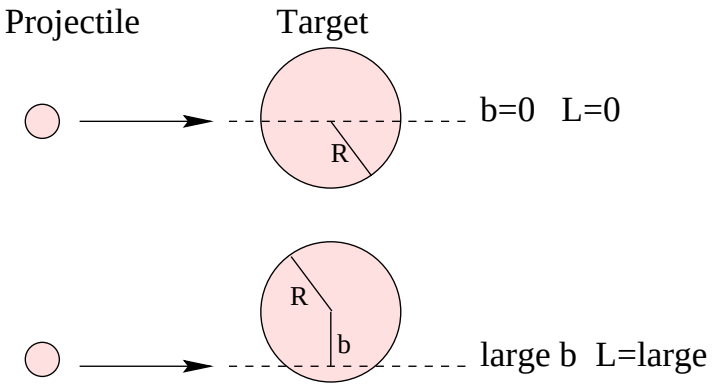

Figure 2.1: A schematic diagram showing the effect of the impact parameter **b** on the angular momentum transferred to the compound nucleus.

$$E_{cb} = \frac{Z_p Z_t e^2}{4\pi\epsilon_0 r} MeV; \qquad r = 1.2(A_1^{1/3} + A_2^{1/3}) fm \tag{2.1}$$

If **P** is the linear momentum of the projectile, the impact parameter **b** can be directly related to the total angular momentum **L** of the colliding system by,

$$\mathbf{L} = \mathbf{b} \times \mathbf{P}. \tag{2.2}$$

A high-spin state is populated when the impact parameter is small enough to ensure complete fusion of the target and beam nuclei, but large enough to ensure the transfer of large amounts of angular momentum, as indicated in Fig. 2.1.

2.2 Compound Nucleus Decay

The decay probability depends only on the total energy given to the system and not the process of formation [Boh36]. The compound nucleus will decay by a variety of different channels. For the reaction studied in this work,

$$^{58}Ni + {}^{58}Ni \rightarrow {}^{116}Ba^* \rightarrow X + xp + y\alpha + zn, \tag{2.3}$$

the process will involve the initial formation of a compound nucleus, which will occur in $\sim 10^{-20}$s. The decay of the highly excited rapidly rotating system proceeds via particle evaporation. Protons, alpha particles and neutrons will carry away large amounts of energy but little angular momentum. For the extremely neutron deficient compound nucleus

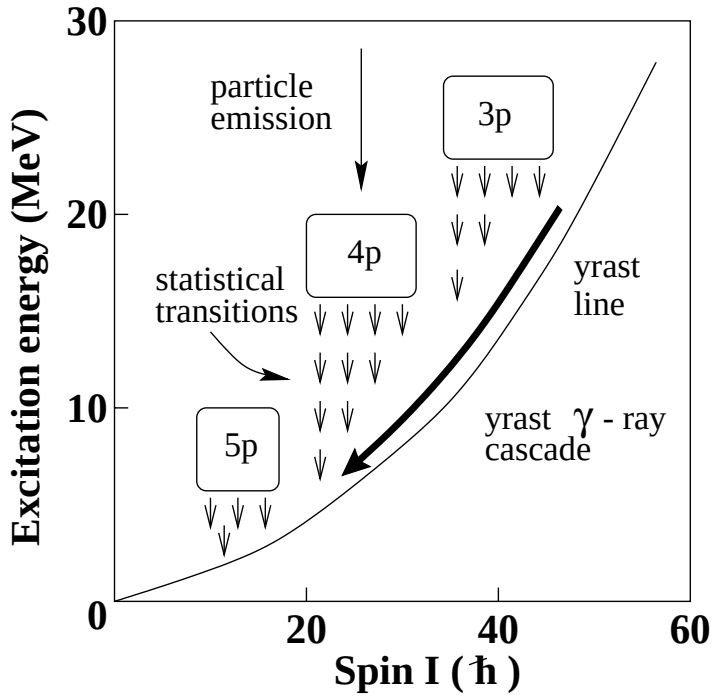

Figure 2.2: Excitation energy plotted versus spin showing the decay of a neutron-deficient compound nucleus following a heavy-ion fusion-evaporation reaction.

(^{116}Ba*) formed in this work, it is energetically favourable for charged particles to be emitted and particle evaporation will continue until the particle separation energy (8-10 MeV) is reached. At this point, after 10^{-15}s, it is no longer energetically possible for a particle to be emitted and the de-excitation continues by a cascade of γ-rays. At these excitation energies the density of nuclear states is very high, therefore the γ-rays depopulating these states are too weak and closely spaced to be resolved. After 10^{-12}s, the excitation energy of the nucleus is lowered and the level density is reduced to a point where discrete γ-ray transitions and decay sequences can be observed. This stage removes large amounts of angular momentum and energy from the system. Approximately 10^{-9}s later the nucleus will reach the ground state configuration.

The diagram of excitation energy against spin (Fig. 2.2) clearly illustrates the stages described. The study of sequences of γ-ray transitions which have the lowest energy for a given spin, termed yrast, or those near yrast, termed yrare, forms the basis of high spin nuclear spectroscopy.

2.3 Heavy-Ion Beam Production

In order to form a compound nucleus, the incident projectile must have sufficient kinetic energy to overcome the Coulomb repulsion of the target nucleus. The incident kinetic energy is then converted to excitation energy and shared equally amongst the constituent nucleons of the newly formed compound nucleus.

The purpose of an accelerator of charged particles is to enable a beam of a specific kind of particles to obtain a chosen kinetic energy and then to focus this beam onto the target nuclei. The 250 MeV ^{58}Ni beam required for this experiment was provided by the 88 inch cyclotron, located at the Lawrence Berkeley National Laboratory (LBNL), Berkeley, CA.

The 88 inch cyclotron is a third generation sector-focused cyclotron, combining the high beam intensity obtained from first generation machines with high beam energies possible with second generation machines. It is fed by two Electron Cyclotron Resonance (ECR) high charge-state ion sources which enable the production of heavy-ion beams from helium to neon with energies up to 32 MeV/nucleon. The cyclotron is a circular device, in which a beam of particles, bent into a circular path by a magnetic field makes many cycles receiving a small energy increment in each orbit until the particle energy reaches the MeV range.

2.4 Target Choice

The choice of target thickness for a high spin γ-ray spectroscopy experiment will be a compromise between the number of statistics obtainable and the requirement of a good energy resolution. The possible target choices are a thin target, a thick target or a backed target.

The use of a thin ($\approx$500μg/cm^2) foil will reduce the scattering of the recoils in the target. This reduces the spread in recoil velocities which, through the Doppler effect, cause a degradation in the energy resolution. The residual nuclei recoil into vacuum and decay with a full recoil velocity (see section 2.18). A thin target will decrease the maximum obtainable event rate but short-lived, high-spin states will be observable.

A thick target ($\geq$2mg/cm^2) enables a higher event rate to be obtained, however the scattering of recoils in the target will result in a poor energy resolution for the observed γ-rays. A backed target typically consists of a thin target mounted on a backing of several

milligrams of Gold (Au) or Lead (Pb). This high density backing ensures the recoiling nuclei are stopped in the target. The residual nuclei may now decay when the recoils have fully stopped eliminating the Doppler shift and broadening effects. Short-lived high-spin states will however be emitted while the recoils are slowing down in the target, resulting in a smearing out of the observed γ-rays.

The target for this work consisted of two thin ($500\mu g/cm^2$) self-supporting ^{58}Ni targets of approximately $1cm^2$ in size. The target was enriched to isotope purity levels in excess of 95% to reduce the probability of creating unwanted reaction products. The choice of two targets induces less Doppler broadening than a single $1000\mu g/cm^2$ target while ensuring maximum reaction rates and hence statistics.

2.5 Interaction of γ-rays with matter

Gamma radiation is emitted from the de-excitation of a nuclear state. The measurement of a γ-ray is achieved by allowing the γ-ray to interact with a detector material. This process may occur in three primary ways.

1. The photoelectric effect
2. Compton scattering
3. Pair production

Each process leads to the partial or complete transfer of the γ-ray photon energy to the detector material.

2.5.1 The Photoelectric Effect

The photon undergoes a reaction with an absorber atom in which the photon completely disappears. An energetic photoelectron, usually from the most tightly bound (or K) shell, is ejected by the atom with a kinetic energy given by

$$E_{e^-} = h\nu - E_b, \tag{2.4}$$

where $h\nu$ is the incident photon energy and E_b is the electron binding energy.

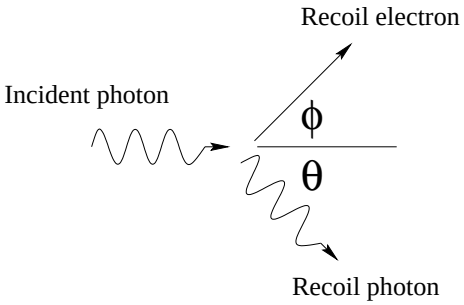

Figure 2.3: Schematic diagram of a Compton scattering interaction.

The interaction also creates an ionised absorber atom with a vacancy in one of its bound shells. This is filled though the capture of a free electron from the medium or internal rearrangement in the atom, resulting in a characteristic X-ray photon being emitted.

2.5.2 Compton Scattering

The interaction takes place between the incident γ-ray photon and an electron in the absorbing material. The incoming γ-ray photon is scattered through an angle θ with respect to its original direction. The photon transfers a portion of its energy to the electron producing a recoil electron, as shown in Fig. 2.3. The expression that relates the energy of the scattered photon ($h\nu^{'}$) to the incident photon energy ($h\nu$) and scattering angle for any given interaction is

$$h\nu' = \frac{h\nu}{1 + \frac{h\nu}{m_0c^2}(1 - cos\theta)}, \tag{2.5}$$

where m_0c^2 is the electron rest mass (0.511 MeV).

2.5.3 Pair Production

If the energy of a γ-ray exceeds twice the rest mass energy of an electron (1.02MeV) the process of pair production is possible. In the interaction (which must take place in the Coulomb field of the nucleus), a γ-ray photon disappears and is replaced by an electron positron pair. The excess energy above 1.02MeV goes into the kinetic energy of the electron and positron. The positron will subsequently annihilate after slowing down in the absorbing medium, producing two annihilation photons which may subsequently be detected.

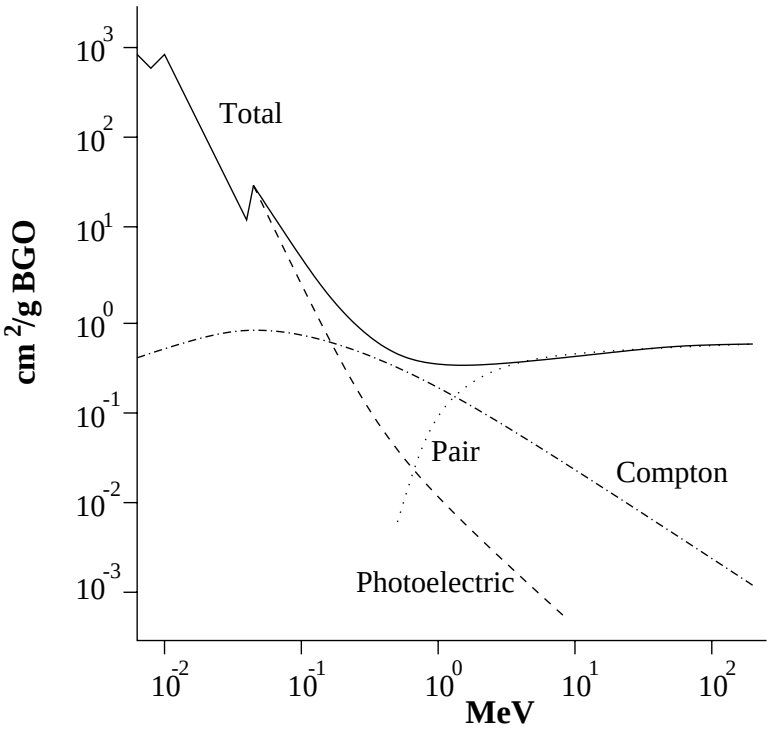

Figure 2.4: Photon mass attenuation coefficient plot for γ-rays incident on BGO [kno89].

2.6 Attenuation coefficients

If a beam of γ-ray photons was incident on a material, each of the interaction processes discussed in section 2.5 removes a γ-ray photon from the beam either by absorption or scattering away from beam direction. The probability per unit length that the γ-ray photon is removed from the beam as it interacts with a material can be described as,

$$\mu = \mu(\text{photoelectric}) + \mu(\text{compton}) + \mu(\text{pair}). \tag{2.6}$$

μ is termed the linear attenuation coefficient and is simply a sum of the three processes. The number of transmitted photons I after the beam has covered a distance x can be expressed in terms of the incident number of photons I_0 as

$$I = I_0 e^{-\mu x}. \tag{2.7}$$

Fig. 2.4 shows the total mass attenuation coefficient for the popular γ-ray detection medium bismuth germanate (BGO) and the constituent contributions to the total [kno89]. The photoelectric effect is the predominant mode of interaction for γ-rays of relatively low

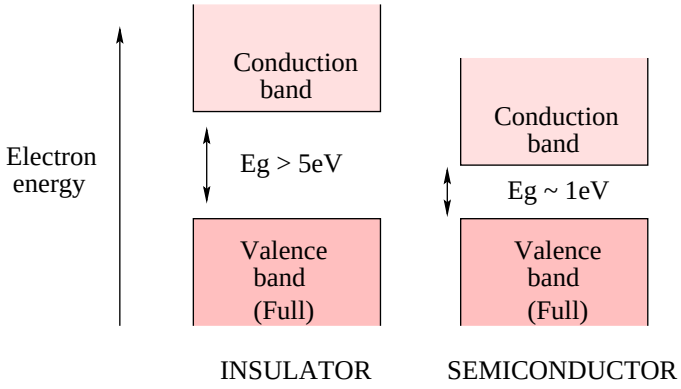

Figure 2.5: The electron band structure in insulators and semiconductors.

energy ($\leq$ 400 keV). In the low energy region of Fig. 2.4 discontinuities in the curve or 'absorption edges' appear at energies corresponding to the binding energies of electrons in the various shells of the absorber atoms. The highest lying edge corresponds to the binding energy of the K-shell electron.

The γ-ray transitions studied in this work have energies in the range of 100 keV up to 3 MeV. Compton scattering will therefore be the dominant process of interaction. In order to reduce the unwanted background which will be obtained in a γ-ray spectrum, due to the partial deposition of energy in the detector, a technique named Compton suppression has been developed. A discussion of this technique can be found in section 2.9.

2.7 Semiconductor Detectors

2.7.1 Semiconductor Properties

The periodic lattice of a crystalline material creates allowed energy bands for electrons within that solid. The energy of an electron will be confined to one of the energy bands. The bands themselves may be separated by ranges of forbidden energies, an example is shown in Fig. 2.5.

The lower valence band contains electrons that are bound to specific lattice sites within the crystal; these are part of the covalent bonding which constitutes the inter-atomic forces within the crystal. The conduction band represents electrons which are free to move through the crystal. Electrons in this band contribute to the electrical conductivity of the material.

The bands are separated by a band gap. A large band gap >5eV will classify a material as an insulator, a small ≈1eV band gap constitutes a semiconductor. The valence band in both cases will be full.

At a non-zero temperature, thermal energy is shared by the electrons in the crystal. A valence electron can gain sufficient energy to be excited from the valence to the conduction band, creating an electron-hole pair. When γ-radiation interacts with a semiconductor the significant effect is the production of many electron-hole pairs. The average energy expended by the γ-ray to produce one electron-hole pair is called the ionisation energy ε. It is experimentally observed to be largely independent of both energy and type of incident radiation. The number of electron-hole pairs produced can therefore be related to the energy of the incident radiation, provided the radiation is fully stopped.

In order to collect the charge carriers from a semiconductor detector the application of an electric field across the crystal is required. This will typically require an applied voltage of the order of thousands of volts. Even in the absence of ionising radiation all semiconductor detectors show a finite conductivity and therefore a steady state leakage current is observed. Random fluctuations in this leakage current will obscure the small signal currents following an ionising event, resulting in a significant source of noise.

The solution is to put a p-n junction in the semiconductor, that is p-type and n-type semiconductors placed in direct contact. This results in a migration of charge carriers, leaving a region empty of charge carriers in the vicinity of the interface of the two materials. The depletion region created constitutes an active area where radiation will interact and result in its detection. By applying a large reverse bias across the p-n junction the depletion region can be made larger. For further information on semiconductor detectors see Ref. [kno89].

2.7.2 High purity germanium detectors

The use of germanium of normal semiconductor purity cannot produce depletion depths of larger than 3mm. γ-ray detectors require much larger depletion regions because γ-radiation is very penetrating. The thickness of the depletion region is given by

$$d = \left(\frac{2\varepsilon V}{eN}\right)^{\frac{1}{2}}, \tag{2.8}$$

where V is the reverse bias and N is the net impurity concentration.

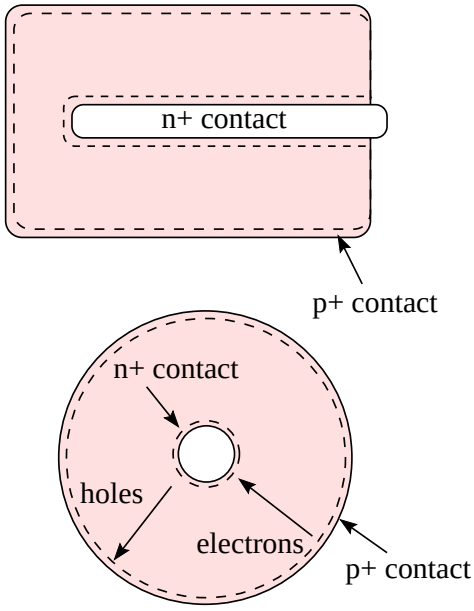

Figure 2.6: Bulletised closed end coaxial n-type HPGe detector. Electrical contact surfaces are shown.

By a reduction in N the depletion region can be made larger. Germanium detectors made from ultra pure germanium are termed high purity germanium (HPGe) detectors. They are available with depletion depths of 1cm or more, with impurity levels as low as 10^9 atoms/cm^3, which compares to 10^{12} atoms/cm^3 for germanium of normal semiconductor purity. If the remaining low level impurities are acceptors the electrical properties of the crystal are mildly p-type. If donor impurities remain, high purity n-type germanium is produced.

It is not possible to operate HPGe detectors at room temperature (300K). The small band gap of germanium (0.7eV) would enable thermal excitation of electrons across the band gap to produce large amounts of thermal noise. The germanium crystal is therefore cooled to liquid nitrogen temperature (77K), greatly reducing thermal noise.

In order to produce a HPGe detector with as large an active volume as possible, which is required for γ-ray spectroscopy, detectors are constructed using a bulletised closed end coaxial configuration (see Fig. 2.6). Part of the central core of the HPGe crystal is removed and electrical contacts are placed over the outer cylindrical surface and the flat front end, forming a $p+$ contact. The inner core of the crystal forms the $n+$ contact. By manufacturing

the crystal long in the axial direction, active volumes as large as 400cm^3 can be achieved.

HPGe detectors have a relatively low ionisation energy of ≈ 3 eV. This produces a large number of electron-hole pairs for a given γ-ray interacting in the detector. This has two key benefits:

- There is a reduction in the statistical fluctuation in the number of charge carriers per pulse.
- There is a larger amount of charge created per interaction, giving a superior signal to noise ratio.

A HPGe detector will therefore have a good energy resolution, typically the full width at half maximum (FWHM) for a 1.3MeV γ-ray is 2 keV.

HPGe detectors are sensitive to performance degradation caused by radiation damage. Fast neutrons increase the amount of hole trapping within the active volume of the detector. Measured peaks in the pulse height spectrum will show a tail toward the low energy side, resulting in a degradation in the γ-ray energy resolution. The HPGe detectors used in this work are n-type. p-type detectors, whose signals are dominated by hole collection, are much more affected (perhaps 20 times more sensitive) by radiation damage.

2.8 Inorganic Scintillators

The mechanism for scintillation in inorganic materials depends on the energy states determined by the crystal lattice of the material. In the same way as a semiconductor, electrons have discrete bands with a band gap between the valence band and the conduction band. Absorption of energy results in the elevation of an electron from the valence band to the conduction band. When it returns to the valence band a photon is emitted. This is however an inefficient process giving photons of too high an energy to be visible.

The probability of photon emission during de-excitation is enhanced by adding small amounts of impurity, called activators, to the scintillator. They create special sites in the lattice which alter the normal energy band structure, resulting in energy states being created in the band gap. The electrons de-excite through these states, which results in visible photons being produced.

A major limitation of scintillator detectors is their relatively poor energy resolution. In order to convert the incident radiation to light and subsequent generation of an electrical signal, a number of inefficient steps are required. The energy required to produce a photoelectron is ≈100eV. The statistical fluctuation in this number places a limitation on the energy resolution that can be achieved.

2.8.1 Bismuth Germanate

Bismuth Germanate (BGO) is a scintillator material commonly used by γ-ray spectroscopists. The large atomic number (83) and high density (7.3g/cm^3) of bismuth result in it having a high stopping power for γ-rays. Relative to another commonly used scintillator for γ-ray studies sodium iodide (NaI), 6cm of BGO is required to absorb a 1MeV γ-ray as opposed to 14cm of NaI. The light yield from BGO is relatively low (15% that of NaI) so it is used when the need for high γ-ray counting efficiency outweighs energy resolution requirements. BGO is a pure inorganic scintillator, requiring no trace activator. The luminescence is associated with the optical transition of the Bi^{3+} ion, which is a major constituent of the crystal. There is a large shift between the optical absorption and emission spectra of the Bi^{3+}, resulting in little self absorption and therefore the crystal remains transparent to its own emission over many centimetres.

2.8.2 Caesium Iodide

Caesium Iodide (CsI) is an alkali halide like the other common scintillator sodium iodide (NaI). It is commercially available with thallium or sodium as an activator material. CsI has a higher efficiency for γ-ray detection than NaI. CsI(Tl) has the very useful property of a variable decay time depending on the type of particle that interacts in the medium. This allows pulse shape discrimination (PSD) techniques to be employed, to differentiate between various types of radiation.

2.9 Compton suppression

An ideal γ-ray detector will give a single well resolved peak with no associated continuum for each γ-ray interaction. Therefore a ^{60}Co source (often used for detector calibration) placed

in front of a HPGe detector should give two clear, well defined peaks at 1173 and 1332keV respectively. Unfortunately, the energy region in which γ-ray spectroscopists are interested (0.2 - 2MeV) is the region where the most common γ-ray interaction in a detector will be Compton scattering, as detailed in section 2.5.2. This results in the γ-ray only depositing a fraction of its energy in the HPGe detector before it scatters out, meaning a large Compton continuum is observed in the pulse height spectrum. Other sources of background include backscatter peaks which are observed when γ-rays Compton scatter from the surrounding material into the detector and annihilation peaks from electron-positron decay after pair-production from high energy γ-ray interactions. In order to study high spin nuclear structure a way of improving the peak to total in the observed pulse height spectrum has to be found.

2.10 The Escape Suppressed Spectrometer

The observed pulse height spectrum can be improved if the primary γ-ray detector is surrounded by another detector which uses coincidence techniques to veto events which have not deposited their full energy in the HPGe detector. In practice a HPGe-detector is surrounded by the scintillator BGO, which has a high γ-ray stopping power. A γ-ray which Compton scatters out of the HPGe detector will be seen in coincidence in the BGO detector, this event can then be rejected by electronic suppression.

A schematic diagram of the escape suppression shield electronics is shown in Fig. 2.7. The output from the germanium detector pre-amplifier, which amplifies and shapes the signal from the detector crystal to form a negative pulse of $\sim$100mV is split into two paths. One signal is fed into a spectroscopy amplifier where the pulses are integrated and shaped for $\sim 2\mu$s to form a positive signal. The magnitude of this signal is proportional to the energy of the interacting photon. The signal can then be digitised using an analogue to digital converter (ADC) and used for subsequent processing. The other signal is fed into a timing filter amplifier (TFA) which provides fast amplification ($\sim$ns), producing a larger amplitude ($\sim$V) negative output pulse. The pulse is fed into a constant fraction discriminator (CFD), which will trigger a fixed time after the leading edge of the input pulse reaches a constant fraction of its final amplitude. This is providing the signal is greater than the minimum discriminator level which is set to reject unwanted noise pulses. The output of the CFD is a negative logic pulse 1V in amplitude and 50ns in width. This signal is delayed ($\sim$ns) to

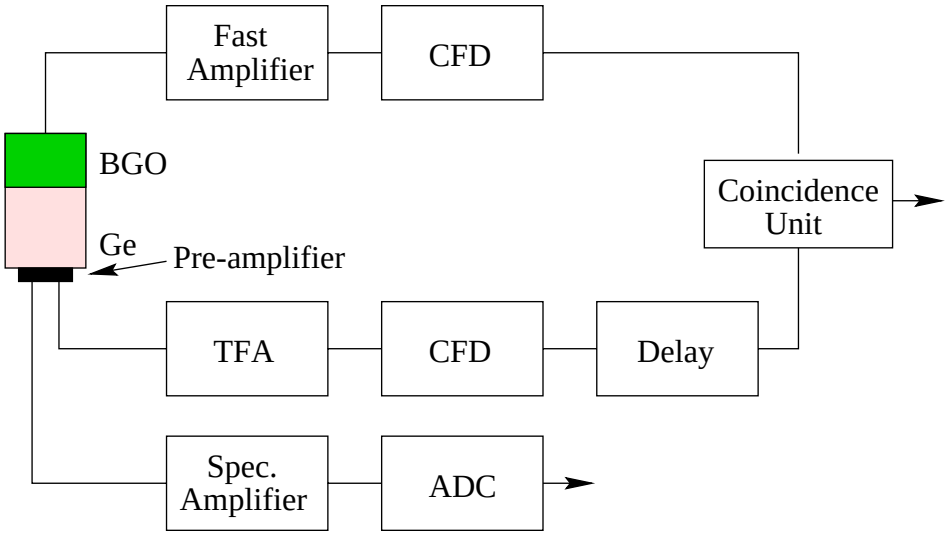

Figure 2.7: A schematic diagram of the escape suppression shield electronics, used to veto Compton scattered events. Only events which do not meet the coincidence unit requirements are accepted.

ensure it will coincide with a timing signal from the BGO should it be present. A similar process is used to extract time information from the BGO detector and a 1V amplitude 200ns duration negative output pulse is extracted from the CFD. If a coincidence between the HPGe detector and BGO detector is registered the high resolution energy signal will be vetoed. The HPGe - BGO combination used in this work is termed an ESS (Escape Suppressed Spectrometer) [bea92]. Such a device as employed in the GAMMASPHERE [lee90] detector array is shown in Fig. 2.8.

Each ESS consists of a large central n-type coaxial germanium crystal of dimensions 8cm long by 7.2cm diameter. The detector has a relative efficiency of ≈78% (relative to a 3inch by 3inch NaI crystal, for detecting a 1.33 MeV γ-ray. The central crystal is surrounded by a BGO Compton shield consisting of six wedge shaped crystals around the germanium and one cylindrical backplug behind it. Each scintillator element is viewed by two 1 inch diameter photomultiplier tubes (PMTs). The copper liquid nitrogen cold finger makes thermal contact with the germanium crystal by a non-central route. An optional 'hevimet shield' made of tungsten alloy covers the front face of the BGO crystals. The purpose of this is to prevent a 'false veto' which would occur if a γ-ray directly interacted with the

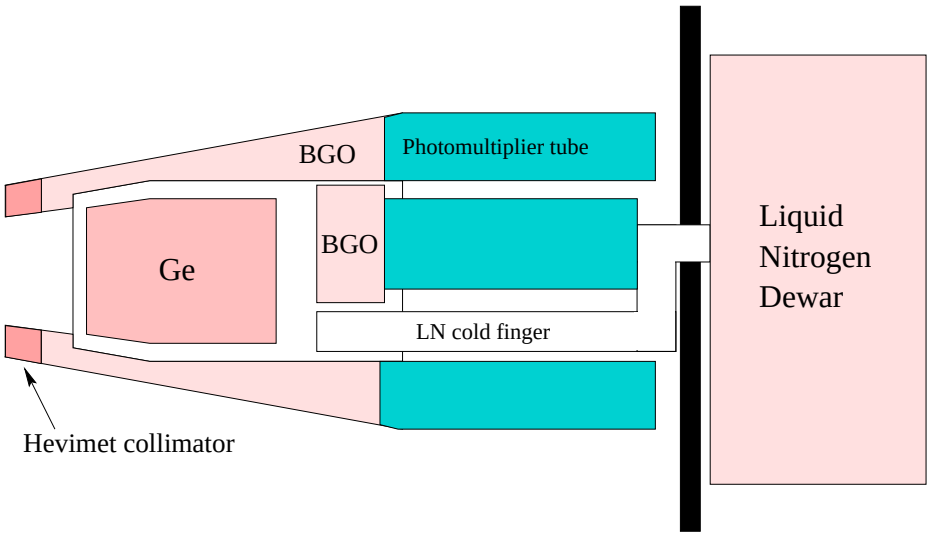

Figure 2.8: Schematic diagram of a GAMMASPHERE escape suppressed spectrometer.

BGO. The front 2cm of the detector construction is tapered to improve the packing of the detector elements in the GAMMASPHERE array of ESS detectors around the target position.

The improvement in peak to total (PT) afforded by using a BGO shield in coincidence with a HPGe detector is significant. Without a shield the germanium detector has a PT of 0.25, this improves to 0.6 with the shield activated. An representative set of spectra are shown in Fig. 2.9.

2.11 Large γ-ray detector arrays

Following a heavy-ion fusion-evaporation reaction, approximately 30 γ-rays are typically emitted. If relationships between these γ-rays are to be established, knowledge of coincidence information is required. In order to supply this information, large arrays of HPGe detectors have been constructed.

The GAMMASPHERE detector array is an array of large volume HPGe detectors which for this work was sited at the Lawrence Berkeley National Laboratory, Berkeley, California. GAMMASPHERE consists of up to 110 ESS detectors mounted in a 4π configuration surrounding a target. In the array the detectors are mounted at 17 different angles relative to the beam direction. With the full complement of 110 detectors, 47% coverage of the full sphere with germanium is achieved, giving a total photo-peak efficiency of 9.9%. For this

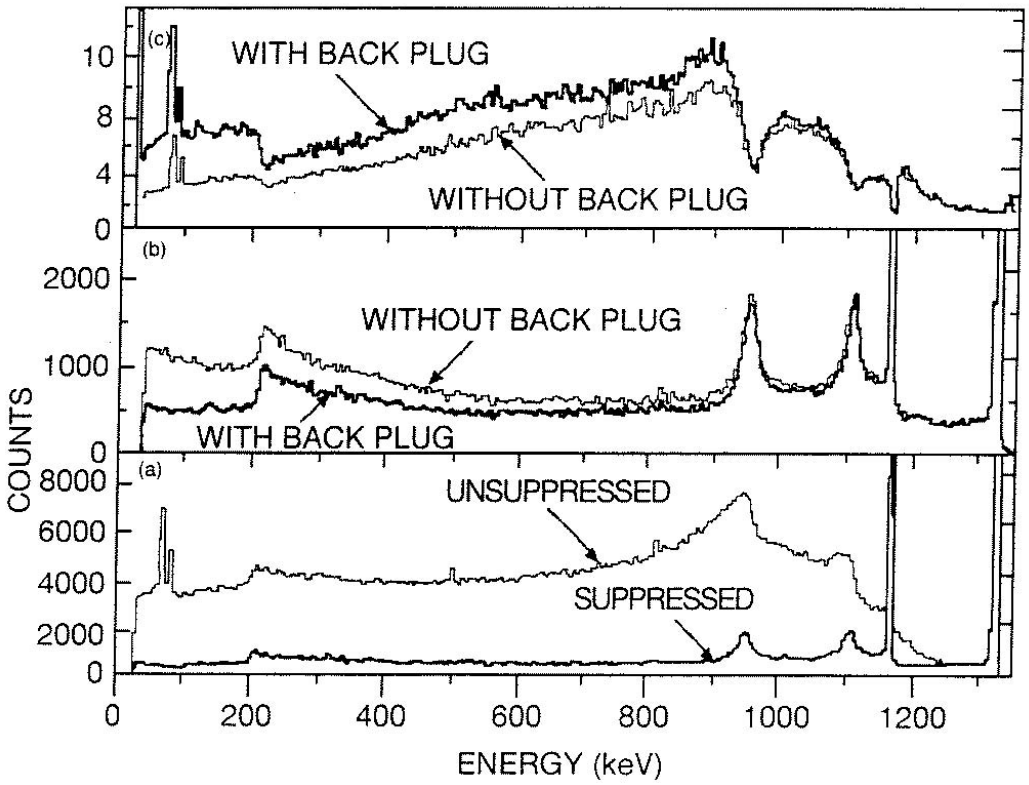

Figure 2.9: An illustrative set of γ-ray spectra obtained by placing a ^{60}Co source in front of an ESS element of the GAMMASPHERE array. (a) shows the large improvement in PT achieved when the BGO suppression shield is used. (b) shows the advantage of using a BGO back plug (c) is the ratio of unsuppressed to suppressed spectra with and without the back plug [bax92].

work the array contained 83 ESS detectors, 15 of the remaining positions were occupied by liquid scintillator neutron detectors, which are discussed in section 2.15. The configuration of GAMMASPHERE is shown in Fig. 2.10.

From a cascade emitting 30 γ-rays the GAMMASPHERE array may typically detect 5 suppressed interactions in coincidence. This would then be called a 5 fold event (γ^5). High-fold coincidence data benefits greatly from the improvement in PT (peak to total) afforded by using an ESS detector. The relationship that the observed signal to noise $\propto (PT)^n$, where n is the fold, means a suppressed PT of 0.6 in a 5 fold event gives a factor of 80 improvement over a non suppressed PT of 0.25.

The quality of the spectra obtained from a large array such as GAMMASPHERE can be

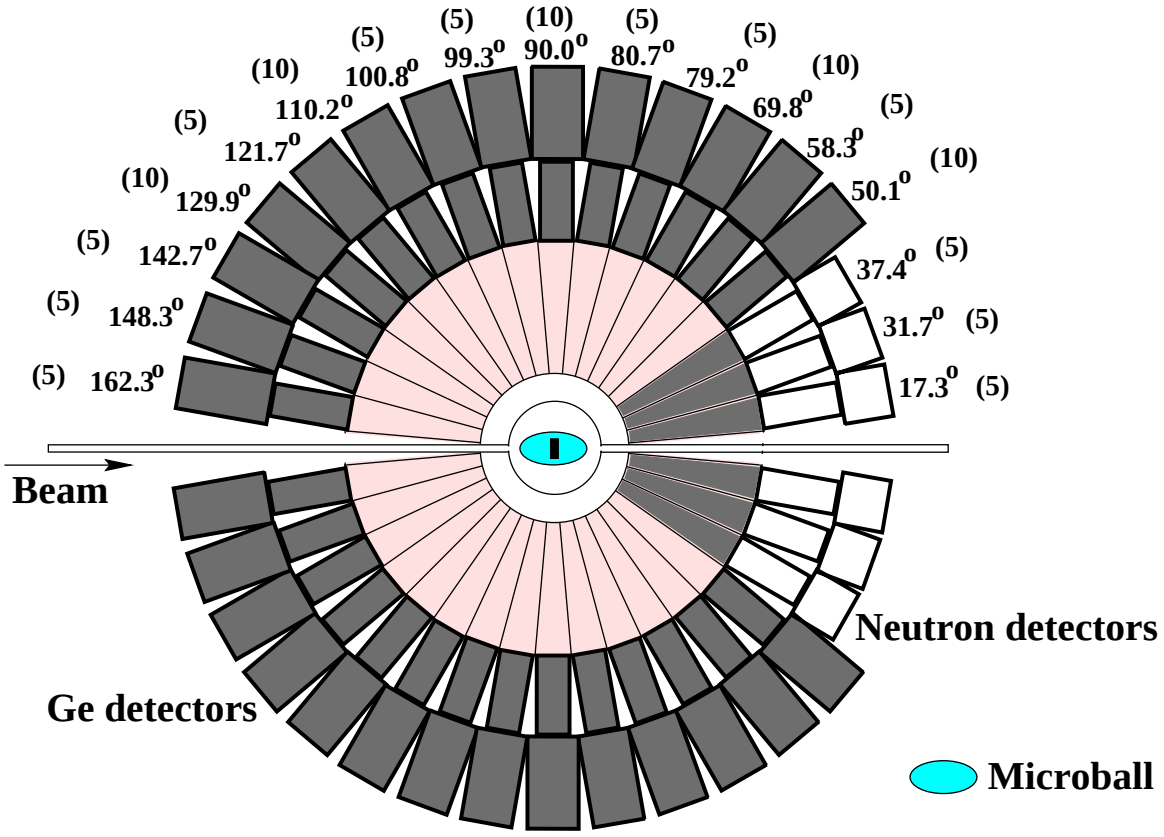

Figure 2.10: A schematic diagram of the GAMMASPHERE array containing the MICROBALL and Neutron detectors as used in this work.

classified by quoting the resolving power of the array. It is not sufficient to just improve the overall efficiency of the system. It is also necessary to be able to resolve the γ-rays from the complex background obtained. The resolving power can be quoted [twi93] as,

$$R = \left[\frac{SE_\gamma}{\Delta E_\gamma} . PT \right]^n \tag{2.9}$$

where SE_γ is the average energy separation of the γ-rays, which is fixed by nuclear structure and ΔE_γ is the FWHM (full width at half maximum) of the detector. This can be improved by limiting the opening angle of the detector, which can be achieved by detector segmentation as discussed in section 2.18.

2.12 The GAMMASPHERE electronics system

2.12.1 Introduction

A large array of HPGe detectors requires a complex electronics and data acquisition system (DAQ). The GAMMASPHERE array has 110 ESS detectors associated with it, each requires a number of signal cables and high voltage supplies. The system must be able to handle the high data rate from the detectors (possibly 20kHz) while remaining easily configurable. Possibilities include

- Detector threshold adjustments via software
- The addition of ancillary detectors
- Future system upgrades

The industry standard Nuclear Instrumentation Modules (NIM) is an impractical solution for such a large detector array because each box provides only one function. The GAMMASPHERE electronics and DAQ system is based on the VXI standard. VXI is an extension of the VME format (VME eXtention for Instrumentation). The large board size used considerably reduces the cabling and therefore improves reliability. Each VXI board processes the signals from two detector modules.

2.12.2 High voltage

The high voltage (HV) supply for each ESS is computer controlled. The supply comes from a small wedge shaped box mounted on the detector dewar. This supplies the 850V for each of the 14 PMTs corresponding to the 7 BGO elements and the -5kV required for the HPGe detector.

2.12.3 Signal processing

Each HPGe detector provides four primary signals: two energy signals, one for the 4MeV high resolution germanium readout and the second for a 20MeV low resolution signal; the third is a logic pulse for timing purposes which is used to determine $\gamma - \gamma$ coincidence; the final output is the side channel energy, which is used with the electrically segmented detectors which are described in section 2.18.

The 7 BGO signals from each ESS are amplified separately using 10× amplifiers mounted in the wedge shaped box attached to each dewar. The signal then enters the VXI electronics where the signals are processed. The outputs are a BGO sum energy for each shield and a logic pulse associated with a 100keV discriminator used for Compton suppression when analysed with the HPGe timing signal.

Each event in the GAMMASPHERE is subjected to a multiplicity condition; if this is satisfied the various signals produced by the event are recorded for off-line purposes. The system is reset if the condition is not achieved. The master trigger system is initiated by a Compton suppressed germanium fast signal ('clean' ge signal), 800ns is then allowed for the trigger multiplicity to be met and the event readout takes $10\mu s$.

2.12.4 Data Readout

The good events pass through an event builder which formats the data and sends it to be stored for off-line purposes on Exabyte tapes, which have a 5GB capacity and a data rate of 450kb/s. The data can be written to two tapes in parallel giving a data rate of 900kb/s. For each event, the information written to tape included: the event length, total Ge and BGO multiplicities, the identification number of the detectors that fired, high resolution Ge energies, the Ge side channel energy, Ge detector time signals and the BGO sum energy. In addition to this any ancillary detector information added to the GAMMASPHERE signals can be written out. At the same time, the data is sent to workstations enabling online data analysis.

2.13 Channel Selection Techniques

The reaction studied in this work:

$$^{58}\mathrm{Ni} + ^{58}\mathrm{Ni} \rightarrow ^{116}\mathrm{Ba}^{*} \rightarrow \mathrm{X} + \mathrm{xp} + \mathrm{y}\alpha + \mathrm{zn},$$

produces the most neutron-deficient compound nucleus in this mass region that can be formed with stable beams and targets, in order to access the light Xe and Te nuclei. Following the heavy-ion fusion-evaporation reaction, the total cross-section is fragmented into a large number of exit channels, resulting in a large number of residual nuclei being simultaneously populated. The low Coulomb barrier combined with the pressure for decay towards

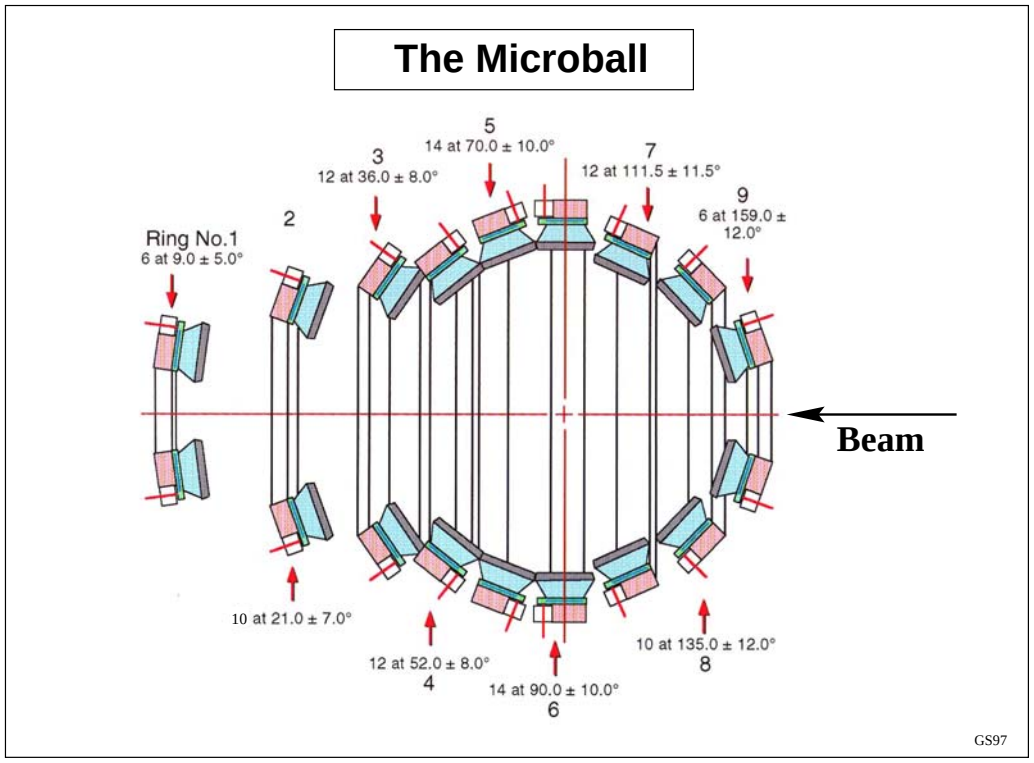

Figure 2.11: Schematic diagram of the MICROBALL charged particle detector [sar96].

stability causes proton and alpha emission to dominate over neutron evaporation. In order to study the reaction residues a number of methods of channel selection have been utilised.

2.14 The MICROBALL Charged-Particle Detector

2.14.1 Introduction

The MICROBALL [sar96] is a 4π charged-particle detection device, designed for use with the GAMMASPHERE array. The purpose of such a charged-particle detector is to detect and discriminate between light charged-particles such as protons, deuterons and alpha particles, evaporated following a fusion-evaporation reaction.

The device consists of 95 closely packed CsI(Tl) elements arranged in 9 rings with increasing forward segmentation, see Fig. 2.11. The MICROBALL is installed completely surrounding the target position inside the GAMMASPHERE scattering chamber, as shown in Fig. 2.10. The non-spherical arrangement covers 97% of 4π. The segmentation is required to

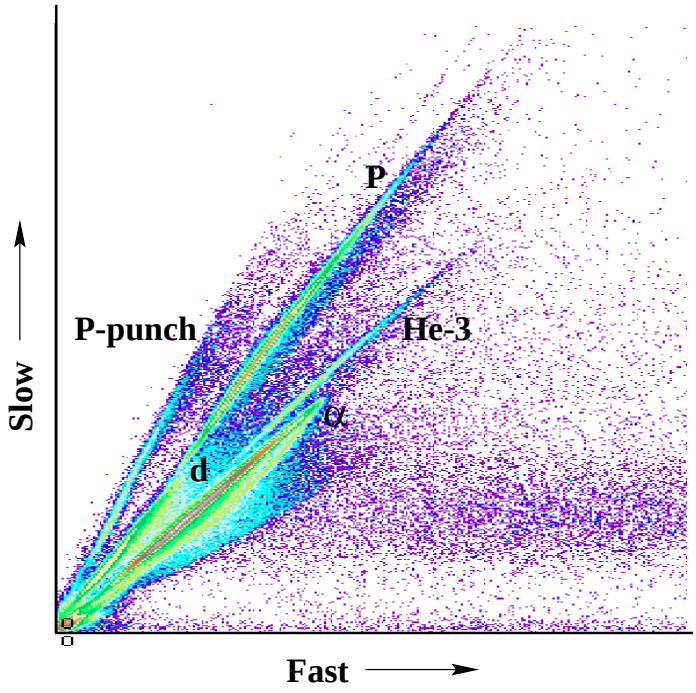

Figure 2.12: Total energy (slow) against fast component for the MICROBALL from the $^{58}\mathrm{Ni} + ^{58}\mathrm{Ni}$ reaction studied in this work. The separation for protons, deuterons, He-3 and alpha particles is clear.

distribute the counting rate nearly equally among the detectors, since most emitted charged particles are forward focused. This allows the device to keep up with the high counting rates (≈10k) of GAMMASPHERE. The design is such that the problem of absorption and scattering of γ-rays through the MICROBALL before they reach the ESS detectors is minimised. This is achieved by using thin (2mm) CsI and coupling each element with Si photo-diodes to read out the scintillation light.

Section 2.8.2 details the use of CsI(Tl) as a detection medium. Excellent particle identification (PID) is achieved by using pulse shape discrimination (PSD) to separate the two decay components of CsI(Tl). The fast component has a mean decay time $\tau = 0.4 - 1.0\mu s$, the amplitude being dependent upon the interacting particle type. The slow component of the light has a $7\mu s$ decay time but it is independent of particle type. An experimental spectrum illustrating the quality of PID possible with the MICROBALL is shown in Fig. 2.12. The separation between protons, deuterons, He-3 and alpha particles is clear, particularly at higher energy where this technique works the best. If the energy of the incident protons

exceeds ≈40 MeV, then they can 'punch' through the CsI(Tl) depositing only a fraction of their full energy in a detector element. This effect is marked by P-punch in Fig. 2.12. These events occur on a faster time scale than full energy proton hits and so are well separated from such events.

2.14.2 Signal Processing

The preamplifiers are mounted 120cm from the MICROBALL, outside of the GAMMASPHERE supporting frame structure. They are charge sensitive devices integrating to produce pulses with a 600ns rise time and a 300μs decay time placing a limit on the maximum count rate achievable in each detector element to ≈4000 counts/s. A low and high frequency 2 stage shaper was used to recover the two light components of the CsI(Tl) producing the energy and PID signals.

The electronics were integrated into a set of CAMAC (Computer Automated Measurement and Control) standard modules, which were controllable by a PC workstation, enabling software adjustment of the discriminator and energy settings. A clean high-fold ESS coincidence was used to trigger the MICROBALL, which enabled the number and type of charged particles detected in coincidence with a γ-ray cascade to be recorded. The signals were digitised using FERA (Fast Encoding and Readout ADCs) modules which gave a signal output of detector number, energy, PID and zero crossover time (see section 2.14.3). The readout of the full MICROBALL information is achieved by an interface module which reads the FERA and attaches the information to the GAMMASPHERE readout system for each event.

2.14.3 Particle Selection

Particle identification was achieved in two principle ways: (i) Pulse shape discrimination (PSD), described in section 2.14.1 and illustrated in Fig. 2.12. (ii) Zero Crossover Time (ZCT), detailed here and illustrated in Fig. 2.13.

A time signal was obtained from the crossover time of the differentiated fast signal of the constant fraction discriminator (CFD), subtracting from this the RF time of the cyclotron. The resultant signal enables PID to be achieved. An example spectrum obtained from off-line sorting is shown in Fig. 2.13. The plot shows two clear peak regions, the lower

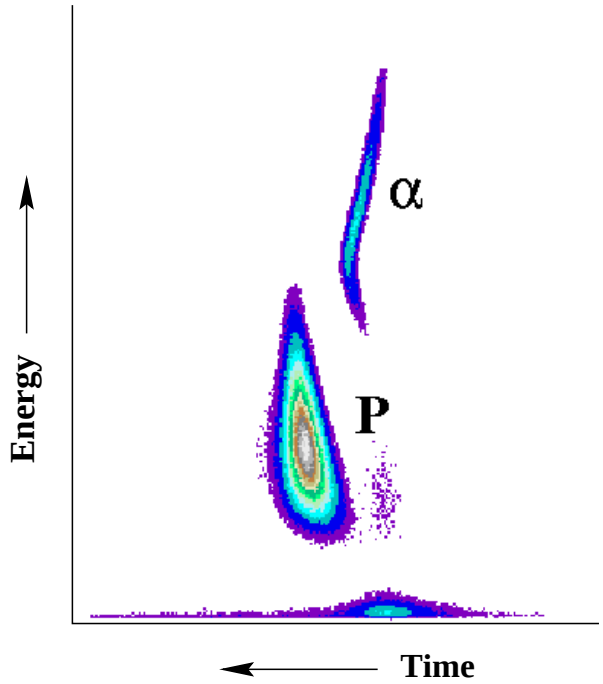

Figure 2.13: Plot of Energy against zero crossover time (ZCT). Notice the excellent α-time resolution.

energy peak detected with a longer time interval represents protons. The α-particles have a better time resolution partly due to their higher energy. The PID however is not as good as that achievable by plotting the ratio R of slow/fast against total energy, demonstrated in Fig. 2.14. By combining both techniques and plotting ZCT against R, the optimum particle selection is achieved, shown in Fig. 2.15. The number of equally spaced peak regions shown on this figure originate from the beam pulsing from the cyclotron. These MICROBALL spectra have no prompt time requirement from GAMMASPHERE and therefore the beam pulsing is observed. Software polygonal gates were placed around the prompt proton and α regions in Fig. 2.15 and spectra were incremented. The results of requiring 3p, 4p and 2pα gates are shown in Fig. 2.22. The clear difference between these spectra illustrates how effectively the MICROBALL particle selection technique works.

The MICROBALL is 90% efficient for the detection of protons. Consider that for a typical reaction exit channel such as 4p, the efficiency for the detection of these 4 protons will be 0.9^4 or 66%. This will mean that the reaction channel selection with the MICROBALL will not be perfect. A further method of channel selection to enhance the MICROBALL results

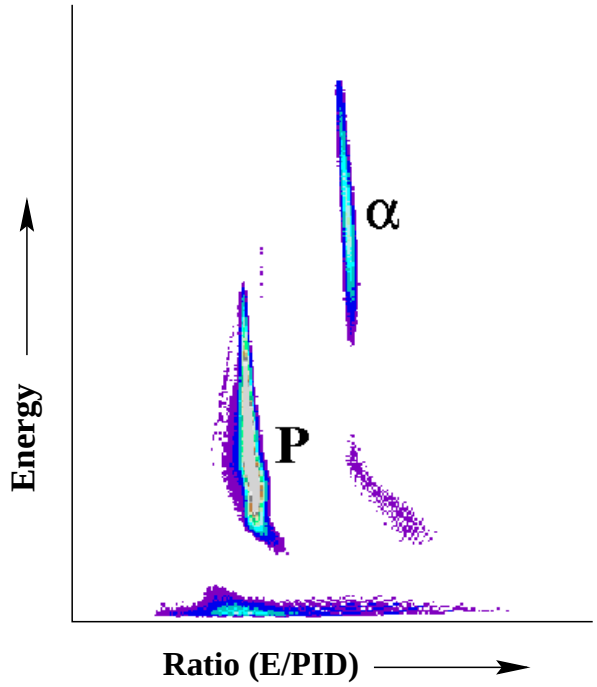

Figure 2.14: Plot of energy against the ratio of fast to slow component (R).

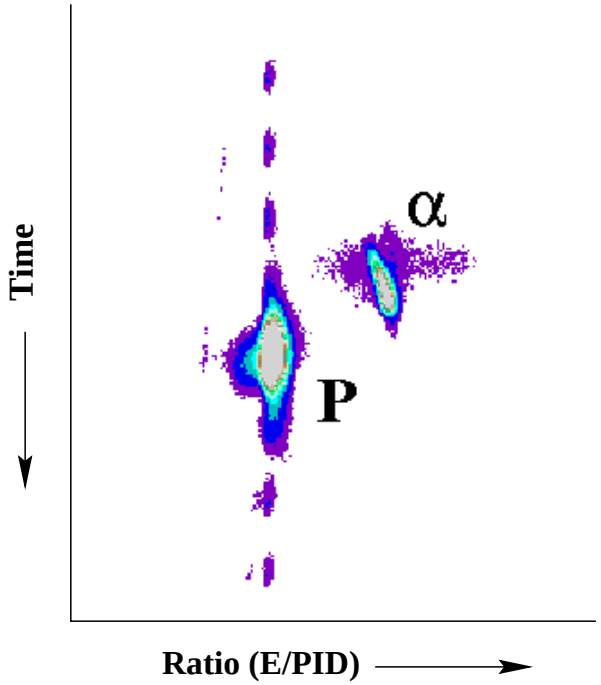

Figure 2.15: Plot of ZCT against the ratio R.

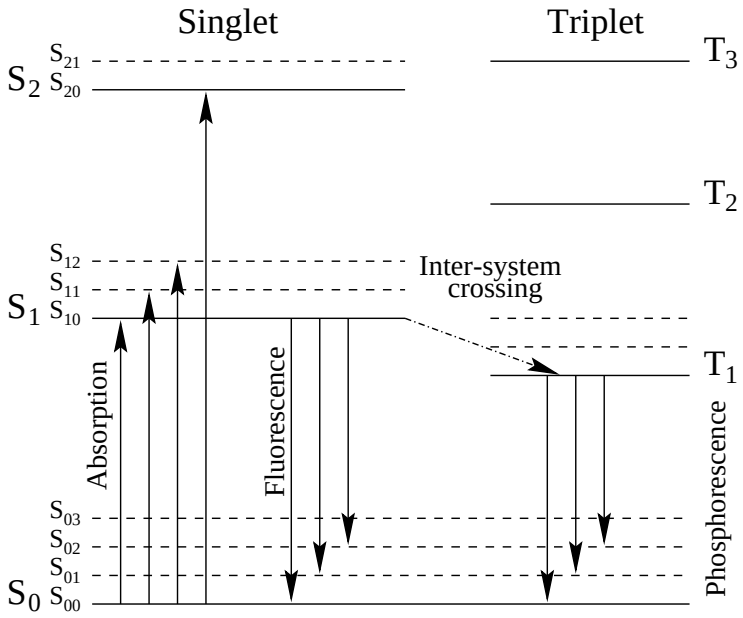

Figure 2.16: Energy levels of an organic molecule with π-electron structure.

has been used and is discussed in section 2.17.

2.15 Neutron Detection

2.15.1 Organic Scintillators

The fluorescence process in an organic scintillator arises from the energy level structure of a single molecule. This is an important result meaning scintillation can be observed independent of the physical state of the material. This is very different to inorganic scintillators where a regular crystalline lattice is required as a basis for the scintillation process.

The NE213 organic scintillator used in this work has organic molecules with symmetry properties which give rise to a π-electron structure, which is illustrated in Fig. 2.16. Energy is absorbed by exciting electrons into any one of a number of excited states. A series of singlet and triplet states are shown in Fig. 2.16. Organic scintillators have energy spacings of $\approx$4eV between S_{00} and S_{10} states. Each of these configurations is subdivided into a series of levels with much finer spacing ($\approx$0.15eV) corresponding to vibrational states in the molecules.

The absorption of energy gives singlet electronic states which are excited quickly ($\approx$ps),

then de-excite to the S_{10} electron state by radiationless internal conversion. The scintillation light (fluorescence) is emitted in transitions between the S_{10} state and one of the vibrational ground states. The lifetime of a triplet state T_{10} is much longer than that of a singlet state S_{10} giving delayed light output, characterised as phosphorescence.

The neutron detectors used in this work contain the liquid organic scintillator NE213. It is produced by dissolving an organic scintillator in a solvent. NE213 is manufactured by Nuclear Enterprises Ltd and is designed for use where pulse shape discrimination between neutrons and γ-rays is required.

2.15.2 Fast neutron detection

The most common method of fast neutron detection utilises the elastic scattering of neutrons by light nuclei. The scattering interaction transfers a portion of the incident neutron kinetic energy to the target nucleus resulting in a recoil nucleus. The maximum fractional energy transfer in neutron elastic scattering occurs for the target nucleus being hydrogen because the mass of the target and projectile are equal. A neutron detector which utilises this principle is termed a proton recoil fast neutron detector.

2.16 GAMMASPHERE neutron detectors

2.16.1 Introduction

For this work the GAMMASPHERE array of ESS detectors (see section 2.11) was augmented using the MICROBALL charged-particle detector (see section 2.14.1) and an array of neutron detectors, in order to provide the channel selection capability required. Fig. 2.10 shows how the NE213 liquid scintillator neutron detectors were mounted into the GAMMASPHERE frame structure. The three most forward angles relative to the beam direction had their ESS detectors removed, reducing the array complement by 15. A total of 15 large volume liquid scintillator neutron detectors were mounted in order to detect neutrons in the recoil cone following the heavy-ion fusion-evaporation reaction in the target. The configuration of neutron detectors installed for this work had a total efficiency for the detection of a neutron of $\approx 5\%$.

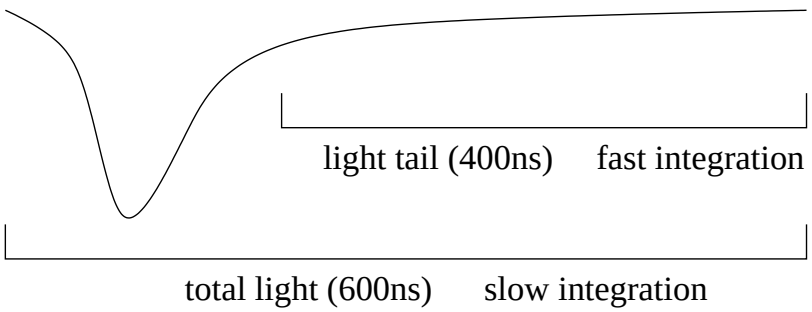

Figure 2.17: An illustration of the anode signal from the liquid scintillator neutron detectors, indicating how the pulse is integrated in order to achieve pulse shape discrimation (PSD).

2.16.2 Neutron - γ discrimination

NE213 is a proton recoil fast neutron detector. In order to distinguish between the detection of neutrons and γ-rays in the liquid scintillator, two methods of particle identification have been utilised.

Pulse Shape Discrimination (PSD): this method is based on the difference in intensity of the slow component of the light pulse in the organic scintillator. This intensity is relatively larger for recoiling protons due to a neutron interaction, than electrons from a γ-ray interaction. Fig. 2.17 illustrates how pulse shape discrimination is achieved. By integrating the anode pulse from the scintillation detector for different periods of time, two output signals can be extracted. The use of pulse shape discrimination assures a high detection efficiency for neutrons since a low detection energy threshold can be set.

Time of Flight (TOF): in the present experiment, the neutron detectors were mounted further away from the target position than the ESS detectors, which were 25cm from the target. The 40cm detector-to-target position distance enabled time of flight (TOF) neutron-γ discrimination to be used in addition to PSD. The two methods of neutron-γ discrimination provide an excellent selection capability when combined.

Fig. 2.18 shows a schematic diagram of the electronics employed for the GAMMASPHERE neutron detectors. The anode signal from the liquid scintillator neutron detector is fed into two separate units. One unit performs pulse shape discrimination of the output pulse, producing pulses which were integrated for two different periods of time. A fast integration of 400ns provides the n-γ sensitive signal, a slow integration of 600ns provides the total

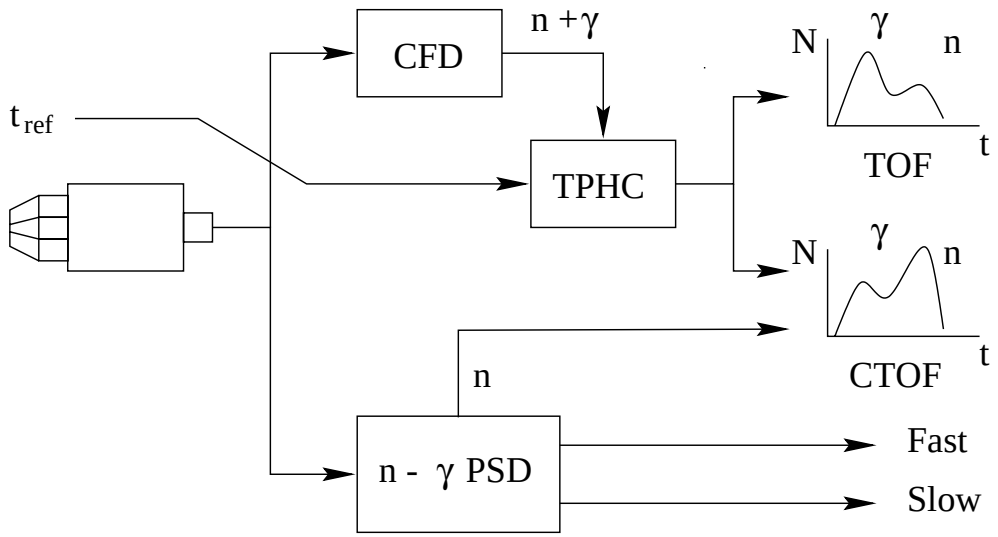

Figure 2.18: Schematic diagram of the GAMMASPHERE neutron detection electronics.

energy deposited in the scintillator. The other unit uses a CFD to provide a logic pulse which provides the stop in a TAC which uses the RF of the 88inch cyclotron as a time reference start. This gives a time of flight spectrum. Since neutrons will travel slower than γ-rays, the TOF spectrum will contain two peaks, enabling n-γ discrimination.

Fig. 2.18 shows four output signals from the neutron electronics. A fifth signal giving the detector numbers that fired in an event is also provided. The five signals are digitised and readout via an interface module, the information is then added to the GAMMASPHERE readout system. The neutron detectors are triggered by a clean high fold germanium signal from the GAMMASPHERE enabling the number of neutrons detected in coincidence with a γ-ray cascade to be stored.

Representative spectra from the time of flight electronics are shown in Fig. 2.19. The top spectrum is ungated and a clear separation between n-γ can be seen. Notice the y-axis is logarithmic, indicating that the number of γ-rays interacting in the scintillator is a factor of 10^3 larger than the number of neutrons interacting. This is to be expected in such a neutron deficient mass region. Placing a hardware neutron gate (from PSD) on the TOF spectrum gives the clean TOF spectrum (Fig. 2.19(B)) showing a clear n-γ discrimination on a linear scale.

The PSD electronics produced outputs for fast and slow neutron pulse integration.

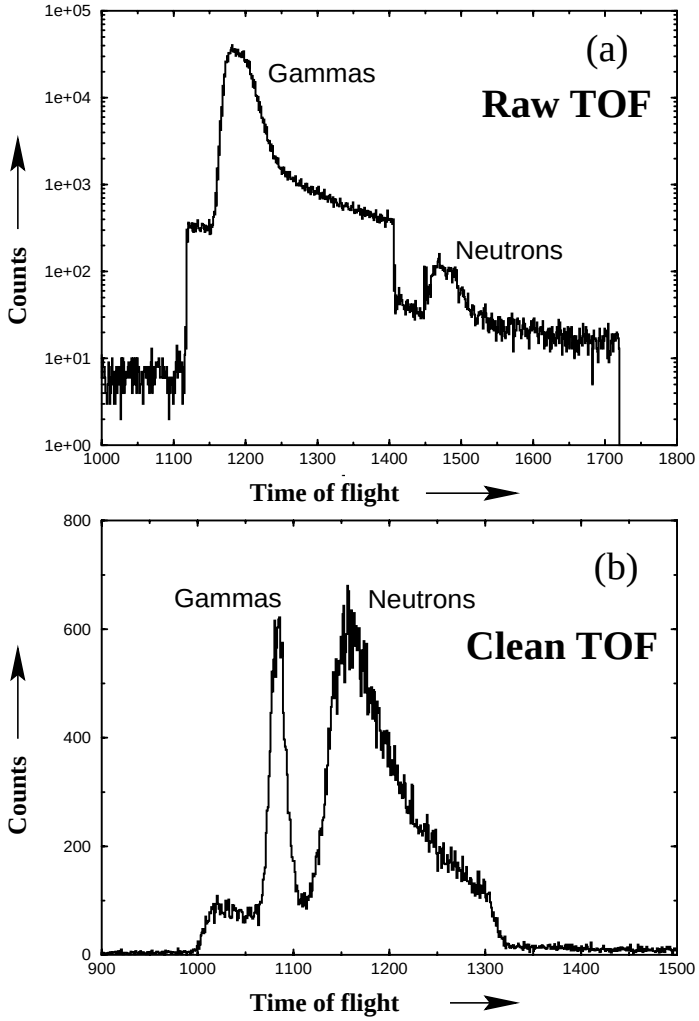

Figure 2.19: In beam neutron time of flight results. (a) the raw TOF is an ungated spectrum. (b) the clean TOF is hardware neutron gated as indicated in Fig. 2.18.

The fast pulse is dependent on the type of interaction in the detector and the slow pulse represents the total energy deposited. By plotting the fast output against the slow (energy) output, the result shown in Fig. 2.20 is obtained. The top spectrum shows how the n-γ discrimination varies as a function of neutron energy. If a narrow region of energy (or gate) is selected on the energy axis, the one dimensional spectrum shown in the lower plot is obtained. The n-γ discrimination obtained is clear, however for low neutron energies the separation possible between the neutron and γ-ray signals from PSD is poor.

The best PSD will be possible for high energy neutrons, where the neutrons produce a higher energy recoil proton in the scintillator. The TOF discrimination technique gives the best separation for low energy neutron events. A low energy neutron will arrive significantly

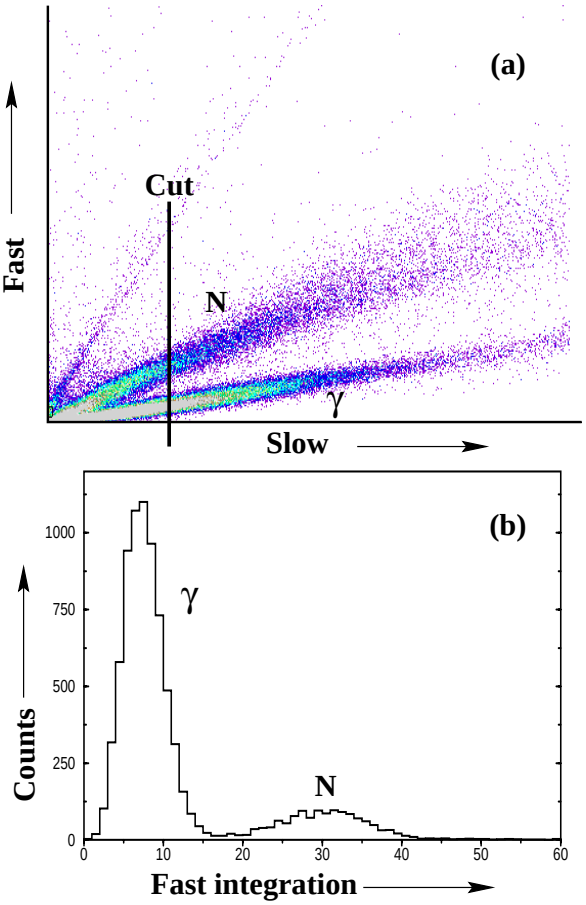

Figure 2.20: In beam neutron pulse shape discrimination results. (a) shows the how n-γ discrimination varies as a function of the energy deposited in the scintillator. (b) The result of a gate being placed on the slow (energy) axis. Clean n-γ discrimination is not possible for incident neutrons with a low energy.

later at the neutron detector affording better n-γ discrimination. Therefore, by using a combination of the TOF and PSD discrimination methods (similar to the MICROBALL, see Fig. 2.15) excellent neutron selection can be achieved, as indicated in Fig. 2.21. By placing a polygonal gate around the neutron signal and projecting out spectra, extremely clean uncontaminated neutron channels can be extracted from the data. An example neutron gated spectrum is shown in Fig. 2.22(d). A requirement of 3p1n has been set in order to select ^{112}I; notice that this spectrum contains no contamination from 3p (^{113}I), which is shown in Fig. 2.22(a). The low number of counts obtained in the ^{112}I spectrum for which 1 neutron has been requested, compared to the pure charged particle evaporation channels can be attributed to two main causes;

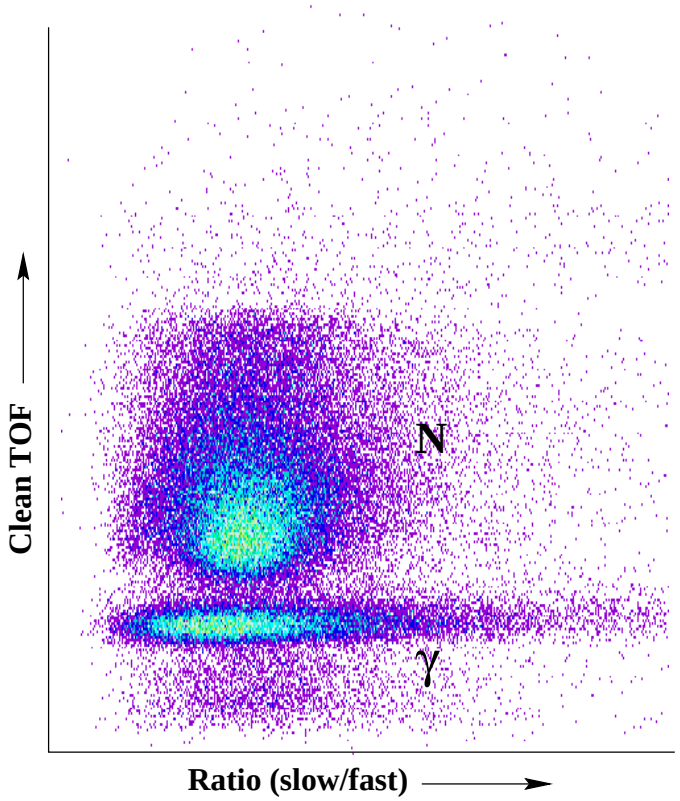

Figure 2.21: Neutron-γ discrimination using PSD and TOF combination gating.

- Charged particle emission dominates over neutron emission in compound nucleus decay in this extremely neutron deficient mass region.
- The total quoted efficiency for the detection of a neutron was only 5%.

The second point means that the extremely weakly populated ($\sim 100\mu$barn) channels which decay by the emission of two neutrons will only be detected with an efficiency of 0.05^2 or 0.25%. Indeed two neutron channels were incremented from the data obtained and the statistics observed were extremely poor. However the requirement of two neutrons did not prevent large contamination from the one neutron channels. The explanation for this came from analysing which neutron detectors fired in a two neutron event. A large proportion of two neutron signals came from adjacent detectors, this was due to a neutron scattering from one detector to another. This resulted in a large number of actual one neutron events being misinterpreted as two neutron events. A solution to this problem is to demand that two non-adjacent neutron detectors fire in a two neutron event.

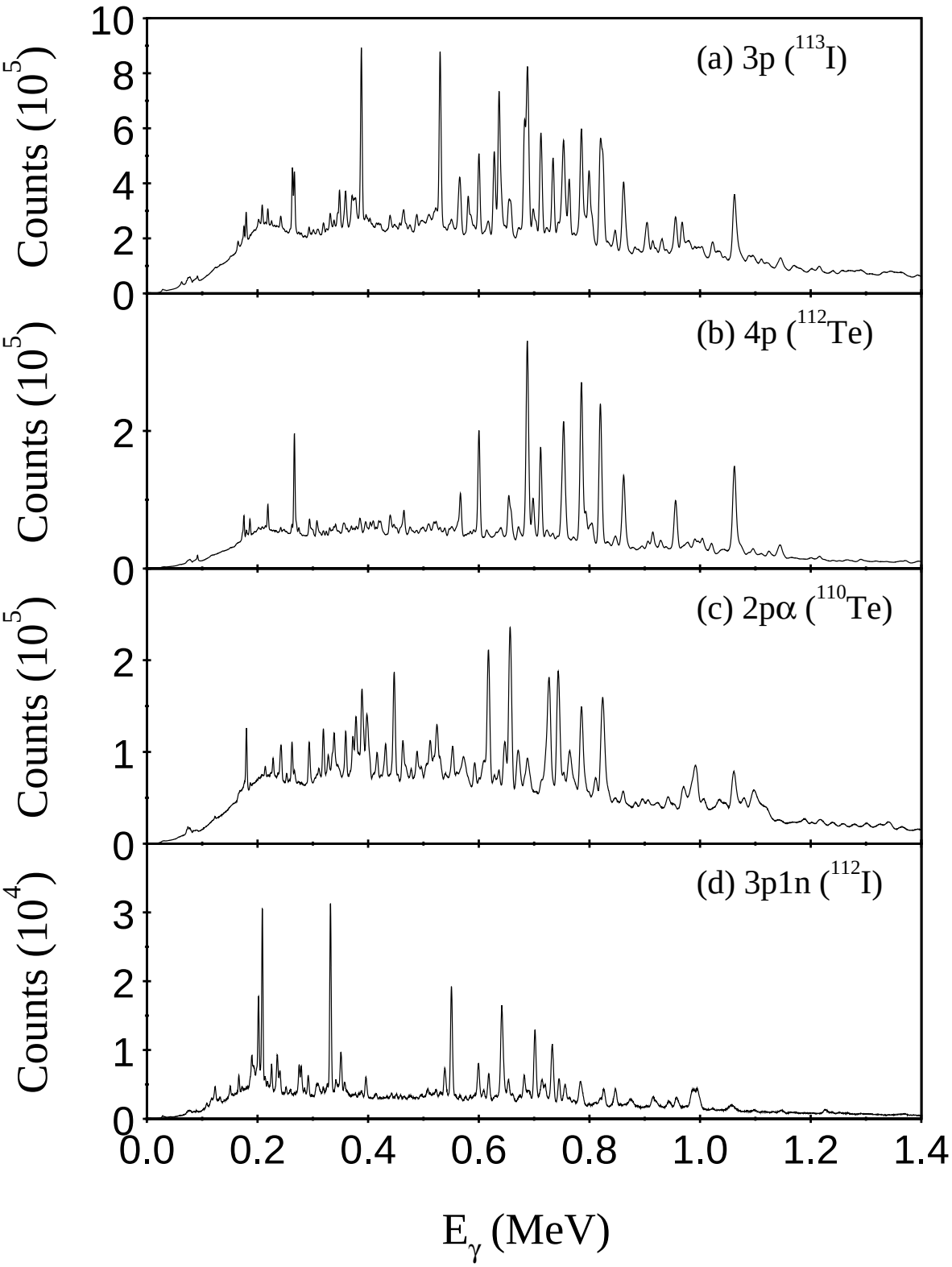

Figure 2.22: Examples of charged-particle and neutron gated γ-ray spectra. Notice the low number of counts in the neutron-gated channel (d) compared to the pure charged particle evaporation channels.

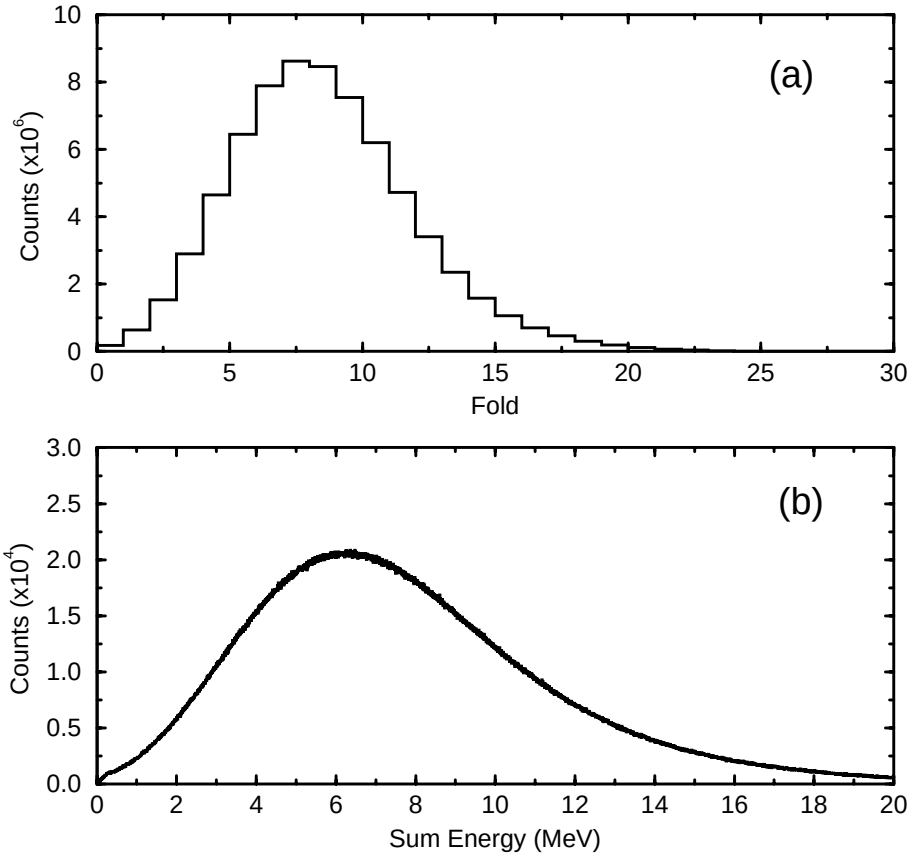

Figure 2.23: Fold and sum energy plots for GAMMASPHERE measured with 83 BGO elements. The sum energy calibration assumes 2.5 keV/channel.

2.17 γ-ray Fold and Sum energy

The entry point for reaction products produced in a fusion-evaporation reaction in the excitation energy versus total angular momentum plane is different depending upon which reaction channel formed the product, ie. it is dependent on the number of evaporated particles, see Fig. 2.2.

Residual nuclei formed by the evaporation of fewer particles leave the nucleus in a state of higher spin and excitation energy than channels with higher particle emission multiplicities. If a highly efficient γ-ray detection medium is placed around the target position then the total sum energy and fold of the γ-rays emitted can be measured. The practical way to achieve this measurement is to use a BGO inner ball, that is a detector system based on an arrangement of a large number of small BGO scintillator elements which fit in between the individual HPGe detectors in the array. Energy resolution is not important therefore BGO is an ideal candidate. The number of detectors that fire (fold), k, gives an estimate

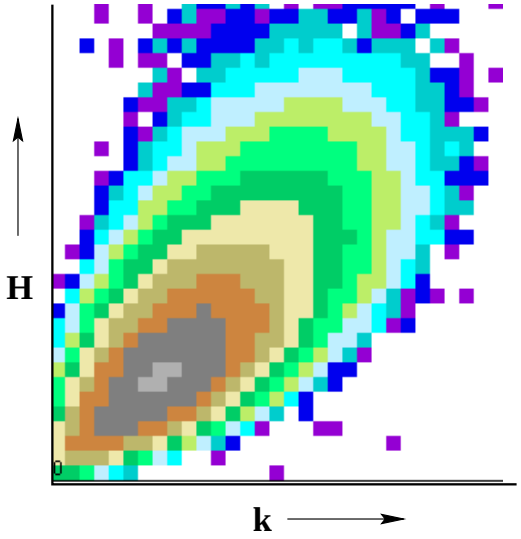

Figure 2.24: 2D total (BGO + Ge) fold and sum energy plot.

of the total γ-ray multiplicity of the cascade (related to the initial angular momentum of the system). The total sum energy, H, emitted in a decay cascade gives information on the initial excitation energy of the nucleus.

The GAMMASPHERE array did not contain a BGO inner ball. However, by removing the hevimet collimators from the front of the germanium detectors the front of the BGO suppression shields were exposed. Since each ESS has 7 associated BGO elements combined to give one signal and the array contained 83 HPGe detectors this gives 83 BGO elements. This arrangement will however suffer from two problems;

- It will not give the BGO coverage and therefore efficiency of a BGO inner ball.
- It will give false vetoes in the BGO shields which will effect high multiplicity events.

The substantial advantage that improved reaction channel selection provides for this work means that these points can be disregarded.

Fig. 2.23 illustrates fold and sum energy results from the GAMMASPHERE array. The average BGO fold (k) is 7, the average BGO sum energy (H) is 7 MeV, indicating an average γ-ray energy of 1 MeV is deposited in the BGO. The H and k observed in the HPGe detectors can be added to the BGO values to give a total H and k for each event. By setting software gates in off-line sorting on a two dimensional total fold and sum energy energy plot, Fig. 2.24, the results shown in Fig. 2.25 were obtained. The figure shows 2pα

and 5p MICROBALL gated spectra with the extra requirements of high and low Hk. The 3 particle evaporation channel 2pα selects ^{110}Te studied in this work. The high Hk spectrum gives the best result because with only 3 particles being evaporated, a higher sum energy and fold would be expected for the entrance of this channel in the excitation energy against spin regime. The resulting spectra removes a large degree of contamination from the 4 particle channel 3pα of ^{109}Sb, γ-rays from this nucleus can typically be seen at low energy (180 keV). For the 5p case the low Hk gate would be the correct choice. Fold and sum energy gating is therefore a useful technique to improve on the channel selection possible with the MICROBALL.

2.18 Gainmatching and Doppler Correction

The γ-ray events recorded on tape will have energies that depend on the incident γ energy, the amplifier gains in the electronics and the Doppler shifts of the γ-ray energies. The effects of the amplifier gains and the Doppler shifts have to be corrected for using the computer software methods of gainmatching and a v/c correction respectively, before analysis of the the data can begin. The method of using a computer to manipulate the data recorded on tape is referred to as 'sorting' the data.

Before and after the experiment, a selection of radioactive calibration sources (^{152}Eu, ^{56}Co and ^{182}Ta) were mounted in the target position in the array. The data collected using these sources were then sorted into individual spectra to enable gain corrections to be applied in order that a total projection of all the detectors could be constructed. The sources were chosen such that a broad distribution of energies could be used to provide excellent gain coefficients.

The recoils leave the target with a velocity 4.5% of the speed of light and decay in flight. The observed γ-rays therefore exhibit a Doppler shift in their measured energies (E_γ), depending on the angle of the detector (θ) which detects them given by,

$$E_\gamma \approx E_0 \left(1 + \frac{v}{c} cos\theta\right). \tag{2.10}$$

The Doppler correction is achieved by knowing the recoil velocity v and the angle θ of each detector. For this work, the GAMMASPHERE array had ESS detectors mounted in rings at 14 different angles relative to the beam direction. The recoil velocity v was determined by

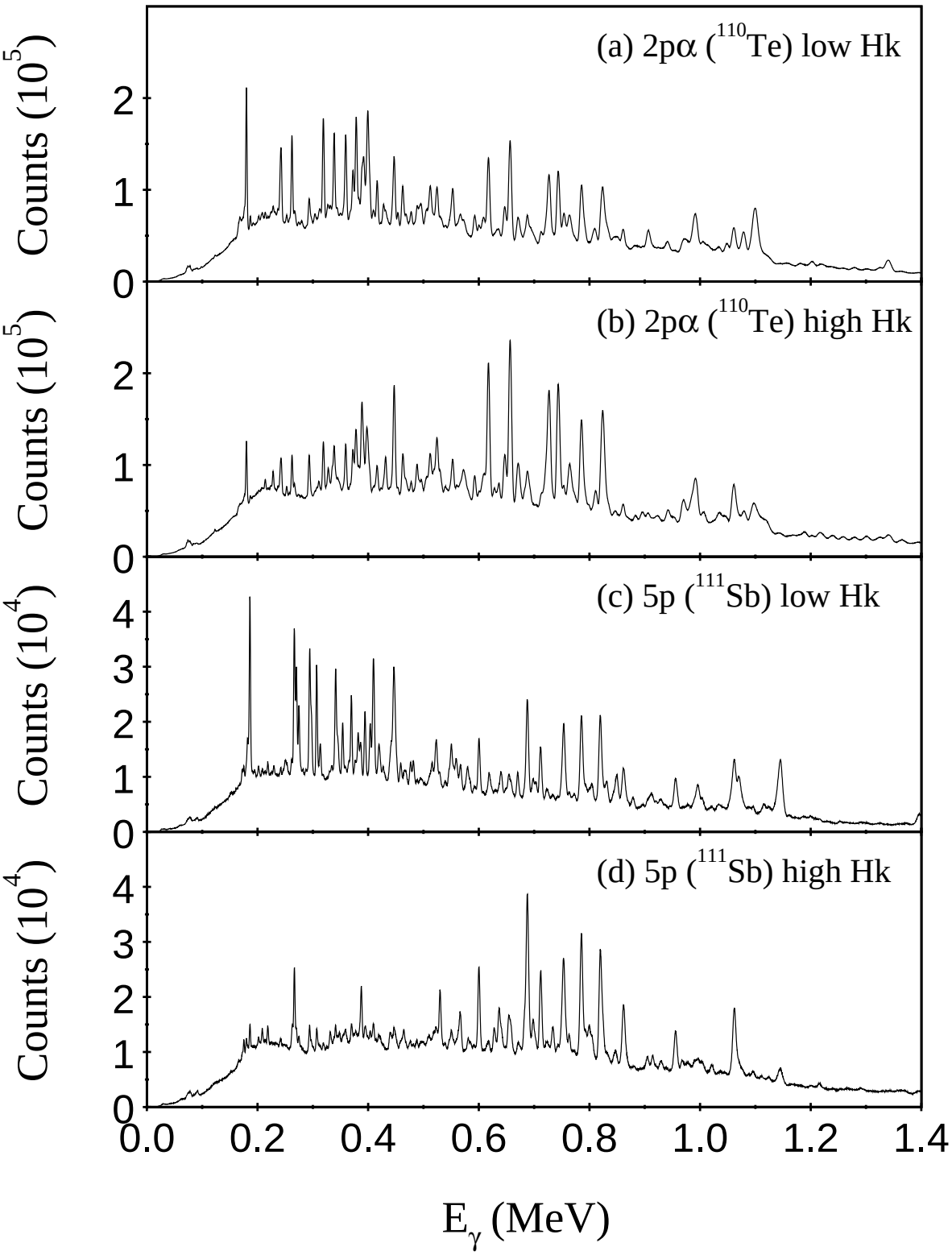

Figure 2.25: 2pα and 5p γ-ray spectra gated by high/low fold and sum energy requirements.

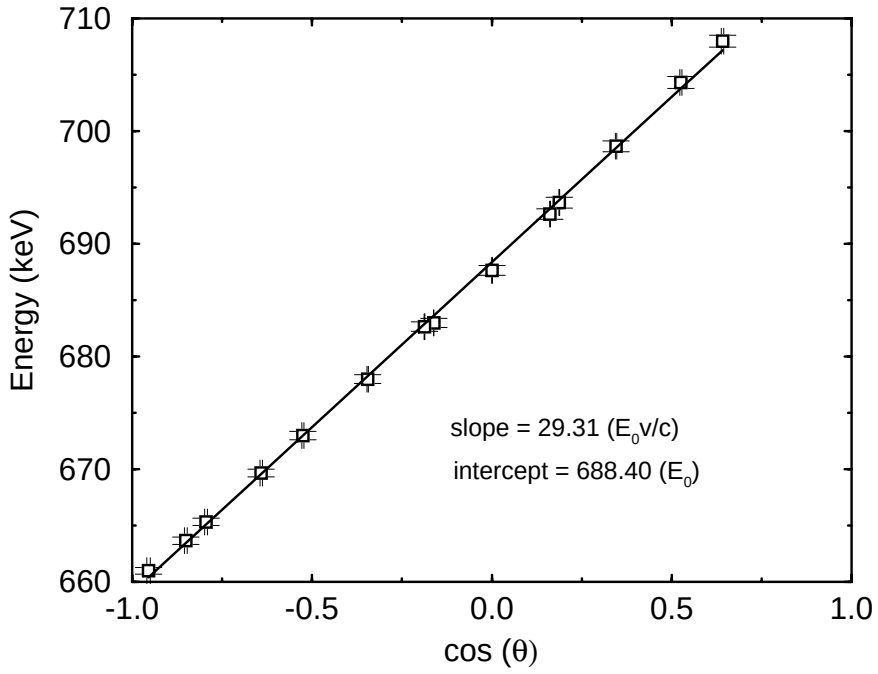

Figure 2.26: Graph of measured peak energy versus cos(θ) for the 688keV transition in ^{113}I giving a v/c of 4.26%.

measuring the energy of the 688keV γ-ray in ^{113}I as a function of the cosine of the angle θ of each GAMMASPHERE ring. The gradient of the resultant plot shown in Fig. 2.26 gives a recoil velocity of $4.26 \pm 0.02\%$ of the speed of light.

The intrinsic resolution of an ESS is ≈2.0keV at 1.3MeV. This will not be observed in practice from a large γ-ray array. The major factors affecting the observed resolution can be summarised as; (i) The intrinsic resolution of the detector system ($\Delta E_{int} \sim 2.0$keV); (ii) The Doppler broadening due to the finite opening angle of the detectors (ΔE_{open}),this term is maximised at $\theta = 90^{\circ}$; (iii) Broadening caused by the evaporation of particles increasing the recoil cone (ΔE_{vel}); (iv) The target. In the target Doppler broadening arises from the slowing down of the recoils and the angular spread of the recoils in the target (ΔE_{ang}). This may be summaries as;

$$\Delta E_{\gamma} = \sqrt{(\Delta E_{int}^2 + \Delta E_{open}^2 + \Delta E_{vel}^2 + \Delta E_{ang}^2)} \tag{2.11}$$

In order to help reduce the Doppler broadening resulting from the finite detector opening angle, 70 of the 110 GAMMASPHERE detectors were electrically segmented into two D-shaped halves (see Fig. 2.27). The high resolution total energy signal is read out from the centre

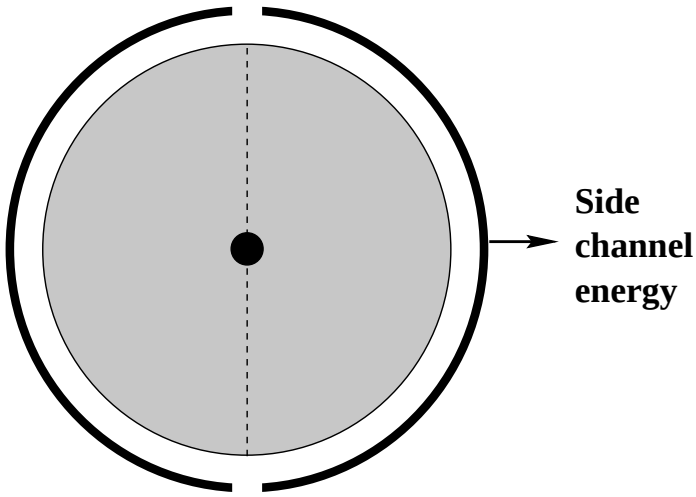

Figure 2.27: Schematic diagram of a GAMMASPHERE segmented detector.

contact. A side channel signal is read from one half of the outer segmented contact. The magnitude of the side channel signal may be used to determine in which side of the detector the γ-ray interacted. By examining the ratio of the side channel energy to the high resolution energy, a reduction on the effective detector opening angle is achieved. The contribution to the Doppler broadening from the detector opening angle is thus reduced. Further details of this technique are outlined in sec. 3.5.2.

2.18.1 Kinematic Doppler Reconstruction

The relation in equation 2.10 assumes the recoils are emitted along the beam direction. This assumption, while valid for fusion-evaporation reactions which result in heavy ($\geq$ mass 120) recoil nuclei, becomes less so for lighter systems. The emission of light particles has the effect of broadening the recoil cone which results in γ-rays with a poor resolution being observed. The quality of the spectra studied in this work will benefit if an improvement on this assumption can be made.

For reactions which result in the formation of a neutron deficient compound nucleus, the decay is primarily by the emission of charged particles. The detection of these charged particles can be used to reconstruct the recoil vector of the residual nucleus event by event. For a neutron deficient reaction channel such as the one studied in this work, substantial

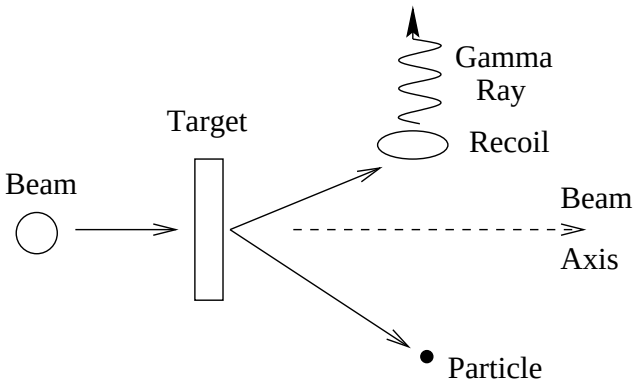

Figure 2.28: A schematic diagram showing how the emission of a charged particle can alter the direction of the recoiling nucleus relative to the beam direction.

improvements in the observed γ-ray energy resolution can be achieved.

Fig. 2.28 shows the effect of particle emission on the recoiling nucleus. The emission of a proton, or in particular an alpha particle, which has a larger mass, will change the direction of the recoil slightly. The MICROBALL measures the momentum and direction (θ,ϕ) of each charged particle emitted in the heavy-ion fusion-evaporation reaction. Once these values are determined, the direction and momentum of the recoiling nuclei can be reconstructed [sew94]. This new direction is then used to define the γ-ray emission angle for each germanium detector relative to the recoil. By using

$$E_0 = E_{lab}\frac{1 - \mathbf{d_r}.\mathbf{d}_\gamma}{\sqrt{1 - d_r^2}}, \tag{2.12}$$

where E_0 is the observed energy, E_{lab} is the energy in the lab frame, $\boldsymbol{d_r}$ is the direction of the recoil and $\boldsymbol{d_\gamma}$ is the direction of the γ-ray, the measured γ-ray energy resolution is improved.

The relation expressed in equation 2.12 requires a knowledge of the recoil velocity. A selection bias by the MICROBALL means the recoil velocity will be different for each reaction channel (ie. 4p and 2pα). In order to determine the optimum value of v/c for the 2pα exit channel which is studied in this work, values close to 4.26 obtained in section 2.18 were used. The resolution of the 657 keV $2^+ \rightarrow 0^+$ transition in ^{110}Te was measured. The results obtained are shown in Fig. 2.29.

The results fitted with a parabola determined 4.32% as the optimum value of v/c to use

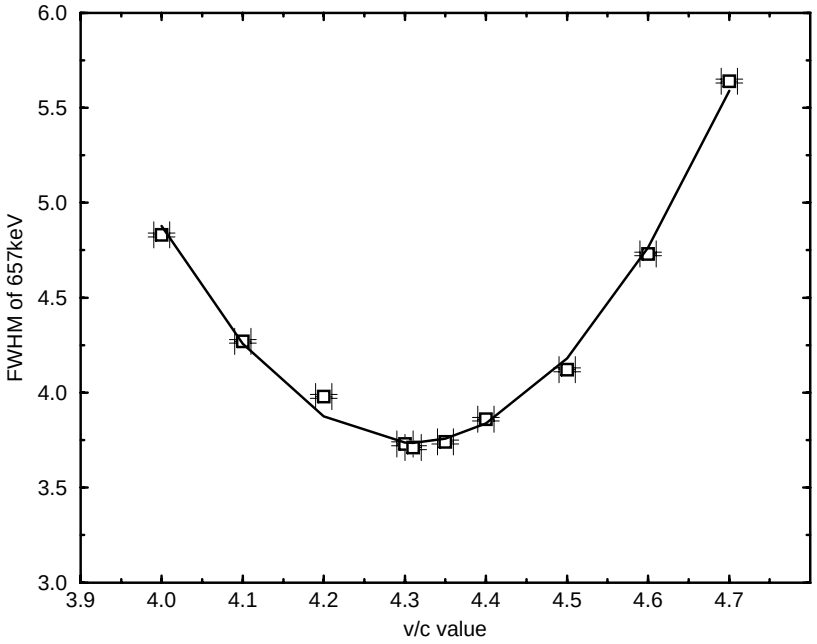

Figure 2.29: The resolution obtained for the $2^+ \rightarrow 0^+$ transition in ^{110}Te as a function of the v/c choice, using the kinematic Doppler correction in the MICROBALL.

for the 2pα exit channel. Using this value, the resolutions obtained with and without the kinematic Doppler reconstruction technique were measured for the lowest seven transitions in the ground state band of ^{110}Te. Fig. 2.30 shows the improvement obtained.

Before the kinematic recoil correction was used, the resolution at 1MeV was 8.0keV. This was improved to 5.5keV using the kinematic correction.

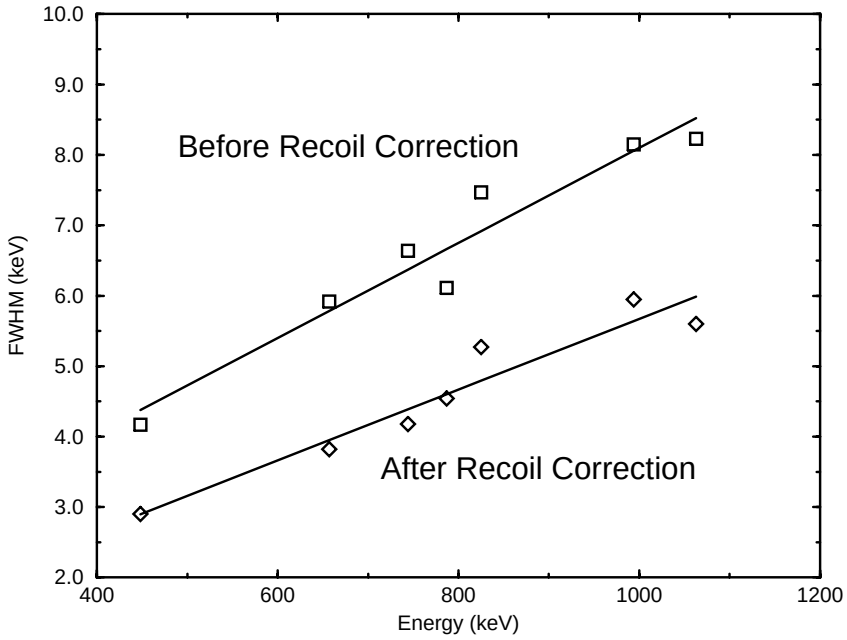

Figure 2.30: The improvement in the resolution of the observed γ-rays using the kinematic Doppler correction technique.

Chapter 3

Results

3.1 Physics Motivation

The extremely neutron deficient region of the nuclear chart with A$\sim$110, studied in this work and illustrated in Fig. 3.1, contains a wealth of nuclear structure information. The physics of the region is dominated by the close proximity of the Z=50 spherical closed shell, which has the consequence that nearby nuclei have a close to spherical ground state configuration. This manifests itself with the observation of strongly single particle level structures typified in nuclei such as ^{108}Sn [wad96] and ^{109}Sb [sch96] at low spin.

These exotic proton rich nuclei provide an ideal case in which to observe the competition between the collective and single particle degrees of freedom. With a limited number of valence nucleons available outside the ^{100}Sn closed core, collective modes of excitation are theoretically possible, and in this valence space level structures may be observed up to termination. So called 'band termination' will occur when the microscopic contribution from each valence nucleon to a collective structure is exhausted. Evidence for collective structures at high spin in this mass region has been found in a number of Sn [wad96], Sb [lan98a] and I [war95] isotopes. There is evidence that particle-hole excitations across the Z=50 shell gap may stabilise the deformed collective structures observed in these nuclei.

Nuclei in this mass region lie in a region of the nuclear chart where single particle levels differing in total and orbital angular momentum by $3\hbar$ are close to the Fermi surface. This occurs because of the close proximity to the 'octupole magic' number 56. An interesting proposition is that nuclei with N$\sim$Z both near an octupole magic number might exhibit

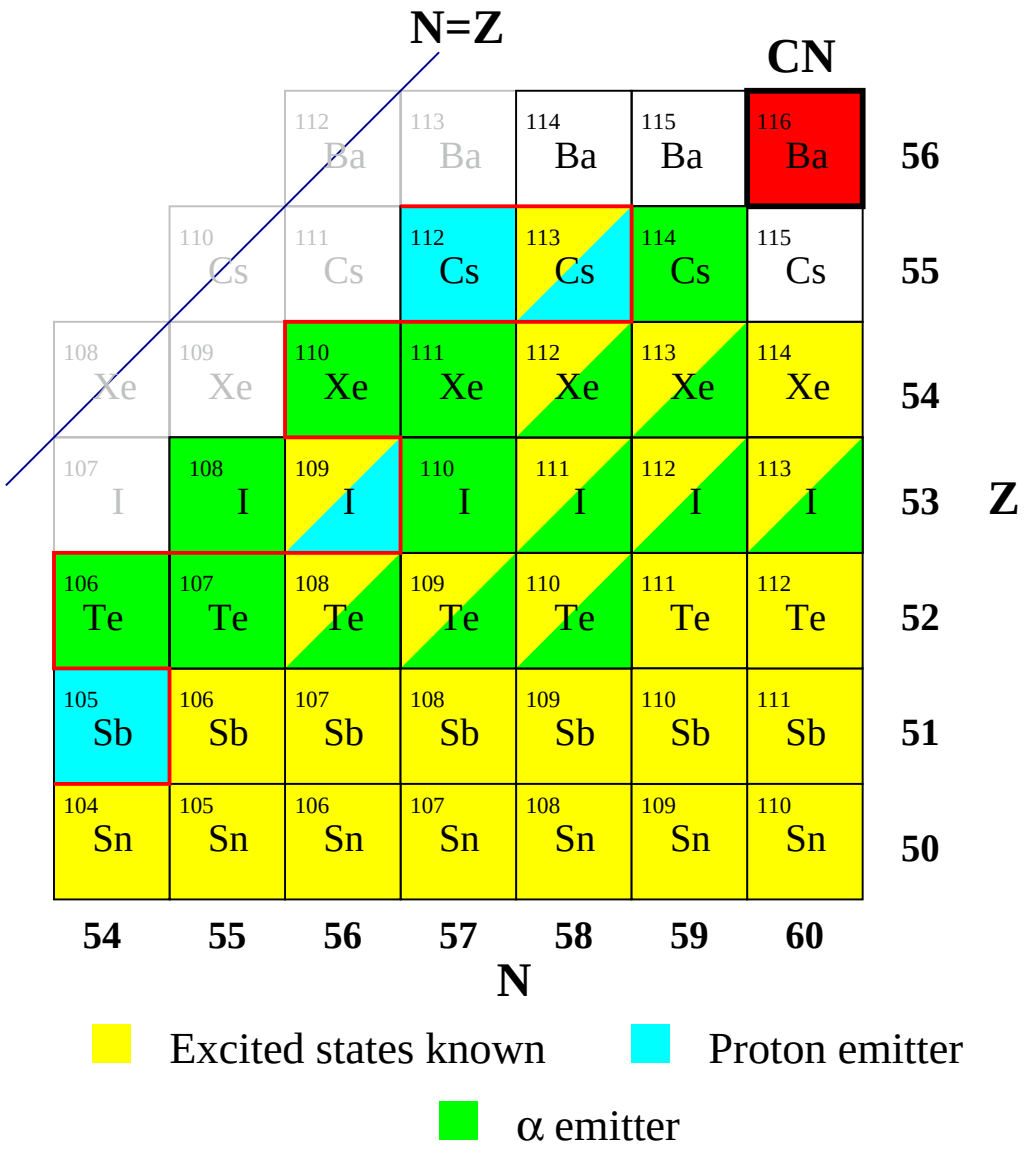

Figure 3.1: The mass 110 region studied in this work. Nuclei in which excited states are known are coloured in yellow, experimental knowledge of these isotopes extends almost to the N=Z line. Ground state alpha and proton emitters are coloured, together with the compound nucleus ^{116}Ba* which is indicated in the top right hand corner of the figure.

especially strong octupole effects. Theoretical calculations have predicted octupole degrees of freedom in the light Ba, Xe and Te nuclei [hee94]. Indeed recent experimental evidence [lan98b] has provided further motivation for a more complete analysis.

3.2 Previous work on the light tellurium isotopes

3.2.1 ^{110}Te - The N=58 isotone

The neutron deficient nucleus ^{110}Te has 52 protons (Z) and 58 neutrons (N), lying close to the Z=50 spherical closed shell. The nucleus is therefore predicted to have a very small prolate ground state deformation. The nucleus belongs to the set of N=58 isotones including ^{108}Sn [wad96] and ^{109}Sb [sch96] which provided the first evidence for deformed collective structures at high spin in this mass region, and ^{112}Xe which is predicted to show strong octupole correlation effects.

The $2^+ \rightarrow 0^+$ transition in ^{110}Te was first identified in 1985 following the β decay of ^{114}Cs [tid85] (^{114}Cs$\rightarrow^{114}$Xe$\rightarrow^{110}$Te). The assignment was later confirmed by mass gated γ-ray spectra obtained with the EUROGAM γ-ray spectrometer, which was mounted at the end of the Daresbury recoil separator, then situated at the Daresbury Laboratory, UK. [pauUP].

The reaction ^{58}Ni(^{58}Ni,α2p)^{110}Te was utilised by E.S.Paul *et al.* [pau94] to populate high spin states in ^{110}Te with a beam energy of 250 MeV. The Tandem Accelerator Superconducting Cyclotron (TASCC) facility at the Chalk River Laboratories of AECL Research was used to provide a ^{58}Ni beam incident on a 1mg/cm^2 ^{58}Ni target with a thick ^{197}Au backing. $\gamma - \gamma$ data were collected using the 8π spectrometer, which consists of 20 (25%) Compton-suppressed HPGe detectors plus a 71-element BGO inner ball calorimeter. Approximately 3.5×10^7 events were collected in just 8 hours of beam time. The level scheme deduced from this experiment is illustrated in Fig. 3.2. Spin and parity assignments were made following an angular correlation analysis using the method of Directional Correlation from Oriented states (DCO), see sec. 3.5.1 for an explanation of this technique.

The use of a thick target precluded a high spin analysis, but ensured excellent resolution for the analysis of γ-ray transitions at low spin. The existence of octupole correlation effects in this nucleus was postulated in Ref. [pau94] due to the enhanced nature of the observed

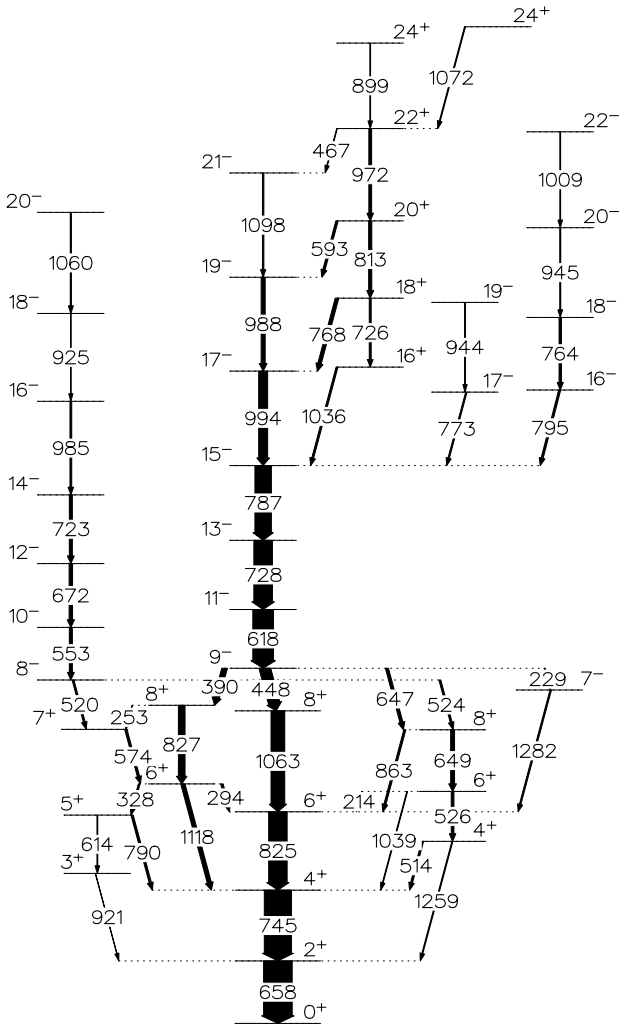

Figure 3.2: The level scheme for ^{110}Te prior to this work [pau94].

E1 transitions. However, no evidence for any collective rotational structure was observed, the low spin level scheme instead being explained in terms of collective vibrations. In this work the GAMMASPHERE array has provided increased statistics and the use of a thin target has enabled a more complete high spin analysis.

3.2.2 Identification of ^{109}Te

The first excited states of ^{109}Te were identified in 1994 following γ-ray correlation with β-delayed protons (from ^{109}Sb) and alphas using the then novel method of recoil decay tagging [pau95]. A 240 MeV ^{58}Ni beam supplied by the Daresbury tandem Van de Graaf accelerator was incident on a ^{54}Fe target mounted in the EUROGAM array of HPGe detectors. The

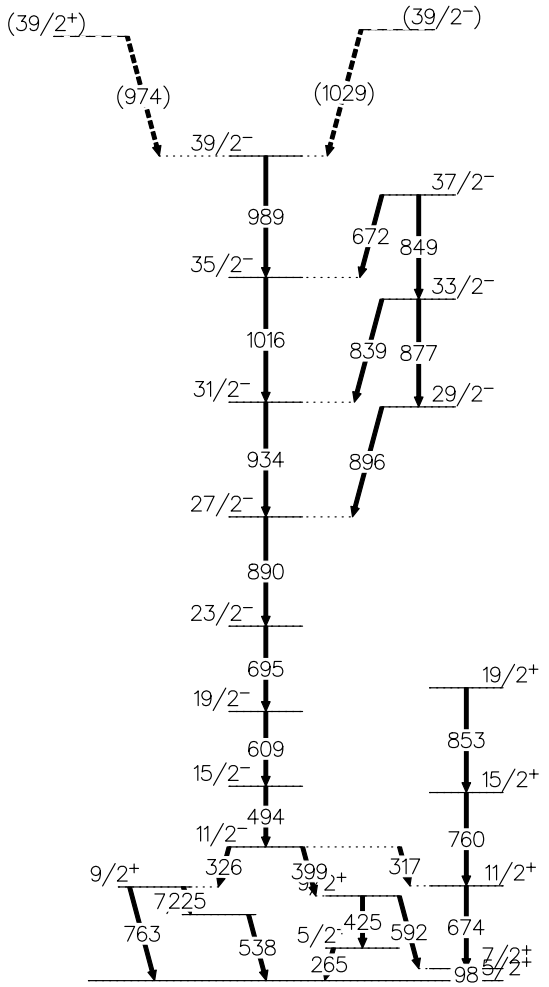

Figure 3.3: The level scheme for ^{109}Te prior to this work [dom95].

Daresbury recoil separator and the Edinburgh Double-sided Silicon Strip Detector (DSSD) were used to separate the beam from the recoils and detect β-delayed protons respectively. A decay scheme for ^{109}Te populated by the 2pn exit channel was hence constructed.

Another experiment established ^{109}Te by in-beam spectroscopy in 1994 using the reaction ^{54}Fe(^{58}Ni,2pn)^{109}Te. The experiment was performed at the Niels Bohr Institute using a 270 MeV ^{58}Ni beam incident on a 10mg/cm^2 thick ^{54}Fe target. The NORDBALL detector system which consisted of 15 Compton suppressed HPGe detectors was augmented with a 30 element BaF_2 calorimeter, a 21 element Si ball for the detection of charged particles and 11 liquid scintillator neutron detectors in order to provide a clean channel selection capability. $4.2\times10^8\gamma-\gamma$ events were collected and sorted into particle gated $\gamma-\gamma$ 2D spectra (matrices). The level scheme deduced from this work is shown in Fig. 3.3. $\gamma-\gamma$ angular

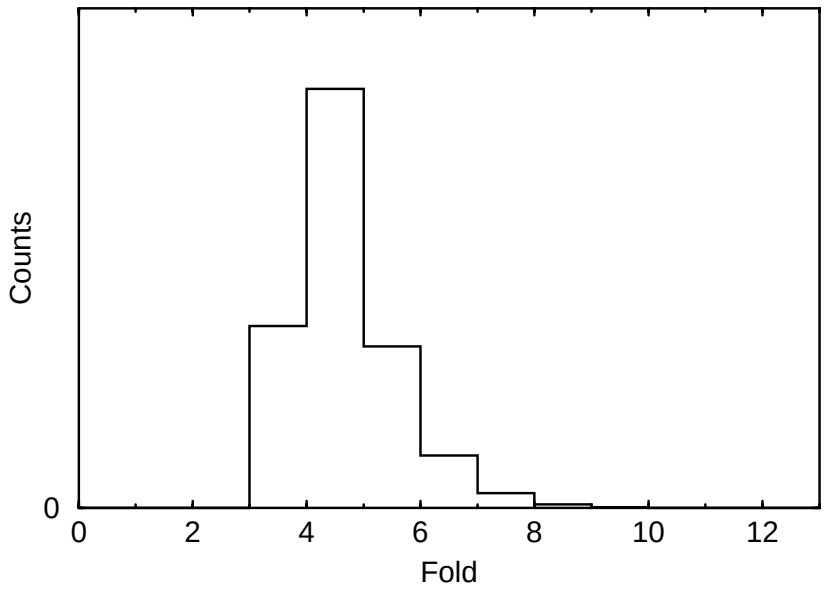

Figure 3.4: The γ-ray fold distribution recorded for this work, illustrating a maximum for fold is 3, 4 and 5.

correlation intensity ratios were used in an attempt to determine the multipolarity of the γ-ray transitions.

3.3 Data analysis techniques

High spin states in ^{110}Te were populated using the ^{58}Ni(^{58}Ni,2pα)^{110}Te fusion-evaporation reaction and ^{109}Te using the ^{58}Ni(^{58}Ni,2pαn)^{109}Te reaction. The data were written to tape for events containing a minimum of 3 suppressed γ-ray events in coincidence with a charged particle being detected in the MICROBALL, together with the number of associated neutrons. This ensured that clean exit channel selection was possible. A total of 1.4×10^9 events were recorded in four days of beam time. The number of suppressed HPGe detectors that fired within 50ns of the trigger, referred to as the germanium fold, recorded for this work is shown in Fig. 3.4. It illustrates that quadruple suppressed γ-events represent the largest single fold contribution, however there is a significant contribution to the data set from much higher fold events.

Each event may be unpacked into several lower fold events. An event that contains three γ-rays (E_{γ_1}, E_{γ_2}, E_{γ_3}) can be unpacked into three γ-γ coincidences (E_{γ_1}, E_{γ_2}) (E_{γ_1}, E_{γ_3}) and (E_{γ_2}, E_{γ_3}). In the same way a quadruple event may be unpacked into 4 triples

or 6 doubles and so on. Clearly the unpacking procedure will result in a large increase in the effective number of lower fold (triple and quadruple) events. A typical example is that the largest contribution (28%) to unpacked quadruples (γ^4) comes from fold 6 events even though these represent less than 6% of the data.

The high statistics, high fold coincidence data set obtained from the GAMMASPHERE spectrometer in this work, allows the possibility of placing multiple selection criteria, referred to as gates, on γ-ray transitions in order to enhance weak features in the data set. An example of demanding higher fold from a list of 16 γ-ray energies for terminating band 1 in ^{113}I, which is one of the strongest channels populated in this work involving the evaporation of three protons, is shown in Fig. 3.5. As the required number of energies is increased from a minimum of one up to four, the contamination from other structures is reduced and the apparent intensity of the band improves. Note that no background subtraction has been performed. However the total number of counts in the spectra are reduced as the fold is increased and when four coincident γ-rays are required the spectrum shows a large degree of statistical fluctuation. In order to maximise statistics and minimise contamination a compromise must be reached between the gating fold and the required statistics.

In order to utilise the GAMMASPHERE array to its fullest extent, computer software which allows the high fold analysis of γ-ray data has been written. RADWARE[rad95] allows the high fold data to be unfolded offline into constituent single, double, triple or quadruple coincidence events. The data can then be replayed into a multi-dimensional spectrum for analysis.

An event which consists of two γ-rays detected in coincidence is termed a $\gamma - \gamma$ coincidence. Such an event can be sorted into a two-dimensional spectrum, termed a matrix. The event is sorted by incrementing the matrix at positions E_{γ_1}, E_{γ_2} and E_{γ_2}, E_{γ_1}. A higher fold event such as one which contains 3 γ-rays is first decomposed into constituent $\gamma - \gamma$ coincidences, three in this case, which are then incremented twice into the matrix, totalling six increments. A so called symmetric matrix is produced by this procedure, because the matrix is symmetrical about its main diagonal. If one sets a gate on one axis of the matrix, everything that is in coincidence with that γ-ray will be projected into a 1d spectrum for the user to view. The RADWARE program ESCL8R provides a graphical interface to facilitate a detailed analysis.

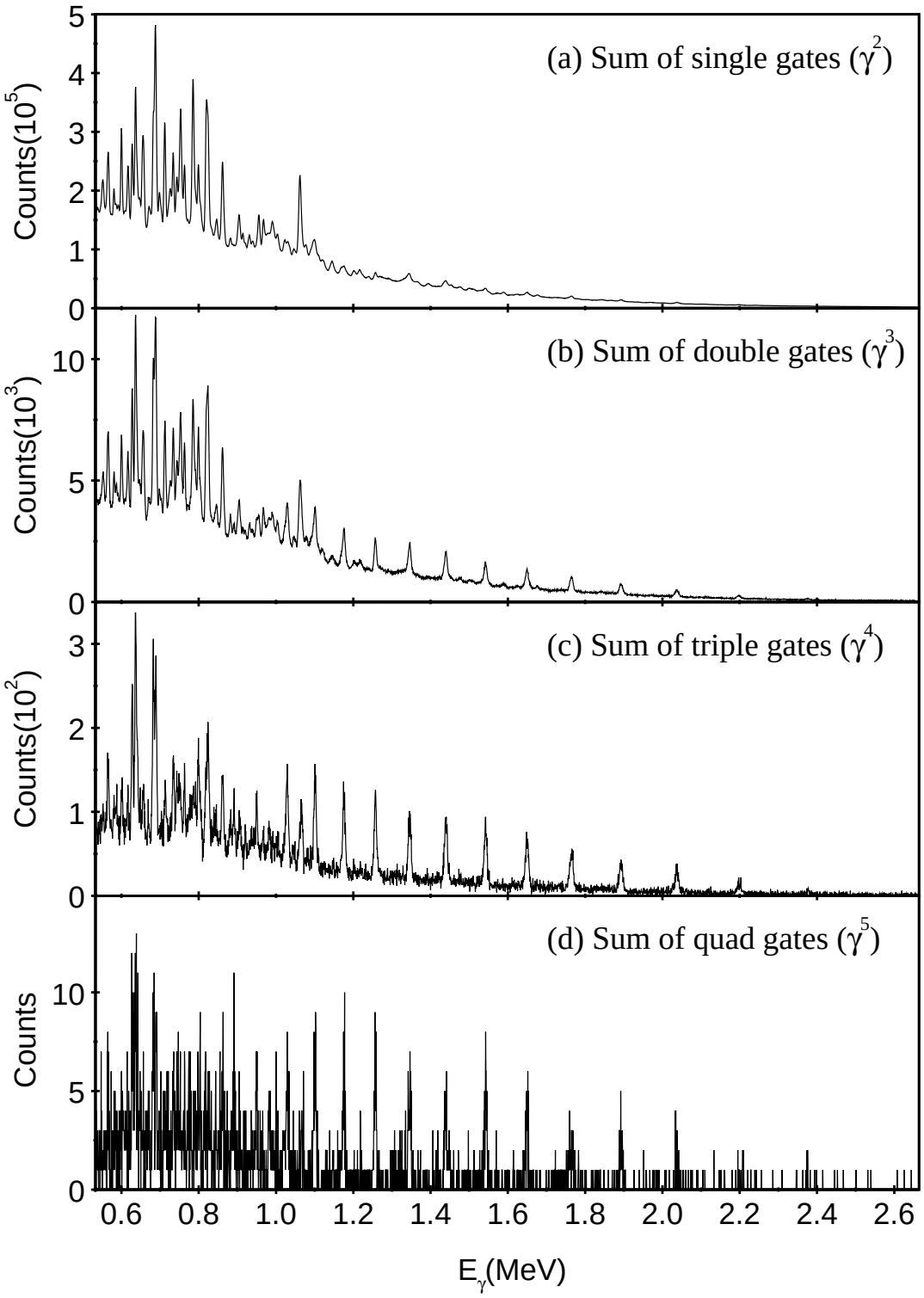

Figure 3.5: Terminating band 1 in ^{113}I. The effect of requiring higher fold from a list of 16 γ-rays is illustrated. The figure indicates that sums of triple gates from γ^4 coincidences provide the optimum choice. No background subtraction has been performed.

The analysis of higher fold data is afforded by the use of the RADWARE package LEVIT8R. The data can be unfolded into constituent triple coincidence events and incremented into a three dimensional spectrum, termed a cube. Such a method of data storage enables two gates to be required, only γ-rays which are coincident with both gates are projected onto the third axis of the cube to form a 1d spectrum.

The fold distribution obtained for the GAMMASPHERE array shows that fold four events represent the peak fold. This high fold data can be unfolded into constituent quadruple coincidence events and replayed into a RADWARE format hypercube. The analysis of the hypercube was afforded by the use of the 4DG8R graphical analysis program. The program allows three gates to be set, events which are coincident with all three gates are then projected onto the fourth axis of the hypercube to form a 1d spectrum.

The increasing number of dimensions needed to store the γ events has the effect of increasing the storage requirements. A typical γ^2 matrix may require 30MB of disk space, while a γ^4 hypercube can require 10GB of storage space, however the combination of the GAMMASPHERE array and the powerful RADWARE analysis software enables the full potential of a data set to be investigated.

All the 1d spectra projected from the multi-dimensional arrays obtained in RADWARE possess a background which results from Compton scattering, random coincidence events and unresolved statistical γ-ray transitions. The contribution to the spectra from such sources is unwanted and may swamp weak structures. RADWARE uses a simplified variant of the automated method of Palameta and Waddington [rad95] in order to account for background in the multi-dimensional arrays.

3.4 Efficiency calibration

In order to extract meaningful intensity values from the data set, the data must first be corrected for the efficiency of the detection device. The relative efficiency of a HPGe detector is generally expressed relative to the response of a 3×3inch cylindrical NaI(Tl) detector to the 1.3MeV γ-ray from a ^{60}Co source placed 25cm from the detector. The GAMMASPHERE HPGe detectors are quoted as 75% efficient.

The pulse height spectra obtained in this work contain γ-rays with energies ranging from ∼100keV up to 3MeV. The response of a HPGe-detector to γ-ray photons of varying

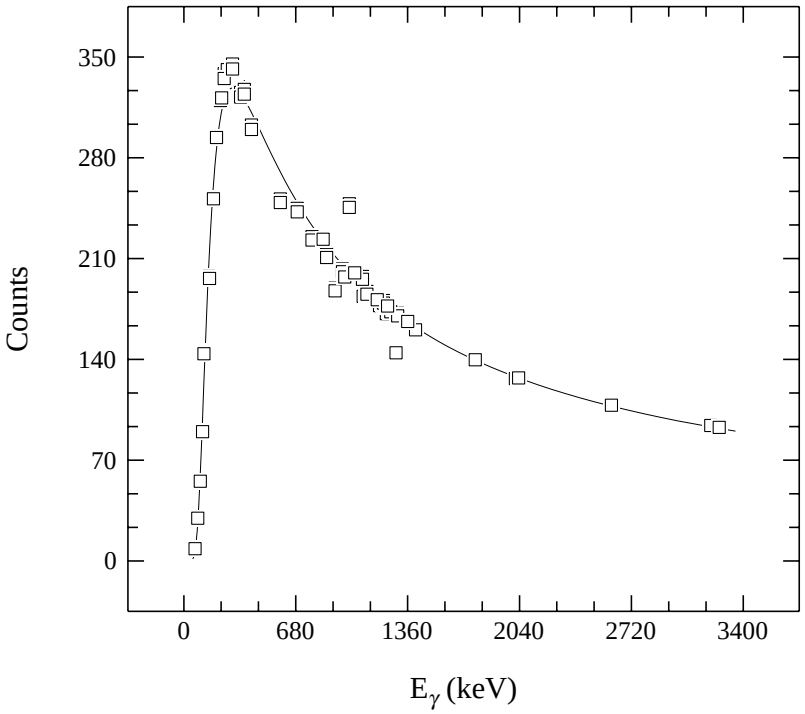

Figure 3.6: Efficiency calibration curve for the GAMMASPHERE array with 83 HPGe detectors obtained using ^{152}Eu, ^{56}Co and ^{182}Ta sources.

energy has therefore to be calibrated. The total photopeak efficiency of the GAMMASPHERE array has been measured using a selection of radioactive sources chosen such that a broad distribution of energies from keV to MeV was available. The sources ^{152}Eu, ^{56}Co and ^{182}Ta were mounted in the target position of the array and data were acquired for offline analysis. A total projection of the pulse height spectra for each source was obtained after the initial gainmatching procedure was completed.

An energy calibration was performed on the source spectra, the peaks were then fitted using an automated peak fitting routine to obtain the peak intensities. The peak fitting routine assumed the peaks to be composed of three primary components; a Gaussian; a skewed Gaussian and a smoothed step function increasing the background on the low energy side of the peak. The transition intensities were compared with known standard source data using the EFFIC code [orn] from which efficiency information was extracted.

The efficiency curve obtained for the GAMMASPHERE array with 83 HPGe detectors is shown in Fig. 3.6. The curve has a characteristic shape, with a sharp drop off at low energy and a continuous drop with increasing energy, explained with the knowledge that a HPGe detector is very poor at detecting low energy γ-rays, with energy $\leq$70keV, because these

will be absorbed in the aluminium can surrounding the Ge-crystal. At higher energies there is a larger probability that the γ-rays will not interact in the crystal. The efficiency curve obtained has a turnover point of 260keV. The presence of the MICROBALL charged particle detector results in the turnover point being slightly higher in energy than expected. This results in a reduction in the low energy γ-ray detection efficiency due to increased absorption of low energy transitions in the thin CsI(Tl) elements. The efficiency fit obtained allows valid intensity information to be extracted from the data.

3.5 Level scheme construction

The ordering of transitions in the level schemes obtained in this work relies on knowledge of coincidence relationships between the γ-ray transitions and their relative γ-ray intensities. To assist in assigning spins and parities to transitions in the level schemes, the multipolarities were extracted from the data by conducting an angular correlation analysis. A measurement of the linear polarisation for some of the transitions has been attempted, enabling the electric or magnetic character of the γ-ray transitions to be determined.

3.5.1 Angular Correlations

Following a heavy-ion fusion-evaporation reaction, the residual nuclei are aligned with their spin directions in a plane perpendicular to the beam direction. The population of the magnetic substates is usually assumed to form a Gaussian distribution about the direction of alignment. For two γ-rays which are detected at angles θ_1 and θ_2 with respect to a plane perpendicular to the beam axis, where the angle $\Delta\phi = \phi_1 - \phi_2$ is defined as the angle between the planes subtended by this axis and the outgoing γ-rays, then the intensity of a γ-transition defined using these terms is given by the angular correlation function,

$$W(\theta_1, \theta_2, \Delta\phi). \tag{3.1}$$

A complete angular correlation analysis has not been attempted in this work, instead the method of Directional Correlation from Oriented states (DCO) [fle89] was used to assist with the assignment of transition multipolarities. By a comparison of the intensities of the γ-rays observed at backward angles and those observed at angles near 90° sufficient information can be obtained to distinguish between γ-rays of multipolarity one and two.

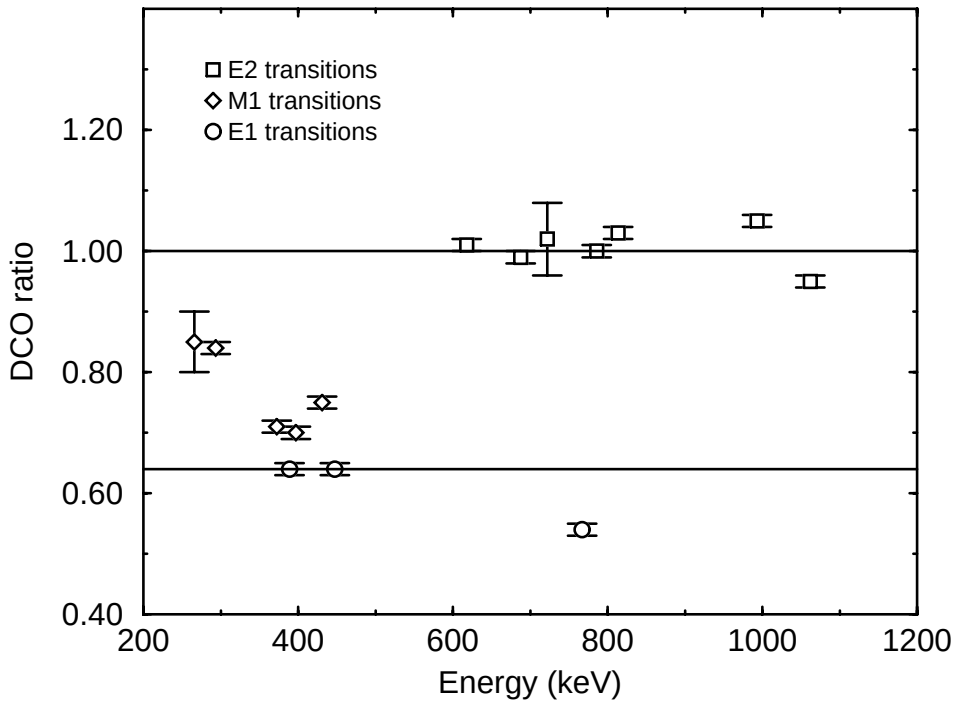

Figure 3.7: Illustrative experimental DCO ratio results for ^{110}Te from this work. Clear separation between stretched dipole and quadrupole stretched quadrupole transitions is evident. Transitions with a degree of multipole mixing are illustrated for the purpose of completeness.

Two matrices containing $\gamma - \gamma$ coincidences from detectors at $\theta \approx 90^{\circ}$ and all angles and $\theta \approx 130^{\circ}$ (backwards) and all angles respectively, were constructed. It was possible to project out 1-d spectra by placing gating requirements on the all axis of both matrices, allowing the experimental DCO ratio,

$$R_{DCO} = \frac{W(\theta_1, \theta = all, \Delta\phi = all)}{W(\theta_2, \theta = all, \Delta\theta = all)} \equiv \frac{I_{\gamma\gamma}(\theta_1, \theta[gate])}{I_{\gamma\gamma}(\theta_2, \theta[gate])}. \tag{3.2}$$

to be determined for each γ-ray transition. One drawback of the DCO method is the R_{DCO}, defined in equation 3.2, which depends on the multipolarity of the gating transitions. For this work only stretched E2 transitions were used as gates. The intensity ratios obtained were compared to values of known stretched quadrupole $\leftrightarrow$ stretched quadrupole and stretched quadrupole $\leftrightarrow$ stretched dipole transitions simplifying an otherwise complicated analysis and providing an essential calibration. This approach yields R_{DCO} for pure stretched quadrupole and pure stretched dipole transitions of 1.0 and 0.63 respectively. Representative experimental DCO ratio results obtained in this work are shown in Fig. 3.7.

A positive or negative mixing ratio (δ) will perturb the measured value from that of

its pure counterpart. Knowledge of the electromagnetic character of a γ-ray transition can be inferred from the extent of the multipole mixing. A pure stretched dipole transition should have a DCO value of 0.63, however a magnetic dipole transition is likely to contain a degree of multipole mixing. Non stretched E2 decay can compete producing a mixed M1/E2 transition with a perturbed DCO value. This assumption allows a measured pure dipole DCO ratio to be inferred as an E1 because E1/M2 mixing is not significant. The electromagnetic character of transitions which have been inferred in such a way should be regarded as extremely tentative assignments.

3.5.2 Linear Polarisation

In this work a determination of the electric or magnetic character of the emitted γ radiation has been attempted by using the GAMMASPHERE array as a Compton polarimeter. The technique uses the knowledge that a γ-ray will always Compton scatter preferentially in a direction which is perpendicular to its electric field vector. The GAMMASPHERE segmented HPGe detectors provide a facility to observe the fraction of clean events which share their energy between both sides of the detector (shared S) and those which confine themselves to one side (confined C), see Fig. 3.8.

The classification of a 'confined' or 'shared' event depends on interaction position of a γ-ray in the HPGe crystal. The high resolution total energy signal is read out from the centre contact. A side channel signal is read from one half of the outer segmented contact. The magnitude of the side channel signal may be used to determine the interaction point of a γ-ray in the detector by examining the ratio R of the previously calibrated side channel energy to that of the high resolution energy. If the ratio is more than 90% or less than 10% the event can be considered 'confined' to the right or left respectively. An intermediate value implies a 'shared' event.

The experimental linear polarisation for the GAMMASPHERE array is defined as [sch95],

$$P = \frac{1}{Q}\frac{1}{\sqrt{\eta}}\left[\frac{\eta C - S}{C + S}\right] \tag{3.3}$$

where C and S represent confined and shared events respectively, Q is the γ-ray polarisation sensitivity and η is the relative efficiency for the detection of confined and shared events. The number of confined and shared events can be used to calculate an experimental asymmetry,

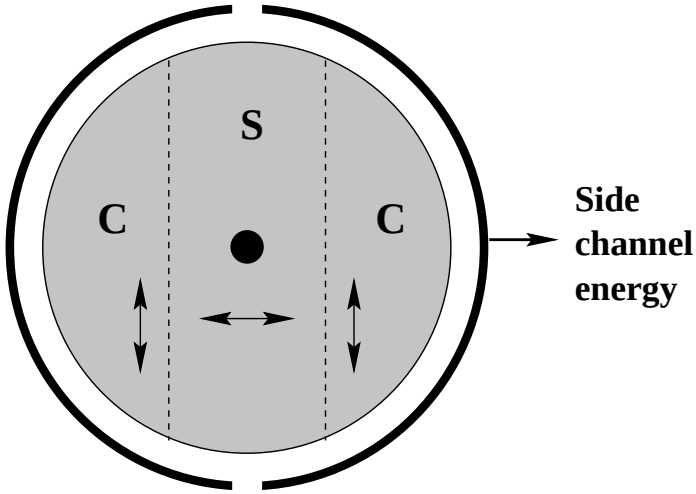

Figure 3.8: A schematic diagram of a GAMMASPHERE segmented detector. Notice how events which are confined to one side of the detector (C) or scatter (S) between both sides of the detector are determined.

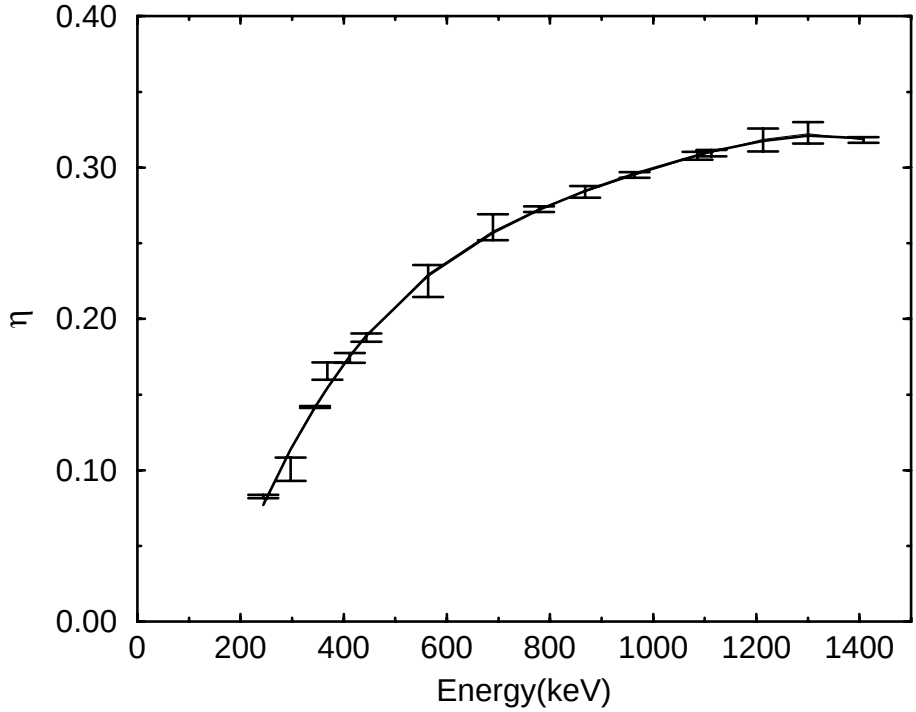

Figure 3.9: Measurement of the relative efficiency for the detection of confined and shared events (η), obtained using a ^{152}Eu radioactive source.

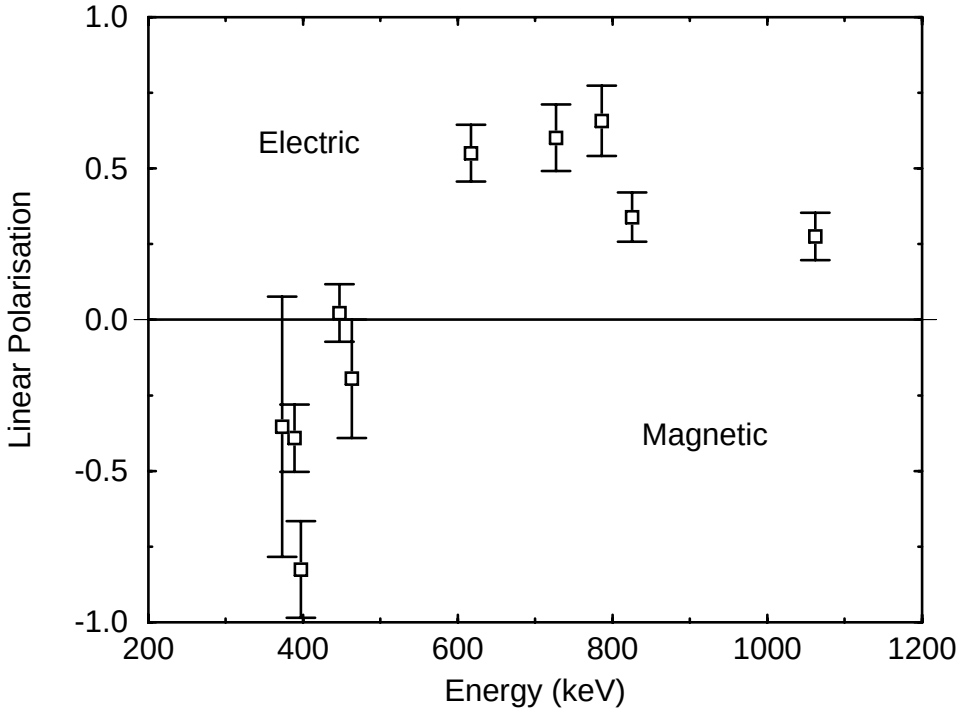

Figure 3.10: Experimental linear polarisation results obtained in this work. Transitions electric in nature have a positive polarisation, magnetic transitions have a negative polarisation. Mixed M1/E2 transitions provide values close to zero.

which is used to determine the linear polarisation using the above relation. A measurement of the polarisation sensitivity of the GAMMASPHERE segmented detectors from [sch95] has been used, with values that range between 0.052 at 415 keV to 0.043 at 1368 keV. The magnitude and energy dependence of Q were interpolated using a Monte Carlo simulation.

In this work a measure of the detection efficiency for confined and shared events η has been obtained. Total projection spectra for a ^{152}Eu source mounted in the GAMMASPHERE target position were analysed for shared and confined events. γ-ray intensity measurements were extracted using the RADWARE program GF2 using the standard peak fitting procedure previously discussed in sec.3.4. The ratio of shared events to confined events was obtained and plotted, the result is shown in Fig. 3.9.

The figure shows a smooth variation with incident γ-ray energy. At low energy, the probability of an event Compton scattering is low, therefore the relative efficiency rapidly decreases. The curve approaches a value of $\sim$0.3 for increasing energy. The curve indicates that for low energy γ-rays (E$\leq$200keV) it will be difficult to extract any useful polarisation information.

Knowing the relative efficiency for the detection of confined and shared events, the polarisation sensitivity and the ratio of confined to shared events from the experimental data, it is possible to extract linear polarisation information. The method involved constructing two matrices from the coincidence data, which was first unfolded into γ^2 doubles. One axis of the matrix corresponded to single hits in any detector, the other axis corresponded to shared events in one matrix and confined events in the other matrix. The single hits axis was used to apply specific ^{110}Te gates in order to obtain good quality spectra.

An example of the experimental linear polarisation results obtained for ^{110}Te is shown in Fig. 3.10, a full set of results are quoted in table.3.2. The values averaged $\sim$0.4 for stretched E2 and E1 transitions, and are closer to zero or negative values for mixed M1/E2 dipole transitions. The reader should note that the GAMMASPHERE segmented detectors were not primarily designed for use as a Compton polarimeter. The polarisation sensitivity is poor in comparison to the EUROGAM clover detector, a composite detector containing 4 HPGe crystals. This detector design allows scatters which are parallel or perpendicular to the reaction plane to be investigated simultaneously, significantly improving polarisation sensitivity.

The experimental results are observed to show large uncertainties. Only modest success in achieving reliable linear polarisation results was therefore achieved. Linear polarisation results are hence only quoted for the strongest transitions.

3.6 Relative yields

In order to access the most neutron deficient residual nuclei, a symmetric reaction (Ni+Ni) has been used to form the compound nucleus. An extremely neutron deficient compound nucleus such as ^{116}Ba* can decay via a large number of exit channels. The use of ancillary detectors to enable channel selection is paramount and the techniques used were discussed in detail in chapter 2. The choice of stable beams and targets is somewhat limited, with the reaction ^{58}Ni + ^{58}Ni the only choice in order to access the most neutron deficient xenon and tellurium isotopes.

Prior to the experiment, statistical codes were used to predict evaporation-residue cross-sections. These codes are generally unreliable at correctly predicting the evaporation residues in such a neutron deficient mass region, typically over estimating the number

Residual Nucleus	Exit Channel	ALICE yield (i)		Experimental Yield (ii)	
		mb	%	arb.units (±10%)	% (±10%)
^{114}Xe	2p	72	14	8	3
^{113}Xe	2pn	9	2	3	1
^{112}Xe	2p2n	6	1	<1	<1
^{113}I	3p	100	20	76	24
^{112}I	3pn	13	3	26	8
^{112}Te	4p	93	19	100	31
^{111}Te	4pn	8	2	5	2
^{110}Te	2pα	81	16	70	22
^{109}Te	2pαn	8	2	2	1
^{109}Sb	3pα	71	14	13	5

Table 3.1: Relative evaporation-residue yields obtained from; (i)the statistical code ALICE (ii) estimated experimental yield.

of neutrons emitted. However, the code ALICE [pla75] has provided reasonable estimates previously for this beam and target combination. The beam energy choice of 250MeV was based on the results from the ALICE calculations, detailed in table 3.1, combined with previous knowledge of this reaction [pau94, pau95].

Table 3.1 also details the estimated relative yields extracted from an all against all 2D matrix replayed into the RADWARE program ESCL8R from the total ungated data set. ESCL8R like the other RADWARE analysis programs determines energy and intensity values using a least squares fitting routine. The intensity values are corrected for the efficiency of the array automatically by the program once an appropriate efficiency curve has been extracted.

The results in table 3.1 show a representative selection of the exit channels populated in this experiment and clearly demonstrate the need for a channel selection capability. Experimentally the strongest three exit channels are shown to involve pure charged particle evaporation; 4p (^{112}Te), 3p (^{113}I) and α2p (^{110}Te) respectively. This indicates that 4 particle evaporation is most likely for the beam energy of 250 MeV. The ALICE calculation obtains

the correct three strongest exist channels, but somewhat under estimates the number of particles emitted, indicating 3p as the strongest channel. ALICE also predicts 2p (^{114}Xe) will carry a significant amount of the reaction cross-section, this prediction is found to be an overestimate of the experimental yield. If the experimental and theoretical results are considered together the choice of beam energy to access the light tellurium isotopes is vindicated.

In order to approach the N=Z line further neutron evaporation is required. The evaporation of one neutron producing a more neutron deficient residual nucleus has a much smaller cross-section since charged particle evaporation is more likely, this is clearly demonstrated experimentally and theoretically. Two neutron exit channels are populated with an extremely low cross-section. Experimentally the yield of such evaporation residues as the N=58 isotone ^{112}Xe, recently identified from this data [smiG], is observed to be somewhat smaller than that predicted by theory. Indeed the most effective way to approach N=Z is by the evaporation of an α-particle. This implicitly removes two neutrons. The neutron deficient nucleus, ^{110}Te is accessed in this way and it represents the third strongest exit channel in the data.

3.7 Results for ^{110}Te

3.7.1 The sorting procedure

In order to extract the optimum quality data for ^{110}Te from the total data set, a detailed analytical procedure was followed. The raw data was first extracted off the magnetic tape and sorted to ensure the γ-ray spectra were correctly gainmatched and Doppler corrected (sec.2.18). A time constraint was then placed on the GAMMASPHERE TAC (Time to Amplitude Converter). The TAC records a spectrum indicating the time after the master trigger at which the γ-ray interacted. The constraint ensured only prompt events were incremented at this stage of the sort. Therefore bad events or those events which were delayed, such as isomeric transitions, were rejected.

The sort then ensured that only events associated with the α2p exit channel were considered, by placing constraints on charged particles detected in the MICROBALL (sec.2.14.1). An inspection of representative 1d γ-ray spectra obtained showed a small amount of parti-

cle mis-identification in the MICROBALL. The primary source of unwanted events, termed contaminants, came from α3p (^{109}Sb). This occurred because one proton was being missed by the MICROBALL due to its reduced efficiency when considering multiple particles.

The BGO elements in the GAMMASPHERE array were used as a calorimeter to provide some degree of fold and sum energy selection. By setting a high threshold, the contamination from channels with a larger number of evaporated particles than ^{110}Te such as ^{109}Sb was greatly reduced (sec.2.17).

The resolution of the observed γ-ray transitions can be significantly improved for this reaction by attempting a kinematic Doppler reconstruction using the MICROBALL. This technique, detailed in sec.2.18.1 uses the knowledge that when a particle such as a proton or an alpha is emitted, the direction of the recoiling nucleus can be changed. By reconstructing each event knowing the interaction point of the charged particles associated with it, the resolution for a 1 MeV γ-ray in ^{110}Te was improved from 8.0keV to 5.5keV.

3.7.2 Analysis Techniques

The initial 1.4×10^9 events were reduced to 6.2×10^7 after the sorting procedure was completed. This represents 5% of the total data recorded. The data were then unfolded into constituent quadruple (γ^4) coincidence events and replayed into a RADWARE format 4-D hypercube with a non-linear gain compression of 2 channels/FWHM. Transitions between 33 keV and 2.8 MeV were stored in the hypercube which had 891 channels per dimension. A total of 2.4×10^8 events were incremented, indicating an average of 4 quadruples per event. The hypercube occupied 1GB of disk space. The 4DG8R package facilitated a detailed analysis of the data. The package enabled one to set γ-ray gates on three axes of the hypercube and project out 1-D spectra onto the fourth axis. A RADWARE format triple coincidence (γ^3) cube was also incremented. A total of 4.2×10^8 events were incremented with an average of 7 triples per event. The same non-linear gain coefficients were used as previously discussed.

3.8 Band Structures in ^{110}Te

The level scheme proposed for ^{110}Te is illustrated in Fig. 3.11. The transition energies are given in keV and their relative intensities are proportional to the widths of the arrows.

The multipolarities of the majority of transitions were determined following a DCO angular correlation analysis. The electric or magnetic character of the γ-ray transitions was, where possible, determined using results from a linear polarisation analysis. A number of transitions have had their electromagnetic character inferred from DCO results. The measured transition energies and the relative intensities of the low spin γ-rays in ^{110}Te are listed in table 3.2. This table also contains a summary of the DCO and linear polarisation results together with the assignments concluded from this analysis. High spin results can be found in tables 3.3 and 3.4.

In order to simplify the discussion of the level scheme proposed for ^{110}Te the bands have been assigned numbers. The numbering system will be used to refer to a specific structure throughout the rest of this work.

The level scheme deduced in this work generally confirms the assignments of [pau94] shown in Fig. 3.2. Differences occur between the published work and the current analysis above the 15^- state in band 3 and above 16^- state in band 4. The improved statistics of the present analysis disprove the assignment of two bands feeding 15^- in band 3 and significantly change band 4. The DCO ratio results are generally in good agreement with those obtained in Ref. [pau94], with linear polarisation results further supporting the existing assignments.

3.9 Low spin positive parity structures

3.9.1 Band 1

The low spin ^{110}Te level scheme is in general a complicated collection of many irregularly spaced levels, containing a number of doublet or near doublet transitions. The ordering of transitions is based primarily on coincidence relationships and intensity arguments. The sequence of levels labelled as 1 includes 5 members and is yrast up to spin 8^+. A background subtracted coincidence spectrum generated by gating on the 657 keV $2^+ \rightarrow 0^+$ transition in a symmetric $\gamma - \gamma$ matrix of ^{110}Te is shown in Fig. 3.12. The transitions in band 1 are clearly visible along with a large number of other γ-rays associated with this nucleus.

Inspection of this gated 1-d spectrum reveals the quality of the spectra observed in this work. The energy resolution obtained following the use of a thin target with a large v/c (4.5%) reaction, improved by the use of detailed analytical techniques 2.18.1, is still

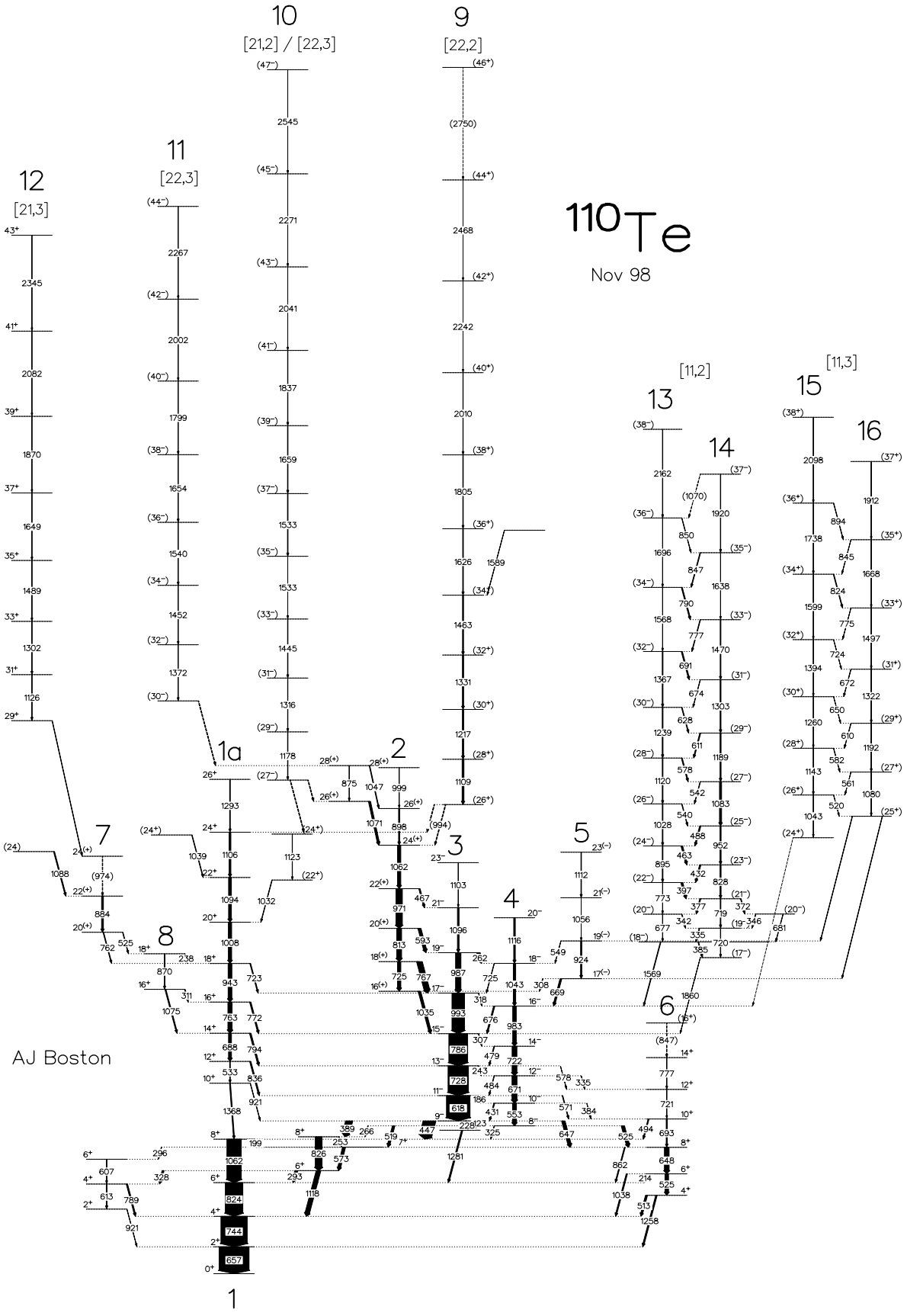

Figure 3.11: The proposed level scheme deduced for ^{110}Te following an analysis procedure using a RADWARE format hypercube. The transition energies are given in keV and their relative intensities are proportional to the widths of the arrows.

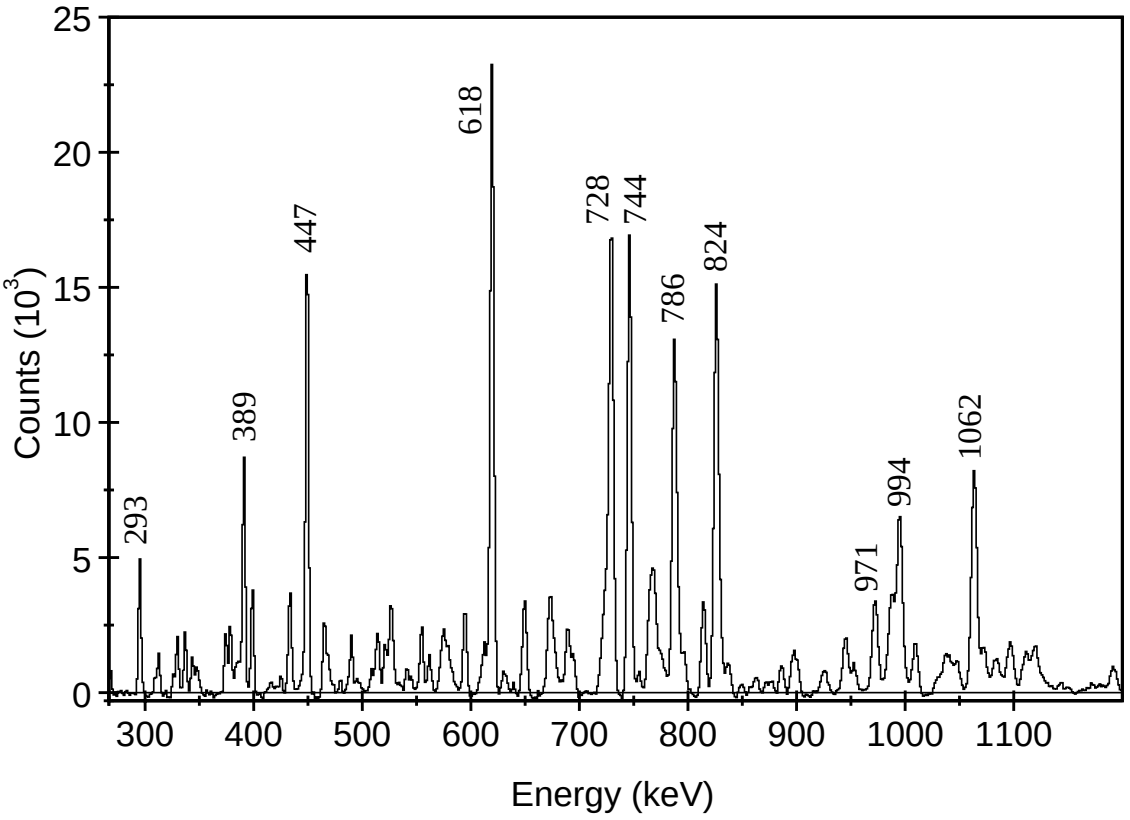

Figure 3.12: A coincidence spectrum generated from the RADWARE matrix analysis code ESCL8R gated on the 657keV $2^+ \rightarrow 0^+$ transition in ^{110}Te. Yrast transitions in bands 1,2 and 3 are visible.

somewhat poor. This has the important consequence that states with a similar energy, ie. those separated by $\approx$2 keV, will not be resolved properly if they are coincident with each other. The term doublet in this work will therefore be used to describe both exact energy doublets and those transitions which cannot be resolved from each other due to the limited energy resolution.

At low spin, sequences of positive parity states observed to the left and right of band 1 have been confirmed and extended. The band to the left now has a 2^+ bandhead consistent with the DCO results, following the addition of a new 607 keV E2 transition. This transition is observed to be fed by a 296 keV M1 transition indirectly carrying intensity from negative parity band 4.

3.9.2 Band 1a

A new structure labelled band 1a which consists of 8 stretched E2 transitions has been identified extending up to a proposed spin of 26^+. A very weak transition of 1368 keV and assumed E2 nature, is observed to directly link band 1a to band 1. The band has been assigned with positive parity following inferred confirmation through DCO ratio results of the E1 nature of the 6 linking transitions observed to decay to negative parity band 3. The intensity profile of band 1a is such that below 12^+ the structure contains almost no intensity suggesting the configuration is strongly unfavoured at this spin. Indeed it is only with the greater selectivity afforded by a γ^4 analysis, that the 533 and 1368 keV transitions could be placed with some confidence. Above spin 12^+ positive parity band 1a carries a significant amount of intensity and is easily identifiable in coincidence spectra, see Fig. 3.13(c). It is observed to be fed by a number of structures which, due to the existence of self coincidence doublet transitions, made the correct positioning of γ-rays somewhat time consuming.

3.9.3 Band 2

Band 2 is built on a 16^+ bandhead. The positive parity assignment has been inferred using the DCO ratio results which suggest an E1 character for the linking transitions to negative parity band 3. Unfortunately the insensitivity of the linear polarisation measurement precluded a meaningful analysis, which would have provided a definitive answer. Band 2 is observed to be yrast above spin 18^+. In the present analysis an additional transition has been added extending the structure to 28^+. Intensity is seen to feed into this band above 24^+, by two proposed E2 transitions connected by a 875 keV γ-ray. A spectrum showing band 2 projected from a RADWARE format γ^3 cube requiring the sum of members of band 2 as double gates is illustrated in 3.13(a).

3.9.4 Band 6

The structure labelled band 6, which strongly feeds yrast band 1 via a number of stretched and non stretched E2 transitions has been significantly extended. Band 6 is built on a proposed 4^+ bandhead, it extends up to a tentative spin of 16^+, with the addition of four new in band transitions. Proposed E1 decays link this structure to negative parity bands 3 and 4. Intensity is observed to rapidly reduce in band 6 above 8^+ making firm spin/parity

assignments difficult above 10^+. A new 494 keV proposed E2 transition is observed to feed the 8^+ state in yrast band 1.

3.9.5 Bands 7 and 8

Band 7 is observed to be built on a proposed (20^+) bandhead. The $16^+ \rightarrow 14^+$ 763 keV transition in band 1a has been identified to be a self-coincident doublet with the 762 keV transition linking band 7 to band 1a. Band 7 is also observed to decay into another structure, labelled 8 through a 525 keV self-coincident triplet transition. This confirms 762 keV as the linking transition to band 1a and therefore the excitation energy of the bandhead for band 7 can be confidently assigned. However it has been difficult to establish the multipolarity of these linking transitions, so the spins of band 7 should be considered tentative. An intense 884 keV transition is observed above the bandhead which is itself fed by a number of structures.

Band 8 was established after the observation of a relatively intense 1075 keV transition above 14^+ in band 1a. Above the bandhead a single 870 keV transition is observed. The structure decays back into band 1a via two M1 transitions of energy 238 and 311 keV which firmly establish the spins of band 8.

3.10 Low spin negative parity structures

3.10.1 Bands 3 and 4

Band 3 was postulated in [pau94] to be built on a 9^- bandhead. This assignment has been confirmed after the electric dipole nature of the 389 and 448 keV transitions which link band 3 to band 1 was established from linear polarisation results. Band 3 is observed to be yrast at moderate spin, indeed transitions in band 3 are clearly visible in Fig. 3.12 which shows γ-rays in coincidence with the $2^+ \rightarrow 0^+$ transition in ^{110}Te. An additional transition assumed to be E2 in character has been added to the top of band 3, extending this structure to 23^-. There is no further evidence for additional transitions, which is to be expected since the new transition is extremely weak and the structure is rapidly becoming non-yrast. At spins 15^- and above, a positive sequence of states, labelled band 2, decays into the negative parity yrast structure.

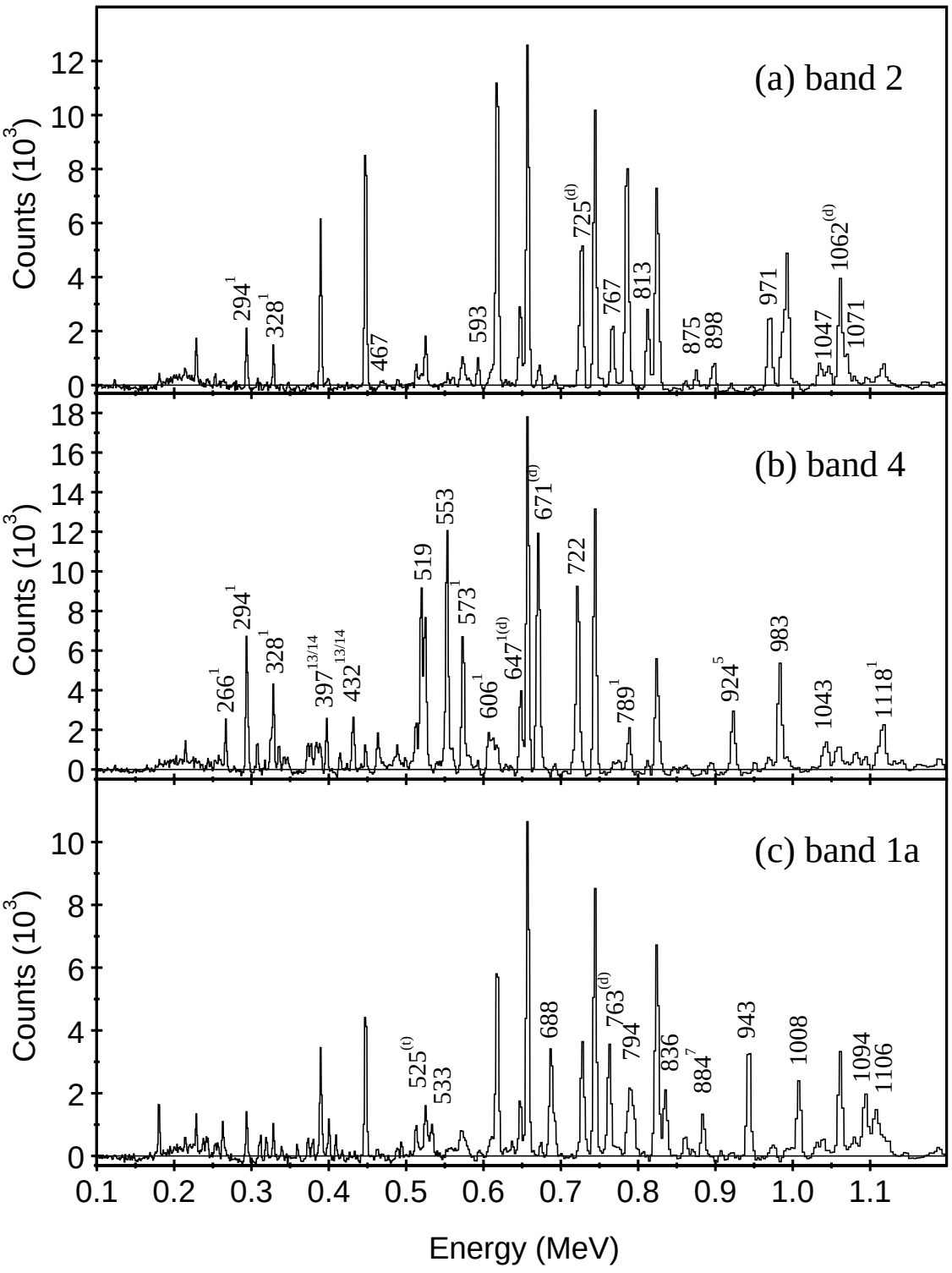

Figure 3.13: Gated spectra projected from a RADWARE format cube from the sum of double gates for relevant band members. Bands 1a, 2 and 4 are illustrated, constituent transitions are labelled. Non-band transitions are labelled with their respective band number. *(d)(t)* denotes a self-coincident doublet (triplet) transition. The strong unlabelled γ-rays are the positive and negative parity yrast structure.

Band 3 is observed to be weakly coupled to another negative parity structure, labelled 4, by a number of M1 transitions. Band 4 is built on a confirmed 8^- bandhead, which decays out through three different routes consisting of 325, 519 and 525 keV transitions populating band 1 in two places and band 6 respectively. The E1 nature of these transitions has where possible been confirmed. The 525keV transition is however a self coincident triplet precluding a firm assignment for this γ-decay. Band 4 continues above 16^- with the addition of 1043 and 1116 keV E2 transitions up to a spin of 20^-.

Below the 9^- bandhead of band 3, a further 7^- state is observed. It decays to the positive parity yrast structure via a 1281 keV E1 transition. A relatively intense 228 keV E2 connects the 9^- and 7^- states. There is no evidence for a transition connecting the the 8^- bandhead of band 4 to the 7^- state. This transition would however be very low in energy, which provides a possible explanation why it may not have been observed.

3.10.2 Band 5

Above the 16^- transition in band 4, intensity is observed to feed in from another structure of undetermined parity, labelled band 5. The 671 keV transition in band 4, is observed to be a self-coincident doublet with a 669 keV γ-ray that is proposed to link band 4 to band 5. The choice of the 669 keV transition as the link to band 4 was confirmed by the observation of a weak 549 keV transition linking the $19^{(-)}$ state in band 5 to the 18^- state in band 4. The 924 keV transition previously assigned to band 4 is now assigned to band 5. Band 5 continues to higher spin with reducing intensity, up to a probable spin of $23^{(-)}$.

3.11 High spin decoupled Bands

Four decoupled bands in ^{110}Te have been identified which extend up to high spin. The level scheme proposed for these bands is illustrated in Fig. 3.11 in the context of the complete ^{110}Te level scheme, and clarified in Fig. 3.14. The spectra for the decoupled bands, illustrated in Fig. 3.15 and Fig. 3.16, were created from the sum of coincident double gates for all listed members of each band. The resulting spectra projected from a γ^3 RADWARE format cube provide excellent insight into the structure of the bands. The non-linear gain compression used in the γ^4 hypercube and γ^3 cube, which have fewer channels at high energy where the experimentally observed energy resolution is relatively poor, has

E_γ (keV)[1]	I_γ (%)[2]	R_{DCO}[3]	P	Multipolarity	Assignment	Band
122.9	1.4	0.33(4)	–	M1/E2	$9^- \rightarrow 8^-$	3→4
186	<1%	–	–	(M1/E2)	$11^- \rightarrow 10^-$	3→4
214.2	3.6	0.56(3)	–	M1/E2	$6^+ \rightarrow 6^+$	6→1
228.0	5.2	0.89(2)	–	E2	$9^- \rightarrow 7^-$	3
238.0	3.4	–	–	(M1/E2)	$18^+ \rightarrow 18^+$	8→1a
242.9	2.0	0.47(2)	–	M1/E2	$13^- \rightarrow 12^-$	3→4
252.8	2.3	0.60(2)	–	M1/E2	$8^+ \rightarrow 7^+$	1
262.0	1.8	0.81(15)	–	M1/E2	$19^- \rightarrow 18^-$	3→4
265.7	1.7	1.19(5)[553]	–	E1	$8^- \rightarrow 8^+$	4→1
293.4	9.8	0.84(1)	-0.02(10)	M1/E2	$6^+ \rightarrow 6^+$	1
295.8	1.3	0.40(4)	–	M1/E2	$7^+ \rightarrow 6^+$	1
307.2	1.4	0.56(2)	–	M1/E2	$15^- \rightarrow 14^-$	3→4
308.3	1.2	–	–	(M1/E2)	$17^- \rightarrow 17^-$	5→3
311.0	4.5	–	–	(M1/E2)	$16^+ \rightarrow 16^+$	8→1a
318	<1%	–	–	(M1/E2)	$17^- \rightarrow 16^-$	3→4
324.6	1.0	0.84(1)	–	E1	$8^- \rightarrow 8^+$	4→1a
328.0	6.4	0.93(2)[618]	–	E2	$6^+ \rightarrow 4^+$	1
335	<1%	–	–	(E1)	$12^- \rightarrow 12^+$	4→6
383.7	1.1	–	–	(E1)	$10^- \rightarrow 10^+$	4→6
388.8	23.4	0.64(1)	0.39(11)	E1	$9^- \rightarrow 8^+$	3→1
430.9	2.9	0.75(1)[4]	0.20(19)[5]	M1/E2	$10^- \rightarrow 9^-$	4→3
447.4	41.5	0.64(1)	0.02(9)	E1	$9^- \rightarrow 8^+$	3→1
466.6	4.3	0.59(2)	–	E1	$22^+ \rightarrow 21^-$	2→3
478.6	2.5	0.33(4)	–	M1/E2	$14^- \rightarrow 13^-$	4→3
483.7	1.5	0.16(1)	–	M1/E2	$12^- \rightarrow 11^-$	4→3
493.9	1.1	–	–	(E2)	$10^+ \rightarrow 8^+$	6→1
512.7	6.5	0.51(3)[553]	–	M1/E2	$4^+ \rightarrow 4^+$	6→1
519.0	8.3	0.59(2)	–	E1	$8^- \rightarrow 7^+$	4→1
524.7	11.8	0.88(1)[4]	0.21(17)[5]	E2	$6^+ \rightarrow 4^+$	6

Table 3.2: Summary of low spin experimental results for ^{110}Te.

E_γ (keV)[1]	I_γ (%)[2]	R_{DCO}[3]	P	Multipolarity	Assignment	Band
525.0	7.2	0.88(1)[4]	0.21(17)[5]	E1	$8^- \rightarrow 8^+$	4→6
525.0	6.1	0.88(1)[4]	0.21(17)[5]	E2	$20^+ \rightarrow 18^+$	7→8
533	<1%	–	–	(E2)	$12^+ \rightarrow 10^+$	1a
549	<1%	–	–	(M1/E2)	$19^- \rightarrow 18^+$	5→4
552.8	14.5	1.09(1)	–	E2	$10^- \rightarrow 8^-$	4
571.4	1.2	–	–	(E1)	$11^- \rightarrow 10^+$	3→6
573.3	10.0	0.39(1)	–	M1/E2	$7^+ \rightarrow 6^+$	1
578	<1%	–	–	(E1)	$13^- \rightarrow 12^+$	3→6
592.8	10.3	0.58(1)	–	E1	$20^+ \rightarrow 19^-$	2→3
606.5	1.5	1.03(3)[553]	–	E2	$6^+ \rightarrow 4^+$	1
613.0	2.4	0.96(3)[553]	–	E2	$4^+ \rightarrow 2^+$	1
617.7	78.5	1.04(1)	0.55(9)	E2	$11^- \rightarrow 9^-$	3
646.8	11.3	0.89(2)[4]	0.22(17)[5]	E1	$9^- \rightarrow 8^+$	3→6
648.2	15.6	0.89(2)[4]	0.22(17)[5]	E2	$8^+ \rightarrow 6^+$	6
657.2	100.0	0.85(1)	0.01(12)	E2	$2^+ \rightarrow 0^+$	1
668.6	5.9	0.91(2)[4]	–	M1/E2	$17^- \rightarrow 16^-$	5→4
670.9	9.5	0.91(2)[4]	–	E2	$12^- \rightarrow 10^-$	4
676	<1%	–	–	(M1/E2)	$16^- \rightarrow 15^-$	4→3
687.5	9.0	0.99(1)	0.61(33)	E2	$14^+ \rightarrow 12^+$	1a
693.2	2.5	–	–	(E2)	$10^+ \rightarrow 8^+$	6
721	<1%	–	–	(E2)	$12^+ \rightarrow 10^+$	6
722.0	16.0	1.02(6)	–	E2	$14^- \rightarrow 12^-$	4
723	<1%	–	–	(E1)	$18^+ \rightarrow 17^-$	1a→3
725	<1%	–	–	(M1/E2)	$18^- \rightarrow 17^-$	4→3
725.1	11.1	1.09(1)[4]	0.65(11)*	E2	$18^{(+)} \rightarrow 16^{(+)}$	2
727.8	68.0	1.09(1)[4]	0.65(11)*	E2	$13^- \rightarrow 11^-$	3
744.3	91.3	0.86(1)	0.39(13)	E2	$4^+ \rightarrow 2^+$	1
762.2	4.3	1.29(2)[4]	–	E2	$20^+ \rightarrow 18^+$	7→8
762.8	14.0	1.29(2)[4]	–	E2	$16^+ \rightarrow 14^+$	1a

E_γ (keV)[1]	I_γ(%)[2]	R_{DCO}[3]	P	Multipolarity	Assignment	Band
766.9	18.7	0.56(1)	–	E1	$18^+ \rightarrow 17^-$	2→3
772.3	4.4	0.63(2)	–	E1	$16^+ \rightarrow 15^-$	1a→3
777	<1%	–	–	(E2)	$14^+ \rightarrow 12^+$	6
785.8	63.0	1.00(1)	–	E2	$15^- \rightarrow 13^-$	3
789.3	4.4	0.53(7)[553]	–	M1/E2	$4^+ \rightarrow 4^+$	1
794.3	5.1	0.65(3)	–	E1	$14^+ \rightarrow 13^-$	1a→3
812.5	16.2	1.03(1)	0.46(12)	E2	$20^{(+)} \rightarrow 18^{(+)}$	2
824.0	61.3	0.96(1)	0.34(8)	E2	$6^+ \rightarrow 4^+$	1
826.3	22.7	0.98(1)	–	E2	$8^+ \rightarrow 6^+$	1
835.5	4.2	0.59(1)	–	E1	$12^+ \rightarrow 11^-$	1a→3
847	<1%	–	–	(E2)	$(16^+ \rightarrow 14^+)$	6
862.1	3.0	0.73(6)[618]	–	E2	$8^+ \rightarrow 6^+$	6→1
870.0	6.1	–	–	(E2)	$18^+ \rightarrow 16^+$	8
875.0	1.2	1.07(4)	–	E2	$28^{(+)} \rightarrow 26^{(+)}$	2
884.0	4.1	1.26(2)	–	E2	$22^+ \rightarrow 20^+$	7
897.5	4.0	–	–	(E2)	$26^+ \rightarrow 24^+$	2
921	<1%	–	–	(M1/E2)	$2^+ \rightarrow 2^+$	1
921	<1%	–	–	(E1)	$10^+ \rightarrow 9^-$	1a→3
924.0	3.9	1.12(4)	–	E2	$19^{(-)} \rightarrow 17^{(-)}$	5
943.3	12.5	1.26(2)	–	E2	$18^+ \rightarrow 16^+$	1a
970.6	21.3	1.05(2)	0.41(16)	E2	$22^{(+)} \rightarrow 20^{(+)}$	2
983.4	11.9	0.99(2)	–	E2	$16^- \rightarrow 14^-$	4
986.9	17.6	0.98(1)	–	E2	$19^- \rightarrow 17^-$	3
993.3	42.1	1.05(1)	0.55(11)	E2	$17^- \rightarrow 15^-$	3
999	<1%	–	–	(E2)	$28^{(+)} \rightarrow 26^{(+)}$	2
1007.7	11.0	0.97(2)	–	E2	$20^+ \rightarrow 18^+$	1a
1031.8	2.9	0.97(5)	–	E2	$22^+ \rightarrow 20^+$	1a
1035.4	8.6	0.63(2)	–	E1	$16^+ \rightarrow 15^-$	2→3
1038.1	4.1	–	–	(E2)	$6^+ \rightarrow 4^+$	6→1

E_γ (keV)[1]	I_γ (%)[2]	R_{DCO}[3]	P	Multipolarity	Assignment	Band
1039.4	2.1	–	–	(E2)	$(24^+ \rightarrow 22^+)$	1a
1043.4	8.1	1.14(4)	–	E2	$18^- \rightarrow 16^-$	4
1047.0	4.0	–	–	(E2)	$28^{(+)} \rightarrow 26^{(+)}$	2
1056.0	1.7	–	–	(E2)	$21^{(-)} \rightarrow 19^{(-)}$	5
1061.8	48.0	0.95(1)	0.28(8)	E2	$8^+ \rightarrow 6^+$	1
1062.2	16.58	0.97(3)	–	E2	$24^{(+)} \rightarrow 22^{(+)}$	2
1071.4	9.3	1.22(2)	–	E2	$26^{(+)} \rightarrow 24^{(+)}$	2
1075.0	3.2	–	–	(E2)	$16^+ \rightarrow 14^+$	8
1087.7	2.5	–	–	(E2)	$(24^+ \rightarrow 22^+)$	7
1094.4	11.5	1.00(3)	–	E2	$22^+ \rightarrow 20^+$	1a
1096.2	3.9	0.98(2)	–	E2	$21^- \rightarrow 19^-$	3
1103	<1%	–	–	(E2)	$23^- \rightarrow 21^-$	3
1106.0	7.6	1.04(3)	–	E2	$23^- \rightarrow 21^-$	1a
1113	<1%	–	–	(E2)	$23^{(-)} \rightarrow 21^{(-)}$	5
1116.2	4.1	1.01(5)	–	(E2	$20^- \rightarrow 18^-$	4
1118.0	15.4	0.99(2)	–	E2	$6^+ \rightarrow 4^+$	1
1122.5	2.0	0.94(6)	–	E2	$24^+ \rightarrow 22^+$	1a
1258.2	4.8	0.92(2)	–	E2	$4^+ \rightarrow 2^+$	6→1
1281.1	4.5	0.50(1)	–	E1	$7^- \rightarrow 6^+$	3→1
1293.1	1.1	–	–	(E2)	$26^+ \rightarrow 24^+$	1a
1368	<1%	–	–	(E2)	$10^+ \rightarrow 8^+$	1a

[1] Energies are estimated to be accurate to ±0.3 keV for strong transitions (>10%) rising to ±0.6 keV for weaker transitions. Energies quoted as integers are estimated to be ±1 keV.

[2] Errors on relative intensities are typically ≤5%.

[3] DCO ratios were obtained from the sum of gates on the 657 and 745 keV quadrupole transitions unless otherwise indicated.

[4] DCO ratio obtained from composite peak.

[5] Linear polarisation result obtained from composite peak.

aided the observation of the less intense high energy transitions. The weak population of these bands has precluded a successful angular correlation analysis, therefore transition multipolarities are assumed. A detailed results summary for these bands is included in table 3.3.

3.11.1 Band 9

Band 9, illustrated in Fig. 3.15(a), is observed to carry ≈8% of the ^{110}Te channel intensity. It is a sequence of 10 γ-ray transitions, assumed stretched E2 in character, increasing in spin up to a tentative (46^+). The intensity of the γ transitions is observed to decrease rapidly at high spin ($E_\gamma \geq 1626$ keV), coinciding with an increase in the spacing of adjacent transitions. Below 36^+ in band 9 a 1587 keV transition is observed in coincidence. The transition is visible in the spectrum of band 9 shown in Fig. 3.15(a) and is included for completeness.

Below spin (34^+) in band 9 there is no evidence for intensity feeding out over several transitions, indeed the most intense transition is observed to be the 1109 keV γ-ray. This implies band 9 must decay out to the low spin level structure at approximately spin (26^+). Following a detailed analysis procedure involving the γ^4 hypercube, the tentative assignment of a discrete γ-ray transition linking band 9 to the low spin level scheme at spin (24^+) in band 2 has been made. The 994 keV γ-ray is observed in coincidence spectra obtained from the sum of double gates containing members of band 9, shown in Fig. 3.15(a). The 994 keV transition is observed to be a self coincident doublet which enhances the apparent intensity of transitions in band 9. This unfortunately had the consequence that the multipolarity of the link could not be determined. The spins and parities for band 9 have therefore to be considered tentative and are based on lowest estimates from the observed coincidence spectra. Arguments which use the theoretical interpretation discussed in chapter 4 have been used to provide confidence that the suggested assignment of positive parity even spin is indeed correct.

No further discrete transitions were observed linking band 9 to the low spin level scheme, therefore the requirement that the list of members of decoupled band 9 (A) were in coincidence with the list of members of the ground state bands 1 and 3 (B) was used. The gated spectrum was only incremented if a sum of triple gates meeting the requirement [A/A/B]

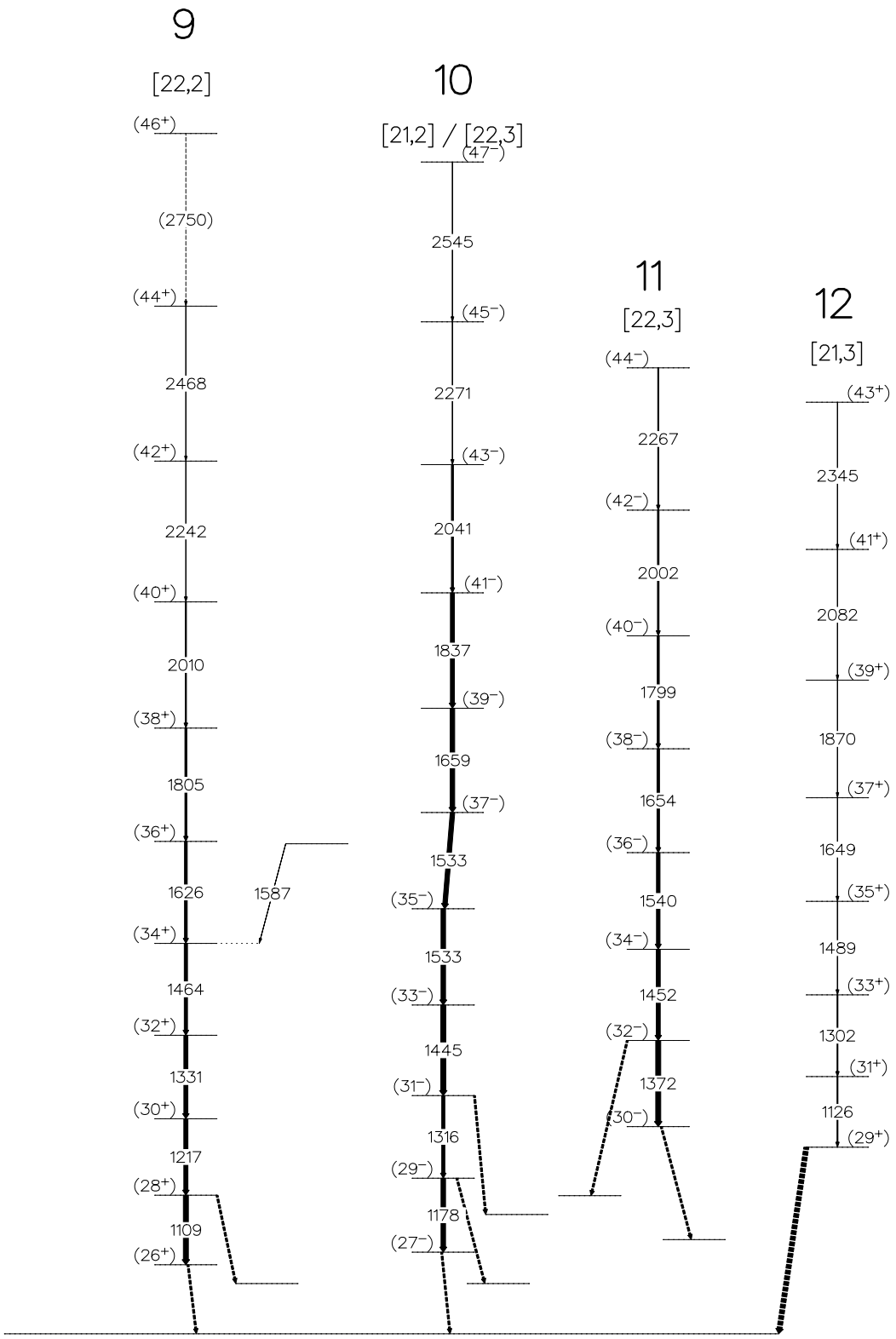

Figure 3.14: The high spin level scheme obtained from this work. Illustrated are the decoupled bands and the possible routes for decay out, determined from investigation of the coincidence spectra.

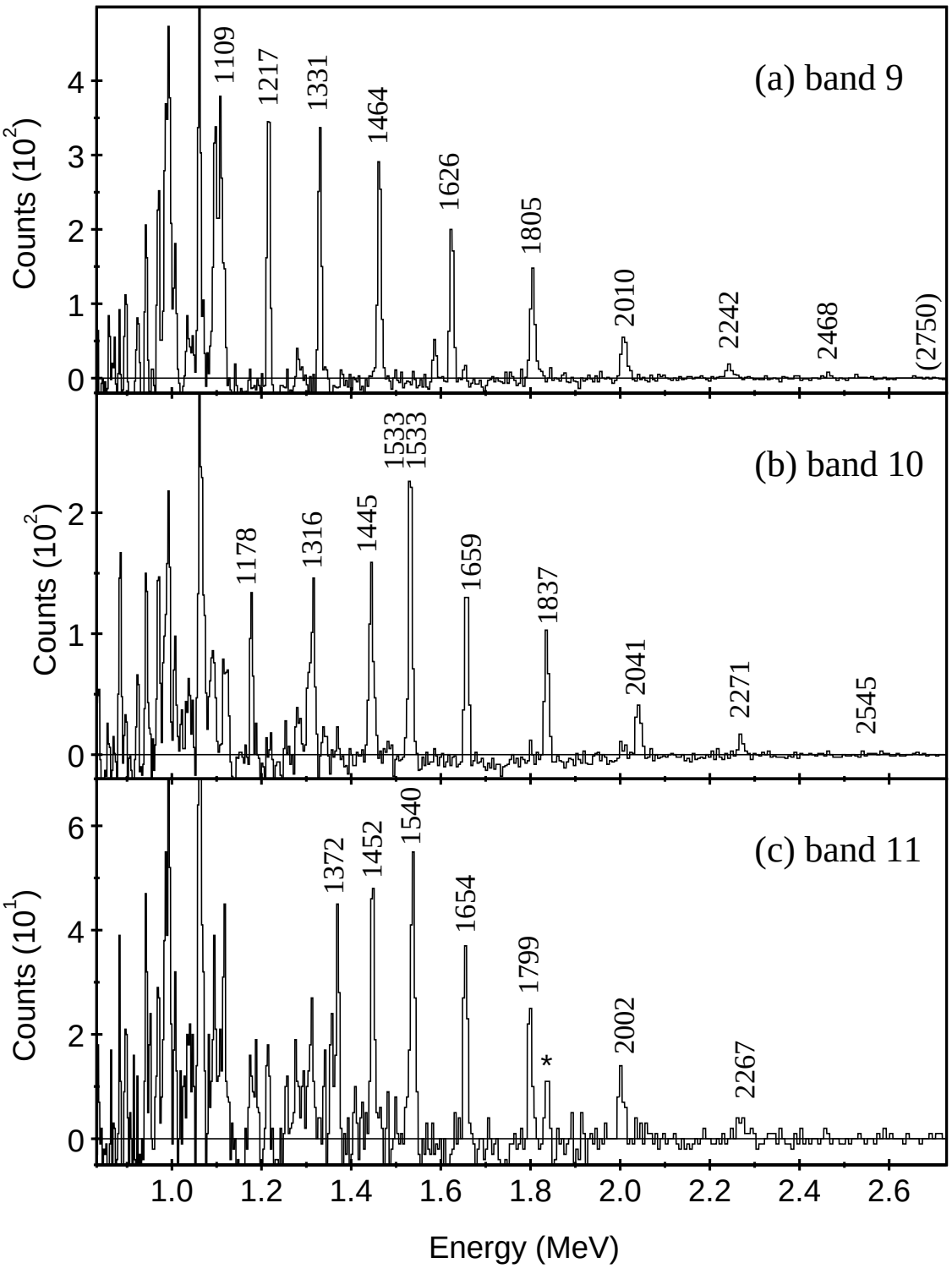

Figure 3.15: Coincidence spectra generated from the sum of double gates on labelled members of the decoupled band structures. Illustrated are the three most intense decoupled structures which represent 8, 6 and 5% of the total channel intensity respectively.

E_γ (keV)[1]	I_γ (%)[2]	Multipolarity	Assignment	Band
1109.0	≡100	(E2)	$(28^+ \rightarrow 26^+)$	9
1216.6	82(3)	(E2)	$(30^+ \rightarrow 28^+)$	9
1330.7	80(3)	(E2)	$(32^+ \rightarrow 30^+)$	9
1463.5	64(3)	(E2)	$(34^+ \rightarrow 32^+)$	9
1625.5	54(3)	(E2)	$(36^+ \rightarrow 34^+)$	9
1805.4	38(2)	(E2)	$(38^+ \rightarrow 36^+)$	9
2010.0	22(2)	(E2)	$(40^+ \rightarrow 38^+)$	9
2242.1	8(4)	(E2)	$(42^+ \rightarrow 40^+)$	9
2468.2	1(1)	(E2)	$(44^+ \rightarrow 42^+)$	9
(2750)	<1%	(E2)	$(46^+ \rightarrow 44^+)$	9
1587.0	17(3)	(E2)	$(36^+ \rightarrow 34^+)$	9
1177.7	62(5)	(E2)	$(29^- \rightarrow 27^-)$	10
1316.4	62(6)	(E2)	$(31^- \rightarrow 29^-)$	10
1445.0	≡100	(E2)	$(33^- \rightarrow 31^-)$	10
1532.9	188(7)*	(E2)	$(35^- \rightarrow 33^-)$	10
1533.0	188(7)*	(E2)	$(37^- \rightarrow 35^-)$	10
1658.6	92(5)	(E2)	$(39^- \rightarrow 37^-)$	10
1837.3	76(5)	(E2)	$(41^- \rightarrow 39^-)$	10
2041.1	36(4)	(E2)	$(43^- \rightarrow 41^-)$	10
2271.1	13(2)	(E2)	$(45^- \rightarrow 43^-)$	10
2545.0	1(1)	(E2)	$(47^- \rightarrow 45^-)$	10
1372.0	74(7)	(E2)	$(32^- \rightarrow 30^-)$	11
1452.0	92(7)	(E2)	$(34^- \rightarrow 32^-)$	11
1540.0	≡100	(E2)	$(36^- \rightarrow 34^-)$	11
1654.0	70(6)	(E2)	$(38^- \rightarrow 36^-)$	11
1799.0	46(5)	(E2)	$(40^- \rightarrow 38^-)$	11
2002.0	23(4)	(E2)	$(42^- \rightarrow 40^-)$	11
2267.0	9(2)	(E2)	$(44^- \rightarrow 42^-)$	11

Table 3.3: A detailed summary of experimental results for the decoupled bands in ^{110}Te. Intensity values are quoted as a percentage of the strongest single transition in each structure. The spins, parities and multipolarities of the transitions should all be considered tentative.

E_γ (keV)[1]	I_γ (%)[2]	Multipolarity	Assignment	Band
1125.6	≡100	(E2)	$(31^+ \rightarrow 29^+)$	12
1302.1	99(8)	(E2)	$(33^+ \rightarrow 31^+)$	12
1489.0	53(5)	(E2)	$(35^+ \rightarrow 33^+)$	12
1649.3	64(8)	(E2)	$(37^+ \rightarrow 35^+)$	12
1869.8	16(4)	(E2)	$(39^+ \rightarrow 37^+)$	12
2082	<1%	(E2)	$(41^+ \rightarrow 39^+)$	12
2345	<1%	(E2)	$(43^+ \rightarrow 41^+)$	12

[1] Energies are estimated to be accurate to ±0.3 keV for strong transitions (>10%) rising to ±0.6 keV for weaker transitions. Energies quoted as integers are estimated to be ±1 keV.

[2] Errors on relative intensities are typically ≤5%.

was met. This approach has revealed possible unobserved decay paths from band 9 into the low spin level structure of ^{110}Te. The possible decay path is indicated in the detailed level schemes illustrated in Fig. 3.11 and Fig. 3.14.

3.11.2 Band 10

Band 10, Fig. 3.15(b), was populated with a lower intensity than band 9, comprising approximately 6% of the total channel intensity. It is observed to consist of 10 assumed stretched E2 γ-ray transitions increasing in spin up to a proposed (47^-). The remarkable feature of this band is the 1533 keV self coincident doublet transition clearly illustrated in Fig. 3.15(b). The placement of adjacent 1533 keV γ-ray transitions was made using intensity arguments following a detailed analysis procedure. The intensity of the band, similar to band 9, is seen to decrease rapidly at high spin above the 1837 keV transition with the spacing between adjacent transitions increasing. Below the 1533 keV self-coincident doublet transition, intensity is observed to feed out of the band structure over the lowest three transitions of 1178, 1316 and 1445 keV. Band 10 is seen to strongly feed band 1a and band 2, however no discrete transitions are observed carrying this intensity.

The tentative spins and parities assigned to band 10 are based on lowest estimates from the observed coincidence spectra with allowances for the angular momentum of the linking

transitions, and the results of theoretical calculations run to determine the configurations of these structures. Using this argument band 10 has been tentatively assigned negative parity and odd spin.

3.11.3 Band 11

Band 11, Fig. 3.15(c), consists of 7 assumed stretched E2 transitions increasing to a proposed tentative maximal spin of (44^-). The structure is populated with an intensity of $\approx$5% that of the total channel intensity. Band 11 shows many similarities to band 10. The band is observed to decay out over the lowest three transitions, although there is no evidence for discrete links between this structure and the low spin level scheme. Assigned spins and parities are based on the same assumptions as for the other decoupled structures. Band 11 is observed to feed band 2 particularly strongly. Above the $(40^- \rightarrow 38^-)$ 1799 keV transition the intensity of the band is observed to decrease sharply with increasing γ-ray spacing.

3.11.4 Band 12

Band 12, Fig. 3.16(a), consists of 7 assumed stretched E2 transitions, increasing in spin up to a tentative (43^+) state. The intensity profile of the band is similar to that of band 9, maximal at low spin, with no evidence for the intensity feeding out over several transitions. At higher spin above 1870 keV the intensity rapidly decreases as the γ-ray spacing increases, above the 2345 keV transition, a lack of statistics precludes the observation of any further states. Band 12 is observed to strongly feed the positive parity structure band 1a. Intensity reaches band 1a through the structures labelled 7 and 8. In particular, intensity is observed to flow through a 1088 keV transition into the relatively intense 884 keV state. With this knowledge the spins and parities of band 12 have been assigned to be consistent with those of the other decoupled structures, in particular the assignment must explain the relatively weak population of 3% the total channel intensity.

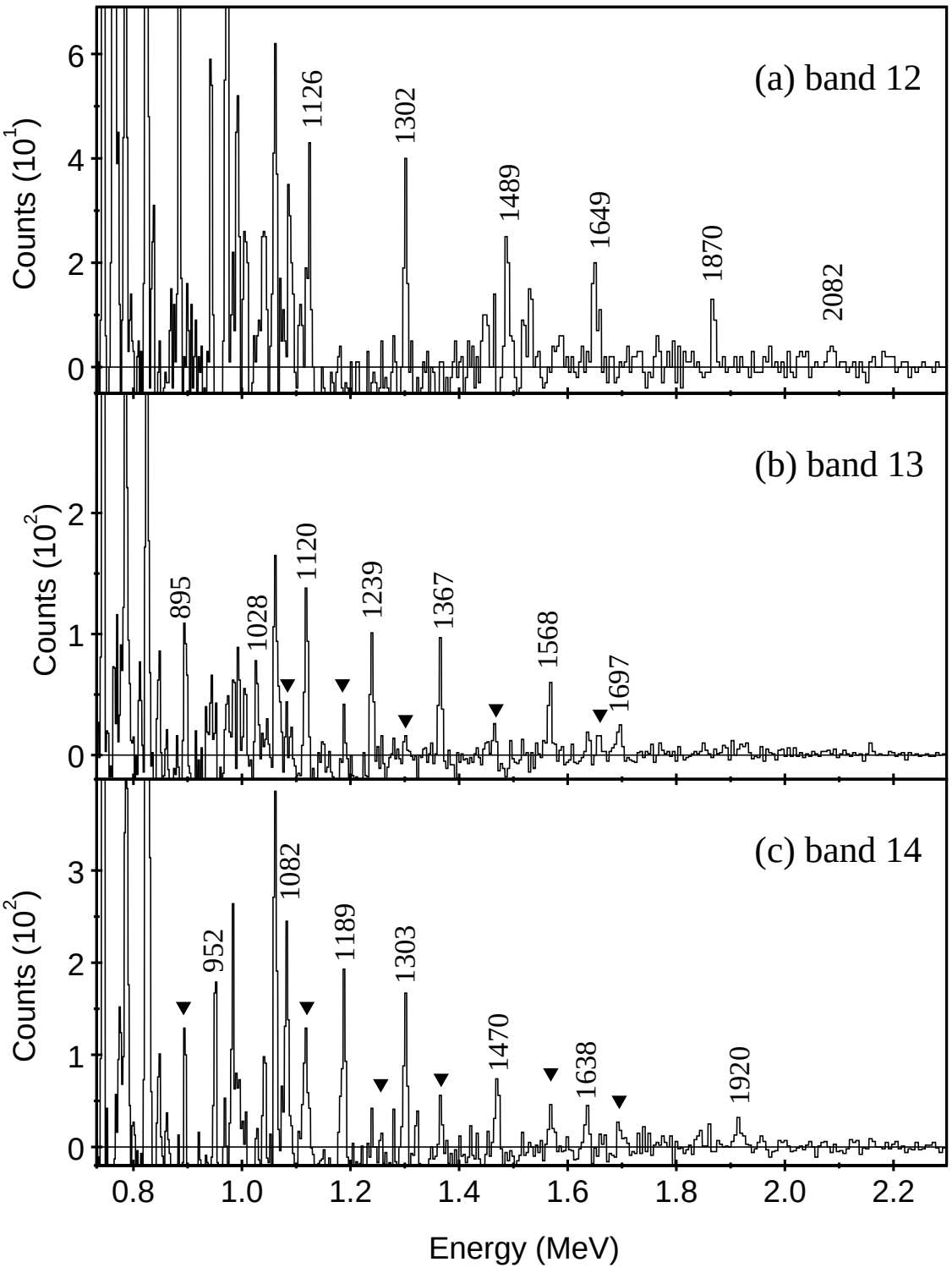

Figure 3.16: Coincidence spectra generated from the RADWARE 3-D analysis code LEVIT8R created from the sum of double gates on labelled members of the bands. (a) decoupled band 12, (b) quadrupole transitions in bands 13 and (c) band 14. The position of the E2 members of the signature partner band are indicated with triangles where appropriate.

3.12 High spin coupled bands

Two strongly coupled band structures have been observed in ^{110}Te extending to high spin. The term 'coupled band' in this context is used to describe a pair of strongly coupled $\Delta I = 2$ band structures with strong $\Delta I = 1$ cross-over transitions. The decay schemes determined for these structures are detailed in Fig. 3.11 in relation to the complete level scheme and illustrated in Fig. 3.17 with more detail. Spectra for the coupled bands are shown in Fig. 3.16(b)(c), Fig. 3.18 and Fig. 3.19. The spectra shown were obtained using a variety of gating techniques in order to enhance the apparent intensity of the observed structures. A sum of double gates from the stretched E2 transitions in each labelled band, projected out from a RADWARE format γ^3 cube was used to create the spectra shown in Fig. 3.16(b)(c) and Fig. 3.18(a)(b). The spectra in Fig. 3.19, which show the quadrupole and dipole members of the interleaved bands, were created using the RADWARE format γ^4 hypercube. The dipole γ-ray transitions (A) were required to be in coincidence with members of the ^{110}Te low spin level scheme (B), satisfying the triple gate requirement [qA/A/B] such that the sum of approximately 350 triple gates were projected into 1-d spectra. The quality of the observed spectra greatly facilitated the analysis of these structures.

Confirmation of the multipolarity of a number of transitions in the bands was made possible following an angular correlation analysis using the method of direction correlation from oriented states (DCO). The DCO results for the most intense transitions in the coupled bands along with relative intensity measurements and assignments can be found in table 3.4.

3.12.1 Band 13

Band 13, illustrated in Fig. 3.16(b) and Fig. 3.19(a), consists of 10 assumed stretched E2 transitions increasing in spin up to a tentative (38^-). The intensity of the γ-ray transitions is observed to decrease with increasing spin, coinciding with an increase in the spacing of adjacent transitions. A discontinuity in this description is however observed above spin (34^-). The energy of the (36^-) state appears depressed relative to what might be expected. A high energy γ transition of 2162 keV is hence observed decaying from (38^-) which is the highest observed spin state.

The intensity of band 13 is seen to reduce sharply over the bottom two observed E2

transitions of 677 and 773 keV. This observation corresponds to intensity feeding out into the low spin negative parity band structures. The observation of reducing intensity in band 9 is clarified by observing the intensity profile of the dipole transitions linking band 9 to band 10. The intensities of the quadrupole in band transitions are confused because these E2 transitions are doublet or near doublet γ-rays with the more intense members of the low spin level structure.

Following a detailed analysis procedure a single high energy discrete link into the low spin level scheme has been observed. The 1569 keV transition of undetermined multipolarity and electromagnetic character decays directly from (18^-) into negative parity band 4 feeding it at spin 16^-. This transition was weak in intensity, and was ascertained following a detailed analysis using a RADWARE format hypercube. Further decay out routes which undoubtedly feed the low spin level structure could not be determined. The tentative spin and parity of the bandhead of band 13 was assigned with reference to the calculations detailed in chapter 4. The agreement between experiment and theory obtained in sec. 4.7.1 is used as a strong argument for the suggested assignment in the absence of experimental results.

3.12.2 Band 14

Band 14, illustrated in Fig. 3.16(c) and Fig. 3.19(a), consists of 10 stretched E2 transitions and is observed up to a probable spin of (37^-). The intensity profile of the band is similar to that of band 13, with decay out observed over the lowest two E2 band members. A single discrete 1860 keV γ-ray transition of undetermined spin and parity is observed linking band 14 into the low spin level scheme at 15^- in negative parity band 3.

A similar intensity profile and structure is observed in band 14 to that of band 13. The intensity of the γ-ray transitions decreases with increasing spin coinciding with an increase in γ-ray spacing. A discontinuity is observed at high spin because the (35^-) state is depressed in energy, resulting in a high energy transition of 1920 keV depopulating the (37^-) maximal spin state. The assignment of the bandhead spin and parity was made from lowest estimates and with reference to the theory discussed in chapter 4, therefore all quoted spins and parities should be considered tentative.

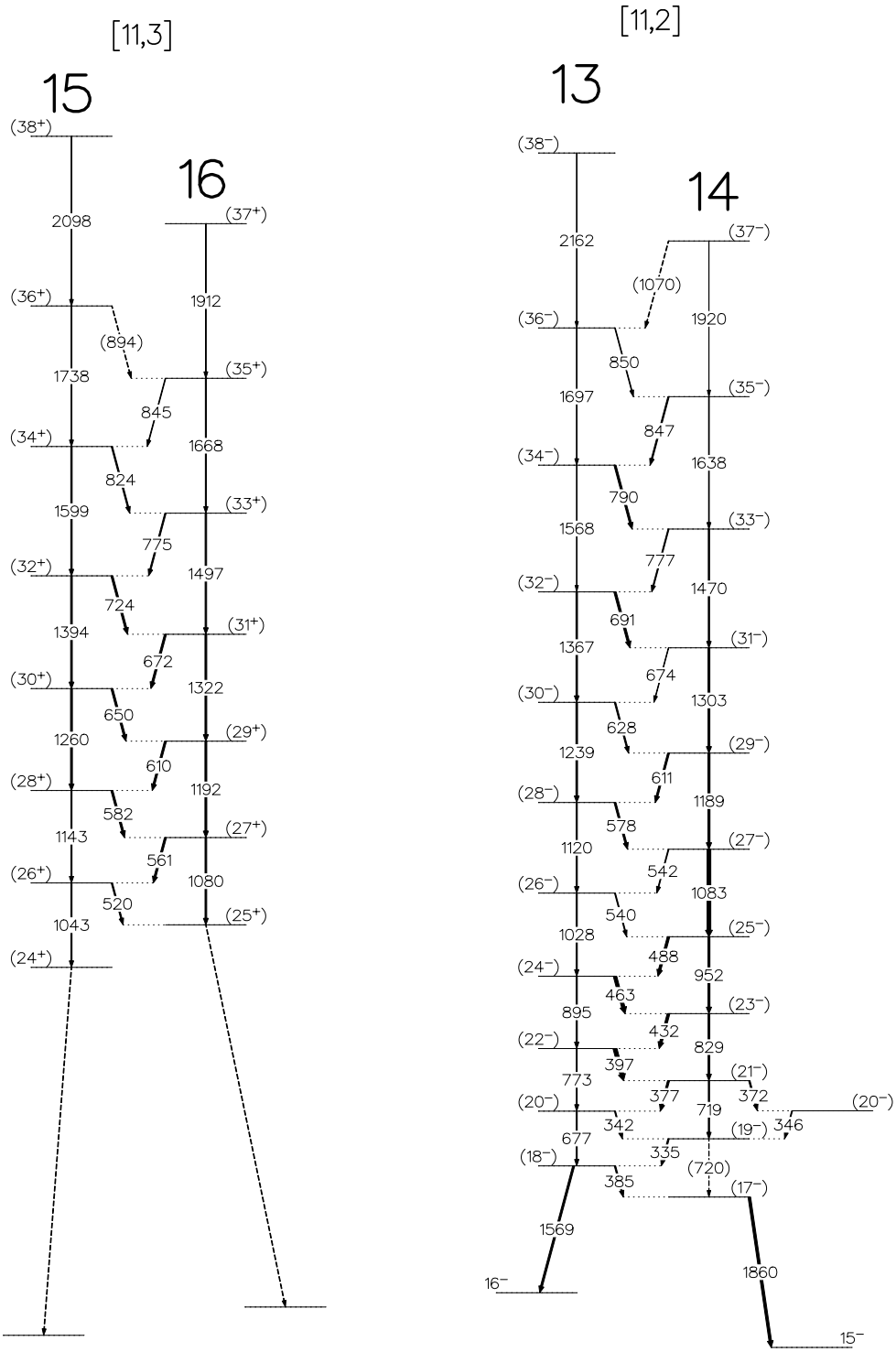

Figure 3.17: The proposed level scheme for the four coupled bands observed in ^{110}Te. The tentative links to the low spin level scheme are illustrated for bands 13 and 14. Proposed decay out routes are indicated for bands 15 and 16.

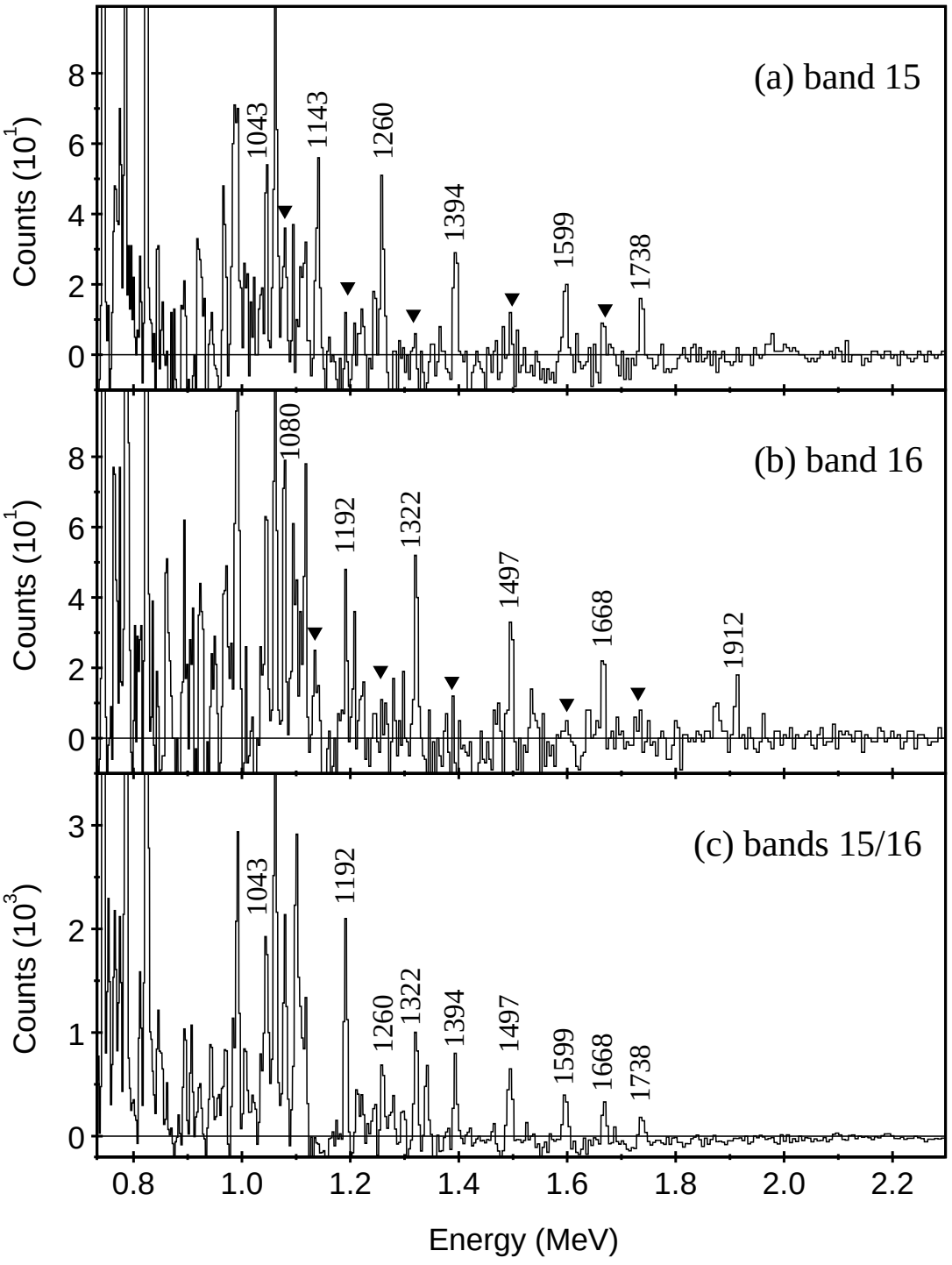

Figure 3.18: Spectra (a) band 15 and (b) band 16 were created from the sum of double gates of labelled members of the individual bands. Spectrum (c) which shows quadrupole members of bands 15 and 16 was created from an individual single gate on the 560 keV dipole transition which represents the most intense dipole transition coupling bands 15 and 16 together.

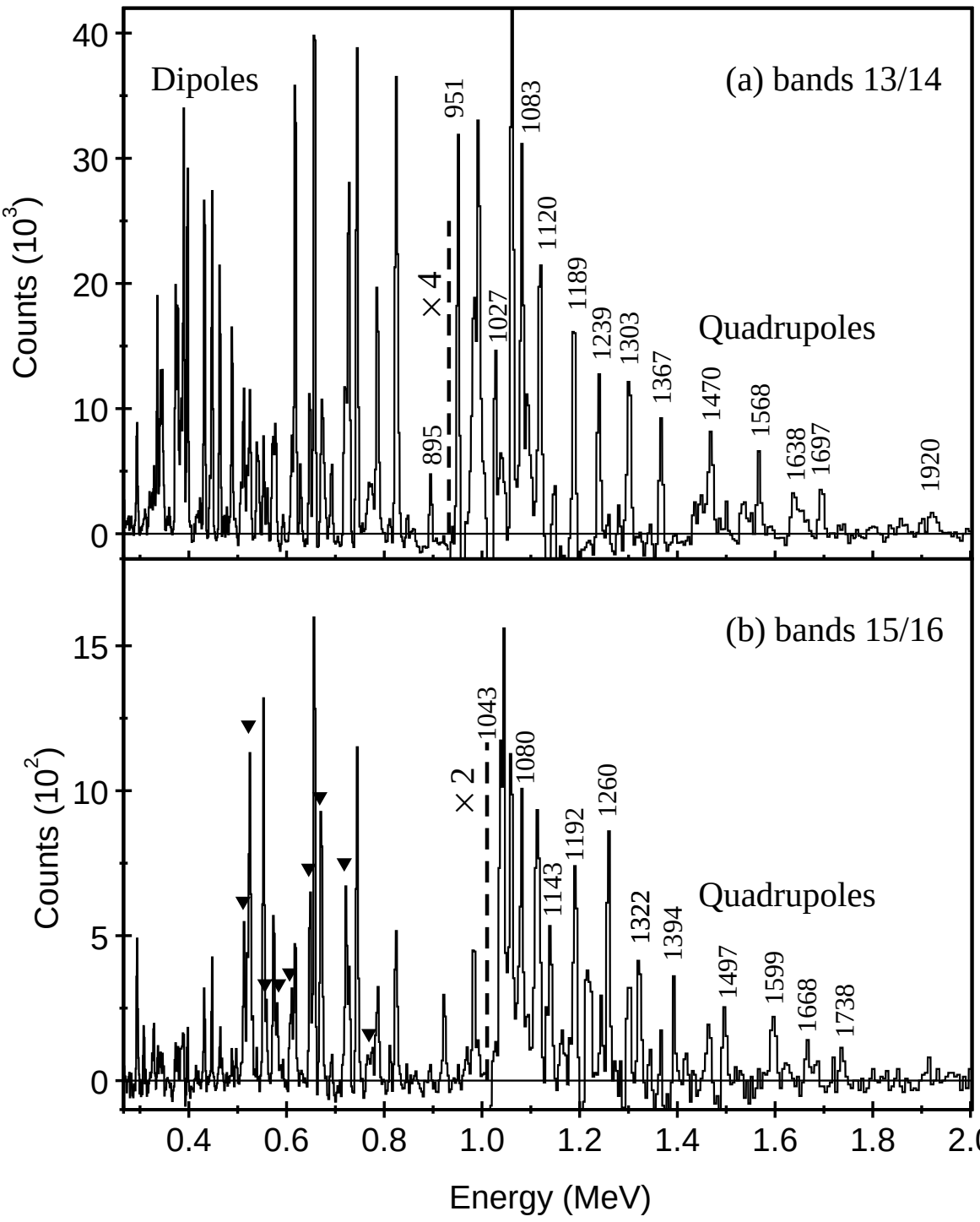

Figure 3.19: A coincidence spectrum generated from the RADWARE 4-D analysis code XM4DG created from the sum of triple gates on dipole members of the coupled bands 13/14 and 15/16, with members of the ground state band in ^{110}Te.

3.12.3 Coupled bands 13 and 14

Bands 13 and 14 are observed to be strongly coupled, linked by a cascade of 20 M1 transitions, extending up to the highest observed spin limit. The intensity of the M1 transitions is observed to be at a maximum near spin (22^-). At higher spin values the reduction in intensity of the M1 transitions is offset by an increase in the E2 transition intensity, enabling the coupled bands to be observed to unusually high spin.

The strongest dipole transitions were confirmed M1 in character following the angular correlation and linear polarisation analysis, the remaining dipole transitions therefore have inferred character. Fig. 3.19(a) shows an example of a 1-d projection created from the sum of 325 triple gates from a RADWARE format hypercube. The quadrupole and dipole transitions which make up the coupled band structure and their associated intensity profiles are clearly visible. The coupled band structure consisting of bands 13 and 14 is observed to carry approximately 14% of the ^{110}Te channel intensity. This high population intensity permits the structure, particularly the low spin dipole transitions which are especially intense, to be easily observed in low spin gates, see Fig. 3.13(b).

Below the 397 keV dipole transition, the coincidence data suggests that there are three possible routes of decay from the (21^-) state. A weak 719 keV E2 transition carries a small proportion of the intensity, the remainder is shared between the 373 and 377 keV transitions. This observation requires the existence of a second (20^-) state, which is confirmed by the observation of a further 346 keV transition decaying back to band 14.

3.12.4 Band 15

Band 15, illustrated in Fig. 3.18(a) and Fig. 3.19(b) is observed to consist of 7 proposed stretched E2 transitions. Inspection of Fig. 3.19(b) reveals that band 15 is populated somewhat less intensely than either bands 13 or 14. The reduction in statistics has complicated the analysis procedure. It has proved impossible to establish discrete links between this structure and the low spin level scheme, however possible routes of decay are indicated on Fig. 3.11. Band 15 is observed to preferentially feed the negative parity low spin structures, in particular bands 3, 4 and 5.

The assignment of spins and parities for band 15 must be considered very tentative. It has been made using lowest estimates, with reference to bands 13 and 14, and with

theoretical predictions provided by the calculations detailed in chapter 4. The reduced population intensity of band 15 implies that bands 13 and 14 should have spin units which are lower and therefore make them energetically favourable to populate relative to band 15. The high spin structure is hence proposed to be built on a (24^+) bandhead, with in band transitions extending to (38^+). The intensity profile of the band 15 is similar to that of bands 13 and 14, with a reduction in intensity observed over the lowest two transitions, 1043 and 1143 keV, where the structure is found to feed intensity into the low spin level scheme. The spacing between adjacent γ-ray transitions is seen to increase as a function of spin. A similar discontinuity in the γ-ray spacing is found to that of bands 13 and 14. The (36^+) transition appears energetically depressed, resulting in a high energy 2098 keV transition depopulating the highest observed state at (38^+).

3.12.5 Band 16

Band 16 is illustrated in Fig. 3.18(b) and Fig. 3.19(b). It consists of 6 assumed stretched E2 transitions increasing from a tentatively assigned bandhead spin of (25^+) up to (37^+). The intensity profile is similar to that of the other coupled structures. No discrete links to the low spin level structure could be ascertained.

3.12.6 Coupled bands 15 and 16

Bands 15 and 16 are observed to be coupled structures. They are linked by a cascade of 11 M1 transitions of varying intensity which are proposed to extend up to the highest observable spins. A number of the M1 γ-rays are near doublet transitions with low spin band members. Inspection of Fig. 3.19(b), illustrates the problem of extracting reliable information regarding the intensities and multipolarities of the transitions. The strongest M1 transition, through which a large proportion of the intensity of the band flows, is the $27^+ \rightarrow 26^+$ 561 keV γ-ray. Placing a single gate on this transition produced the spectrum shown in Fig. 3.18(c), which shows clearly the E2 transitions which make up bands 15 and 16.

E_γ (keV)[1]	I_γ (%)[2]	R_{DCO}[3]	Multipolarity	Assignment	Band
335.3	46(1)	0.93(2)	M1/E2	$(19^- \rightarrow 18^-)$	13/14
341.8	34(1)	–	(M1/E2)	$(20^- \rightarrow 19^-)$	13/14
346.1	21(1)	–	(M1/E2)	$(20^+ \rightarrow 19^-)$	13/14
372.3	50(1)	0.71(1)	M1/E2	$(21^- \rightarrow 20^-)$	13/14
377.3	74(1)	0.67(1)	M1/E2	$(21^- \rightarrow 20^-)$	13/14
397.2	≡100	0.70(1)	M1/E2	$(22^- \rightarrow 21^-)$	13/14
432.0	76(1)	0.72(1)	M1/E2	$(23^- \rightarrow 22^-)$	13/14
463.4	66(1)	0.72(1)	M1/E2	$(24^- \rightarrow 23^-)$	13/14
488.4	46(1)	0.73(1)	M1/E2	$(25^- \rightarrow 24^-)$	13/14
539.7	25(1)	0.85(2)	M1/E2	$(26^- \rightarrow 25^-)$	13/14
542.0	14(1)	0.85(2)	M1/E2	$(27^- \rightarrow 26^-)$	13/14
577.6	31(1)	–	(M1/E2)	$(28^- \rightarrow 27^-)$	13/14
611.1	32(1)	–	(M1/E2)	$(29^- \rightarrow 28^-)$	13/14
628.7	14(1)	–	(M1/E2)	$(30^- \rightarrow 29^-)$	13/14
674.0[5]	38(1)	–	(M1/E2)	$(31^- \rightarrow 30^-)$	13/14
691.0[4]	26(2)	–	(M1/E2)	$(32^- \rightarrow 31^-)$	13/14
777.0[4]	13(2)	–	(M1/E2)	$(33^- \rightarrow 32^-)$	13/14
790.0[4]	16(2)	–	(M1/E2)	$(34^- \rightarrow 33^-)$	13/14
847.0	7(1)	–	(M1/E2)	$(35^- \rightarrow 34^-)$	13/14
850	<1%	–	(M1/E2)	$(36^- \rightarrow 35^-)$	13/14
1070	<1%	–	(M1/E2)	$(37^- \rightarrow 36^-)$	13/14
677.0	25(1)	–	(E2)	$(20^- \rightarrow 18^-)$	13
719.1[5]	66(1)	–	(E2)	$(21^- \rightarrow 19^-)$	14
719.9[5]	66(1)	–	(E2)	$(19^- \rightarrow 17^-)$	14
774.0	14(1)	–	(E2)	$(22^- \rightarrow 20^-)$	13
829.0[4]	52(3)	–	(E2)	$(23^- \rightarrow 21^-)$	14
895.0	27(1)	–	(E2)	$(24^- \rightarrow 22^-)$	13
951.9	29(1)	–	(E2)	$(25^- \rightarrow 23^-)$	14

Table 3.4: Detailed summary of the experimental results for the coupled bands in ^{110}Te.

E_γ (keV)[1]	I_γ (%)[2]	R_{DCO}[3]	Multipolarity	Assignment	Band
1027.8	20(1)	–	(E2)	$(26^- \rightarrow 24^-)$	13
1083.2	42(1)	–	(E2)	$(27^- \rightarrow 25^-)$	14
1119.5	35(1)	–	(E2)	$(28^- \rightarrow 26^-)$	13
1189.4	24(1)	–	(E2)	$(29^- \rightarrow 27^-)$	14
1239.4	20(1)	–	(E2)	$(30^- \rightarrow 28^-)$	13
1302.6	17(1)	–	(E2)	$(31^- \rightarrow 29^-)$	14
1367.0	16(1)	–	(E2)	$(32^- \rightarrow 30^-)$	13
1469.5	14(1)	–	(E2)	$(33^- \rightarrow 31^-)$	14
1567.8[4]	12(1)	–	(E2)	$(34^- \rightarrow 32^-)$	13
1569.2[4]	12(1)	–	(E2)	$(18^- \rightarrow 16^-)$	13
1638.2	8(1)	–	(E2)	$(35^- \rightarrow 33^-)$	14
1697.2	7(1)	–	(E2)	$(36^- \rightarrow 34^-)$	13
1860	<1%	–	(E2)	$(17^- \rightarrow 15^-)$	14
1920	<1%	–	(E2)	$(37^- \rightarrow 35^-)$	14
2162	<1%	–	(E2)	$(38^- \rightarrow 36^-)$	13
519.9[4]	150(5)	–	(M1)	$(26^+ \rightarrow 25^+)$	15/16
560.5	≡100	–	(M1)	$(27^+ \rightarrow 26^+)$	15/16
582.1	71(2)	–	(M1)	$(28^+ \rightarrow 27^+)$	15/16
609.7	88(3)	–	(M1)	$(29^+ \rightarrow 28^+)$	15/16
649.8[4]	122(3)	–	(M1)	$(30^+ \rightarrow 29^+)$	15/16
671.6[4]	184(4)	–	(M1)	$(31^+ \rightarrow 30^+)$	15/16
723.6[5]	236(3)	–	(M1)	$(32^+ \rightarrow 31^+)$	15/16
775.2	45(2)	–	(M1)	$(33^+ \rightarrow 32^+)$	15/16
824.2[5]	213(6)	–	(M1)	$(34^+ \rightarrow 33^+)$	15/16
845.1	13(2)	–	(M1)	$(35^+ \rightarrow 34^+)$	15/16
894.2	<1%	–	(M1)	$(35^+ \rightarrow 34^+)$	15/16
1043.3	56(3)	–	(E2)	$(26^+ \rightarrow 24^+)$	15
1079.8	37(2)	–	(E2)	$(27^+ \rightarrow 25^+)$	16
1142.5	25(1)	–	(E2)	$(28^+ \rightarrow 26^+)$	15

E_γ (keV)[1]	I_γ (%)[2]	R_{DCO}[3]	Multipolarity	Assignment	Band
1191.5	14(1)	–	(E2)	$(29^+ \rightarrow 27^+)$	16
1259.8	26(1)	–	(E2)	$(30^+ \rightarrow 28^+)$	15
1322.4	16(1)	–	(E2)	$(31^+ \rightarrow 29^+)$	16
1394.4	15(1)	–	(E2)	$(32^+ \rightarrow 30^+)$	15
1497.4	16(1)	–	(E2)	$(33^+ \rightarrow 31^+)$	16
1598.5	11(1)	–	(E2)	$(34^+ \rightarrow 32^+)$	15
1668.1	8(1)	–	(E2)	$(35^+ \rightarrow 33^+)$	16
1738.4	6(1)	–	(E2)	$(36^+ \rightarrow 34^+)$	15
1911.5	5(1)	–	(E2)	$(37^+ \rightarrow 35^+)$	16
2098	<1%	–	(E2)	$(38^+ \rightarrow 36^+)$	15

[1] Energies are estimated to be accurate to ±0.3 keV for strong transitions (>10%) rising to ±0.6 keV for weaker transitions. Energies quoted as integers are estimated to be ±1 keV.

[2] Errors on relative intensities are typically ≤5%.

[3] DCO ratios were obtained from the sum of gates on the 657 and 745 keV quadrupole transitions unless otherwise indicated.

[4] Energy doublet : Intensity measurement is that of composite peak.

[5] Energy triplet : Intensity measurement is that of composite peak.

3.13 Results for ^{109}Te

3.13.1 The sorting procedure

The sorting procedure used to select ^{110}Te which was discussed in sec.3.7.1 was followed. In order to isolate ^{109}Te, which forms as a residual nucleus through the α2pn exit channel, the extra requirement of one neutron detected in coincidence with a γ-event was added. The BGO elements in the GAMMASPHERE array were again used as a calorimeter. A low energy cut was placed on the fold and sum energy, which corresponded to a four particle exit channel.

The initial 1.4×10^9 events were reduced to 4.7×10^5 following the sorting procedure. The data were then unfolded into constituent double (γ^2) coincidence events and replayed into a RADWARE format matrix. A total of 2.2×10^6 $\gamma-\gamma$ events were incremented, indicating an

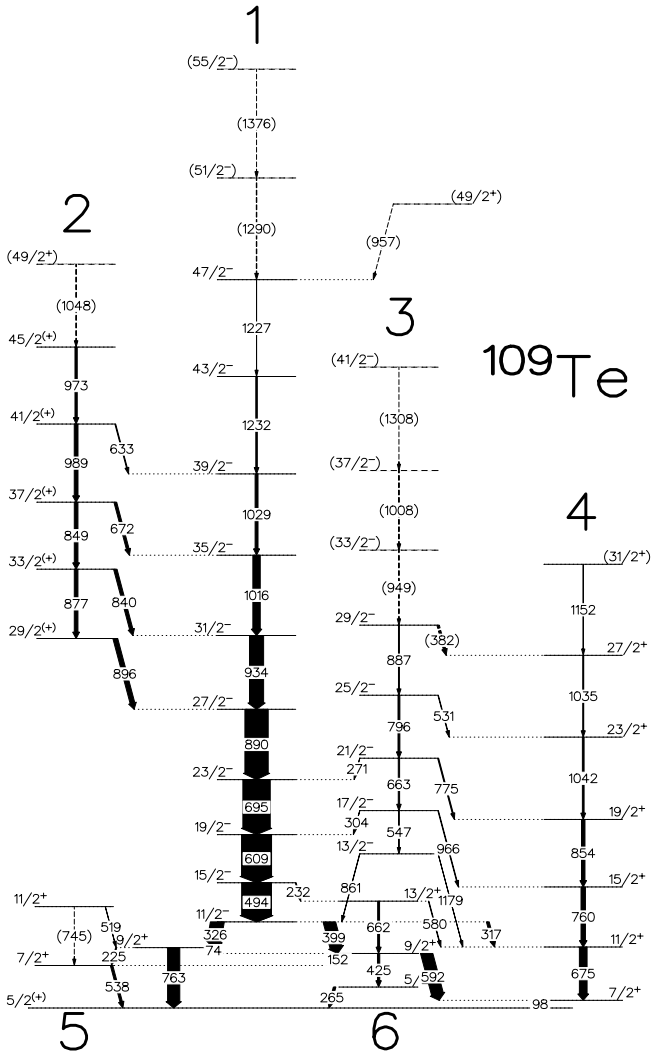

Figure 3.20: The proposed level scheme for ^{109}Te. The transition energies are given in keV and their relative intensities are proportional to the widths of the arrows.

average of ≈5 doubles per event. The data set was also incremented into a γ^3 cube in order to provide an improved selection capability. A total of 2.2×10^5 events were incremented, which in itself is a very low number of statistics to justify the construction of a cube. The data was of sufficient quality however, that the γ^3 cube greatly facilitated the analysis.

The requirement of one neutron detected in coincidence with a γ-ray event was found to significantly reduce the number of statistics obtained. Following the sorting procedure, the exit channel populating ^{109}Te yielded just 2% of the statistics obtained for ^{110}Te, which involved pure charge particle evaporation.

3.13.2 Band structures in ^{109}Te

The level scheme proposed for ^{109}Te from this work is illustrated in Fig. 3.20. Transition energies are given in keV and their relative intensities are proportional to the widths of the arrows. An angular correlation analysis using the method of directional correlation from oriented states (DCO) was used to determine the multipolarity of the majority of transitions in the data. The large error in the angular correlation intensity ratios obtained for the weaker transitions does not allow precise spin assignments for the higher lying states.

The weak population intensity of the ^{109}Te exit channel precluded the successful determination of linear polarisation results for this nucleus, therefore the electromagnetic character of a number of γ-rays was inferred using DCO results from the degree of multipole mixing obtained. The measured transition energies, relative intensities and DCO results together with band and spin assignments concluded from the analysis are summarised in table 3.5.

Inspection of the level scheme proposed for ^{109}Te reveals a structure containing a complicated pattern of many irregularly spaced levels, containing doublet or near doublet γ-ray transitions. Such a level structure is typical of nuclei in close proximity to the Z=50 shell gap. In order to facilitate a discussion of the band structures illustrated in Fig. 3.20, a unique number has been assigned to each band, which will be used throughout the rest of the discussion.

The level scheme presented here significantly extends that proposed in Ref. [dom95]. This work confirms the positioning of γ-ray transitions proposed in Ref. [dom95], however a number of transitions have differing parity.

A selection of coincidence spectra included to demonstrate the quality of the data obtained are illustrated in Fig. 3.21. These spectra illustrate the total ungated projection, of the γ^2 matrix, Fig. 3.21(a). The effect of placing one coincidence requirement (gate) on the 494 keV $15/2^- \rightarrow 11/2^-$ transition in the matrix, Fig. 3.21(b), and a double gating requirement on the 494 and 609 keV transitions in the γ^3 cube Fig. 3.21(c). The later plot shows that there are a sufficient number of counts in the γ^3 cube to enable an enhanced selection capability.

The selection procedure used to isolate ^{109}Te is responsible for the remarkably clean ungated spectrum obtained, Fig. 3.21(a). Transitions in band 1 are particularly strong and have been labelled. It is evident that as the number of coincidence requirements is increased,

there is a significant fall in the number of statistics obtained. However the quality of the observed spectra improves with a reduction in contamination from γ-ray transitions in nearby nuclei, such as ^{108}Sb. ^{108}Sb represents the strongest contaminant observed in this data set. It is produced through α3pn exit channel and is incremented because of mis-identification in the MICROBALL, due to the reduced efficiency for the detection of many charged particles, see sec. 2.14.1.

3.13.3 Bands 1 and 3

The sequence of levels labelled band 1 is built on an $11/2^-$, 1.09 MeV bandhead. It has been extended from $35/2^-$ up to $47/2^-$ with the addition of three new transitions. Band 1 now contains nine proposed stretched E2 transitions following confirmation of their E2 character from the DCO analysis. It also may contain a further two tentative γ-rays extending the structure to $(55/2^-)$ which, due to a lack of statistics, could not be firmly assigned. Band 1 is observed to be yrast up to spin $39/2^-$ and therefore it is clearly visible in the selection of coincidence γ-ray spectra obtained for ^{109}Te, illustrated in Fig. 3.21.

γ-ray sequences 2 and 3 decay into band 1 via a number of stretched dipole transitions. Indeed the newly identified band 3 is proposed to be the signature partner to band 1. Band 3 is built on a $13/2^-$ bandhead at an excitation energy of 1.95 MeV. It contains four proposed stretched E2 transitions extending in spin up to $29/2^-$. Band 3 is linked to band 1 via three weak ΔI=1 transitions. The 861 keV transition is a direct decay from $13/2^- \rightarrow 11/2^-$, the 304 and 271 keV γ-rays are tentatively proposed as up-hill stretched M1 transitions. Five inferred E1 transitions are observed to feed intensity out of band 3 into a structure labelled 4.

3.13.4 Band 2

Band 2 has been extended from $37/2^+$ up to a tentative $(49/2^+)$. The structure is built on a $29/2^+$ bandhead below which all the intensity feeds into band 1. Band 2 is now assigned with positive parity because of the four inferred E1 dipole transitions which link this structure to band 1.

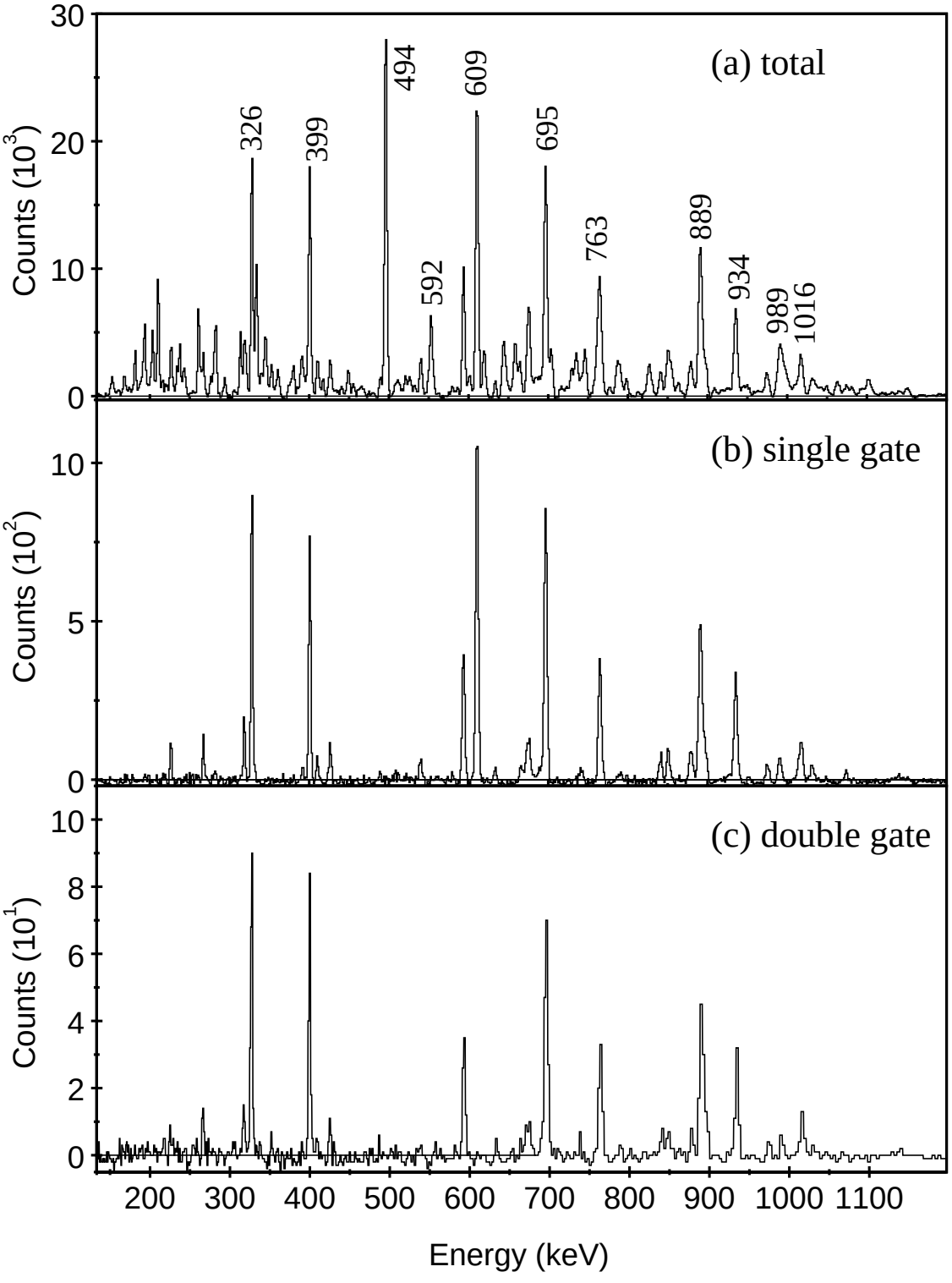

Figure 3.21: Coincidence spectra illustrating the spectrum quality obtained for ^{109}Te. (a) represents an ungated projection of the symmetric 2pαn $\gamma-\gamma$ matrix used for the analysis, a number of ^{109}Te transitions are labelled. (b) the spectrum obtained once a single gate on 494 keV is required. (c) a double gate on 494 and 609 keV projected from a γ^3 2pαn cube.

3.13.5 Band 4

Band 4 has a $7/2^+$ bandhead and decays directly to the ground state of ^{109}Te. The 98 keV transition which carries the intensity of band 4 into the ground state has a confirmed M1 character, firmly establishing the spins and positive parity of band 4. The structure has been extended from $19/2^+$ up to $(31/2^+)$ with the addition of three new proposed stretched E2 transitions. Band 4 is fed by band 3 through a number of ΔI=1 transitions of assumed E1 character.

3.13.6 Bands 5, 6 and other low spin structures

A number of stretched dipole and stretched quadrupole transitions feed intensity from bands 1−4 into the $5/2^+$ ground state of ^{109}Te. The majority of these low spin transitions are relatively intense, allowing their multipolarity to be determined from angular correlation results. Using these results the low spin decay scheme was constructed.

Bands 5 and 6 present themselves naturally out of the large number of γ-ray transitions observed at low spin. Band 5 may represent tentative evidence for a pair of positive parity signature partner bands, based on $5/2^+$ and $7/2^+$ bandheads. Band 6 is a positive parity structure which consists of two stretched E2 transitions. It is based on a $5/2^+$ bandhead, linked to the ground state of ^{109}Te by a proposed non-stretched magnetic dipole (M1) transition of 265 keV.

Several weak transitions were observed in coincidence with band 1. These transitions could not be unambiguously placed in the level scheme, the appropriate levels are shown dashed in Fig. 3.20.

E_γ (keV)[1]	I_γ (%)[2]	R_{DCO}[3]	Multipolarity	Assignment	Band
98.4	8.1	0.90(10)	M1/E2	$7/2^+ \rightarrow 5/2^+$	4→6
152	<1%	–	(M1/E2)	$9/2^+ \rightarrow 7/2^+$	6→5
225.3	13.1	0.75(4)	M1/E2	$9/2^+ \rightarrow 7/2^+$	5
265.5	11.0	0.71(6)	M1/E2	$5/2^+ \rightarrow 5/2^+$	6
271	<1%	–	(M1/E2)	$21/2^- \rightarrow 23/2^-$	3→1
304	<1%	–	(M1/E2)	$17/2^- \rightarrow 19/2^-$	3→1
317.2	16.8	1.02(8)	E1	$11/2^- \rightarrow 11/2^+$	1→4
326.5	56.7	0.61(3)	E1	$11/2^- \rightarrow 9/2^+$	1→5
382	<1%	–	(E1)	$29/2^- \rightarrow 27/2^+$	3→4
399.2	61.0	0.64(3)	E1	$11/2^- \rightarrow 9/2^+$	1→6
424.8	9.8	0.97(5)	E2	$9/2^+ \rightarrow 5/2^+$	6
494.5	=100.0	1.10(4)	E2	$15/2^- \rightarrow 11/2^-$	1
530.7	3.3	–	(E1)	$25/2^- \rightarrow 23/2^+$	3→4
538.5	10.7	0.80(6)	M1/E2	$7/2^+ \rightarrow 5/2^+$	5
547	<1%	–	(E2)	$17/2^- \rightarrow 13/2^-$	3
580	<1%	–	(M1/E2)	$13/2^+ \rightarrow 11/2^+$	6→4
592.1	33.5	0.69(3)	M1/E2	$9/2^+ \rightarrow 7/2^+$	6
609.1	89.5	1.02(3)	E2	$19/2^- \rightarrow 15/2^-$	1
632.6	3.3	0.58(8)	E1	$41/2^+ \rightarrow 39/2^-$	2→1
661.3	4.4	0.98(8)	E2	$13/2^+ \rightarrow 9/2^+$	6
663.3	7.2	1.03(7)	E2	$21/2^- \rightarrow 17/2^-$	3
672.2	4.4	0.88(7)[4]	E1	$37/2^+ \rightarrow 35/2^+$	2→1
674.8	27.0	0.88(7)[4]	E2	$11/2^+ \rightarrow 7/2^+$	4
695.2	80.1	1.00(3)	E2	$23/2^- \rightarrow 19/2^-$	1
760.3	18.3	0.88(3)[4]	E2	$15/2^+ \rightarrow 11/2^+$	4
763.2	43.7	0.88(3)[4]	E2	$9/2^+ \rightarrow 5/2^+$	5
775.3	2.7	–	(E1)	$21/2^- \rightarrow 19/2^+$	3→4

Table 3.5: Detailed summary of the experimental results for ^{109}Te.

E_γ (keV)[1]	I_γ (%)[2]	R_{DCO}[3]	Multipolarity	Assignment	Band
796.2	5.2	–	(E2)	$25/2^- \rightarrow 21/2^-$	3
839.6	8.6	0.80(7)	E1	$33/2^+ \rightarrow 31/2^-$	2→1
848.8	20.2	0.90(7)	E2	$37/2^+ \rightarrow 33/2^+$	2
853.8	12.1	0.94(9)	E2	$19/2^+ \rightarrow 15/2^+$	4
861	<1%	–	(M1/E2)	$13/2^- \rightarrow 11/2^-$	3→1
877.4	14.5	0.89(6)	E2	$33/2^+ \rightarrow 29/2^+$	2
886.7	3.0	–	(E2)	$29/2^- \rightarrow 25/2^-$	3
889.6	62.7	1.01(5)	E2	$27/2^- \rightarrow 23/2^-$	1
895.7	14.7	0.62(8)	E1	$29/2^+ \rightarrow 27/2^-$	2→1
933.7	34.3	1.01(4)	E2	$31/2^- \rightarrow 27/2^-$	1
949	<1%	–	(E2)	$33/2^- \rightarrow 29/2^-$	3
966	<1%	–	(E1)	$17/2^- \rightarrow 15/2^+$	3→4
973.4	9.3	0.93(6)	E2	$45/2^+ \rightarrow 41/2^+$	2
989.4	30.6	0.93(6)	E2	$41/2^+ \rightarrow 37/2^+$	2
1008	<1%	–	(E2)	$37/2^- \rightarrow 33/2^-$	3
1015.8	18.0	0.96(5)	E2	$35/2^- \rightarrow 31/2^-$	1
1029.2	7.8	1.19(13)	E2	$39/2^- \rightarrow 35/2^-$	1
1035.3	4.9	–	(E2)	$27/2^+ \rightarrow 23/2^+$	4
1042.1	10.1	0.98(6)	E2	$23/2^+ \rightarrow 19/2^+$	4
1151.6	1.1	–	(E2)	$31/2^+ \rightarrow 27/2^+$	4
1179	<1%	–	(E1)	$13/2^- \rightarrow 11/2^+$	3→4
1227.0	3.6	1.20(9)[4]	E2	$47/2^- \rightarrow 43/2^-$	1
1232.2	4.1	1.20(9)[4]	E2	$43/2^- \rightarrow 39/2^-$	1

[1] Energies are estimated to be accurate to ±0.3 keV for strong transitions (>10%) rising to ±0.6 keV for weaker transitions. Energies quoted as integers are estimated to be ±1 keV.

[2] Errors on relative intensities are typically ≤5%.

[3] DCO ratios were obtained from the sum of gates on the 495 and 609 keV quadrupole transitions unless otherwise indicated.

[4] DCO ratio obtained from composite peak.

Chapter 4

Discussion

Introduction

A numerous variety of nuclear structure phenomena are associated with nuclei in close proximity to the Z=50 closed shell. Even-even tellurium isotopes manifest behaviour typical of vibrational structures at low spin, here multi-phonon excitations describe the observed band structures. At higher spins however, certain two quasiparticle configurations coupled to the underlying vibrational structure become yrast. Specific non-collective oblate states composed of aligned single particle angular momentum are observed in this regime, where such a structure is energetically favourable. At high spin, particle-hole excitations across the Z=50 shell gap have been observed to stabilise deformed collective structures. These structures extend up to the highest values of angular momentum available for their specific configurations.

The tellurium isotopes have their neutron and proton Fermi surfaces located in the main 50-82 shell, consequently inspection of a relevant single-particle Nilsson diagram illustrates N=4 orbitals $s_{1/2}$, $d_{3/2}$, $d_{5/2}$ and $g_{7/2}$ with positive parity and the N=5 negative parity intruder orbital $h_{11/2}$ will play an important role in explaining any observed band structures.

This chapter attempts to explain the rich variety of nuclear structure phenomena observed within the single and quasiparticle Nilsson formalism. Theoretical calculations which use a configuration-dependent shell-correction approach with a cranked Nilsson potential without pairing [afa95] have been used to provide additional interpretation for the collective high spin structures in ^{110}Te observed for the first time in this work.

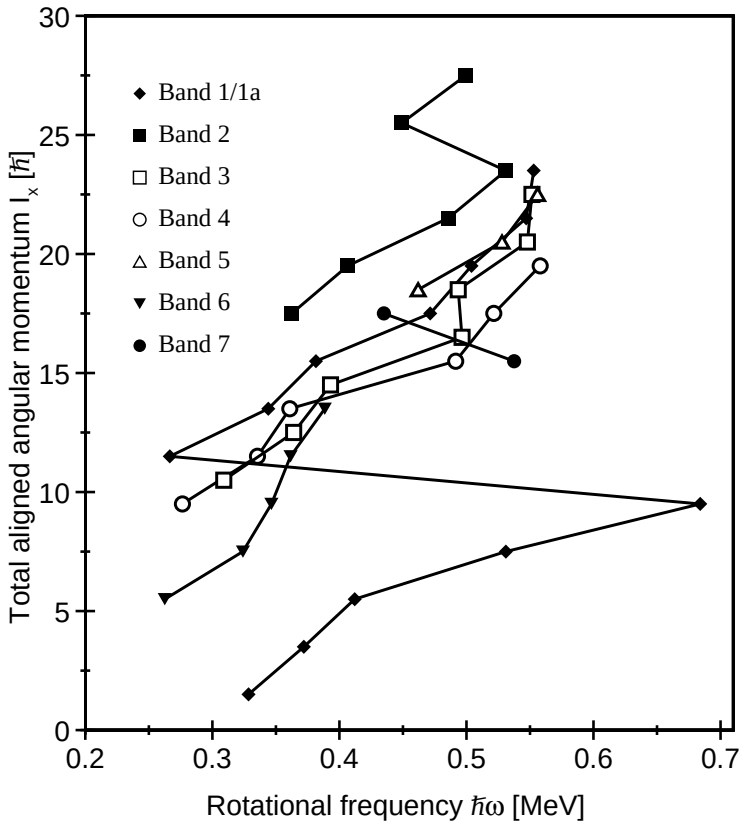

Figure 4.1: Total aligned angular momentum plot for the low spin band members in ^{110}Te. Positive parity states are labelled with filled symbols.

Throughout this discussion experimental and theoretical configurations are labelled using the $[p_1 p_2, n]$ nomenclature where the number of particles relative to the Z=N=50 doubly closed shell are considered such that, p_1 represents the number of $\pi g_{9/2}$ holes, p_2 represents the number of $\pi h_{11/2}$ particles and n represents the number of $\nu h_{11/2}$ particles [afa95].

4.1 Low spin band structures in ^{110}Te

4.1.1 Experimental alignment plots

The rotational behaviour of ^{110}Te has been investigated by observing the total aligned angular momentum along the rotation axis, which can be expressed as,

$$I_x = \sqrt{(I + 1/2)^2 - K^2}. \tag{4.1}$$

Where I is the angular momentum (spin) and K is the projection of the total angular momentum onto the symmetry axis. By plotting I_x as a function of rotational frequency,

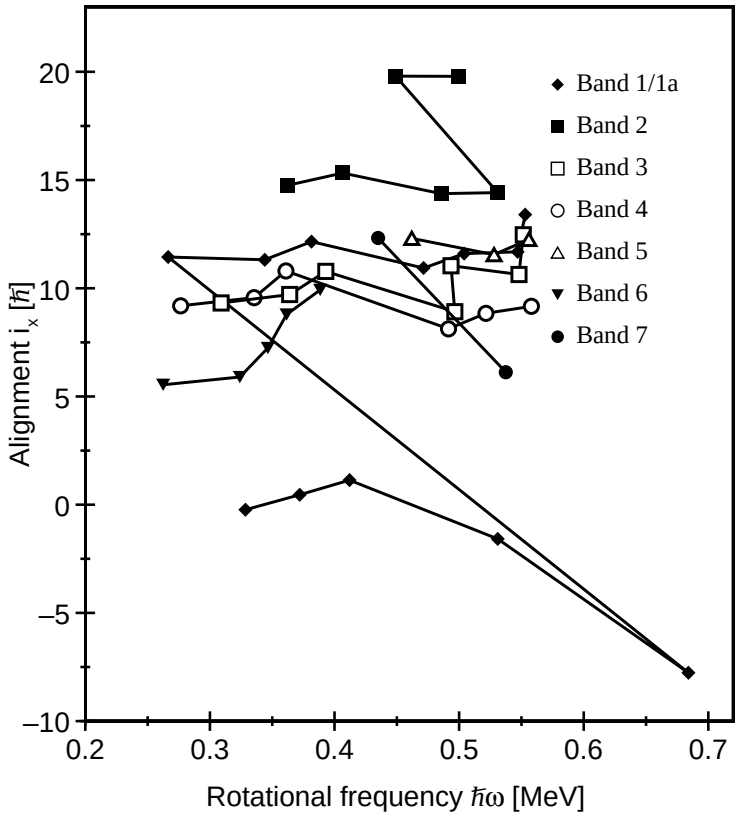

Figure 4.2: Alignment plot for the low spin band members in ^{110}Te. Positive parity states are labelled with filled symbols.

the plot shown in Fig. 4.1 was produced. The rotational frequency can be defined by $\hbar\omega = dE/dI_x$ which approximates to $\hbar\omega \approx E_\gamma/2$ for stretched quadrupole transitions.

Fig. 4.1 indicates that a number of quasiparticle alignments are taking place. In order to investigate further the differences between the various configurations it is useful to introduce the relative quantities e' and i_x, the experimental routhian and alignment respectively. In order to obtain these quantities it is necessary to transform the experimental data into the intrinsic frame of the nucleus. This requires the subtraction of a core contribution, leaving the single particle energy and spin contributions solely from the valence nucleons. The experimental alignment can be written,

$$i_x(\omega) = I_x(\omega) - I_{x,ref}(\omega). \tag{4.2}$$

The reference $I_{x,ref}(\omega)$ is generally obtained from the ground state band of a rotational even-even nucleus. The assumption at low spin that the nuclear moment of inertia is proportional to the square of the rotational frequency is used to define an energy reference

based on a variable moment of inertia,

$$\mathcal{J}^{(1)}_{ref} = \mathcal{J}_0 + \mathcal{J}_1\omega^2. \tag{4.3}$$

$\mathcal{J}_0$ and $\mathcal{J}_1$ are Harris parameters which are obtained by a fit to the reference band.

The nucleus ^{110}Te has a vibrational ground state band structure which prevents the extraction of good Harris parameters, therefore a reasonable fit has been made to transitions in band 3 above the neutron alignment. The rotational reference, $I_{x,ref}$ is hence defined by,

$$I_{x,ref}(\omega) = \omega(\mathcal{J}_0 + \mathcal{J}_1\omega^2) - i_0. \tag{4.4}$$

The Harris parameters $\mathcal{J}_0$=18.6$\hbar^2$MeV^{-1} and $\mathcal{J}_0$=31.3$\hbar^2$MeV have hence been extracted together with i_0=5$\hbar$. These values provide a reasonable reference over the whole frequency range. The resulting alignment plot for low spin band members in ^{110}Te is shown in Fig. 4.2. The behaviour of the $I_x - \omega$ plot for these low spin structures shows that ^{110}Te is not a good rotor.

The experimental routhian can simply be expressed as,

$$e'(I) = E^{\omega}_{expt}(I) - E^{\omega}_{ref}(I). \tag{4.5}$$

A routhian represents energy levels in the rotating frame. It is a useful quantity to plot because it provides precise information about crossing frequencies, enabling the configuration of a structure to be more readily determined from comparison with theoretical cranked shell model calculations. A plot showing the routhian e' as a function of rotational frequency $\hbar\omega$ for band 1/1a is illustrated in Fig. 4.6 which can be found in sec. 4.2.1.

4.1.2 Low spin rigid-rotor plot

In order to provide further information about the structure of a specific configuration it is useful to plot the excitation energy ($E(I)$) of band members minus a rigid rotor (core) reference ($E_{rig}(I)$), such a plot is referred to as a rigid-rotor plot. This is achieved using the relation,

$$E_{rig}(I) = \frac{\hbar^2}{2\mathcal{J}_{(rig)}} I(I+1) \tag{4.6}$$

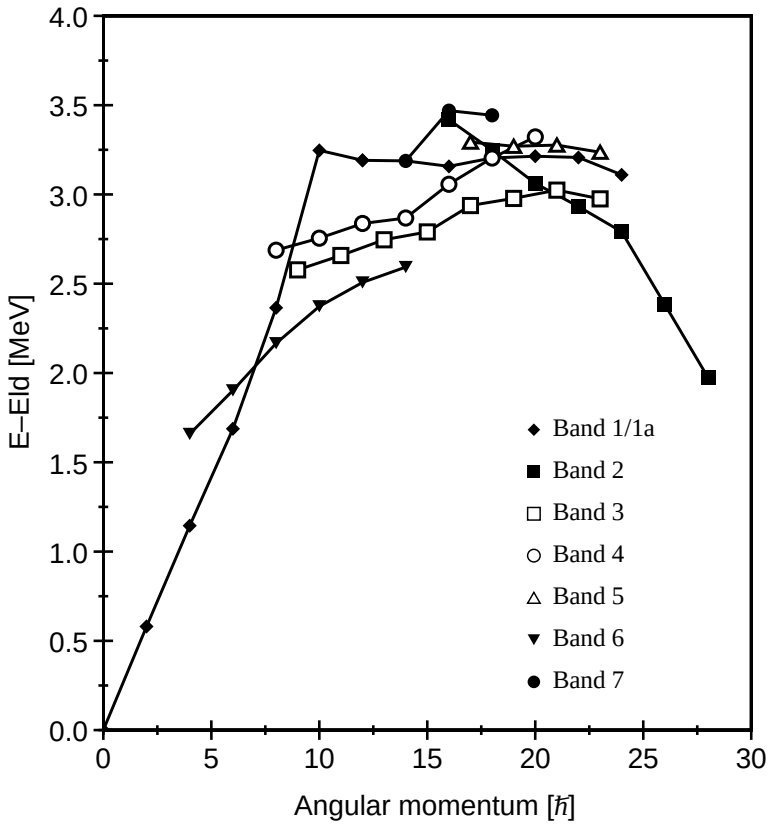

Figure 4.3: A rigid rotor plot showing the low spin band members in ^{110}Te. Positive parity states are labelled with filled symbols.

Where $J_{(rig)}$, the rigid body moment of inertia, is expressed by convention relative to ^{158}Er calculated at ε_2 =0.20 [sim94] such that,

$$\frac{\hbar^2}{2\mathcal{J}_{(rig)}} = 0.007 \left[\frac{158}{A}\right]^{5/3}. \tag{4.7}$$

A rigid-rotor plot for low spin band members in ^{110}Te is shown in Fig. 4.3.

4.1.3 Cranked shell model calculations

Shell model calculations using a cranked Nilsson potential have been performed for ^{110}Te, in order to provide further theoretical interpretation for the low/medium spin regime. The calculations were performed for both protons and neutrons using a set of input parameters derived from deformation self-consistent cranking calculations, based on the total routhian surface (TRS) formalism [naz87, wys88, naz89]. The TRS calculation for the vacuum configuration, which describes the ground state band in ^{110}Te, produced invaluable information

Rotational Frequency	Deformation	Deformation	Q_0	Trixiality
[MeV/$\hbar$]	[β_2]	[ε_2]	[eb]	[γ]
0.000	0.149	0.135	2.00	–0.04°
0.065	0.146	0.132	1.95	–0.2°
0.129	0.141	0.127	1.88	–0.2°
0.194	0.146	0.132	1.95	–1.3°
0.259	0.148	0.134	1.98	–0.9°
0.324	0.152	0.137	2.04	0.9°
0.388	0.169	0.151	2.27	3.1°
0.453	0.173	0.154	2.32	6.6°
0.518	0.171	0.153	2.30	7.0°
0.582	0.167	0.150	2.24	9.3°

Table 4.1: Theoretical values of the Woods-Saxon quadrupole deformation parameter β_2, the Nilsson quadrupole deformation parameter ε_2, the associated quadrupole moment and the triaxiality γ presented as a function of rotational frequency. β_2 and γ values were extracted from TRS calculations performed for the vacuum configuration in ^{110}Te.

about the deformation and triaxiality of ^{110}Te as a function of rotational frequency. These results are summarised in table 4.1. Note that the TRS calculations are based on a Woods-Saxon potential where the nuclear shape is characterised by the β_λ deformation parameters. In contrast, the cranked Nilsson calculations use the ε_λ parameterisation. For small deformations $\varepsilon_2 \approx 0.95\beta_2$, and these inferred values together with an associated value of the quadrupole moment (Q_0) are also shown in table 4.1. For further details see sec.1.2 or Ref. [lob70, ben89].

The results show that ^{110}Te has a small but finite deformation at low spin which gradually increases as a function of rotational frequency. The triaxiality parameter is close to zero at low spin, becoming finite and positive for higher values of rotational frequency. For the purpose of the cranked shell model calculations ^{110}Te can therefore be described as having a weakly prolate energy minimum with deformation parameters ε_2 ~0.135 and γ ~-0.04°. The pairing gap obtained from the TRS calculations was Δ_p=1.030MeV for protons and Δ_n=1.420MeV for neutrons.

Protons				Neutrons			
Shell model	Nilsson orbital	(π, α)	Label	Shell model	Nilsson orbital	(π, α)	Label
$g_{7/2}$	$[422]3/2^+$	$(+, +1/2)$	A	$g_{7/2}$	$[413]5/2^+$	$(+, +1/2)$	a
$g_{7/2}$	$[422]3/2^+$	$(+, -1/2)$	B	$g_{7/2}$	$[413]5/2^+$	$(+, -1/2)$	b
$d_{5/2}$	$[420]1/2^+$	$(+, +1/2)$	C	$d_{5/2}$	$[411]3/2^+$	$(+, +1/2)$	c
$d_{5/2}$	$[420]1/2^+$	$(+, -1/2)$	D	$d_{5/2}$	$[411]3/2^+$	$(+, -1/2)$	d
$h_{11/2}$	$[550]1/2^-$	$(-, -1/2)$	E	$h_{11/2}$	$[550]1/2^-$	$(-, -1/2)$	e
$h_{11/2}$	$[550]1/2^-$	$(-, +1/2)$	F	$h_{11/2}$	$[550]1/2^-$	$(-, +1/2)$	f
$h_{11/2}$	$[541]1/2^-$	$(-, -1/2)$	G	$h_{11/2}$	$[541]1/2^-$	$(-, -1/2)$	g
$h_{11/2}$	$[541]1/2^-$	$(-, +1/2)$	H	$h_{11/2}$	$[541]1/2^-$	$(-, +1/2)$	h

Table 4.2: Labelling of the quasiparticle levels adopted in this work.

The chosen input parameters produced the quasiparticle plots shown in Fig. 4.4(a)(b). These plots are drawn relative to the proton or neutron Fermi surface and therefore provide excellent insight into which orbitals are aligning and at what frequency such an alignment may occur. Such knowledge greatly aids the assignment of a configuration for an experimentally observed band structure.

In Fig. 4.4(a) and Fig. 4.4(b) frequencies at which alignments take place are labelled by the aligning orbitals. The notation that is adopted represents the lowest energy proton (neutron) orbitals of positive-parity as A, B, C... (a, b, c...) and the corresponding negative-parity proton (neutron) orbitals as E, F, G... (e, f, g...). The parity and signature (π, α) of the levels are: $(+,+1/2)$ - solid lines; $(+,-1/2)$ - dotted lines; $(-,-1/2)$ - dashed lines; $(-,+1/2)$ - dot dashed lines. The labelling of the quasiparticle orbitals is clarified in table 4.2.

Brief inspection of the quasiparticle diagrams reveals that for the vacuum configuration neutrons will be the first particles to align. The theory predicts the first neutron alignment will occur at $\omega_{ef} = 0.44$ MeV/$\hbar$. The first proton alignment is predicted to occur at $\omega_{AB} = 0.54$MeV/$\hbar$.

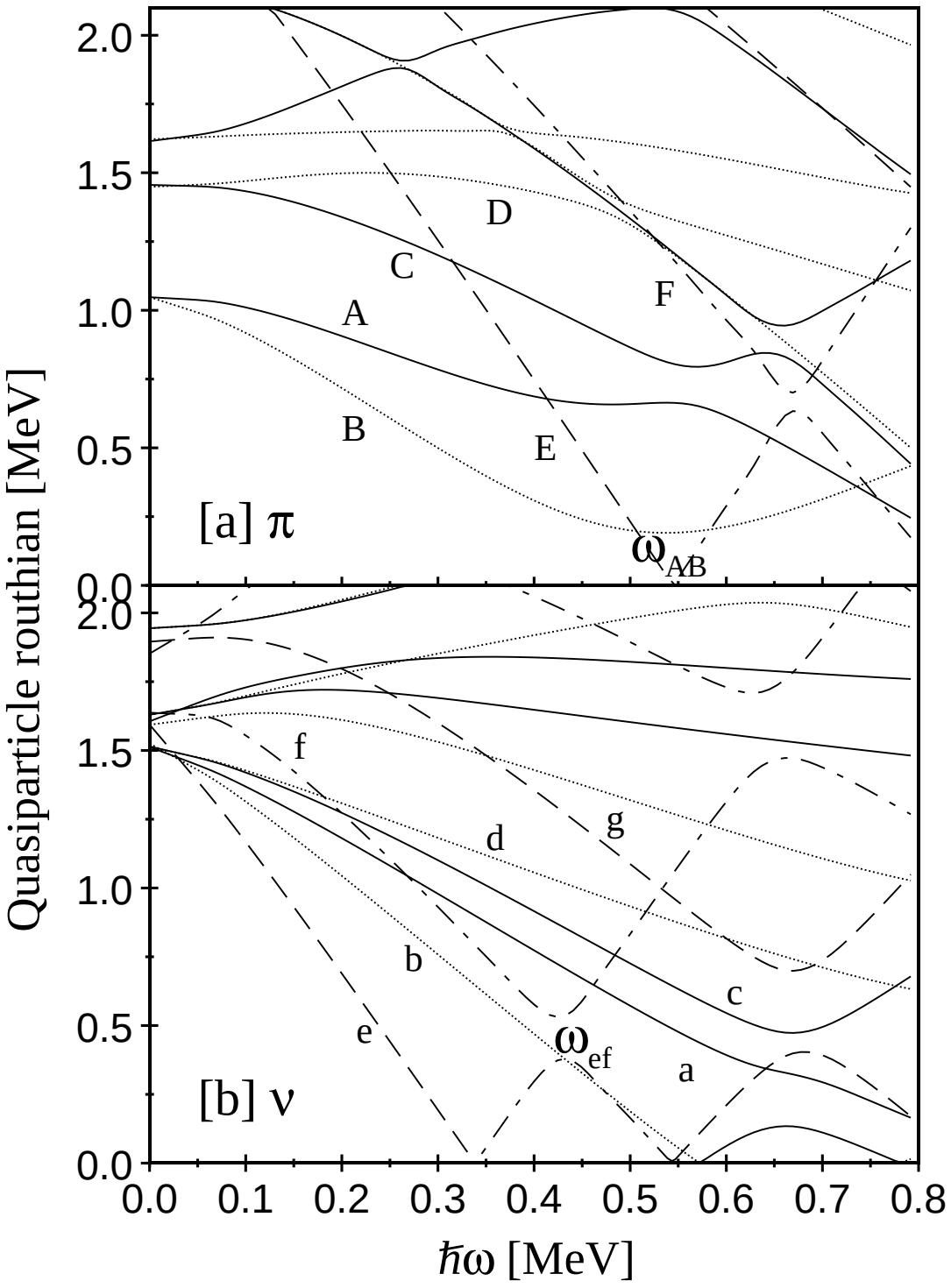

Figure 4.4: Cranked shell model calculations for ^{110}Te. [a] for protons [b] for neutrons. The calculations use the Nilsson potential with deformation parameters ε_2=0.135, ε_4=-0.04 and γ=-0.2°. The pairing gap used was Δ_p =1.030 MeV and Δ_n =1.420 MeV.

4.2 Low spin positive-parity states in ^{110}Te

4.2.1 Band 1

The proximity of the neutron deficient tellurium isotopes to the $Z = N = 50$ doubly closed shell has the consequence that the sufficient number of valence particles outside of the closed core required to induce low-spin collectivity are not available. Tellurium isotopes are therefore expected to have a small quadrupole ground state deformation ($\varepsilon_2 \sim 0.135$) and hence a low-spin decay scheme dominated by single-particle effects.

In common with other even tellurium isotopes, band 1, the ground-state band in ^{110}Te is vibrational rather than rotational in character. The $E(4^+)/E(2^+)$ energy ratio (2.13) in ^{110}Te is much closer to the pure vibrational limit (2.00) than the rotational limit (3.33). Fig. 4.5 shows the $E(4^+)/E(2^+)$ energy ratio systematics for even tellurium isotopes between ^{108}Te and ^{124}Te, the vibrational nature of these isotopes is clearly illustrated by the close proximity of the $E(4^+)/E(2^+)$ energy ratio to two. The excitation energy of the 2^+ state is observed to be at a minimum for ^{120}Te, near the middle of the neutron N=50−82 shell.

The low-lying states with $I^\pi \leq 8^+$ in the even tellurium isotopes have been interpreted in terms of phonon states where $\pi[g_{7/2}]^2$ or $\pi[g_{7/2} \otimes d_{5/2}]$ proton configurations are coupled to the spherical (Z=50) tin core states [lon86, cho82]. Indeed in ^{110}Te several positive-parity states are observed at low spin, shown to the left and the right of band 1. These structures consist of even-spin and odd-spin members connected by both quadrupole and dipole transitions, characteristic of such structures.

The band illustrated to the left of band 1 in Fig. 3.11 is an interesting case. Prior to this work this structure was assigned with odd spin with a 3^+ bandhead feeding the 2^+ yrast state by a stretched M1 transition. The presence of a low lying 3^+ level can be interpreted as a three-phonon harmonic vibrator 3^+ state. This state should however appear at an energy equal to that of the yrast 6^+ state contrary to experimental observations. A low lying 3^+ state would however be observed if ^{110}Te was a triaxial rotor, a difficult interpretation given the accepted vibrational nature of the tellurium isotopes. The current analysis reassigns the bandhead as 2^+, the state is now interpreted as part of a two-phonon multiplet. Such a state would have an excitation energy similar in energy to that of the 4^+ state and would consistent with the expected vibrational interpretation.

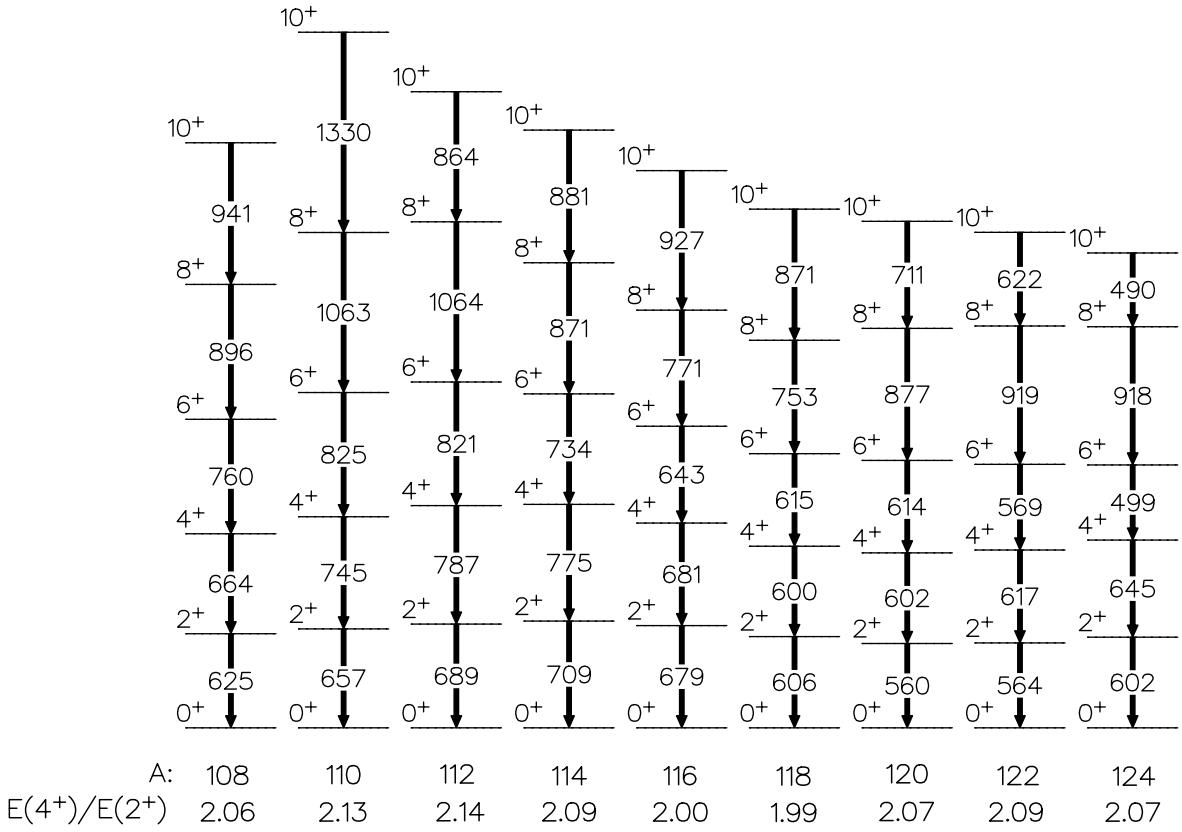

Figure 4.5: Even tellurium systematics. The close proximity of the $E(4^+)/E(2^+)$ energy ratio to two illustrates the vibrational nature of the tellurium isotopes.

4.2.2 Band 1a

Above spin 8^+, a sharp drop in intensity is observed in band 1 coinciding with the structure becoming non-yrast, a feature illustrated in the low spin rigid-rotor plot of Fig. 4.3 where negative parity band 3 is observed to become yrast at spin 9^-. Inspection of the low-spin alignment plot illustrated in Fig. 4.2, reveals that a sharp backbend is observed indicating that a particle alignment has taken place. The non-yrast positive parity structure labelled band 1a continues above the backbend.

In common with other even tellurium isotopes the positive parity states above 10^+ can be interpreted in terms of an aligned $\nu[h_{11/2}]^2$ configuration. These low-Ω $h_{11/2}$ orbitals close to the Fermi surface will be among the first to align. Confirmation of this interpretation is

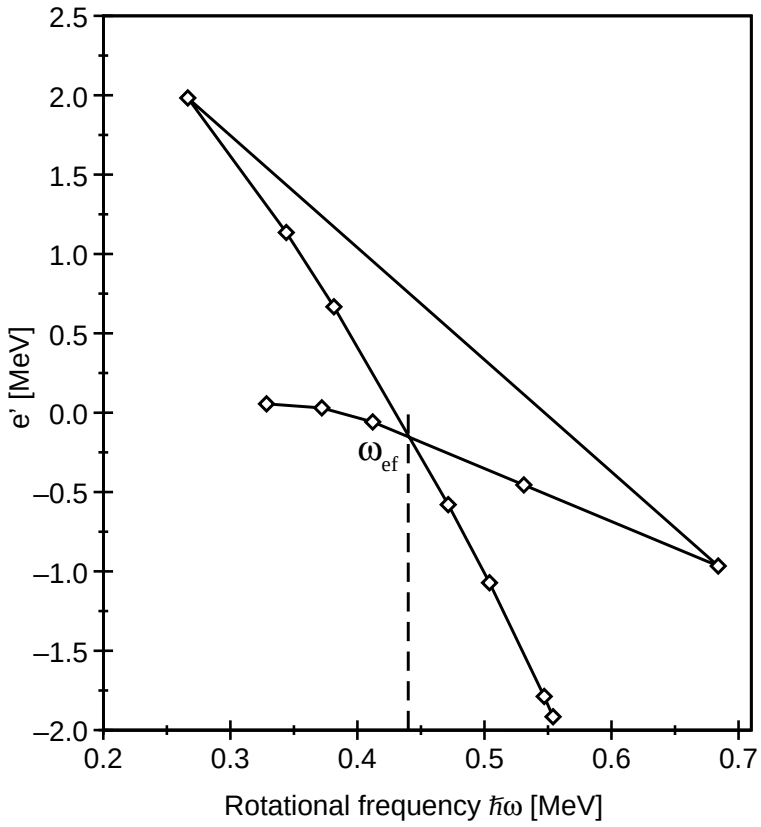

Figure 4.6: Experimental routhian plot for ^{110}Te band 1/1a. The plot shows the frequency (ω_{ef}=0.44 MeV/$\hbar$) at which a pair of $h_{11/2}$ quasineutrons align.

afforded with reference to Fig. 4.2, the low spin alignment plot, which reveals band 1 gains 10$\hbar$ in alignment before continuing as positive parity band 1a. This increase is consistent with that expected for a $\nu[h_{11/2}]^2$ alignment.

Precise determination of the experimental crossing frequency for the alignment in bands 1/1a was possible through the construction of an experimental routhian plot. The plot shown in Fig. 4.6 indicates a crossing frequency of ω_c=0.44 MeV/$\hbar$. Comparison with the cranked shell model calculations discussed in sec.4.1.3 shows that a pair of $h_{11/2}$ quasineutrons are predicted to align at ω_{ef}=0.44 MeV/$\hbar$. This confirms the accepted interpretation, in which band 1a may be characterised as a weakly deformed prolate rotor, is applicable for ^{110}Te.

In other even tellurium isotopes the positive parity $\nu[h_{11/2}]^2$ configuration is observed yrast up to high spin. However this is not observed in ^{110}Te where the positive parity band structure is observed non-yrast. Here the neutron Fermi surface (N=58) lies below

the $\nu h_{11/2}$ subshell. This makes the $\nu[h_{11/2}]^2$ configuration less energetically favourable allowing negative parity structures to compete.

The low spin rigid-rotor plot, Fig. 4.3, shows positive parity band 1a, is well above yrast until spin$\sim 20^+$. This explains the weak population of this configuration above the alignment at ω_{ef}=0.44 MeV/$\hbar$, 10^+ and why it has only been established from this new data set. Band 1a is observed to behave as an almost perfect rigid-rotor up to 24^+, above which the observed intensity of the structure is greatly reduced.

4.2.3 Band 2

The structure of band 2 is discussed within the scenario of octupole collectivity in sec.4.4.

4.2.4 Band 6

Band 6 is a positive parity structure with a 4^+ bandhead extending in spin above the $\nu[h_{11/2}]^2$ alignment with decreasing intensity up to a tentative (16^+). The alignment plot illustrated in Fig. 4.2 implies band 6 is rotational in nature with the γ-ray energies increasing smoothly with spin. This structure can be tentatively interpreted in terms of a deformed 4-particle 2-hole [22,2] structure (discussed in sec. 4.6.1) involving a $\pi[(g_{9/2})^{-2}(h_{11/2})^2] \otimes \nu[(h_{11/2})^2]$ configuration. This provides possible evidence for shape coexistence at low spin in ^{110}Te. Inspection of a rigid-rotor plot, Fig. 4.3, for band 6, shows it yrast above spin 8^+. The intensity observed in the structure is however not consistent with this interpretation, further supporting the shape coexistence argument.

4.3 Low spin negative-parity states in ^{110}Te

4.3.1 Bands 3 and 4

Negative parity bands 3 and 4 are populated with significant intensity in ^{110}Te, in marked contrast to other even tellurium isotopes. This observation is explained because the position of the neutron Fermi surface makes the $\nu[h_{11/2}]^2$ configuration less energetically favourable allowing these negative parity structures to compete. ^{110}Te provides a unique opportunity to investigate these negative parity structures since their population intensity has allowed

a detailed spectroscopic study of the bands, which included the observation of a number of interlinking magnetic dipole transitions.

Band 3 which is negative parity and odd signature (−,1) is yrast at moderate spin. Inspection of the low spin rigid rotor plot for ^{110}Te (Fig. 4.3) illustrates clearly that band 3 is favoured energetically over band 4 throughout and is therefore the favoured signature for this particular configuration. The experimental alignment plot, Fig. 4.2, shows bands 3 and 4 have similar alignment, which is typical of signature partner bands. Both structures show an initial alignment less than that of the $\nu[h_{11/2}]^2$ configuration. This implies a two quasineutron configuration involving one $h_{11/2}$ neutron coupled to a positive parity orbital, which gives the negative parity for this structure.

Below the 9^- bandhead of band 3, a low-lying 7^- state is observed which decays back to the yrast low spin structure via a 1281 keV E1 transition. Such low lying states have been observed in a number of even tellurium nuclei (^{112}Te−^{132}Te) and they have been explained in terms of a low-lying two quasiparticle state. This involves the $h_{11/2}$ orbital in a two quasineutron $\nu[h_{11/2} \otimes d_{5/2}]_{7-}$ configuration, which explains the confirmed negative parity of the state. It might therefore be expected that bands 3 and 4 are built on a $\nu[h_{11/2} \otimes d_{5/2}]$ configuration. Indeed inspection of a relevant single particle diagram, similar to that shown in Fig. 1.4 but calculated for neutrons, implies this configuration is probable.

In this mass region the $d_{5/2}[411]3/2^+$ and $g_{7/2}[413]5/2^+$ Nilsson orbitals are almost degenerate. The cranked shell model (CSM) quasineutron diagram calculated for ^{110}Te and illustrated in Fig. 4.4(b) shows clearly how close the $d_{5/2}$ and $g_{7/2}$ orbitals are at low spin. The most energetically favoured orbital from the CSM calculations is the $g_{7/2}$ orbital, for which the positive parity negative signature level is lowest in energy, which agrees with what is observed experimentally.

Further experimental evidence to clarify the configuration of these structures was collated. The ratios of the reduced transition probabilities, $B(M1; I \rightarrow I-1)/B(E2; I \rightarrow I-2)$ can be extracted by measuring the intensity ratios of competing $\Delta I = 1$ and $\Delta I = 2$ transitions. The M1/E2 intensity ratios were measured by placing a double coincidence requirement on the two transitions lying above each state of interest, in order to ensure good quality spectra were obtained. The ratios of the reduced transition probabilities were

E_γ	I^π	Band	R_{DCO}	B(M1)/B(E2)	B(M1)	B(M1)	$\lvert g_K - g_R \rvert$
(keV)	Initial			$([\mu_N/eb]^2)$	(μ_N^2)	(W.u.)	
123	9^-	3	0.33(4)	–	–	–	–
431[1]	10^-	4	0.75(1)	0.05(1)	0.006(1)	0.003(0.5)	0.12(1)
186	11^-	3	–	0.17(5)	0.021(6)	0.012(4)	0.22(4)
484	12^-	4	0.16(1)	0.12(3)	0.015(3)	0.009(2)	0.19(2)
243	13^-	3	0.47(2)	0.19(8)	0.025(8)	0.014(4)	0.24(3)
479	14^-	4	0.33(4)	0.20(4)	0.027(5)	0.015(3)	0.24(3)
307	15^-	3	0.56(2)	0.11(4)	0.015(4)	0.008(3)	0.18(3)
318	17^-	3	0.74(4)	0.15(2)	0.020(3)	0.011(1)	0.21(1)

Table 4.3: Measured magnetic dipole strengths in ^{110}Te coupled bands 3 and 4 assuming $Q_0 = 200\text{efm}^2$ for $\varepsilon_2 = 0.135$. [1] 431 keV is a self-coincident doublet.

then determined as,

$$\frac{B(M1; I \to I-1)}{B(E2; I \to I-2)} = \frac{1}{1.43 \times 10^4} \frac{1}{\lambda_{E2/M1}} \frac{[E_\gamma(E2; I \to I-2)]^5}{[E_\gamma(M1; I \to I-1)]^3} (\mu_\text{N}^2 \text{e}^{-2}.\text{fm}^{-4}) \qquad (4.8)$$

where the ΔI=1 transitions were assumed to have no E2 admixture. B(M1) values were extracted using a quadrupole moment of Q_0=200efm^2 to obtain the B(E2) rate from the rotational model, eqn.1.53 [Boh75]. This Q_0 value was chosen based on the predicted low spin quadrupole deformation of $\varepsilon_2 \sim 0.135$ for the light tellurium isotopes, a value obtained from cranking calculations using the total routhian surface (TRS) formalism [wys88]. An estimate of $|g_K - g_R|$ was obtained from the equation,

$$B(M1) = \frac{3}{4\pi} [g_K - g_R]^2 K^2 |\langle IK10 | I-1K \rangle|^2 \mu_N^2. \qquad (4.9)$$

B(M1)/(E2) values together with the DCO ratio results obtained for the dipole transitions are summarised in table 4.3.

The B(M1)/B(E2) results can be used to assign single-particle configurations, therefore the observation of dipole transitions has aided the assignment of this structure. A plot of the experimental B(M1)/B(E2) values against spin is shown in Fig. 4.7(a). The plot also shows theoretical configurations calculated using the Dönau and Frauendorf semi-classical formalism [don87, fra81]. The theoretical plots illustrated are for the $\nu[[413]5/2^+ \otimes [550]1/2^-]$

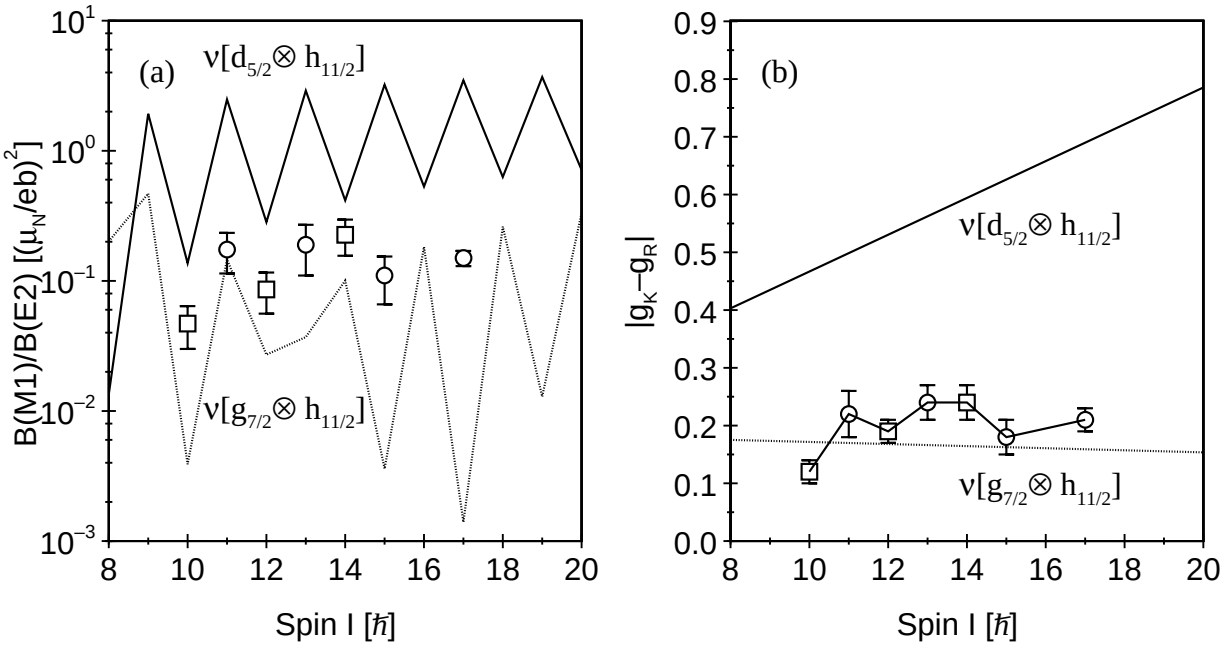

Figure 4.7: Experimental and theoretical (a) B(M1)/B(E2) ratios of reduced transition probabilities. (b) $|g_K - g_R|$ values, assuming Q_0 =200efm^2. (a)(b) Band 3 is labelled with square symbols, band 4 with circles. Calculations are for the $\nu[[413]5/2^+ \otimes [550]1/2^-]$ ($\nu[g_{7/2} \otimes h_{11/2}]$) and $\nu[[411]3/2^+ \otimes [550]1/2^-]$ ($[d_{5/2} \otimes h_{11/2}]$) two-quasiparticle configurations.

($\nu[g_{7/2} \otimes h_{11/2}]$) and $\nu[[411]3/2^+ \otimes [550]1/2^-]$ ($[d_{5/2} \otimes h_{11/2}]$) configurations.

The B(M1)/B(E2) values obtained for the dipole transitions in bands 3 and 4 show a small but pronounced signature effect or 'stagger'. The calculated B(M1)/B(E2) values show a staggering effect because an experimental estimate of 0.147 MeV for the signature splitting of bands 3 and 4, extracted from an experimental routhian plot, was included in the calculation. The experimental B(M1)/B(E2) values are observed to be a factor of ten smaller than what would be expected for a pure $\nu[h_{11/2} \otimes d_{5/2}]$ configuration. The values appear to be in better agreement with the estimate for a $\nu[h_{11/2} \otimes g_{7/2}]$ configuration.

The DCO results obtained are in general below 0.63, a value which would be expected for a pure stretched dipole transition. This observation implies that transitions in bands 3 and 4 have a negative mixing ratio (δ). The sign of δ is related to the structure of a state by,

$$\text{sign } \delta = \frac{\text{sign}(g_K - g_R)}{Q_0}. \tag{4.10}$$

In order for $\delta < 1$ then $g_K - g_R < 0$. The observed DCO ratios imply that bands 3 and 4

are based on a neutron configuration, in agreement with CSM calculations which show no interacting proton levels at low spin.

An estimate of the experimental $|g_K - g_R|$ values extracted from the B(M1)/B(E2) results is shown in Fig. 4.7(b) together with smoothed theoretical values. $|g_K - g_R|$ gives the contribution to the magnetic dipole moment from a valence nucleon (g_K) minus that of the collective rotation of the core (g_R). g_R can be approximated to Z/A which gives 0.47 for ^{110}Te. The experimental $|g_K - g_R|$ results which average ≈ 0.2 imply a g_K value of 0.67 or -0.27. The low DCO ratio results imply a negative mixing ratio and therefore a value of $g_K = -0.27$. The theoretical configurations overlayed on Fig. 4.7(b) strongly imply bands 3 and 4 are based on a $\nu[h_{11/2} \otimes g_{7/2}]$ configuration.

It is therefore proposed that bands 3 and 4 are built on a $\nu[h_{11/2} \otimes g_{7/2}]$ configuration with a degree of mixing from the $\nu[h_{11/2} \otimes d_{5/2}]$ state necessary to explain the observation of a low lying 7^- state and specific non-collective oblate states which are discussed in detail in sec.4.5.

4.4 Evidence for octupole correlation effects

Positive-parity bands 1a and 2 are connected to negative-parity band 3 by a number of inferred electric dipole (E1) transitions. Band 3 has been interpreted in terms of a $\nu[h_{11/2} \otimes g_{7/2}/d_{5/2}]$ configuration. Since these orbitals differ in both l and j by 3 it is proper to consider the possibility of octupole correlation effects. It should be noted that for all tellurium isotopes, there is no definitive evidence that the dipole transitions, which infer octupole correlations, are electric in nature. Confirmation of their electromagnetic character is therefore paramount.

In this mass region the strongest octupole effects have been calculated for barium (Z=56), xenon (Z=54) and tellurium (Z=52) isotopes with Z=56. These nuclei are predicted to show a softness with respect to octupole deformation in their ground states [ska90]. The Strutinsky calculations of Ref. [ska90] also exhibit octupole deformed minima for the ground states of both ^{108}Te and ^{110}Te.

In order to investigate the configuration of band 2, the magnitude of the intrinsic electric dipole moment (D_0) for ^{110}Te has been extracted by measurement of γ-ray branching ratios. The ratios of the reduced transitions probabilities, $B(E1; I \rightarrow I-1)/B(E2; I \rightarrow I-2)$ can

E_γ	I^π	Band	R_{DCO}	B(E1)/B(E2)	B(E1)	B(E1)	$\|D_0\|$
(keV)	Initial			(10^{-6}fm^{-2})	$(10^{-3}\text{e}^2\text{fm}^2)$	10^{-3}(W.u.)	(efm)
767	18^+	2→3	0.56(1)	0.63**	0.89**	0.60**	0.087**
593	20^+	2→3	0.58(1)	1.31(11)	1.86(15)	1.25(10)	0.126(10)
467	22^+	2→3	0.59(2)	1.69(53)	2.41(74)	1.63(52)	0.144(46)
794	14^+	1a→3	0.65(3)	0.15(2)	0.21(3)	0.15(2)	0.060(9)
773	16^+	1a→3	0.63(2)	0.12(1)	0.16(1)	0.11(1)	0.037(3)

Table 4.4: Measured electric dipole strengths in ^{110}Te assuming $Q_0 = 200\text{efm}^2$ for $\varepsilon_2 = 0.135$. DCO results are included to illustrate the pure nature of these dipole transitions. (**Measurement from [pau94], uncertainly <10%).

be extracted by measuring the intensity ratios of competing $\Delta I = 1$ and $\Delta I = 2$ transitions. The E1/E2 intensity ratios were measured by placing a double coincidence requirement on the two transitions lying above each state of interest, in order to ensure good quality spectra were obtained. The γ-ray branching ratio $\lambda = I_\gamma(\Delta I = 2)/(I_\gamma(\Delta I = 1)$ was hence extracted and the ratio of the reduced transition probabilities calculated using,

$$\frac{B(E1; I \to I-1)}{B(E2; I \to I-2)} = \frac{1}{1.3 \times 10^6} \frac{1}{\lambda_{E2/E1}} \frac{[E_\gamma(E2; I \to I-2)]^5}{[E_\gamma(E1; I \to I-1)]^3} (\text{fm}^{-2}) \qquad (4.11)$$

assuming the $\Delta I = 1$ transitions were pure stretched dipole in character, with no E2 admixture.

The experimental B(E1) values were obtained using a quadrupole moment $Q_0 = 200\text{efm}^2$ to obtain the B(E2) rate from the rotational model (eqn.1.53)[Boh75]. The use of an assumed value of Q_0 means the absolute values for B(E1) and D_0 should only be considered accurate to within ±25%.

The results, including B(E1)/B(E2) ratios extracted for band 1a and band 2, are summarised in table 4.4 together with deduced B(E1) strengths and an estimate of the size of the intrinsic dipole moment D_0, obtained using the approach of [Lea86] with eqn. 1.53. The associated errors shown in table 4.4 are only due to the measured branching ratios. The B(E1) strengths extracted from this work for ^{110}Te and ^{109}Te, together with the systematics of B(E1) strengths extracted in this mass region are shown in Fig. 4.8

The magnitude of D_0 results obtained for ^{110}Te band 2 agrees with values listed in

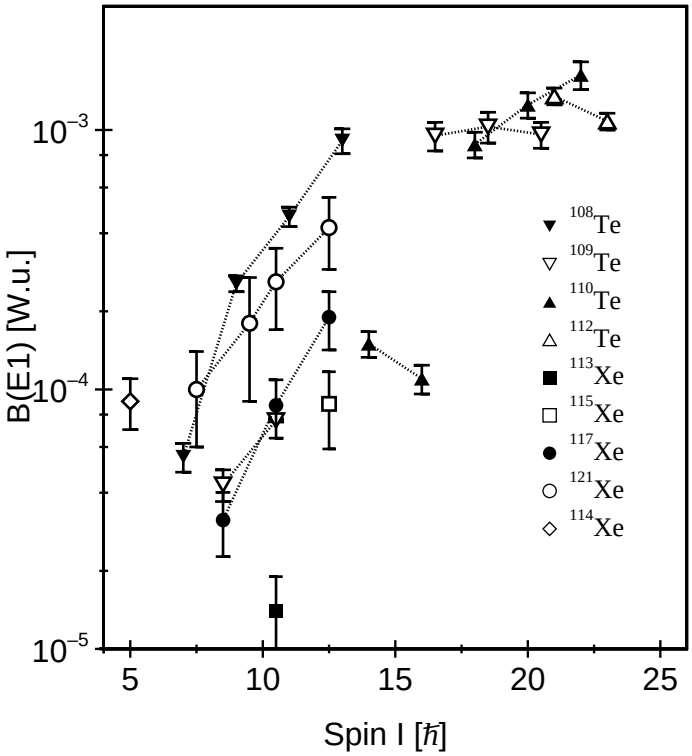

Figure 4.8: B(E1) results for ^{110}Te and neighbouring nuclei.

[pau94], the use of a backed target to provide excellent spectrum resolution in this reference afforded the measurement of the 18^+ transition which was not possible here. Table 4.4 includes new D_0 values for band 1a.

Inspection of Fig. 4.8 reveals the strongest B(E1) strengths are observed for the near-spherical tellurium isotopes with B(E1)$\sim 10^{-3}$W.u. Indeed the B(E1) strengths obtained for ^{110}Te are the largest of all the tellurium isotopes. This value is similar to those found in the neutron rich barium isotopes which lie on an octupole magic number (Z=56). The values obtained are slightly smaller than those observed in the Ra-Th region [But96] the most well developed region for octupole effects. In comparison the B(E1) strengths for the light xenon isotopes are considerably weaker. The B(E1) strengths obtained for band 2 are one order of magnitude higher that those obtained for band 1a, although the results for band 1a are still considerably enhanced when compared to B(E1) values measured in other regions of the nuclear chart, $\sim 10^{-5}$W.u.

The enhanced E1 strength observed in ^{110}Te is cited as evidence for octupole correlation effects. The octupole character of the nucleus may be induced by either static deformation or dynamic vibrational effects. In order to try to determine the origin of the E1 enhancement

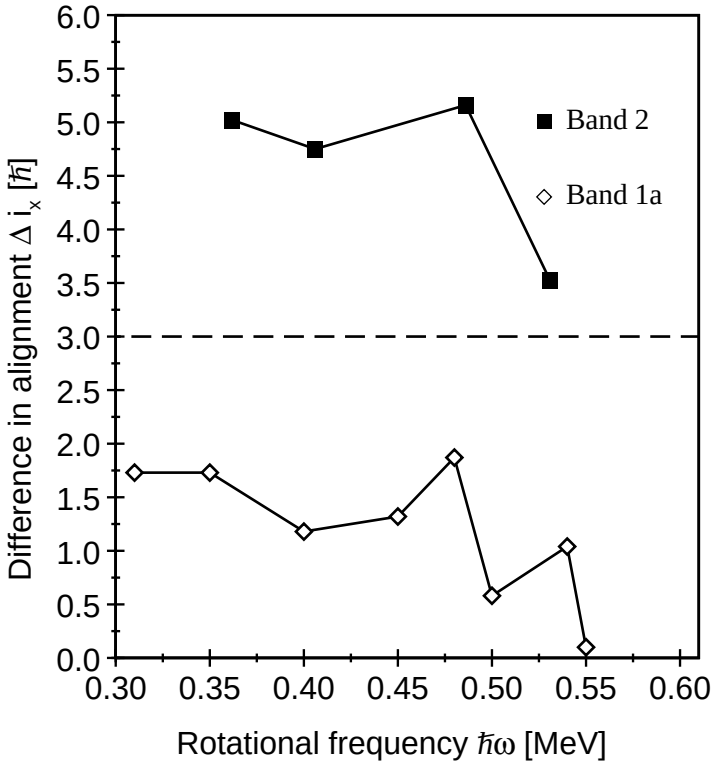

Figure 4.9: Δi_x plot for bands 1a and 2 in ^{110}Te. A value of zero is expected for a nucleus with stable octupole deformation. A value of three is expected in the vibrational case.

a plot of Δi_x, the difference in aligned angular momentum between two structures, has been plotted against the rotational frequency of the nucleus, $\hbar\omega$. A plot of Δi_x against $\hbar\omega$ illustrates the behaviour of octupole nuclei at high spins. Δi_x has been calculated by subtracting from the value of i_x for each positive parity state an interpolated smoothed value for the negative parity states at the same value of $\hbar\omega$. The resultant plot is shown in Fig. 4.9.

The coupling of an octupole phonon to the negative parity $\nu[h_{11/2} \otimes g_{7/2}/d_{5/2}]$ states should yield a Δi_x value of three, marked by the dashed line. Here the octupole phonon quickly aligns with the rotational axis as $\hbar\omega$ increases [roh88]. A value of zero is expected for nuclei which possess stable octupole deformed shapes.

The strongly enhanced E1 strengths for band 2 in ^{110}Te coupled with the evidence from Fig. 4.9 that an octupole phonon coupled to the core may be responsible for the observed structure provides strong evidence that ^{110}Te may have an octupole degree of freedom at high spin. Recent results obtained for ^{108}Te [lan98b] agree with the results obtained for ^{110}Te. ^{108}Te shows a pronounced spin dependence of the E1 transition moment, which

increases as a function of spin. Such a dependence is also observed in ^{110}Te, however it is not as marked as in ^{108}Te. It has been postulated that rotation may stabilise octupole deformation at high spin [smi95]. The spin dependence of D_0 could be considered as evidence for this interpretation.

The calculations of [ska90] exhibit octupole deformed minima for the ground states of both ^{108}Te and ^{110}Te, however the energy gains of the octupole minima compared to the reflection-symmetric minima are only 60 and 10 keV respectively. It is therefore predicted in Ref. [ska90] that the tellurium isotopes should show at best the characteristics of octupole vibration rather than rigid rotation of a reflection-asymmetric shape. The results obtained in this work would support this interpretation. These results are also in agreement with calculations using Hartree-Fock+BCS (static correlations) and generator-coordinate (dynamic correlations) methods [hee94] which suggest that octupole collectivity is enhanced by dynamical correlations.

The weaker E1 strengths (and hence smaller D_0) obtained for band 1a when considered alongside the Δi_x plot does not provide such compelling evidence for octupole correlation effects. The transitions link bands involving the $\nu[h_{11/2} \otimes g_{7/2}/d_{5/2}]$ and $\nu[h_{11/2}]^2$, states with $\Delta j = \Delta l = 3$, where the single-particle matrix element would be expected to be enhanced.

4.5 Evidence for aligned non-collective oblate states

Isotopes of tellurium with A$\geq$112 show characteristic favoured oblate states at medium spin [pau95a]. Tellurium is two protons above the Z=50 closed shell, allowing it to break spherical symmetry and have a small but finite deformation ($\varepsilon_2 = 0.135$). The induced small deformation requires a high angular velocity to generate collective angular momentum, this has the consequence that specific non-collective oblate states, representing the maximal alignment of a subset of the valence particles, may become yrast.

Inspection of the low-spin rigid-rotor plot for ^{110}Te, illustrated in Fig. 4.3, reveals dips at 14^- and 16^+ which may be interpreted as energetically favoured aligned single-particle states. With the aid of recent work [pau95a] which investigated the structure of aligned single-particle states along the yrast line in light tellurium isotopes, using self-consistent cranking calculations based on the TRS formalism, it is possible to make an assignment of

these states with reasonable confidence.

An unexpectedly low lying energetically favoured state is observed at $I^{\pi} = 16^{+}$ in band 1a, a structure based on the $\nu[h_{11/2}]^2$ configuration. This state can be assigned as a fully aligned $\pi[(g_{7/2})^2]_{6^+} \otimes \nu[(h_{11/2})^2]_{10^+}$ oblate configuration. Such a low lying 16^+ state based on the same configuration has been experimentally observed in the heavier tellurium isotopes ^{114}Te, ^{116}Te, ^{118}Te and ^{120}Te. In ^{110}Te, the 16^+ state is observed to be non-yrast (see Fig. 4.3) unlike its counterparts in the heavier tellurium isotopes. This observation can possibly be explained by considering the neutron Fermi surface in ^{110}Te is now below the $\nu[h_{11/2}]$ subshell (see section 4.2.2). It is therefore energetically unfavourable, but not improbable, for such a configuration to exist. No evidence has been found for such a state in the heavier even-even isotope ^{112}Te, however the availability of the good high-fold data set used in this work will enable a more detailed analysis of this nucleus.

A further low-lying non-collective oblate state with negative parity is predicted at 14^-. This configuration is based on the aligned $\pi[(g_{7/2})^2]_{6^+} \otimes \nu[(d_{5/2})(h_{11/2})]_{8^-}$ arrangement of valence particles. Such a state is observed in ^{110}Te in band 4. The configuration depresses the 14^- energy in the negative parity band structure and it is clearly observable in Fig. 4.3, the low spin rigid-rotor plot. Previously ^{112}Te was the lightest tellurium isotope were evidence for this oblate state had been observed.

4.6 High spin band structures in ^{110}Te: Terminating bands

This section discusses the high spin properties of ^{110}Te. Prior to this work no collective high spin structures had been observed in this nucleus, the following discussion offers an interpretation of the new results. Calculations have been performed using a configuration-dependent shell-correction approach with a cranked Nilsson potential, neglecting pairing correlations. These calculations described in Ref. [ben85, rag95, afa95], using the Nilsson parameter set [zha89], have been used to provide a theoretical interpretation of the experimentally observed band structures.

4.6.1 Band 9

A number of band structures which extend up to high spin have been observed in ^{110}Te. The most intense of these structures, labelled band 9, extends up to a tentative spin of

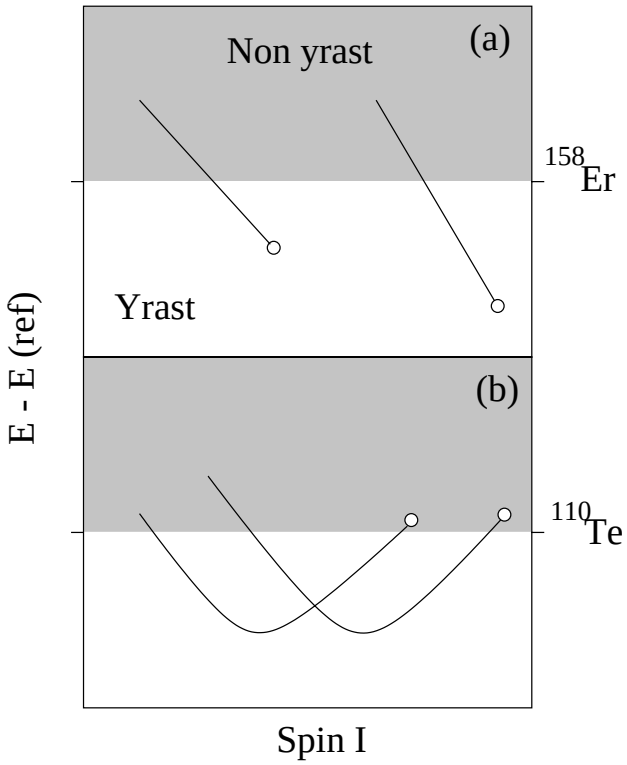

Figure 4.10: Schematic diagram illustrating the differences between (a) favoured and (b) unfavoured or smooth band termination.

(46^+). The γ-ray spectrum of band 9 (Fig. 3.15), manifests a gradual increase in the energy spacing between adjacent γ-ray transitions with increasing transition energy. Such an observation shows the characteristics of smooth band termination.

A band structure will terminate when all the valence particles which describe a particular configuration have aligned with the rotation axis and therefore contribute the maximum alignment consistent with the Pauli exclusion principle. Terminating bands were first observed in nuclei around $^{158}_{68}$Er [sim94]. Here the terminating configuration is only yrast, and therefore observable, over the last couple of transitions. Such termination is often described as 'favoured' because the terminating state is energetically favoured, this is schematically illustrated in Fig. 4.10(a), a high spin rigid-rotor plot.

The theory of smooth band termination describes the nucleus in a form of collective-rotational behaviour, where the nuclear shape gradually evolves from a collective prolate shape ($\gamma \sim 0^\circ$) to a noncollective oblate shape ($\gamma = +60^\circ$) over a number of γ-ray transi-

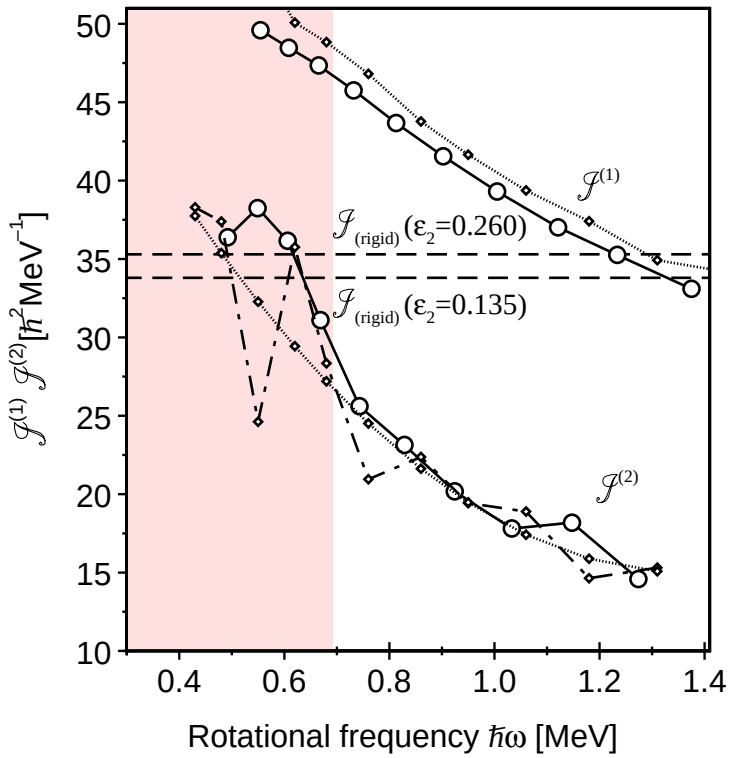

Figure 4.11: Kinematic $\mathcal{J}^{(1)}$ and dynamic $\mathcal{J}^{(2)}$ moments of inertia extracted for band 9. The dashed line indicates the rigid-body moment of inertia ($\mathcal{J}_{(rigid)}$) calculated for two possible quadrupole deformation values. The dotted lines represent theoretical $\mathcal{J}^{(1)}$ and $\mathcal{J}^{(2)}$ values obtained from calculations [afa95]. The shaded area represents the region in which pairing correlations are important.

tions. The specific configuration is generally yrast throughout, enabling a particular configuration to be observed all the way to termination. Typically it is energetically expensive to make the final terminating state, manifest as an upturn in the rigid rotor plot, which leads to this kind of termination being referred to as 'unfavoured', this is illustrated in Fig. 4.10(b).

Nuclei near the Z=N=50 doubly closed shell, such as ^{110}Te, are particularly good candidates for observing smooth terminating structures up to termination. Here only a limited number of valence nucleons are available outside of the doubly closed shell, and therefore the angular momentum necessary to reach termination is accessible using a conventional heavy-ion fusion-evaporation reaction. ^{110}Te can be considered as a $^{100}_{50}$Sn doubly magic core plus 10 valence particles.

Band structures which have been understood within the framework of smooth band ter-

mination, such as those discussed in the Sb [wad93, wad94, jan94, sch96, tho95, lan98a] and Xe [pau98a, scr98] nuclei, share several experimental features. One characteristic feature is a gradual decrease in the value of the dynamic moment of inertia ($\mathcal{J}^{(2)}$) to unusually low values ($\sim \mathcal{J}_{rigid}/3$) with increasing rotational frequency. The $\mathcal{J}^{(2)}$ measures how transition energies change with increasing spin, therefore it is a very sensitive indicator of nuclear behaviour.

Fig. 4.11 shows a plot of the kinematic moment of inertia $\mathcal{J}^{(1)}$ and $\mathcal{J}^{(2)}$ as a function of rotational frequency for band 9 in ^{110}Te. The plot also shows the predicted rigid body moment of inertia $\mathcal{J}_{(rigid)}$ corresponding to two possible values of the deformation parameter ε_2, and theoretically calculated $\mathcal{J}^{(1)}$ and $\mathcal{J}^{(2)}$ values obtained from calculations detailed in [afa95], discussed later. The rigid body moment of inertia can be simply related to a deformed nuclear shape using the expression,

$$\mathcal{J}_{(rig)} = 0.128A^{5/3}[1 + 0.29\varepsilon_2] \qquad [\hbar^2 MeV^{-1}]. \tag{4.12}$$

A value of ε_2=0.135 represents the deformation calculated using the TRS formalism for the ground state band in ^{110}Te, see sec.4.1.3. The larger value of deformation is predicted at the bandhead of band 9. This number arises from the configuration-dependent calculations performed for ^{110}Te which predict the deformation for a specific configuration. The larger configuration-specific value is therefore considered in this discussion.

For a rotating rigid-body the dynamic and kinematic moments of inertia should be approximately equal ($\mathcal{J}^{(2)} \approx \mathcal{J}^{(1)}$). This is clearly not an appropriate description of band 9 where the $\mathcal{J}^{(2)}$ is observed to be much smaller than the$\mathcal{J}^{(1)}$. The dynamic moment of inertia is also observed to fall to 40% that of the predicted rigid-body value. The large difference ($\mathcal{J}^{(1)} - \mathcal{J}^{(2)}$) implies that a substantial amount of the angular momentum is generated by non-collective single-particle contributions [afa95], implying a terminating configuration. The experimental evidence therefore suggests that band 9 represents the first example of a smooth terminating band in ^{110}Te.

In order to help determine a possible configuration for band 9, a comparison with theory has been made. The calculations of Ref. [afa95] enable individual configurations to be followed over a large spin range, up to their maximal termination spins. They provide information about a number of properties associated with a particular configuration, which facilitated a detailed comparison with experimental results.

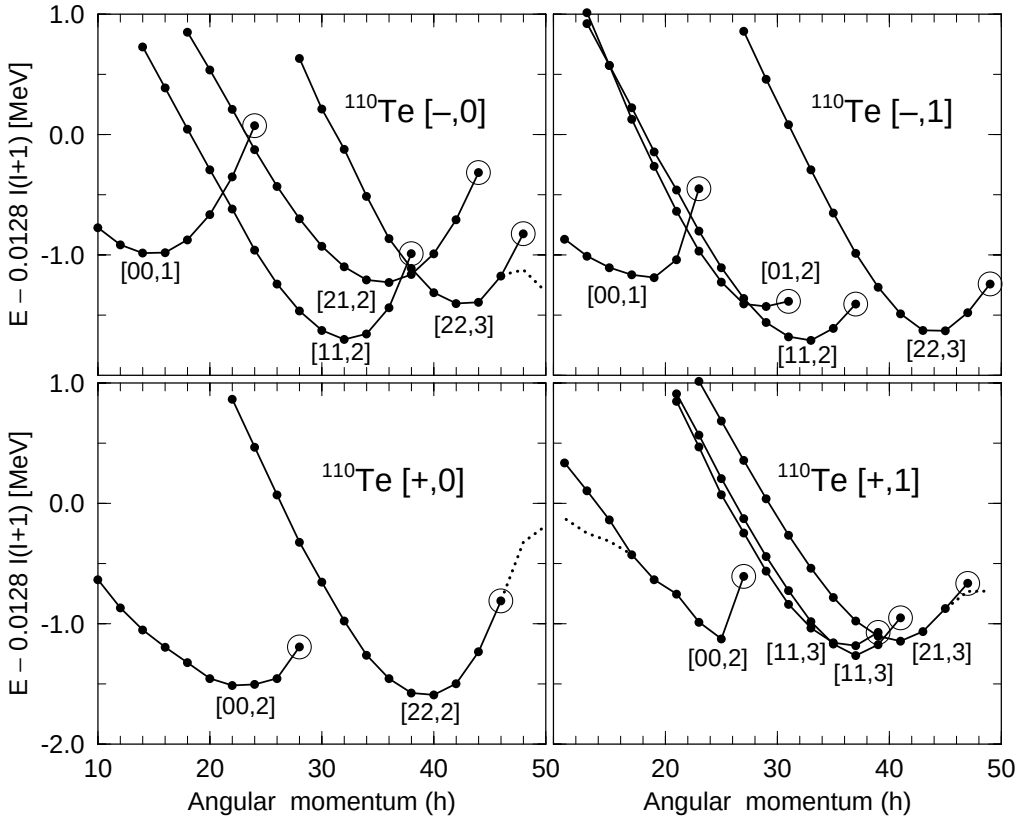

Figure 4.12: Theoretical rigid-rotor plots for the most energetically favoured configurations in ^{110}Te, obtained from calculations based on a configuration-dependent shell-correction approach using a cranked Nilsson potential without pairing [afa95]. The plots are divided into the four combinations of parity and signature $[\pi, \alpha]$. Individual configurations are labelled $[p_1 p_2, n]$ as described in the text. The large open circles indicate band termination states ($\gamma = +60^\circ$) for specific configurations.

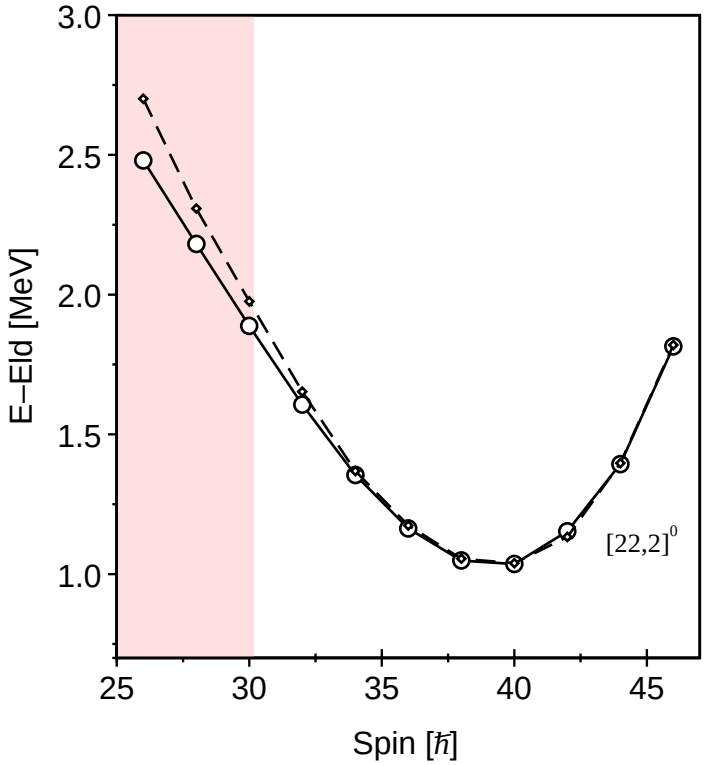

Figure 4.13: Experimental and theoretical rigid-rotor plot for band 9. Experimental points are marked by circles and connected by a solid line, theoretical results are indicated by a dashed line.

Theoretical rigid-rotor plots were constructed from the output of the calculations for the most energetically favoured configurations in ^{110}Te. The plots were divided into the four combinations of parity and signature. The individual configurations are labelled $[p_1 p_2, n]^{\alpha}$, where p_1 is the number of proton holes in the $g_{9/2}$ orbital, p_2 is the number of $h_{11/2}$ protons and n is the number of $h_{11/2}$ neutrons and α is the total signature. The resulting plots are illustrated in Fig. 4.12.

By plotting the excitation energy of band 9 minus a rigid-rotor reference, an experimental rigid rotor plot was constructed, as illustrated in Fig. 4.13. The shape of the experimental and theoretical rigid-rotor plots for the high spin structures illustrated here are consistent with the theory of smooth band termination.

Inspection of Fig. 4.12 reveals a large number of possible configurations which are energetically favourable are predicted to exist. Comparison of the relative excitation energies of the theoretical structures indicates that the $[22,2]^0$ configuration is predicted to be the lowest energy, and therefore strongest populated configuration in the spin range of band 9. It is rea-

sonable therefore to assign band 9 as the positive parity even signature [22,2] configuration. This configuration involves the two particle-two hole excitation of two $g_{9/2}$ protons across the Z=50 shell gap into the $h_{11/2}$ orbital. This scenario is often referred to as a core-excitation. $[22,2]^0$ terminates with a, $\pi[(g_{9/2})_8^{-2}(h_{11/2})_{10}^2(g_{7/2}d_{5/2})_6^2]_{24} \otimes \nu[(h_{11/2})_{10}^2(g_{7/2}d_{5/2})_{12}^6]_{22}$ with respect to the Z=50 closed shell. The maximal spin possible with this configuration is therefore 46^+, when all the valence particles have aligned along the rotation axis. This represents the maximum spin experimentally observed for band 9.

Confirmation of this assignment is provided if the theoretical and experimental rigid-rotor plots are overlayed on the same plot, as illustrated in Fig. 4.13. Absolute energy values should not be considered in this comparison since the experimental and theoretical ground states are not related, therefore the theoretical plot has been shifted vertically to overlap the experimental configuration at $35 \leq I45\hbar$.

The comparison between the theory and experiment can be seen to be excellent. The minima and slopes of the rigid-rotor plots are in good agreement. At spins of $\leq 30\hbar$ deviations between theory and experiment can be attributed to the neglect of pairing correlations in the theoretical calculations. Regions of the plots for which pairing correlations are important are indicated by a grey shading. The upbend in the rigid-rotor plot is believed to be related to the difficulty in aligning the proton $g_{9/2}$ holes when they are surrounded by aligned particles and because the neutron $g_{7/2}$ and $d_{5/2}$ subshells are half filled so the spin contribution from the last particles in these subshells is close to zero.

Further confirmation of the $[22,2]^0$ assignment is afforded with reference to the $\mathcal{J}^{(1)}$ and $\mathcal{J}^{(2)}$ plots for band 9 illustrated in Fig. 4.11. The theoretical values of $\mathcal{J}^{(1)}$ and $\mathcal{J}^{(2)}$ for the $[22,2]^0$ configuration extracted from the calculations are overlayed on top of the experimental values. Some of the discontinuities in the theoretical moments of inertia are numerical in nature, and will be magnified in the calculations, especially for the theoretical values of $\mathcal{J}^{(2)}$ [afa95]. The theoretical plots therefore show the calculated values of $\mathcal{J}^{(1)}$ and a polynomial fit to the theoretical values of $\mathcal{J}^{(2)}$. As an illustration the theoretical and smoothed theoretical values of the $\mathcal{J}^{(2)}$ are shown in Fig. 4.11.

Good agreement is observed between theory and experiment. The slope and magnitude of the experimental $\mathcal{J}^{(2)}$ is reproduced well by the calculations. The theoretical value of $\mathcal{J}^{(1)}$ shows the same trend as experiment, it is however consistently larger than the

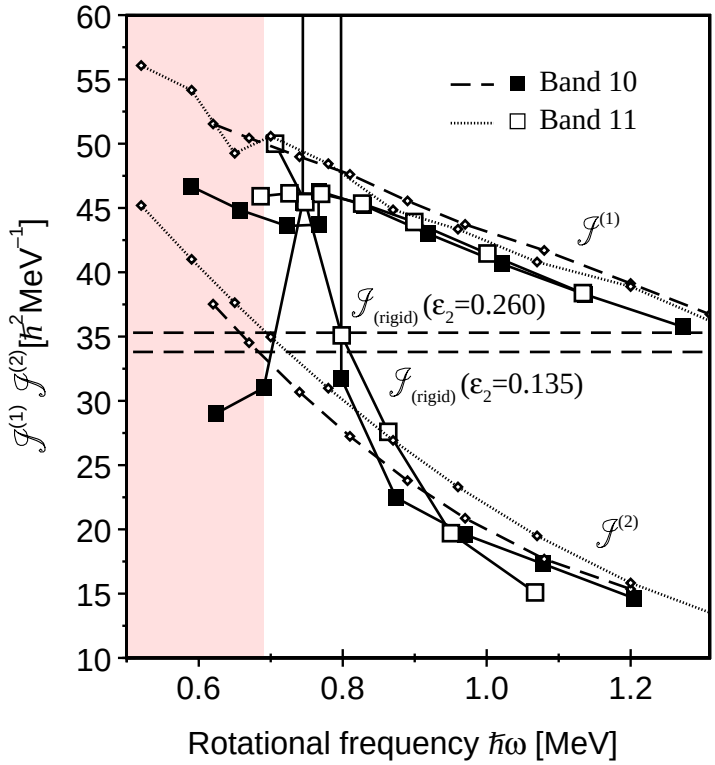

Figure 4.14: Kinematic $\mathcal{J}^{(1)}$ and dynamic $\mathcal{J}^{(2)}$ moments of inertia extracted for bands 10 and 11. The flat dashed lines indicate the rigid-body moment of inertia calculated for two possible quadrupole deformation values. The dotted/dashed lines represent theoretical $\mathcal{J}^{(1)}$ and $\mathcal{J}^{(2)}$ values obtained from calculations [afa95].

experimental value. This observation may imply a misassignment of the tentative spins for the band 9, however the present assignment justified through coincidence and relative intensity arguments would seem probable.

In conclusion band 9 represents the first observation of a smooth terminating band in ^{110}Te. It has been a assigned a $[22,2]^0$ configuration confirming the experimental parity of band 9, which assumed the 994 keV transition tentatively linking this structure to the low spin level scheme is stretched E2 in nature. The high quality data obtained in this work has enabled band 9 to be observed up to predicted termination.

4.6.2 Bands 10 and 11

Bands 10 and 11 also show the characteristics of smooth band termination. The increase in γ-ray spacing which is apparent in their γ-ray spectra (Fig. 3.15(b)(c)) produces a decrease

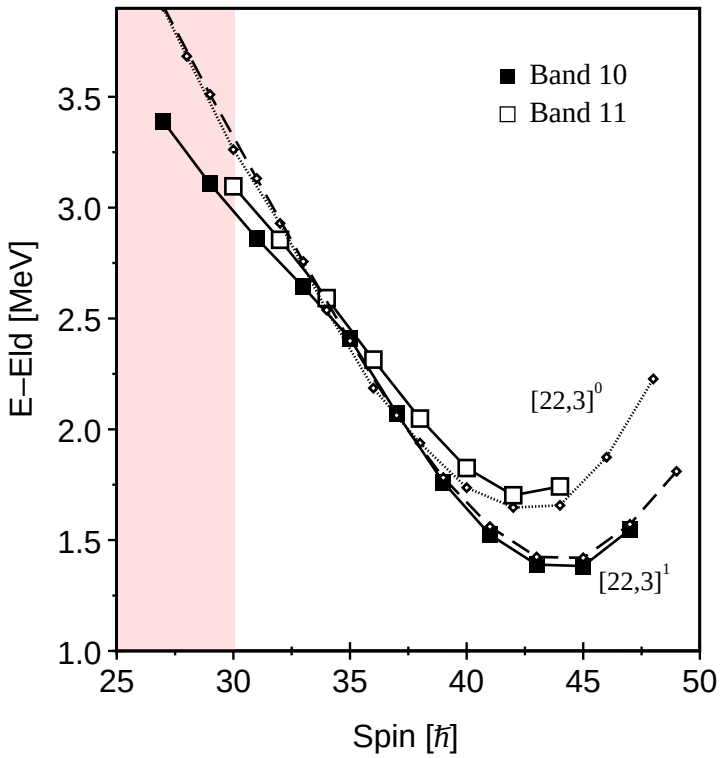

Figure 4.15: Experimental and theoretical rigid-rotor plot for bands 10 and 11. Experimental points are marked by symbols and are connected by a solid line. Open symbols represent the even signature component. Theoretical results are indicated by a dashed/dotted line.

in the dynamic moment of inertia ($\mathcal{J}^{(2)}$) to unusually low values, see Fig. 4.14. A characteristic minimum is also observed in the experimental rigid-rotor plots produced for these structures, Fig. 4.15. The position and shape of the minimum observed is configuration-dependent, so thought must be given to the excitation energy and spins of these structures before a firm assignment of a configuration can be made.

Approximate spins were assigned to bands 10 and 11 using relative intensity and coincidence arguments. With reference to the calculations the estimate of the spins can be quoted with more confidence. Band 10 represents the second most intense high spin terminating band in ^{110}Te. From knowledge of the relative theoretical excitation energies, this implies the negative parity, odd signature [22,3]^1 configuration is the most probable interpretation of its structure. This configuration which involves three $h_{11/2}$ neutrons terminates with, $\pi[(g_{9/2})_8^{-2}(h_{11/2})_{10}^2(g_{7/2}d_{5/2})_6^2]_{24} \otimes \nu[(h_{11/2})_{13.5}^3(g_{7/2}d_{5/2})_{11.5}^5]_{25}$. The total possible spin/parity available with this configuration is 49^-.

A more confident assignment of the spins for band 11 has been made possible using

the assumption that band 11 is the signature partner to band 10. Inspection of the γ-ray spectra for these structures (Fig. 3.15(b)(c)) together with knowledge of their kinematic and dynamic moments of inertia at high spin, implies this assumption is reasonable.

Fig. 4.14 shows a comparison of the theoretical and experimental values of $\mathcal{J}^{(1)}$ and smoothed values $\mathcal{J}^{(2)}$ for bands 10 and 11. The agreement at high spin can be considered reasonable for both $\mathcal{J}^{(1)}$ and $\mathcal{J}^{(2)}$. For lower values of spin where pairing becomes more important the agreement is less satisfactory. Band 10 is observed to undergo a structural change, illustrated as a large discontinuity at ω_c=0.76 MeV/$\hbar$ on the $\mathcal{J}^{(2)}$ plot, and as a slope change in the rigid-rotor plot (Fig. 4.15) at spin (35$\hbar$). This observation is not observed in the theoretical $\mathcal{J}^{(2)}$, because this is a configuration-dependent calculation.

The reason for the discontinuity is difficult to place within the theory. One possible explanation is that band 10 represents the $[22,3]^0$ even-signature configuration, which is observed to be crossed by the $[21,2]^0$ configuration, illustrated in Fig. 4.12. However this interpretation is not supported by the experimental evidence. Firstly, the $[22,3]^0$ configuration should represent the weaker signature of the [22,3] configuration and secondly, the discontinuity is theoretically predicted at a much higher spin than is experimentally observed, even allowing for an uncertainty in the spin assignments of these structures. The most probable explanation is that band 10 is indeed the $[22,3]^1$ configuration, as previously alluded. This structure will be crossed by a $[21,2]^1$ configuration which is not illustrated in Fig. 4.12 because it is less energetically favourable. Such an interpretation would explain the experimental observations.

A sharp discontinuity in the dynamic moment of inertia is not observed in band 11, see Fig. 4.15. However the slope of the $\mathcal{J}^{(2)}$ is observed to increase. One might have expected to observe a discontinuity because of the theoretically predicted $[21,2]^0$ crossing. The reason for the absence of an effect is unclear.

The comparison between the experimental and theoretical rigid-rotor plots, illustrated in Fig. 4.15 is very good. The slopes and relative position of the minima are seen to be in good agreement. This provides further evidence that the band assignments are reasonable. Fig. 4.15 shows neither band 10 nor 11 is observed to termination. Band 10 is observed up to (47^-) a further transition is required to reach termination. Two further transitions are required to extend the more weakly populated band 11 to termination. The non-observation

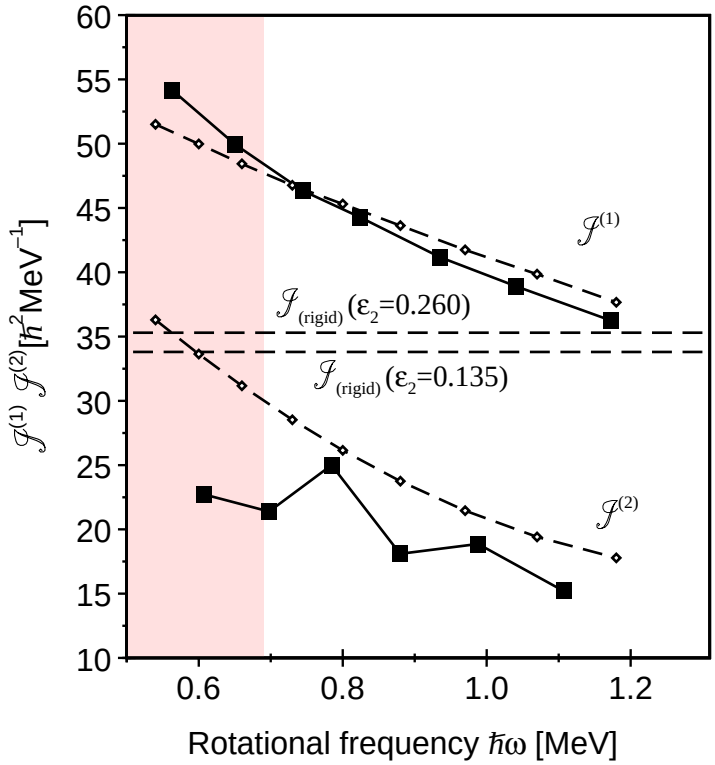

Figure 4.16: Kinematic $\mathcal{J}^{(1)}$ and dynamic $\mathcal{J}^{(2)}$ moments of inertia extracted for band 12. The flat dashed lines indicate the rigid-body moment of inertia calculated for two possible quadrupole deformation values. The dotted/dashed lines represent theoretical $\mathcal{J}^{(1)}$ and $\mathcal{J}^{(2)}$ values obtained from calculations [afa95].

of the extra transitions is purely due to the statistical uncertainties apparent at such high spin.

4.6.3 Band 12

Band 12 represents the most weakly populated of the high spin decoupled bands in ^{110}Te. The structure remains unlinked to the low spin level scheme leaving the spins, parity and approximate excitation energy of the band uncertain. Inspection of the γ-ray spectrum for band 12, Fig. 3.16(a) reveals an increase in the spacing between adjacent γ-ray transitions as a function of spin. This manifests itself as a decrease in the value of the $\mathcal{J}^{(2)}$ consistent with the scenario of smooth band termination, Fig. 4.16.

With reference to the theoretical calculations one might expect to observe a further positive parity structure, the most probable configuration for this structure is therefore

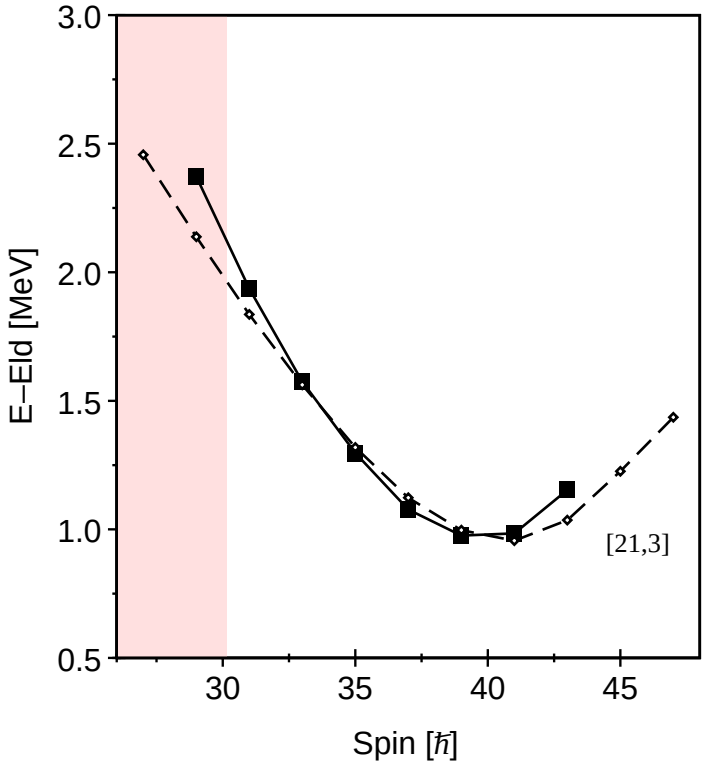

Figure 4.17: Experimental and theoretical rigid-rotor plot for band 12. Experimental points are marked by symbols and are connected by a solid line. Open symbols represent the even signature component. Theoretical results are indicated by a dashed/dotted line.

$[21,3]^1$. Using the theoretical calculations as a guide, together with experimental coincidence and relative intensity arguments, a very tentative assignment of spins and parities was made for this structure. A comparison of the experimental and theoretical $\mathcal{J}^{(1)}$ and $\mathcal{J}^{(2)}$ values is shown in 4.16.

The results show a reasonable agreement between the experimental and theoretical values of the $\mathcal{J}^{(1)}$ and $\mathcal{J}^{(2)}$. With reference to Fig. 4.17, which shows the experimental and theoretical rigid-rotor plots assuming the $[21,3]^1$ configuration, the agreement is again reasonable. The position of the minimum in the rigid-rotor curve is observed to be one unit of spin different between theory and experiment. On this basis, the assignment of band 12 as a $[21,3]^1$ configuration must therefore be described as tentative.

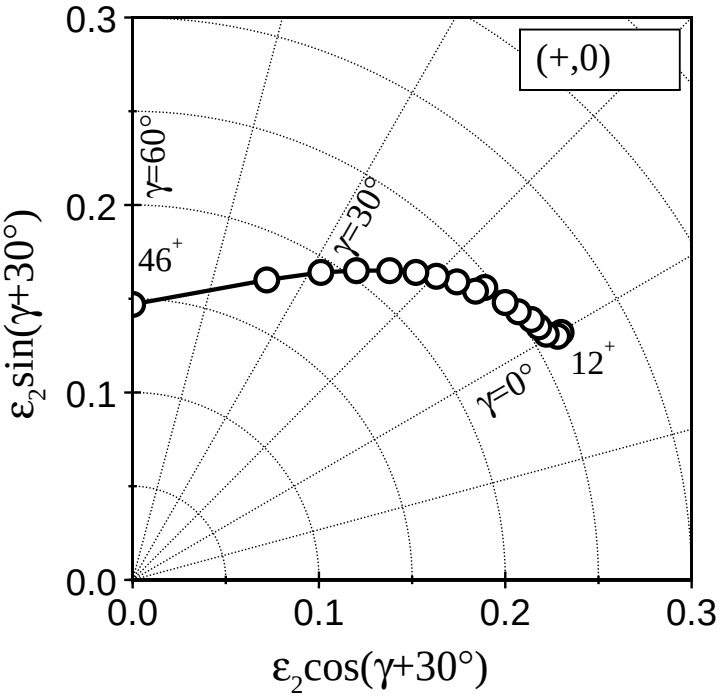

Figure 4.18: Calculated shape trajectory in the $\varepsilon_2 - \gamma$ plane for the $[22,2]^0$ configuration.

4.6.4 Summary

Four high spin terminating bands involving two-particle two-hole excitations across the Z=50 shell gap have been established in ^{110}Te. One of these structures has a tentative link to the low spin level scheme and has been observed up to termination. The other three structures have been assigned very tentative spins and parities based on lowest estimates from coincidence relationships and comparison between theory and experiment.

The four high spin structures show similar trends in the $\mathcal{J}^{(1)}$, $\mathcal{J}^{(2)}$ and rigid-rotor plots which have been constructed from the experimental data obtained. The trends observed are explained within the scenario of smooth band termination, where as the nucleus rotates the valence particles gradually align their spins along the rotation axis. Changes in the intrinsic nuclear shape for the $[22,2]^0$ configuration are plotted on the $\varepsilon_2 - \gamma$ plane in Fig. 4.18. They show a gradual shape change over the spin range from 12^+ up to termination at 46^+ as the nuclear shape traces a path through the triaxial γ-plane from collective prolate ($\gamma = 0°$) to non-collective oblate ($\gamma = 60°$).

Low to medium spin states in nuclei close the the Z=50 shell gap, such as ^{110}Te, are

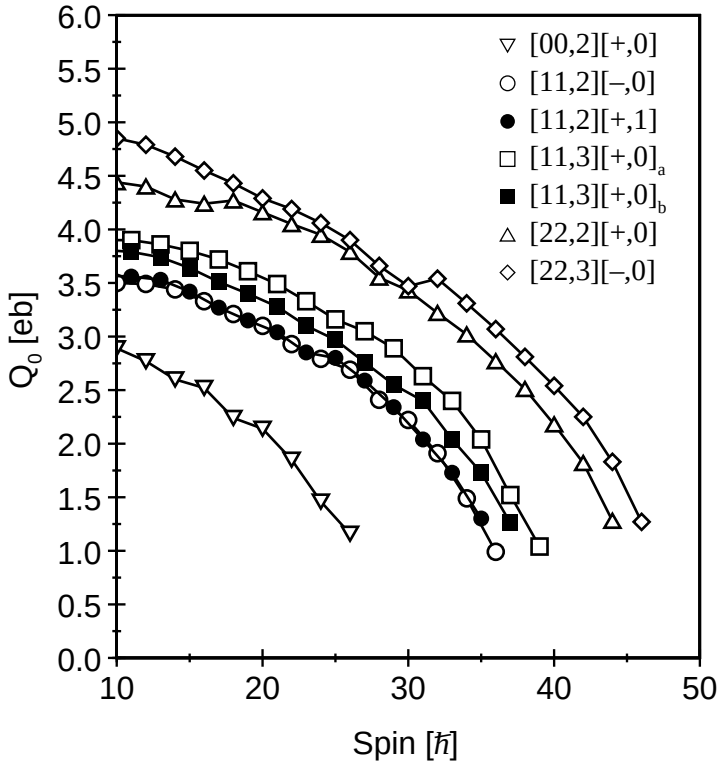

Figure 4.19: Calculated intrinsic quadrupole moments (Q_0) for a number of energetically favoured configurations in ^{110}Te.

based on a near spherical nuclear shape. Indeed ^{110}Te which has 10 valence particles relative to the $^{100}_{50}$Sn core, has the small but finite deformation of $\varepsilon_2 = 0.135$. The core-excited configurations which involve two protons being excited from the upsloping $\pi[g_{9/2}]$ orbital into the deformation driving downsloping $\pi[h_{11/2}]$ orbital mean it is energetically favourable for the nucleus to adopt a more deformed shape. Particle-hole excitations across the Z=50 shell gap also increase the effective number of 'valence' particles, with the addition of two holes in the $\pi[g_{9/2}]$ orbital. This increase in the effective number of valence particles allows the collective rotational degree of freedom to compete with the underlying single-particle nature of ^{110}Te.

The calculations used in this work predict the quadrupole moment associated with a particular configuration as a function of spin. This reveals a typical quadrupole moment at the bottom of a 2p-2h terminating band in ^{110}Te of 4.4eb, corresponding to a ε_2 deformation of 0.27. This represents a strongly prolate shape, which explains why the terminating structures initially appear very collective in nature.

The collective nature of these bands is predicted to decrease as the band spin increases

towards termination. This manifests itself as a decrease in the quadrupole moment (Q_0) with increasing spin as the band approaches the non-collective terminating state. A direct measurement of Q_t (see sec. 1.11.2) for ^{108}Sn and ^{109}Sb indicated a gradual decrease in Q_t consistent with predictions [wad98]. This measurement should be followed up for ^{110}Te, in order to verify what is proposed in this work. Theoretical values of Q_0 as a function of spin for a number of different configurations involving differing numbers of particles being excited across the Z=50 shell gap, are shown in Fig. 4.19. Fig. 4.19 indicates that the 2p-2h configuration represents the most deformed system observed in ^{110}Te.

4.7 High spin ΔI=1 bands

Four band structures which are linked by a number of magnetic dipole transitions have been observed extending to high spin in ^{110}Te. These so called 'coupled' structures provide an important insight into how angular momentum is generated in nuclei close to Z=50 doubly magic closed shell.

4.7.1 Bands 13 and 14

Bands 13 and 14 represent a strongly coupled band structure, with a cascade of 20 M1 transitions extending up to high spin. This structure has been tentatively linked to the low spin level structure by two high energy transitions of undetermined multipolarity. In order to try to determine a configuration for these band structures, the experimentally observed transitions have been compared to calculations which use a configuration-dependent shell-correction approach without pairing [afa95].

The significant population intensity of bands 13 and 14 suggests the configuration which best describes the bands should be energetically favoured at spins $20-30\hbar$. With reference to the theoretical rigid-rotor plots illustrated in Fig. 4.12, and using relative excitation energy arguments a number of probable configurations can be identified. The theory predicts configurations which involve the excitation of one $g_{9/2}$ proton across Z=50 shell gap, such structures are required in order to explain the observation of strongly coupled bands. These configurations produce structures which extend up to moderately high spin, similar to what is experimentally observed. The most energetically favoured of these configurations is the [11,2], negative parity assignment.

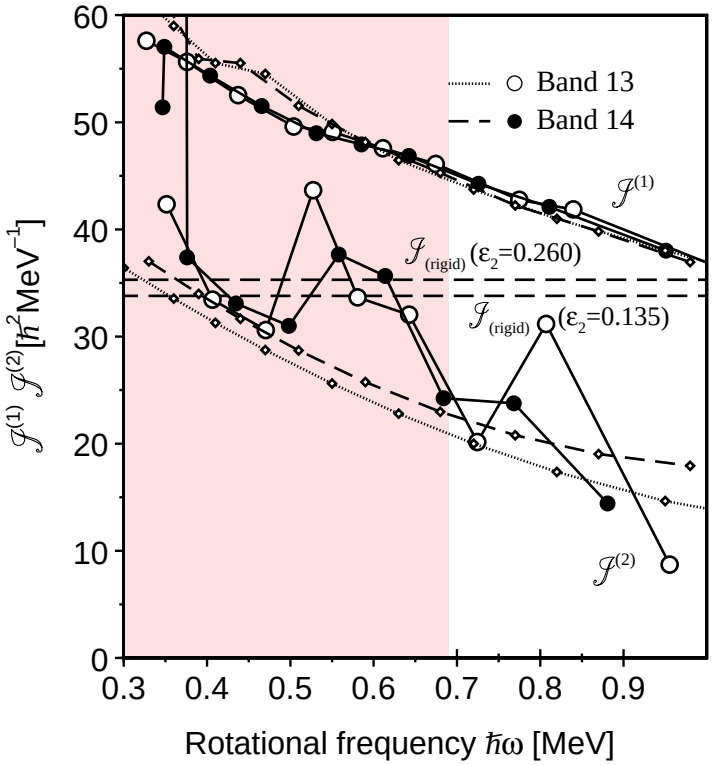

Figure 4.20: Kinematic $\mathcal{J}^{(1)}$ and dynamic $\mathcal{J}^{(2)}$ moments of inertia extracted for coupled bands 13 and 14. The dashed lines indicate the rigid-body moment of inertia calculated for two possible quadrupole deformation values. The dotted/dashed lines represent theoretical $\mathcal{J}^{(1)}$ and $\mathcal{J}^{(2)}$ values obtained from calculations [afa95].

The [11,2] configuration requires that the γ-ray transitions which link bands 13 and 14 to the low spin level scheme are E2 in nature, ensuring the necessary negative parity configuration. This assignment establishes a bandhead spin of 16^- and 17^- for bands 13 and 14 respectively. With this knowledge, a comparison between the experimental and theoretical values of $\mathcal{J}^{(1)}$ and $\mathcal{J}^{(2)}$ for this configuration was constructed, the resultant plot is illustrated in Fig. 4.20. It should be noted however, because a reliable experimental determination of the multipolarity of the linking γ-ray transitions could not be made, the spins are uncertain by $1\hbar$ and the parity is inferred from the configuration.

The experimental and theoretical values of $\mathcal{J}^{(1)}$ are shown to agree remarkably well. The theory is able to reproduce almost exactly the experimentally observed numbers at higher values of rotational frequency, where the inclusion of the pairing interaction is less important. The smoothed theoretical value of the $\mathcal{J}^{(2)}$, reproduces the general trend of the experimental values. However it is clear that structural features evident in the experimental

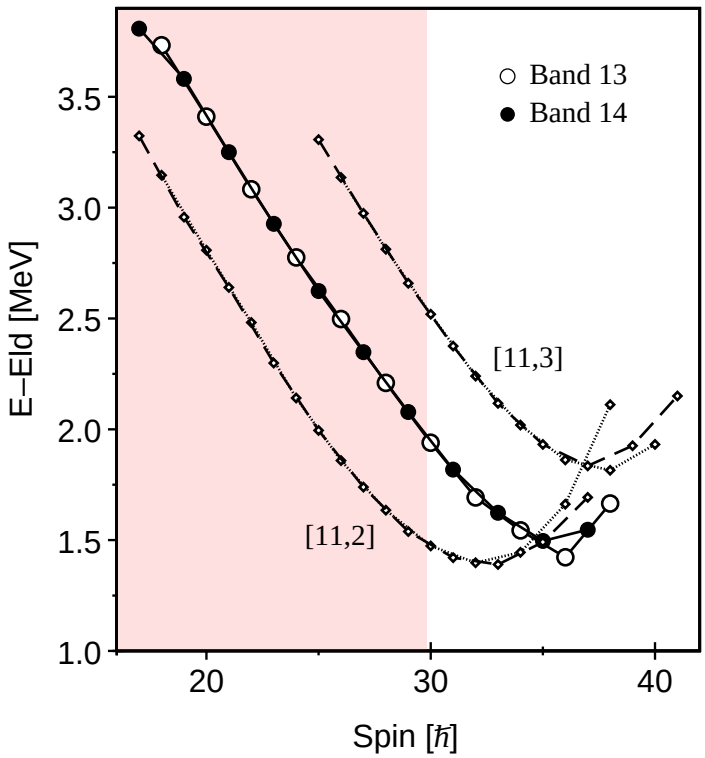

Figure 4.21: Experimental and theoretical rigid-rotor plots for coupled bands 13 and 14. Band 13 [−,0]: open circles, dotted line. Band 14 [−,1]: filled circles, dashed line.

results are beyond the scope of the current theoretical interpretation.

Theoretical values of the excitation energy minus a rigid-rotor reference are compared to experimental values in Fig. 4.21. Theoretical plots for the two signature partners of the [11,2] configuration are shown alongside theoretical results for the somewhat less energetically favoured [11,3] positive parity configuration. The [11,3] configuration is included to allow a proper comparison.

The agreement obtained between experiment and theory for the [11,2] configuration is less than satisfactory. The theory is observed to reproduce the slope of the experimental values well, it is however unable to reproduce the position of the experimental minimum with 3 units of spin separating the experimental and theoretical minima. Indeed the position of the experimental minimum is a better match with that of the [11,3] configuration, giving a 2 $\hbar$ separation. The assignment of a [11,3] configuration for this structure would however be in strong disagreement with the experimentally observed intensity of bands 13 and 14.

There is strong experimental evidence to suggest that the coupled structure made up of bands 13 and 14 may be described within the scenario of smooth band termination. Firstly,

E_γ	$I_i \rightarrow I_f$	Band	R_{DCO}	B(M1)/B(E2)	B(M1)	B(M1)	$\lvert(g_K - g_R)\rvert$
keV	initial			$([\mu_N/eb]^2)$	(μ_N^2)	(W.u.)	
397	22	13	0.70(1)	12(1)	3.4(3)	1.9(2)	1.1(1)
431[1]	23	14	0.75(1)	–	–	–	–
463	24	13	0.72(1)	19(3)	4.8(7)	2.7(4)	1.3(2)
488	25	14	0.73(1)	10(2)	2.6(5)	1.4(3)	1.0(1)
540[1]	26	13	0.85(2)	10(2)	2.5(5)	1.4(3)	0.9(1)
543[1]	27	14	0.85(2)	7(1)	1.6(2)	0.9(1)	0.7(1)
578	28	13	–	26(5)	5.0(9)	2.8(5)	1.3(2)
611	29	14	–	17(3)	3.1(5)	1.8(3)	1.1(1)
628	30	13	–	9(2)	1.6(4)	0.9(2)	0.7(1)
674	31	14	–	17(5)	2.4(7)	1.3(4)	0.9(2)

Table 4.5: Measured magnetic dipole strengths for coupled bands 13 and 14 in ^{110}Te. B(M1) and $|g_K - g_R|$ results assume a variable Q_0 extracted from configuration-dependent calculations. [1] Energy doublet : Intensity measurement is that of composite peak.

the general shape of the experimental rigid-rotor plot, which shows a steady decrease to a minimum and then upbend in the data points and secondly, the dynamic moment of inertia ($\mathcal{J}^{(2)}$) results, which are observed to fall to unusually low values relative to the kinematic moment of inertia ($\mathcal{J}^{(1)}$). If this interpretation is correct than ^{110}Te provides the first evidence for coupled smooth terminating bands extending to high spin in any region of the nuclear chart.

In order to provide further insight into the experimentally observed band structures, the ratios of the reduced transition probabilities; $B(M1; I \rightarrow I-1)/B(E2; I \rightarrow I-2)$ have been extracted by measuring the intensity of competing ΔI =1 and ΔI =2 transitions. The results, collated in table.4.5, were calculated using the recipe described in sec.4.3.1. Appropriate values of the quadrupole moment were used to obtain the B(E2) rate from the rotational model, in order to extract B(M1) values. The values of Q_0 were obtained for the [11,2] configuration from the configuration-dependent calculations, described in [afa95]. A plot of the theoretical values of Q_0 as a function of spin, is illustrated in Fig. 4.19 for a

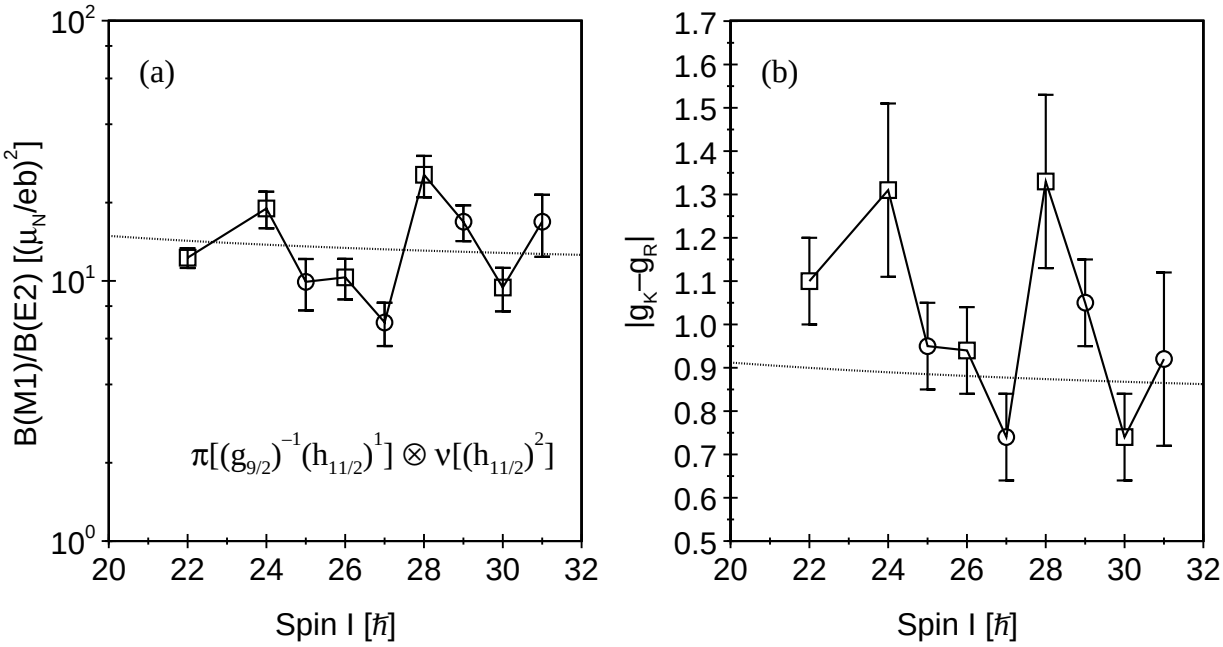

Figure 4.22: Experimental and theoretical (a) B(M1)/B(E2) ratios of reduced transition probabilities. (b) $|g_K - g_R|$ values assuming a variable Q_0 extracted from configuration-dependent calculations. (a)(b) Band 13 is labelled with square symbols, band 14 with circles.

number of configurations in ^{110}Te. Table. 4.5 also contains a summary of the DCO ratio results extracted for a number of the more intense dipole transitions.

A plot of the experimental B(M1)/B(E2) values against spin is shown in Fig. 4.22(a). The figure also shows theoretical values for the [11,2] configuration calculated using the Dönau and Frauendorf semi-classical formalism [don87, fra81]. A very good agreement is observed between the theoretical calculations and experimentally observed values. The experimental numbers are a factor of ten larger than those obtained for the M1 transitions in the negative parity low spin structure of bands 3 and 4 (sec. 4.3.1). This implies bands 13 and 14 are much more strongly coupled than the low spin structures. Indeed the B(M1)/B(E2) values obtained for bands 13 and 14 are sufficiently large to be comparable with those values obtained for N=58 isotone ^{108}Sn [jen98a], a nucleus where the coupled bands have been interpreted within the Tilted Axis Cranking (TAC) formalism [fra93], this scenario is discussed in sec. 4.7.3.

The DCO ratio results obtained are in general above 0.63, a value which would be expected for a pure stretched dipole transition. Such a positive mixing ratio implies a positive

g_K value, which would mean that bands 13 and 14 are based on a proton configuration. In order to try to clarify this interpretation, values of $|g_K - g_R|$ have been extracted for bands 13 and 14, by using a variable quadrupole moment (Q_0) obtained from the theoretical calculations illustrated in Fig. 4.19.

The average value of $|g_K - g_R|$ obtained is approximately 1.0, giving g_K values of 1.47 or -0.53. The agreement between experiment and theory for the [11,2] configuration is good which implies $g_K = 1.47$, allowing bands 13 and 14 to be interpreted in terms of a proton excitation across the Z=50 shell gap.

The evidence provided from the experimental and theoretical analysis of these coupled structures has led to the tentative assignment of bands 13 and 14 as the two signature partner bands of the [11,2] negative parity configuration. The [11,2] structure has a terminating configuration which may be written as, $\pi[(g_{9/2})^{-1}_{4.5}(h_{11/2})^{1}_{5.5}(g_{7/2}d_{5/2})^{2}_{6}]_{16} \otimes \nu[(h_{11/2})^{2}_{10}(g_{7/2}d_{5/2})^{6}_{12}]_{22}$. It involves the excitation of one $g_{9/2}$ proton from below the Z=50 shell gap into the $h_{11/2}$ deformation driving intruder orbital. This configuration gives signature partner bands with maximal spins of 38^- and 37^- for bands 13 and 14 respectively. This interpretation means that both bands 13 and 14 have been observed up their terminating spins.

4.7.2 Bands 15 and 16

Bands 15 and 16 represent another coupled structure, which is populated with a much lower intensity than that observed in bands 13 and 14. Following an inspection of the theoretical rigid-rotor plots illustrated in Fig. 4.12, another structure involving a one $g_{9/2}$ proton excitation was identified. This structure is somewhat less energetically favoured than the [11,2] configuration. This intensity argument is the primary reason why bands 15 and 16 have been tentatively assigned as the [11,3], positive parity configuration. Interestingly the calculations predict one [11,2] configuration and two [11,3] configurations, all showing a small signature splitting. The two energetically favoured [11,3] configurations result from a differing arrangement of the valence particles within the same orbitals.

Bands 15 and 16 remain unlinked to the low spin level scheme leaving the spins, parity and approximate excitation energy of the bands uncertain. However arguments involving the population and relative excitation energies of bands 13, 14, 15 and 16, place limits to their

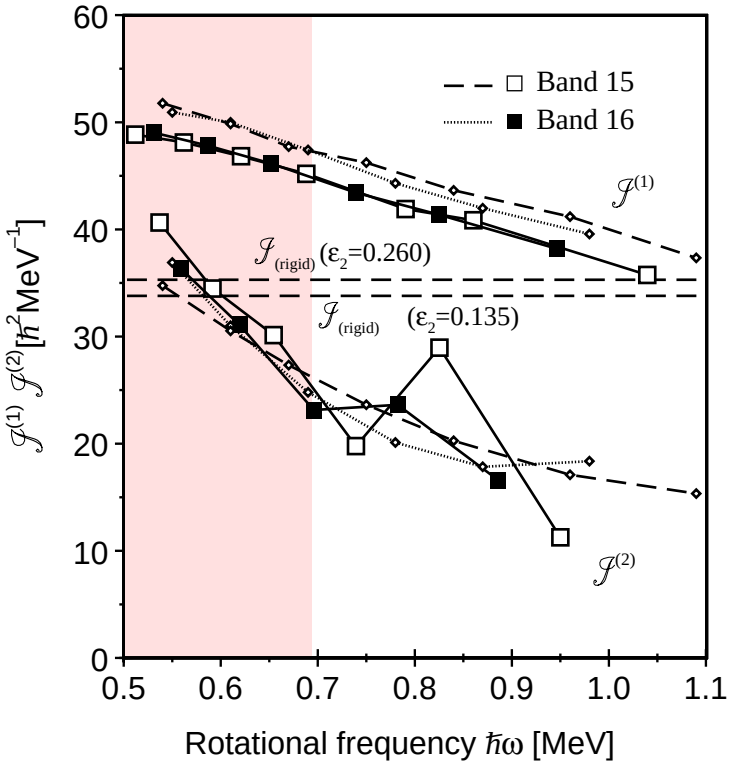

Figure 4.23: Kinematic $\mathcal{J}^{(1)}$ and dynamic $\mathcal{J}^{(2)}$ moments of inertia extracted for coupled bands 15 and 16. The dashed lines indicate the rigid-body moment of inertia calculated for two possible quadrupole deformation values. The dotted/dashed lines represent theoretical $\mathcal{J}^{(1)}$ and $\mathcal{J}^{(2)}$ values obtained from calculations [afa95].

values. Using these assumptions a comparison between the theoretical and experimental kinematic $\mathcal{J}^{(1)}$ and dynamic $\mathcal{J}^{(2)}$ moments of inertia was made, the resulting plot is shown in Fig. 4.23.

The results show in general a reasonable agreement between experiment and theory is obtained. The observed trends are similar to what was seen for bands 13 and 14. Again the theory does not reproduce structural features evident in the experimental results.

A comparison of the experimental and theoretical rigid-rotor plots is shown in Fig. 4.24. This figure also shows the results for bands 13 and 14 for comparison. The agreement between experiment and theory for bands 15 and 16 is reasonable. The relative excitation energy of bands 15/16 and bands 13/14 is reproduced well by the theory. Implying that bands 15/16 should indeed be weakly populated relative to bands 13/14 as experimentally observed.

The experimental data shows a well defined minimum in the rigid-rotor plot, with an

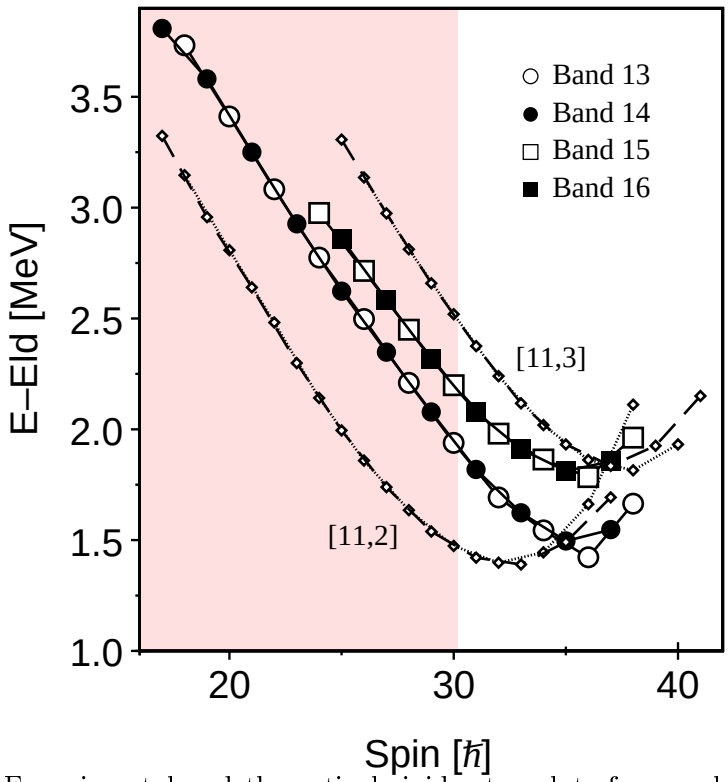

Figure 4.24: Experimental and theoretical rigid-rotor plots for coupled bands 15 and 16. Band 15 [−,0]: open squares, dotted line. Band 16 [−,1]: filled squares, dashed line. Bands 13 and 14 are shown for comparison.

upbend following the minimum. The position of the minimum is however two units of spin different from that predicted by the theoretical calculations. The experimental plot also has a slightly differing slope from that of the theory, providing a further discrepancy between theory and experiment. The conclusion that has to be drawn is that the theoretical calculations do not reproduce the experimental results particularly well for structures based on one-particle one-hole excitations across the Z=50 shell gap.

By using the relative intensity arguments and with comparison to theoretical excitation energies bands 15 and 16 are tentatively assigned as the two signature partner bands of the [11,3] configuration. The [11,3] configuration has a terminating spin given by, $\pi[(g_{9/2})^{-1}_{4.5}(h_{11/2})^{1}_{5.5}(g_{7/2}d_{5/2})^{2}_{6}]_{16} \otimes \nu[(h_{11/2})^{3}_{13.5}(g_{7/2}d_{5/2})^{5}_{11.5}]_{25}$. This configuration gives signature partner bands with maximal spins of 40^+ and 41^+ for bands 15 and 16 respectively. Using this interpretation band 15 is observed up to 38^+, one transition short of termination and band 16 is observed up to 37^+ two transitions away from the terminating state. The non-observation of the additional transitions can be explained by the low number

of statistics observed in these structures at high spin.

4.7.3 Summary

^{110}Te has provided the first evidence, in the A$\sim$100 region of the nuclear chart, for coupled smooth terminating bands extending to high spin. One of the coupled structures has been tentatively linked to the low spin level scheme and is observed up to termination. The calculations performed using a configuration-dependent shell-correction approach with a cranked Nilsson potential without pairing have been used to provide a basic theoretical interpretation for the observed structures. The agreement between theory and experiment obtained for the coupled band structures was however not as good as was observed for the ΔI=2 decoupled band structures, which involved two holes in the proton $g_{9/2}$ orbital.

The coupled band structures structures require a 1p-1h excitation involving a $g_{9/2}$ high-Ω proton hole, which results in coupled ΔI=1 bands with a small signature splitting. Similar structures have been observed in ^{106,108}Sn [jen98a] and ^{108}Sb [jen98b] isotopes. These structures have been interpreted in terms of tilted axis cranking (TAC) calculations, which predict that magnetic rotation should exist around proton or neutron closed shell regions. Magnetic rotation involves the rotation of a large magnetic dipole moment which breaks the spherical symmetry of weakly-deformed nuclei, as opposed to the conventional view of nuclear rotation, where the symmetry is broken by quadrupole deformation induced by distortion of the electric charge distribution.

The theory predicts that bands might be expected to exist based on the near perpendicular coupling at the bandhead of the angular momentum vectors from proton configurations, involving $g_{9/2}$ holes and aligned neutrons in the $h_{11/2}$ orbitals. Such a configuration for a [11,*] configuration has an angular momentum projection on the symmetry axis of $K = 5$. Higher angular momentum states may be generated by the shears mechanism, where the gradual alignment of the two component vectors with the tilted total angular moment vector I increases the total aligned angular momentum. The suggestion is that in a weakly deformed system a high angular velocity would be required to generate collective angular momentum, which allows magnetic rotation to compete.

The weakly deformed even-even N=58 isotone ^{108}Sn, which has 50 protons and 58 neutrons contains two band structures interpreted within the TAC formalism. It shows

the characteristics of the shears mechanism, where the strongly enhanced B(M1) values decrease with increasing angular momentum, since they are proportional to the square of the perpendicular component of the magnetic dipole vector. This manifests itself as a rapid drop off in M1 intensity as a function of spin. It would be reasonable, therefore, to expect that the coupled bands observed in the weakly deformed ^{110}Te nucleus could be described within this formalism.

The coupled bands observed in ^{110}Te are observed to have strong M1 transitions which extend up to near termination. This implies that these structures have a larger deformation and certainly show a significant stability against the shears mechanism. This may be explainable with the knowledge that the ΔI=1 bands interpreted within the TAC formalism are based on a $\nu[h_{11/2}] \otimes \pi[g_{7/2}g_{9/2}^{-1}]$ high-K ($K = 5$) configuration. In ^{110}Te the two extra protons result in the proton from the $g_{9/2}$ orbital being excited into the deformation driving $h_{11/2}$ orbital giving a $\nu[h_{11/2}]^2 \otimes \pi[h_{11/2}g_{7/2}g_{9/2}^{-1}]$ configuration. This extra deformation may be enough to stabilise the ΔI=1 bands observed within this regime.

4.8 ^{109}Te discussion

4.8.1 Introduction

The level scheme proposed for the extremely neutron deficient nucleus $^{109}_{52}\mathrm{Te}_{57}$ has been significantly extended in this work, see Fig. 3.20. In order to offer an interpretation of the existing and newly identified structures, the rotational behaviour of ^{109}Te has been investigated by observing the total aligned angular momentum along the rotation axis I_x. Following the same recipe used for ^{110}Te (discussed in sec. 4.1.1), a plot of I_x as a function of rotational frequency (ω) was constructed and is illustrated in Fig. 4.25.

Inspection of Fig. 4.25 reveals data points with irregular spacings, this indicates that the transitions identified in ^{109}Te are not rotational in nature. Indeed it was not possible to extract a suitable set of Harris parameters for this nucleus and therefore it is impossible to present an alignment plot in this discussion.

Theoretical cranked shell model (CSM) calculations have been performed for ^{109}Te using the prescription described in sec. 4.1.3, in order to provide further interpretation of the observed experimental band structures. The resulting quasiparticle plots for protons and

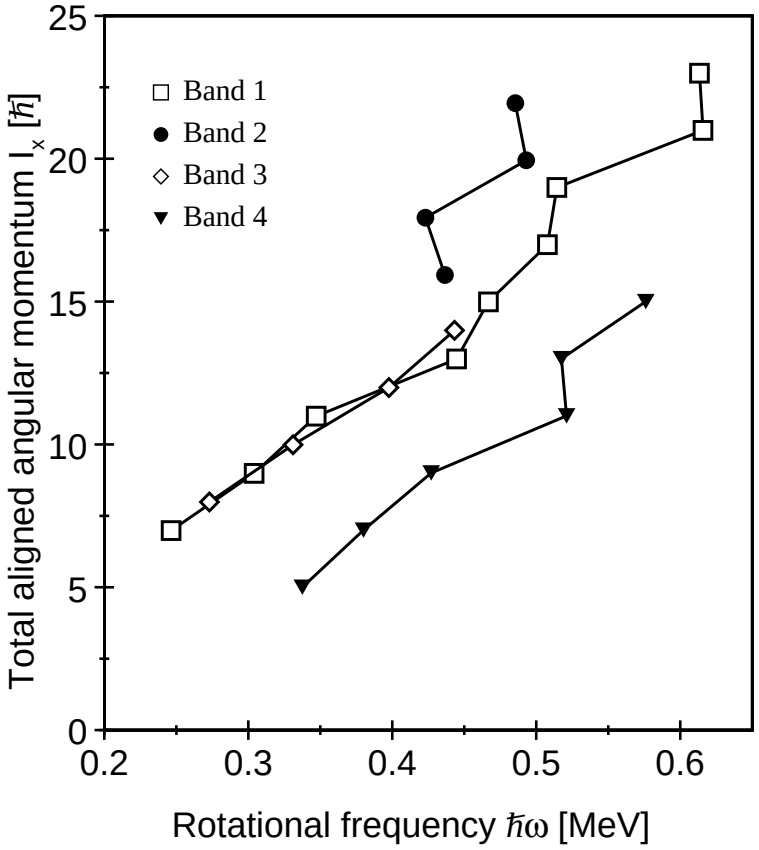

Figure 4.25: Total aligned angular momentum plot for ^{109}Te. Positive parity states are labelled with filled symbols.

neutrons are are shown in Fig. 4.26. The labelling of the quasiparticle orbitals is detailed in table 4.2. The neutron quasiparticle diagram Fig. 4.26(b) shows the most energetically favoured orbital for the odd neutron to residue in at moderate values of rotational frequency.

4.8.2 Low spin transitions in ^{109}Te - bands 5 and 6

Inspection of a single-particle Nilsson diagram similar to the one shown in Fig. 1.4, or the quasiparticle routhian diagram illustrated in Fig. 4.26(b), reveals that the neutron Fermi surface for ^{109}Te lies in the degenerate $\nu[d_{5/2}/g_{7/2}]$ subshells. This is just below the $\nu[h_{11/2}]$ intruder orbital which represents the ground state of odd tellurium isotopes with A$\geq$113.

The ground state of ^{109}Te was assigned in Ref. [dom95] as I^{π}=5/2^{+} on the basis of the systematics of light N=57 nuclei. The present analysis supports this interpretation which allows the ground state of ^{109}Te to be assigned as the $d_{5/2}$ quasineutron configuration.

In common with other tellurium isotopes ^{109}Te is expected to have a small quadrupole

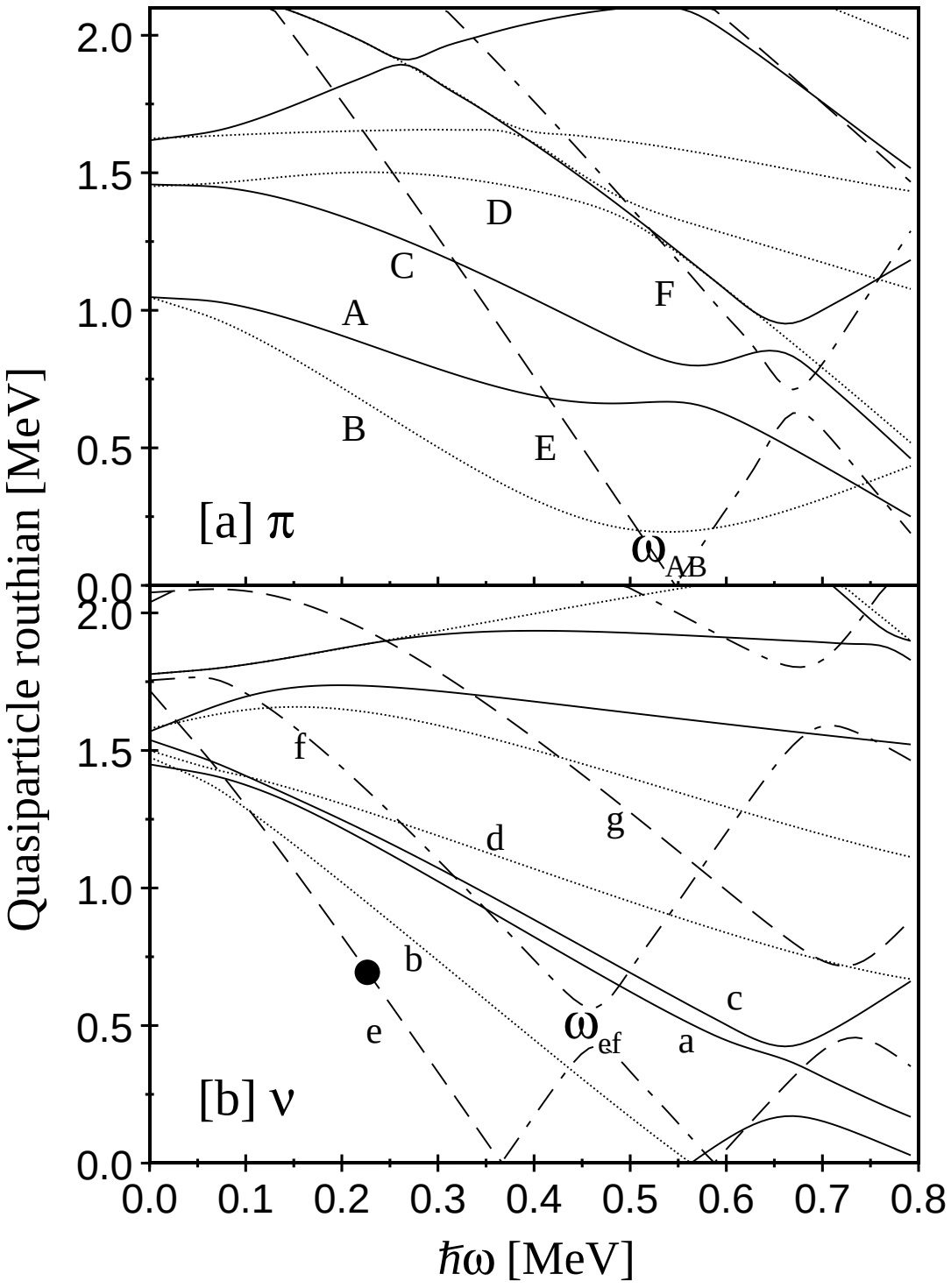

Figure 4.26: Cranked shell model calculations for ^{109}Te. [a] for protons [b] for neutrons. The calculations use the Nilsson potential with deformation parameters ε_2=0.135, ε_4=-0.04 and γ=-0.2°. The pairing gap used was Δ_p =1.030 MeV and Δ_n =1.420 MeV.

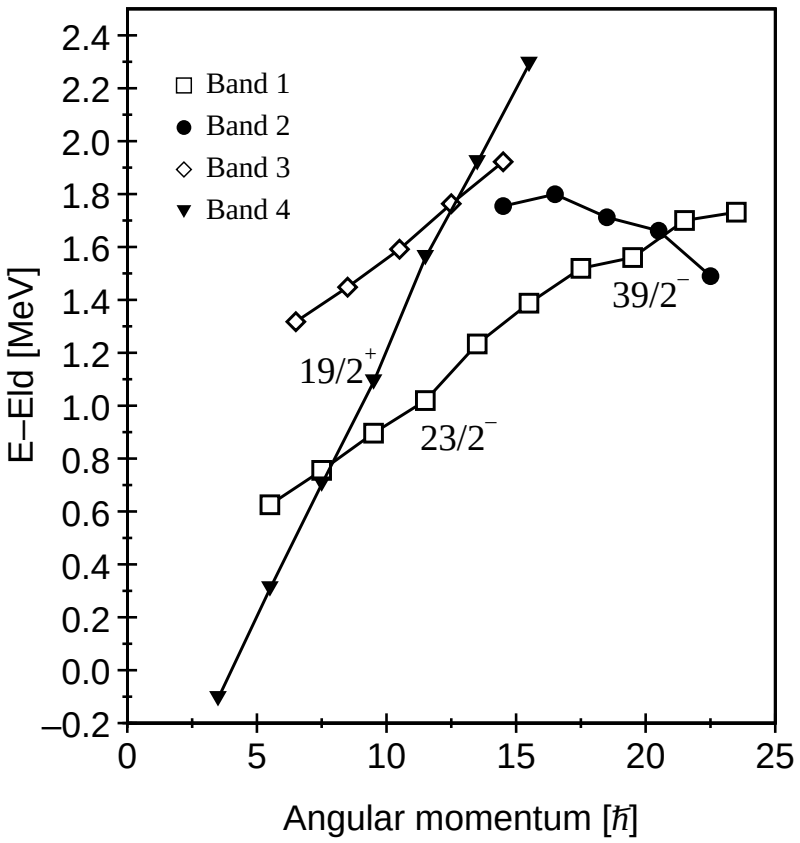

Figure 4.27: Experimental rigid-rotor plot for ^{109}Te. Positive parity states are labelled with filled symbols. Specific non-collective oblate states are indicated.

ground state deformation ($\varepsilon_2 \sim 0.135$) and hence a low spin decay scheme dominated by single-particle effects. The complicated pattern of positive-parity irregularly spaced γ-ray transitions observed below the $11/2^-$ state in ^{109}Te have been interpreted as quasineutron excitations involving the $d_{5/2}$ and $g_{7/2}$ orbitals coupled to quadrupole vibrations [dom95].

4.8.3 Bands 1 and 3

Experimental evidence provided from relative intensity and coincidence arguments implies that bands 1 and 3 are based on a similar configuration. The total aligned angular momentum plot, illustrated in Fig. 4.25, shows bands 1 and 3 have similar values of I_x. Such an observation would be expected for a pair of signature partner bands.

Fig. 4.27 shows the excitation energy minus a rigid-rotor reference, termed a rigid-rotor plot, for the band structures observed in ^{109}Te. With reference to this plot, band 1 is observed to be yrast from spin $19/2^-$ up to spin $39/2^-$. The plot shows that band 1 is

strongly energetically favoured over band 3, which explains the weak population of this structure and hence why it was only observed for the first time in this work. Band 1 can therefore be considered as the favoured signature for this particular configuration.

The assignment of an $11/2^-$ bandhead for band 1, was made with reference to other N=57 nuclei and odd tellurium isotopes [sea98], together with information provided from the CSM calculations. The calculations illustrated in Fig. 4.26(b), show that for increasing rotational frequency a N=5 neutron $h_{11/2}$ intruder orbital becomes strongly energetically favoured. The close proximity of this $\nu h_{11/2}$ orbital to the Fermi surface manifests itself with the observation of a low lying $11/2^-$ state, representing the negative parity negative signature $(\pi, \alpha) = (-, -1/2)$, which is energetically favoured for such a configuration. This interpretation is supported by experimental coincidence and angular correlation results. It is therefore possible to assign bands 1 and 3 as a one quasiparticle configuration based on both signatures of a negative parity $\nu[h_{11/2}]$ intruder orbital. With reference to the quasiparticle diagram it is the $[550]1/2^-$ Nilsson orbital, labelled as e, where the odd neutron resides.

Bands 1 and 3 show values of I_x, Fig. 4.25, consistent with a non-rotational interpretation. This allows these structures to be explained in terms of the $\nu[h_{11/2}]$ orbital coupled to the vibration-like states in the underlying even-even core (^{108}Te) [lan98b].

4.8.4 Band 2

Band 2 is discussed within the scenario of octupole collectivity in sec. 4.9.

4.8.5 Band 4

Band 4 has a firmly assigned $7/2^+$ bandhead based on an angular correlation measurement of the 96 keV transition, which carries intensity into the $5/2^+$ ground state of ^{109}Te. With reference to the neutron CSM calculations, illustrated in Fig. 4.26, it is observed that at low rotational frequency the odd signature $\nu[g_{7/2}]$ orbital, labelled b, is energetically favoured. With increasing rotational frequency the negative parity $\nu[h_{11/2}]$ orbital rapidly becomes the most energetically favoured.

The experimental rigid-rotor plot, shown in Fig. 4.27, shows a similar trend. Band 4 is observed to be yrast at low spin up to $15/2^+$ where negative parity band 1 is then observed yrast. This excellent agreement between theory and experiment allows band 4 to be firmly

E_γ	I^π	Band	R_{DCO}	B(E1)/B(E2)	B(E1)	B(E1)	$\|D_0\|$
(keV)	Initial			(10^{-6}fm^{-2})	$(10^{-3}\text{e}^2\text{fm}^2)$	10^{-3}(W.u.)	(efm)
633	$41/2^+$	2→1	0.58(8)	1.01(9)	1.42(10)	0.96(9)	0.111(10)
672[1]	$37/2^+$	2→1	0.88(7)	1.09(8)	1.52(10)	1.03(8)	0.115(10)
840	$33/2^+$	2→1	0.60(7)	1.02(7)	1.40(8)	0.95(6)	0.110(8)
775	$21/2^-$	3→4	–	0.08(4)	0.11(5)	0.08(4)	0.031(15)
966	$17/2^-$	3→4	–	0.05(3)	0.06(3)	0.04(2)	0.024(12)

Table 4.6: Measured electric dipole strengths in ^{109}Te assuming $Q_0 = 200\text{efm}^2$ for $\varepsilon_2 = 0.135$. [1] Energy doublet : Intensity measurement is that of composite peak.

assigned as built on a $\nu[g_{7/2}]$ configuration.

4.9 Evidence for octupole correlation effects

Band 2 has been assigned positive parity following the establishment of inferred electric dipole (E1) transitions linking this structure to band 1. A number of inferred electric dipole transitions are also observed to link band 3 to band 4. Table 4.6 contains a summary of the DCO results, which suggest a pure dipole nature to these transitions, implying they have an electric character. Confirmation of the electromagnetic nature of these dipole transitions, perhaps through a measurement of the linear polarisation of the γ-rays, is therefore paramount in order to firmly establish their character.

The magnitude of the intrinsic electric dipole moment (D_0) for ^{109}Te has been extracted by measurement of γ-ray branching ratios, using the recipe described in sec. 4.4, in order to try to determine a possible configuration for band 2. The experimental B(E1) values were computed using a quadrupole moment estimate of Q_0=200efm^2, obtained from TRS calculations [wys88]. The results including B(E1)/B(E2) ratios of reduced transition probabilities, B(E1) strengths and estimated D_0 values are summarised in table 4.6. The results are plotted together with the systematics of B(E1) strengths extracted in this mass region in Fig. 4.8, which can be found in sec. 4.4. The use of an assumed value of Q_0 means the absolute values for B(E1) and D_0 should only be considered accurate to with ±25%.

The magnitude of the D_0 results obtained for ^{109}Te band 2 are remarkably similar to

the those measured in ^{110}Te, see Fig. 4.8. The B(E1) strength of $\sim 10^{-3}$W.u. obtained for band 2 in ^{109}Te is similar to results in the neutron rich barium isotopes which lie on an octupole magic number (Z=56) and is slightly smaller than results obtained in the Ra-Th region [But96] the most well developed region for octupole effects.

The enhanced E1 strength observed in ^{109}Te is cited as evidence for octupole correlation effects, see sec. 1.12.1. The vibrational character of ^{109}Te has prevented a meaningful Δi_x plot from being constructed. Δi_x shows the difference in alignment between two structures and can be used to determine the static or vibrational character of the octupole enhancement. Therefore with reference to the results obtained for ^{110}Te, sec. 4.4, it is tentatively concluded that positive parity band 2 can be described in terms of an aligned octupole phonon coupled to the $\nu[h_{11/2}]$ core. Such a conclusion is not unreasonable given the close proximity of orbitals differing in $\Delta j/l$ by 3, namely the $h_{11/2} \leftrightarrow d_{5/2}$ orbitals.

The D_0 results obtained for band 2 in ^{109}Te do not show any noticeable spin dependence. It has been postulated that rotation may stabilise octupole deformation at high spin [smi95]. The results obtained here however have a large associated uncertainty so it is not possible to draw any conclusions from this observation.

The inferred electric dipole transitions which link bands 3 and 4 have values of B(E1) a factor of ten smaller than those observed linking bands 1 and 2. These transitions are not cited as providing evidence for octupole correlation effects.

4.10 Evidence for aligned non-collective oblate states

^{109}Te manifests similar unexpectedly low lying energetically favoured states similar to those observed in ^{110}Te (sec. 4.5). Inspection of the rigid-rotor plot for ^{109}Te illustrated in Fig. 4.27, reveals $23/2^-$, $35/2^-$ and $19/2^+$ as low-lying states, which are labelled for clarity.

The $23/2^-$ state is shown to be particularly favoured. The state can be assigned as a fully aligned $\pi[(g_{7/2})^2_{6^+}] \otimes \nu[(h_{11/2})_{11/2^-}]_{23/2^-}$ oblate configuration. Such a low lying $23/2^-$ state based on the same configuration has been experimentally observed in a number of heavier odd tellurium isotopes.

The excitation energies of the $\nu[h_{11/2}]$ yrast sequences in the odd-A $^{109-121}$Te [sea98] isotopes are compared in Fig. 4.28. There is a smooth behaviour observed between all these isotopes, supporting a similar understating of the configuration of the low spin transitions.

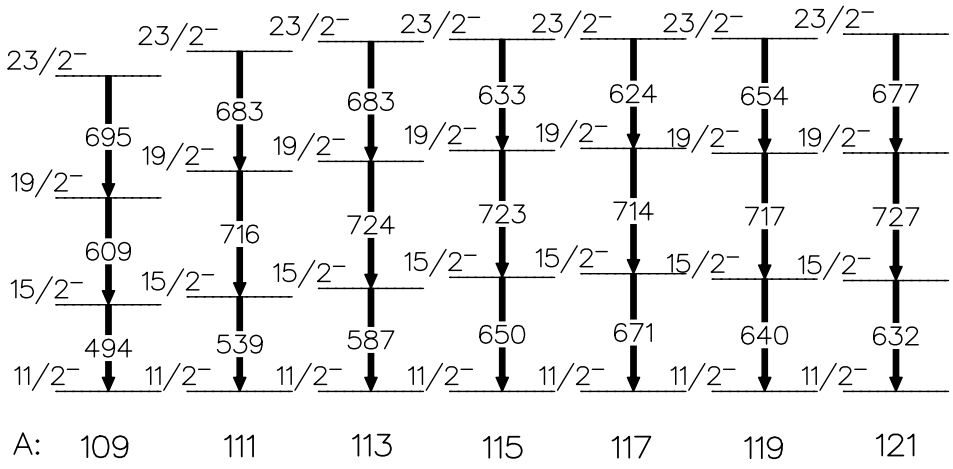

Figure 4.28: Odd tellurium systematics, showing the $\nu[h_{11/2}]$ yrast band structure.

It is noticeable that the $23/2^-$ level is depressed in all of these cases.

The $39/2^-$ state is another particularly low lying point on the rigid-rotor plot. It may present evidence for an aligned state based on the $\pi[(g_{7/2})^2]_{6^+} \otimes \nu[(h_{11/2})^3_{27/2^-}]_{39/2^-}$ oblate configuration. This state is similar to that observed in other heavier odd mass tellurium isotopes such as ^{115}Te [pau95a], wehere a low lying $37/2^-$ state based on this configuration is observed.

A third low lying state is observed in band 4 at $19/2^+$, this state is believed to be based on a fully aligned $\pi[(g^2_{7/2})_{6^+}] \otimes \nu[(g_{7/2})_{7/2^+}]_{19/2^+}$ oblate state which is predicted using TRS calculations [wys88] to be a particular favoured configuration.

Chapter 5

Conclusions and further remarks

The GAMMASPHERE γ-ray spectrometer when used in conjunction with the MICROBALL charged particle detector and a number of neutron detectors, has been shown to be an extremely powerful tool for the purpose of high-spin γ-ray spectroscopy studies.

High-spin states in the neutron deficient even-even ^{110}Te nucleus have been populated using the α2p exit channel. The level scheme of this nucleus has been significantly extended from what was previously known. The large number of statistics obtained has allowed extremely weak structural features to be discerned, allowing a significant insight into how nuclei in close proximity to the Z=50 shell gap behave with increasing values of angular momentum.

At low spin, the ^{110}Te level scheme has been completely reconstructed with the addition of several new band structures. The vibrational nature of the near-spherical tellurium nucleus has been confirmed by the observation of a characteristically single-particle like decay scheme. Evidence has been cited for possible co-existence of a spherical and deformed nuclear shape at low spin. With increasing spin the onset of octupole correlation effects, induced by the close proximity of the $h_{11/2} \leftrightarrow d_{5/2}$ orbitals to the Fermi surface has been postulated. It is suggested that the octupole correlations are induced by the coupling of an octupole phonon to the core.

Evidence for the existence of specific aligned non-collective oblate states has been presented, implying that in a weakly deformed nucleus such as ^{110}Te these oblate configurations can indeed compete with states built on nuclear rotation.

Evidence has been cited for the first time for collective high-spin band structures in this

nucleus. Four new $\Delta I = 2$ bands showing the characteristics of smooth band termination have been identified. One of these structures has been tentatively linked to the low-spin level scheme and has been identified up to its terminating spin. The three other structures have been assigned tentative spins and parities based on excitation energy and coincidence arguments.

These smooth terminating structures have been interpreted using theoretical calculations which use a configuration-dependent shell-correction approach with a cranked Nilsson potential without pairing [afa95]. These structures have been shown to be based on two-particle two-hole excitations across the Z=50 shell gap. Such a configuration establishes a moderately deformed structure which can be traced all the way to termination where it terminates as a non-collective oblate state.

Two strongly coupled $\Delta I = 1$ band structures with characteristic cross-over E2 transitions have been established extending to high spin. These structures involve a one particle - one hole excitation involving the $g_{9/2}$ high-K proton hole which results in coupled $\Delta I = 1$ bands with a small signature splitting. The bands show a significant stability against the shears mechanism, implying that they have a moderate deformation. Indeed it is proposed that these $\Delta I = 1$ bands show the characteristics of smooth band termination and therefore represent the first observation of such structures in any region of the nuclear chart. The configuration-dependent calculations which provided an excellent reference for the $\Delta I = 2$ bands structures did not reproduce the experimental results for these structures well.

High-spin states in the neutron deficient even-odd ^{109}Te nucleus have also been populated using the α2pn exit channel. The low yield obtained with this exit channel precluded the observation of any collective high-spin band structures, however the low spin level scheme has been significantly extended. Evidence is cited for octupole correlation effects and the existence of specific non-collective oblate states.

The thin target data obtained in this experiment and discussed in this thesis has provided a wealth of new information on the light neutron deficient tellurium isotopes. It is essential now to follow up this work in order to provide firm experimental evidence for a number of the conclusions proposed in this work.

Firstly a measurement of the linear polarisation of the inferred E1 transitions which have been used to provide evidence for octupole correlation effects in the tellurium isotopes

is required. Without this fundamental information about the electromagnetic character of these transitions the octupole scenario must remain tentative.

The majority of the high spin bands observed in ^{110}Te have no discrete links to the low spin level structures, hindering a firm assignment of spins and parities for these structures. It is observed that some of the unlinked structures feed into the yrast or near yrast levels with moderate spins. It is therefore reasonable to expect that the lifetimes of the linking transitions are long enough to be observed as stopped lines in a backed target. The use of a large high efficiency array of HPGe detectors combined with a backed target, in order to provide an excellent energy resolution, will therefore provide the data set necessary to establish and characterise the weak linking transitions.

The high-spin band structures in ^{110}Te have been interpreted as showing the characteristics of smooth band termination, a scenario where the nucleus shows a gradual shape change from collective prolate to non-collective oblate as the available valence particles align. This is manifest as a decrease in the transition quadrupole moment (Q_t) with increasing spin as the band approaches the non-collective terminating state. A direct measurement of Q_t for ^{108}Sn and ^{109}Sb indicated a gradual decrease in Q_t consistent with predictions [wad98], this measurement should be followed up for the heavier tellurium and iodine isotopes.

References

[and76] G.Andersson *et al.* Nucl. Phys. **A268**, (1976) 205.

[afa95] A.V.Afanasjev and I.Ragnarsson, Nucl. Phys. **A591**, (1995) 387.

[bax92] A.M. Baxter *et al.* Nucl. Instr. Meth. **A317**, (1992) 101.

[ben85] T.Bengtsson and I.Ragnarsson, Nucl. Phys. **A436**, (1985) 14.

[ben89] R. Bengtsson *et al.* Physica Scripta,**Vol 39**, (1989) 196.

[Boh36] N. Bohr, Nature **344**, 137 (1936).

[Boh75] A. Bohr and B.R. Mottelson, Nuclear Structure Volume II:Nuclear Deformations, W.A. Benjamin Inc. New York (1975).

[bea92] C.W. Beausang *et al.*, Nucl. Instr. Meth. **A313**, 37 (1992).

[But96] P.A. Butler and W. Nazarewicz, Rev. Mod. Phys. **68**, 349 (1996).

[cho82] P. Chowdhury, W.F. Piel Jr., and D.B. Fossan, Phys. Rev. C. **25**, (1982) 813.

[dom95] Zs. Dombradi *et al.*, Phys. Rev. C **51** (1995) 2394.

[don87] F. Dönau, Nucl. Phys. **A471** (1987) 469.

[fle89] A. Kramer-Flecken *et al.*, Nucl. Instr. Meth. **A275** (1989) 333.

[fra81] S. Frauendorf, Phys. Lett. **B100** (1981) 219.

[fra93] S. Frauendorf, Nucl. Phys. **A557** (1993) 259c.

[hee94] P.H. Heenen *et al.*, Phys. Rev. C. **50** (1994) 802.

[jan94] V.P. Janzen *et al.*, Phys. Rev. Lett. **72**, (1994) 1160.

[jen98a] D.G. Jenkins, I.M. Hibbert, C.M. Parry, R. Wadsworth, D.B. Fossan, G.J. Lane, J.M. Sears, J.F. Smith, R.M. Clark, R. Krücken, I.Y. Lee, A.O. Macchiavelli, V.P. Janzen, J. Cameron, and S. Frauendorf, Phys. Lett. **B428** (1998) 23.

[jen98b] D.G. Jenkins, R. Wadsworth, J. Cameron, R.M. Clark, D.B. Fossan, I.M. Hibbert, V.P. Janzen, R. Krücken, G.J. Lane, I.Y. Lee, A.O. Macchiavelli, C.M. Parry, J.M. Sears, J.F. Smith and S. Frauendorf, Phys. Rev. C. **58** (1998) 2703.

[kno89] G.F. Knoll, Radiation Detection and Measurement, Second Edition, Wiley (1989).

[lan98a] G.J. Lane, D.B. Fossan. C.J. Chiara, H. Schnare, J.M. Sears, J.F. Smith, I. Thorslund and P. Vaska, Phys. Rev. C. **58**, (1998) 127.

[lan98b] G.J. Lane, D.B. Fossan, C.J. Chiara, H. Schnare, J.M. Sears, J.F. Smith, I. Thorslund and P. Vaska, Phys. Rev. C. **57**, (1998) R1022.

[Lea82] G.A. Leander *et al.*, Nucl. Phys. **A388** (1982) 453.

[Lea86] G.A. Leander, W. Nazarewicz, G.F. Bertsch and J. Dudek, Nucl. Phys. **A435** (1986) 58.

[lee90] I.Y. Lee *et al.*, Nucl. Phys. **A520**, (1990) 641c.

[lob70] K.E. Löber, M. Vetter and V. Honig, Nucl. Data Tables, **A7** (1970) 495.

[lon86] T. Lonnroth, A. Vitanen, and J. Hattula, Physica Scripta **34**, (1986) 682.

[mar95] J.W. Marsh *et al.*, Nucl. Instr. Meth. **A366** (1995) 340.

[naz87] W. Nazarewicz, G.A. Leander and J. Dudek, Nucl. Phys. **A467**, (1987) 437.

[naz89] W. Nazarewicz, R. Wyss and A. Johnson, Nucl. Phys. **A503**, (1989) 285.

[Nil69] S.G. Nilsson, Nucl. Phys. **A131** (1969) 1.

[orn] Oakridge National Laboratory, Private Communication.

[pau94] E.S. Paul *et al.* Phys. Rev. C. **50** (1994) R534; Phys. Rev. C. **50** (1994) 698.

[pau95] E.S. Paul, P.J. Woods, T. Davinson, R.D. Page, R.J. Sellin, C.W. Beausang, R.M. Clark, R.A. Cunningham, S.A. Forbes, D.B. Fossan, A. Gizon, J. Gizon, K. Hauschild, I.M. Hibbert, A.N. James, D.R. LaFosse, I. Lazarus, H. Schnare, J. Simpson, R. Wadsworth, and M.P Waring, Phys. Rev. C. **51**, (1995) 78.

[pau95a] E.S. Paul, D.B. Fossan, J.M. Sears, and I. Thorslund, Phys. Rev. C. **52** (1995) 2984.

[pau98a] E.S. Paul, H.C. Scraggs, A.J. Boston, D.B. Fossan, K. Hauschild, I.M. Hibbert, P.J. Nolan, H. Schnare, J.M. Sears, I. Thorslund, R. Wadsworth, A.N. Wilson, and J.N. Wilson, Nucl. Phys. **A644** (1998) 3.

[pauUP] E.S. Paul (unpublished).

[pla75] F. Plasil and M. Blann, Phys. Rev. C. (1975) 11.

[rad95] D.C. Radford, Nucl. Instr. Meth. **A361** (1995) 297.

[rag95] I. Ragnarsson, V.P. Janzen, D.B. Fossan, N.C. Schmeing and R. Wadsworth, Phys. Rev. Lett. **74** (1995) 3935.

[roh88] S.G.Rohozinski *et al.*, Rep. Prog. Phys. **51** (1988) 541.

[sar96] D.G. Sarantites *et al.*, Nucl. Instr. Meth. **A381** (1996) 418.

[sew94] D. Seweryniak *et al.*, Nucl. Instr. Meth. **A340** (1994) 353.

[sch95] G.J. Schmid, LBNL, Berkeley, CA.

[sch96] H. Schnare *et al.*, Phys. Rev. C. **54** (1996) 1598.

[scr98] H.C. Scraggs, E.S. Paul, A.J. Boston, J.F.C. Cocks, D.M. Cullen, K. Helariutta, P.M. Jones, R. Julin, S. Juutinen, H. Kankaanpää, M. Muikku, P.J. Nolan, C.M. Parry, A. Savelius, R. Wadsworth, A.V. Afanasjev, and I. Ragnarsson, Nucl. Phys. **A640** (1998) 337.

[sea98] J.M. Sears, I. Thorslund, D.B. Fossan, P. Vaska, E.S. Paul, K. Hauschild, I.M. Hibbert, R. Wadsworth, and S.M. Mullins, Phys. Rev. C. **57** (1998) 1656.

[ska90] J. Skalski, Phys. Lett. **B238** (1990) 6.

[smiG] J.F. Smith, Nuclear Structure 98, Gatlinburg, Conference Proceedings.

[sim94] J. Simpson *et al.*, Phys. Lett. **B327**, (1994) 187.

[smi95] J.F. Smith, Phys. Rev. Lett. **75** (1995) 1050.

[str67] V.M. Strutinsky, Nucl. Phys. **A95** (1967) 420.

[str68] V.M.Strutinsky, Nucl. Phys. **A112** (1968) 1.

[tho95] I. Thorslund *et al.*, Phys. Rev. C. **52**, (1995) R2839.

[tid85] P. Tidemand-Petersson *et al.*, Nucl. Phys. **A437**, (1985) 342.

[twi93] P.J. Twin *et al.*, Nucl. Phys. **A557** (1993) 3c.

[wad93] R.Wadsworth *et al.*, Nucl. Phys. **A559**, (1993) 461.

[wad94] R.Wadsworth *et al.*, Phys. Rev. C. **50**, (1994) 483.

[wad96] R.Wadsworth *et al.*, Phys. Rev. C. **53**, (1996) 2763.

[wad98] R. Wadsworth, R.M. Clark, J.A. Cameron, D.B. Fossan, I.M. Hibbert, V.P. Janzen, R. Krücken G.J. Lane, I.Y. Lee, A.O. Macchiavelli, C.M. Parry, J.M. Sears, J.F. Smith, A.V. Afanasjev, and I. Ragnarsson, Phys. Rev. Lett. **80** (1998) 1174.

[war95] M.P. Waring, E.S. Paul, C.W. Beausang, R.M. Clark, R.A. Cunningham, T. Davinson, S.A. Forbes, D.B. Fossan, A. Gizon, J. Gizon, K. Hauschild, I.M. Hibbert, A.N. James, P.M. Jones and M.J. Joyce, Phys. Rev. C. **51**, (1995) 2427.

[wys88] R. Wyss, J. Nyberg, A. Johnson, R. Bengtsson, and W. Nazarewicz, Phys. Lett. **B215**, (1988) 211.

[zha89] J.-y. Zhang, N. Xu, D.B. Fossan, Y. Liang, R. Ma and E.S. Paul, Phys. Rev. C. **39** (1989)714.